

NASA CONTRACTOR REPORT 166471

ORIGINAL PAGE IS  
OF POOR QUALITY

Flight Dynamics Analysis and  
Simulation of Heavy Lift Airships

Volume II: Technical Manual

(NASA-CR-166471-Vol-2) FLIGHT DYNAMICS  
ANALYSIS AND SIMULATION OF HEAVY LIFT  
AIRSHIPS. VOLUME 2: TECHNICAL MANUAL  
Final Report, Sep. 1979 - Dec. 1982 (Systems  
Technology, Inc.) 314 p HC A14/NP A01

83-22208  
Unclas  
G3/08 09708

Robert F. Ringland  
Mark B. Tischler  
Henry R. Jex  
Roger D. Emmen  
Irving L. Ashkenas



CONTRACT NAS2-10330  
December 1982

**NASA**

NASA CONTRACTOR REPORT 166471

ORIGINAL PAGE IS  
OF POOR QUALITY

Flight Dynamics Analysis and  
Simulation of Heavy Lift Airships

Volume II: Technical Manual

Robert F. Ringland  
Mark B. Tischler  
Henry R. Jex  
Roger D. Emmen  
Irving L. Ashkenas  
Systems Technology, Inc.  
Hawthorne, California

Prepared for  
Ames Research Center  
under Contract NAS2-10330

**NASA**

National Aeronautics and  
Space Administration

**Ames Research Center**  
Moffett Field, California 94035

## FOREWORD

This document is the second in a five volume report which describes a comprehensive digital computer simulation of the dynamics of heavy lift airships and generically similar vehicle.

The work was performed by Systems Technology, Inc., Hawthorne, California for the Aeronautical Systems Branch in the Helicopter and Powered Lift Division of the National Aeronautics and Space Administration, Ames Research Center, Moffett Field, California. The simulation development was carried on between September 1979 and January 1982 and is currently installed on the Ames Research Center CDC 7600 computer. The contract technical monitors for NASA were Dr. Mark Ardema, Mr. Alan Faye, and Mr. Peter Talbot. STI's Program Manager was Mr. Irving Ashkenas.

The authors wish to acknowledge the technical contributions of Mr. Robert Heffley, Mr. Thomas Myers, and Mr. Samuel Craig and the further contributions of Mr. Allyn Hall, Ms. Natalie Hokama and Ms. Leslie Hokama in simulation software development. Special thanks are due to Ms. Kay Wade, Ms. Linda Huffman, Mr. Charles Reaber, and STI's production department for the preparation of the five volumes of this report.

TABLE OF CONTENTS

	<u>Page</u>
1. INTRODUCTION.....	1-1
A. Simulation Overview.....	1-1
B. Documentation.....	1-2
C. Technical Manual Summary.....	1-2
2. HLA MOTION EQUATIONS.....	2-1
A. Motion Equations Overview.....	2-1
B. Notation, Coordinates, Geometry, and Units.....	2-2
C. Kinematic Equations.....	2-15
D. Payload Equations of Motion.....	2-18
E. Multibody Solution Algorithm.....	2-20
F. Hull and LPU Equations of Motion.....	2-23
G. Hull and LPU Constraint Equations.....	2-25
H. Force and Moment Summations.....	2-31
I. State Vector Rate of Change.....	2-32
3. NON-AERODYNAMIC EXTERNAL FORCES AND MOMENTS.....	3-1
A. Scope.....	3-1
B. Gravitational Forces.....	3-1
C. Landing Gear Forces and Moments.....	3-2
D. Sling Forces and Moments.....	3-7
E. Direct Thrust Forces and Moments.....	3-9
F. Cautionary Remarks.....	3-11
4. FLIGHT CONTROL SYSTEM.....	4-1
A. Overview.....	4-1
B. Mixer Box.....	4-1
C. Test Input Features.....	4-4
D. Control Loops.....	4-5
E. Sensors — Choice of State Feedbacks.....	4-8
F. Commands.....	4-9
G. Cautionary Remarks.....	4-11

TABLE OF CONTENTS (Continued)

ORIGINAL PAGE IS  
OF POOR QUALITY

	<u>Page</u>
5. AERODYNAMICS OVERVIEW.....	5-1
A. Introduction.....	5-1
B. Computational Flow.....	5-2
C. Atmospheric Environment.....	5-5
D. Aerodynamic Interference Effects.....	5-9
6. ATMOSPHERIC ENVIRONMENT.....	6-1
A. Model Types and Basic Assumptions.....	6-1
B. Steady Wind Model Equations.....	6-2
C. Discrete Test Input Model.....	6-3
D. Multiple Source Atmospheric Input Model.....	6-6
E. Superposition of the Steady Wind, Discrete, and Multiple Source Models.....	6-15
7. LIFT PROPULSION UNIT AERODYNAMIC FORCES AND MOMENTS.....	7-1
A. Basic Assumptions.....	7-1
B. Velocities Relative to Local Airmass.....	7-3
C. Hull on LPU Velocity Interference.....	7-4
D. Rotor Axis Transformations and Vector Resolutions.....	7-10
E. Rotor Forces and Torques.....	7-14
F. Thrust Coefficient and Induced Flow.....	7-16
G. Additional Interference Effects.....	7-26
H. Rotor Flapping Coefficients.....	7-33
I. Horizontal Force and Torque Coefficients.....	7-34
J. Propeller Forces and Torques.....	7-36
K. Fuselage (Nacelle) Aerodynamics.....	7-38
L. Power Off Forces and Moments.....	7-41
M. Summation of Forces and Moments.....	7-43

TABLE OF CONTENTS (Continued)

ORIGINAL PAGE IS  
OF POOR QUALITY

	<u>Page</u>
8. HULL/TAIL ASSEMBLY AERODYNAMICS.....	8-1
A. Basic Assumptions.....	8-1
B. Velocities and Accelerations Relative to Local Airmass.....	8-4
C. Hull and Tail Relative Velocity Interference Effects.....	8-8
D. Quasi-Steady Hull Aerodynamics.....	8-22
E. Quasi-Steady Tail (On Hull) Aerodynamics.....	8-30
F. Typical Hull-Tail Quasi-Steady Aerodynamic Characteristics.....	8-49
G. Additional Interference Effects.....	8-53
H. Unsteady Aerodynamics and Buoyancy.....	8-61
I. Computational Considerations and Example.....	8-74
9. PAYLOAD AERODYNAMICS.....	9-1
A. Basic Assumptions.....	9-1
B. Velocities <sup>†</sup> Relative to the Local Air Mass.....	9-1
C. Payload Aerodynamic Forces and Moments.....	9-2
10. TRIM STATE CALCULATIONS.....	10-1
A. Overview.....	10-1
B. Trim Algorithm.....	10-2
C. Special Situations.....	10-7
11. LINEARIZATION.....	11-1
A. Overview.....	11-1
B. Equations of Motion.....	11-1
C. Auxiliary Equations.....	11-3
D. Derivative Approximation.....	11-4
E. Eigenvalues and Eigenvectors.....	11-5
REFERENCES.....	R-1
APPENDIX A.....	A-1
APPENDIX B.....	B-1
APPENDIX C.....	C-1

ORIGINAL PAGE IS  
OF POOR QUALITY

LIST OF FIGURES

	<u>Page</u>
2-1. Vector Geometry of Hull, Payload and ith LPU.....	2-10
2-2. Gimbal Angle Rates for ith LPU.....	2-15
2-3. Equations of Motion for Hull and Lift-Propulsion Units (Eq. 2-65).....	2-24
2-4. Constraint Force Terms, $I_{VCEC}$ , in Equations of Motion for Hull and LPUs (Eq. 2-70).....	2-26
2-5. Vector-Matrix Acceleration Constraint Equations (Eq. 2-85).....	2-30
3-1. Landing Gear Model Geometry.....	3-3
3-2. Landing Gear Static Force Model.....	3-3
3-3. Orientation of Direct Thrust Vector Relative to LPU Reference Axes.....	3-10
4-1. Control System Loop Structure.....	4-2
5-1. Computational Flow of Aerodynamic Model.....	5-3
5-2. Atmospheric Input Model.....	5-7
6-1. Discrete Test Input (g) and Input Derivative ( $\dot{g}$ ) Forms.....	6-4
6-2. Geometry for Atmospheric Input Model.....	6-7
7-1. Geometry for Lift Propulsion Unit (LPU).....	7-5
7-2. Hull Wake Geometry for Pure Translational Motion.....	7-6
7-3. Hull Wake Defect Function.....	7-8
7-4. Rotor Coordinate Systems.....	7-14
7-5. Rotor Ground Effect in Hovering Flight.....	7-18
7-6. Sketch of Normalized Inflow Velocity vs. Normalized Vertical Speed for Zero Forward Speed, $GEF = 1$ (No Ground Effect).....	7-24

**ORIGINAL PAGE IS  
OF POOR QUALITY**

	<u>Page</u>
7-7. Rotor Wake Geometry for Non-Hovering Flight; from Ref. 7-2.....	7-28
7-8. Hull Wake Turbulence Effect on Rotor Thrust.....	7-30
7-9. Variation of Hull Interference Parameter KHRB with Rotor Placement.....	7-31
7-10. Orientation of Propeller Shaft Axes Relative to the LPU Reference Frame.....	7-37
8-1. Hull Geometry Vectors.....	8-5
8-2. Rotor-Induced Velocities on HLA Hull in Hover; Thrust Loading (T/A) = 8.26 lb/ft <sup>2</sup> ; from Ref. 8-4.....	8-10
8-3. Ground-on-Hull Velocity Interference Model.....	8-17
8-4. Variation in Ground Induced Flow Rotation Angle (λ') with Nondimensional Hull Height (h) .....	8-20
8-5. Tail Static Y-Force Model.....	8-39
8-6. Flow Regimes for Tail, Rolling Moment Static Model.....	8-46
8-7. Comparison of Akron Airship Data with Quasi- Steady Models.....	8-52
8-8. Simulation Test Configuration.....	8-54
8-9. Quasi-Steady Aerodynamic Characteristics of the Test Configuration.....	8-55
8-10. Rotor Interference Effect on Hull Crossflow Drag Coefficient for Edward Rotor Locations (d̄ = 1.5).....	8-57
8-11. Ground Interference Effect on Hull Crossflow Drag Coefficient.....	8-60
8-12. Typical Tail Vertical Force Time History During a Step Up-Gust Encounter (From Ref. 8-23).....	8-63
8-13. Time History of Aerodynamic Terms During an Oblique Up-Gust Encounter.....	8-88
10-1. Sketch of Secant Approximation.....	10-3

ORIGINAL PAGE IS  
OF POOR QUALITY

LIST OF TABLES

	<u>Page</u>
2-1. Notation Convention.....	2-4
2-2. Integrated and Dependent Variables, HLASIM Program.....	2-33
2-3. Added Integrated Variables, HLAPAY Program.....	2-34
2-4. Changes to Integrated and Dependent Variables, HLAMOR Program.....	2-34
4-1. Test Input Capabilities.....	4-5
4-2. Control Loop Signals.....	4-6
4-3. Control Loop Parameters.....	4-6
4-4. Sensor Signals.....	4-8
4-5. Command Signals.....	4-10
8-1. Tail Aerodynamic Regimes.....	8-37

## SECTION 1

### INTRODUCTION

#### A. SIMULATION OVERVIEW

The heavy lift airship simulation models a hybrid vehicle consisting of a central hull with as many as four lift-propulsion units (LPUs) attached. The LPUs are nacelles each having a main lifting rotor and an auxiliary propeller, and can be characterized as modified helicopters. The model includes a slung payload, a flight control system, landing gears and a mooring point. The characteristics of all model elements are defined in the input data.

The simulation takes the form of three computer programs:

- HLASIM -- models the powered vehicle in flight.
- HLAMOR -- models the unpowered vehicle constrained at one point to a mooring mast.
- HLAPAY -- models the powered vehicle in flight with a slung payload.

The programs all use the same basic algorithm and large parts of each use the same code and share the same data files.

The mathematical model provides for the numerical evaluation of the time rate of change of a multi-element state vector,  $\dot{\underline{S}}$ . The elements of  $\dot{\underline{S}}$  are linear and angular accelerations, linear and angular velocities, and rates of change of certain flight control system variables. In general, the elements of  $\dot{\underline{S}}$  are nonlinear functions of the elements of  $\underline{S}$ , and the input commands and disturbances.

The programs each contain a trimming algorithm (different for each of the three programs) for establishing a specified steady-state condition; certain elements of  $\dot{\underline{S}}$  equal zero. They each contain an integration routine that computes the time history of  $\underline{S}$  using the established trim as an initial condition. Finally, the three programs each include

a linearization algorithm for calculating stability and response derivatives -- rates of change of elements of  $\dot{S}$  with the elements of  $S$  and the input commands and disturbances.

## B. DOCUMENTATION

Simulation documentation, apart from the program listings, is in the form of three manuals. In addition to this Technical Manual, there is a User's Manual and a Programmer's Manual.

This Technical Manual describes the mathematical models embodied in the simulation in considerable detail and with supporting evidence for the model forms chosen. In addition it describes the trimming and linearization algorithms used in the simulation. Appendices to the manual identify reference material for estimating the needed coefficients for the input data and provide example simulation results.

The User's Manual provides the basic information necessary to run the programs. This includes descriptions of the various data files necessary for the program, the various outputs from the program and the options available to the user when executing the program. Additional data file information is contained in the three appendices to the manual. These appendices list all input variables and their permissible values, an example listing of these variables, and all output variables available to the user.

The Programmer's Manual is intended for the maintenance programmer who will support the program. It contains explanations of the logic embodied in the various program modules, a dictionary of program variables, a subroutine listing, subroutine/common-block/cross-reference listing, and a calling/called subroutine cross reference listing. The manual does not repeat data already available in the User's Manual.

## C. TECHNICAL MANUAL SUMMARY

Section 2 describes the inertial and geometric modeling embodied in the HLA simulation as well as the notational conventions, coordinate transformations, etc. The hull and attached LPUs (as many as four) are

modeled as an interconnected set of rigid bodies subject to external forces described in later sections. The equations of motion model each body separately subject to constraining forces acting at the attach points to the hull, as well as to the external forces. The solution algorithm gives accelerations of each body and the constraint forces at the attach points. A subset of the accelerations of the multibody system, the payload accelerations (HLAPAY program only), various displacement rates of change, and certain flight control system variables make up  $\dot{\underline{S}}$ , the rate of change of the state vector.

The external forces acting on the system can be characterized as aerodynamic or non-aerodynamic in origin. The non-aerodynamic forces are discussed in Section 3. This section describes the landing gear model (as many as four landing gears), and the payload suspension cable model (as many as four). The remaining non-aerodynamic forces are due to gravity and direct thrust (e.g., turbine exhaust). The forces at the mooring attach point are constraint forces included in Section 2 -- the HLAMOR program treats the mooring mast as an additional constraint between a point on the hull and the inertial reference frame.

The flight control system model describe in Section 4 incorporates the software equivalent of a "mixer box" whereby the many control faces of the HLA (LPU propeller and rotor controls, movable fins on the hull) are "organized" to provide six approximately orthogonal control points -- one for each degree of hull motion freedom. The trim routine operates using these six equivalent controls in establishing the trim for powered flight conditions. The flight control system also provides for a simple proportional-integral-derivative (PID) closed-loop control structure for maintaining a trim condition and for response to input commands. The structure of the simulation is predicated on allowing comparatively routine modification to the flight control system subroutines to suit the requirements for individual vehicle configurations. Thus rotor rpm and the LPU gimbal angles represent potential additional controls; virtually any motion variable is a potential feedback signal.

The largest body of material in this manual pertains to the modeling of the aerodynamic forces on the HLA. The modeling includes hull

buoyancy and the so-called apparent mass terms, quasi-steady rotor aerodynamics, a variety of aerodynamic interference effects, and provision for random and deterministic aerodynamic disturbances having a spatial distribution appropriate to the large size of the vehicle. The reader is referred to Section 5 for a more detailed summary of the vehicle aerodynamics. Sections 6, 7, 8, and 9 describe the models in detail.

Section 10 describes the trim algorithm used in each of these three programs. For HLASIM and HLAPAY, the algorithm determines the six trim control deflections required for vehicle trim. In the HLAPAY program, it first establishes the trim payload position and associated suspension cable tensions — the latter are forces external to the hull. In the HLAMOR program, the hull attitude is trimmed to null the vehicle accelerations; the landing gear may or may not contribute to the forces acting on the hull depending on net heaviness of the HLA.

The linearization algorithm described in Section 11 uses forward and backward perturbations about the trim conditions to approximate the stability and response derivatives. The derivative set differs for each of the three programs and does not include the closed-loop influence of the flight control system. Auxiliary derivatives are computed for internal and external force variations with perturbations in the state variables, commands and disturbances. These include, for example, the constraint forces acting at the LPU attach points, the cable tensions, etc. The programs also compute the eigenvalues and eigenvectors associated with the characteristic matrix.

Appendix A provides a cross-reference of experimental and analytical sources for the calculation of the hull and tail aerodynamic inputs. Appendices B and C are reprints of technical papers published during the course of the research which are intended to illustrate typical heavy-lift airship dynamics and control characteristics.

## SECTION 2

### HLA MOTION EQUATIONS

#### A. MOTION EQUATIONS OVERVIEW

The equations of motion fall into two groups — those that describe the motion of the HLA itself, and those that model the motion of the payload. The tensions in the cables that connect the HLA to the payload depend upon their relative motion (Section 3) and represent external forces on both bodies.

The payload is modeled as a single rigid body; its equations of motion are straightforward.

The HLA itself is modeled as an interconnected set of five rigid bodies. The central body is the hull assembly consisting of gas envelope, tailfins, mooring mast attach point, landing gears, and the interconnecting and supporting structure. The four peripheral bodies are lift-propulsion units (LPUs) consisting of a fuselage (or nacelle), lifting rotor, and thrusting propeller. These are attached to the hull structure at four points. Each LPU has three angular degrees of freedom relative to the hull but is constrained in translational motion at the attach point.

Equations of motion are written for each of the five bodies in isolation. The forces acting on each include external forces and constraint forces, the latter acting at the attach points in equal but opposite directions for the bodies on either side of the attach point. Because the constraint forces are unknown, the absolute angular and linear accelerations cannot be evaluated directly.

The translational constraints establish kinematic relationships between the motions of bodies on either side of an attach point. When written in terms of angular and linear accelerations of the bodies for all attach points, there results a second set of equations. This second set is solved simultaneously with the first to yield the accelerations

of all five bodies and the constraint forces acting between pairs of bodies.

Because of the constraints, not all of these accelerations are independent. Therefore only a subset is chosen for incorporation in  $\dot{\underline{S}}$ , the rate of change of the system state vector. The subset is different for each of the three programs. Any other velocities and displacements are determined using algebraic equations describing the constrained relationships between the velocity and displacement elements in the state vector,  $\underline{S}$ , and the dependent velocities and displacements.

The remaining elements of  $\dot{\underline{S}}$  are obtained from equations describing displacement rates of change in terms of velocities (kinematics), and from certain flight control system variables (Section 4).

During the course of program development the simulation requirements changed, eliminating the immediate need for angular degrees of freedom between the LPUs and the hull assembly. This has been accommodated in the program code by zeroing the angular rates and accelerations between the bodies at the attach points. The result is that the hull and LPUs behave as a single rigid body. The simulation calculates the torques at the attach points required to constrain the angular motion.

However, the input data requirements still treat the hull and LPUs as individual bodies. This facilitates data alteration; LPU locations can be changed without recalculating inertial properties for the assembly as a whole. Further, re-establishing the angular degrees of motion freedom is a relatively minor change should it be required by the vehicle being modeled.

## **B. NOTATION, COORDINATES, GEOMETRY, AND UNITS**

The physical system modeled in the simulation consists of six bodies. These are the hull (body h) to which are connected four lift-propulsion units (bodies i;  $i = 1, 2, 3, 4$ ) by means of three axis gimbals at each attach point. The sixth is the payload (body p) which is attached to the hull by means of four suspension cables. The hull includes the gas envelope, tail fins and the supporting structure to

which the LPUs are attached. The LPUs each have a lifting rotor, a thrusting propeller, and direct thrust from jet exhaust. For the moored HLA simulation, the hull is connected to a point in the inertial reference frame by an ideal three-axis gimbal.

### 1. Notation Convention

The equations describing the motions of the HLA use the notation convention summarized in Table 2-1. In this convention, subscripts generally refer to vector bases ( $\underline{n}$  is an exception) and underscored variables are vectors. The first superscript refers to the body, the second to the point in the body. For economy in notation, when the point in the body is the mass center the second superscript is left blank. If, in addition, the vector basis is that fixed in the particular body (i.e., first superscript is the same as the subscript), then the first superscript is also left blank. Thus the velocity of LPU attach point  $i$  on the hull expressed in the hull vector basis is denoted by  $\underline{V}_h^{hi}$ , but the velocity of the hull center of mass expressed in the hull vector basis is simply  $\underline{V}_h$ .

Additional subscripts are used to denote the origin of forces and torques. Thus  $\underline{F}_{Ah}$  denotes the aerodynamic force acting at the hull center of gravity expressed in the hull vector basis, whereas  $\underline{F}_h$  denotes a non-specific force acting at this same point.

### 2. Coordinate Systems and Transformations

All axis systems are orthogonal right-handed vector bases in which positive sense angular rotations are right-handed rotations about the respective axes. The inertially fixed axis system or reference frame is denoted by  $(x_I y_I z_I)$  where the  $x_I$  and  $y_I$  axes lie in the horizontal plane and the  $z_I$  axis is directed downward, along the gravitational vertical. Additional axis systems are referenced to the individual bodies making up the HLA.

TABLE 2-1. NOTATION CONVENTION

- $\underline{F}_a^{bi}$  = Force vector acting at point i in body b expressed in the a<sup>th</sup> vector basis
- $\underline{V}_a^{bi}$  = Linear velocity of point i in body b expressed in the a<sup>th</sup> vector basis.
- $\underline{R}_{aj}^{bi}$  = Position vector from point j in body a to point i in body b expressed in the a<sup>th</sup> vector basis. When j is blank, the position vector emanates from the origin of the a<sup>th</sup> vector basis, the mass center of body a.
- $\underline{I}_a^{bi}$  = Moment vector acting at point i in body b expressed in the a<sup>th</sup> vector basis.
- $\underline{\omega}_a^b$  = Angular velocity vector of body b expressed in the a<sup>th</sup> vector basis.
- $\underline{\Omega}_a^b$  = Euler angle rotation of body b with respect to body a. The order of the rotation sequence is defined separately for each a, b pair.
- $L_{ab}$  = Direction cosine matrix such that  $\underline{A}_a = L_{ab}\underline{A}_b$ , where  $\underline{A}_a$  and  $\underline{A}_b$  are generalized vectors expressed in the a<sup>th</sup> and b<sup>th</sup> vector bases, respectively. The transformation is orthogonal, thus  $L_{ab}^{-1} = L_{ab}^T = L_{ba}$ .
- $B_{Eba}$  = Nonorthogonal transformation matrix relating the Euler angle rates of body b to the body axis rates of body b relative to body a expressed in the a<sup>th</sup> vector basis. Thus,
- $$\underline{\dot{\Omega}}_a^b = B_{Eba}(\underline{\dot{\omega}}_a^b - \underline{\dot{\omega}}_a) \quad \text{and} \quad B_{aEb} = B_{Eba}^{-1} \neq B_{Eba}^T.$$
- ( $\dot{\phantom{x}}$ ) = Indicates time derivative of a variable or time derivative relative to the inertial vector basis.
- ( $\overset{\circ}{\phantom{x}}$ ) = Indicates time derivative relative to a non-inertial vector basis.
- ( $\phantom{x}$ )<sup>T</sup> = Indicates transpose (of a matrix or a vector).

a. Hull Assembly

The motions of the HLA are defined in terms of the  $(x_h y_h z_h)$  vector basis which is body-fixed with its origin at the center of mass of the hull assembly. The axes are directed as for an airplane — forward, to the right, and down for  $x_h$ ,  $y_h$ , and  $z_h$ , respectively.

The rotations of the hull vector basis relative to the inertial vector basis are expressed by the usual sequence of three Euler angle rotations — yaw ( $\psi$ ), pitch ( $\theta$ ), and roll ( $\phi$ ) — in going from the inertial frame to the body frame. The transformation of a vector expressed in the inertial basis to the same vector expressed in the hull basis is denoted by

$$\underline{A}_h = L_{hI} \underline{A}_I \quad (2-1)$$

where  $\underline{A}_h$  is a generalized vector in the  $(x_h y_h z_h)$  vector basis,  $\underline{A}_I$  is a generalized vector in the  $(x_I y_I z_I)$  basis and

$$L_{hI} = L_\phi L_\theta L_\psi \quad (2-2)$$

with

$$L_\phi = \begin{bmatrix} 1 & 0 & 0 \\ 0 & \cos \phi & \sin \phi \\ 0 & -\sin \phi & \cos \phi \end{bmatrix} \quad (2-3)$$

$$L_\theta = \begin{bmatrix} \cos \theta & 0 & -\sin \theta \\ 0 & 1 & 0 \\ \sin \theta & 0 & \cos \theta \end{bmatrix} \quad (2-4)$$

ORIGINAL PAGE IN  
POOR QUALITY

$$L_{\psi} = \begin{bmatrix} \cos \psi & \sin \psi & 0 \\ -\sin \psi & \cos \psi & 0 \\ 0 & 0 & 1 \end{bmatrix} \quad (2-5)$$

so that

$$L_{hI} = \begin{bmatrix} \cos \theta \cos \phi & \cos \theta \sin \psi & -\sin \theta \\ \sin \phi \sin \theta \cos \psi & \sin \phi \sin \theta \sin \psi & \sin \phi \cos \theta \\ -\cos \phi \sin \psi & +\cos \phi \cos \psi & \\ \cos \phi \sin \theta \cos \psi & \cos \phi \sin \theta \sin \psi & \cos \phi \cos \theta \\ +\sin \phi \sin \psi & -\sin \phi \cos \psi & \end{bmatrix} \quad (2-6)$$

The transformation is orthogonal, so that the inverse of the direction cosine matrix  $L_{hI}$  is equal to the transpose:

$$L_{hI}^{-1} = L_{Ih} = L_{hI}^T \quad (2-7)$$

The order of the subscripts defines the "direction" of the transformation.

#### b. Lift Propulsion Unit

The vector basis of the  $i$ th LPU ( $x_i, y_i, z_i$ ) is fixed within the LPU and has its origin at the center of mass of the LPU. Its orientation is similar to that for an aircraft — forward, to the right, and down.

The coordinate transformation from the hull-fixed vector basis to the LPU-fixed vector basis follows an unconventional Euler angle sequence chosen to allow large pitch rotations about an axis parallel to the  $y_h$  axis without a singularity appearing in the equations relating the Euler angle rates to the body axis rates. The sequence is pitch ( $\theta_i$ ), yaw ( $\psi_i$ ), and roll ( $\phi_i$ ). The transformation from the hull basis to the LPU basis is

$$\underline{A}_i = L_{ih} \underline{A}_h \quad (2-8)$$

ORIGINAL PAGE IS  
OF POOR QUALITY

where  $\underline{A}_i$  is a generalized vector in the  $(x_i y_i z_i)$  basis and

$$L_{ih} = L_{\phi_i} L_{\psi_i} L_{\theta_i} \quad (2-9)$$

with

$$L_{\phi_i} = \begin{bmatrix} 1 & 0 & 0 \\ 0 & \cos \phi_i & \sin \phi_i \\ 0 & -\sin \phi_i & \cos \phi_i \end{bmatrix} \quad (2-10)$$

$$L_{\psi_i} = \begin{bmatrix} \cos \psi_i & \sin \psi_i & 0 \\ -\sin \psi_i & \cos \psi_i & 0 \\ 0 & 0 & 1 \end{bmatrix} \quad (2-11)$$

$$L_{\theta_i} = \begin{bmatrix} \cos \theta_i & 0 & -\sin \theta_i \\ 0 & 1 & 0 \\ \sin \theta_i & 0 & \cos \theta_i \end{bmatrix} \quad (2-12)$$

so that

$$L_{ih} = \begin{bmatrix} \cos \theta_i \cos \psi_i & \sin \psi_i & -\sin \theta_i \cos \psi_i \\ \sin \theta_i \sin \phi_i & \cos \psi_i \cos \phi_i & \cos \theta_i \sin \phi_i \\ -\cos \theta_i \sin \psi_i \cos \phi_i & & + \sin \theta_i \sin \psi_i \cos \phi_i \\ \sin \theta_i \cos \psi_i & -\cos \psi_i \sin \phi_i & \cos \theta_i \cos \phi_i \\ + \cos \theta_i \sin \psi_i \sin \phi_i & & - \sin \theta_i \sin \psi_i \sin \phi_i \end{bmatrix} \quad (2-13)$$

$\theta_i$  is the pitch angle of the  $i$ th LPU about a gimbal axis parallel to the  $y_h$  axis of the hull;  $\psi_i$  and  $\phi_i$  represent the subsequent yaw then

ORIGINAL PAGE IS  
OF POOR QUALITY

roll rotations of the LPU relative to the hull. The nominal orientation (all angles small) represents the case where the lifting rotor's shaft is directed upward along the negative  $z_1$  axis.

To transform a generalized vector in the LPU vector basis to the inertial vector basis requires multiplication of the direction cosine matrices. Thus

$$L_{I1} = L_{Ih}L_{h1} \quad (2-14)$$

is the transformation matrix needed to relate a vector in the LPU reference frame to the inertial reference frame. The transformation is orthogonal, thus

$$L_{I1}^{-1} = L_{I1}^T = L_{h1}^T L_{Ih}^T = L_{Ih}L_{h1} = L_{I1} \quad (2-15)$$

c. Payload

The descriptions of the vector basis, the angular displacements, and the associated coordinate transformations are identical for the payload and the hull with a change in (or addition of) subscripts. Thus the vector basis is denoted by  $(x_p, y_p, z_p)$ , the Euler angle sequence is yaw ( $\psi_p$ ), pitch ( $\theta_p$ ), then roll ( $\phi_p$ ) to describe its orientation relative to the inertial reference frame.

The transformation from the payload vector basis to the hull vector basis requires multiplication of the direction cosine matrices:

$$L_{hp} = L_{hI}L_{Ip} \quad (2-16)$$

The transformation is orthogonal, thus

$$L_{hp}^{-1} = L_{hp}^T = L_{Ip}^T L_{hI}^T = L_{Ip}L_{hI} = L_{hp} \quad (2-17)$$

### 3. Geometry

The equations of motion which describe the angular accelerations of the various bodies are written in terms of moments about the centers of gravity (mass) of the various bodies. These moments are composed in part of vector cross products of the form  $\underline{R}_a^{ai} \times \underline{F}_a^{ai}$  where  $\underline{R}_a^{ai}$  is the vector position of point i, the application point of the force,  $\underline{F}_a^{ai}$ , relative to the mass center of the body. Figure 2-1 illustrates the geometry of these points and position vectors.

The input data describing the location of these points is given in terms of position relative to a fixed geometric reference point within the body which in general is not the center of gravity. Therefore the desired position vectors represent vector differences between the point in question and the center of gravity location.

The numbering convention of the LPUs, landing gear attach points, and cable attach points is such as to put odd numbers to the left and smaller numbers forward. Thus LPU-3 is the left aft LPU.

#### a. Hull Assembly

The location of the hull center of gravity is denoted by  $\underline{R}_{hcv}^h$ , the location of the center of gravity relative to the center of volume (cv). The several points of force application are as follows:

- Hull mass center to the center of volume, cv

$$\underline{R}_h^{hcv} = -\underline{R}_{hcv}^h \quad (2-18)$$

- Hull mass center to ith LPU attach point (i = 1, 2, 3, 4)

$$\underline{R}_h^{hi} = \underline{R}_{hcv}^{hi} - \underline{R}_{hcv}^h \quad (2-19)$$

- Hull mass center to tail reference center, t

$$\underline{R}_h^{ht} = \underline{R}_{hcv}^{ht} - \underline{R}_{hcv}^h \quad (2-20)$$

ORIGINAL PAGE IS  
OF POOR QUALITY

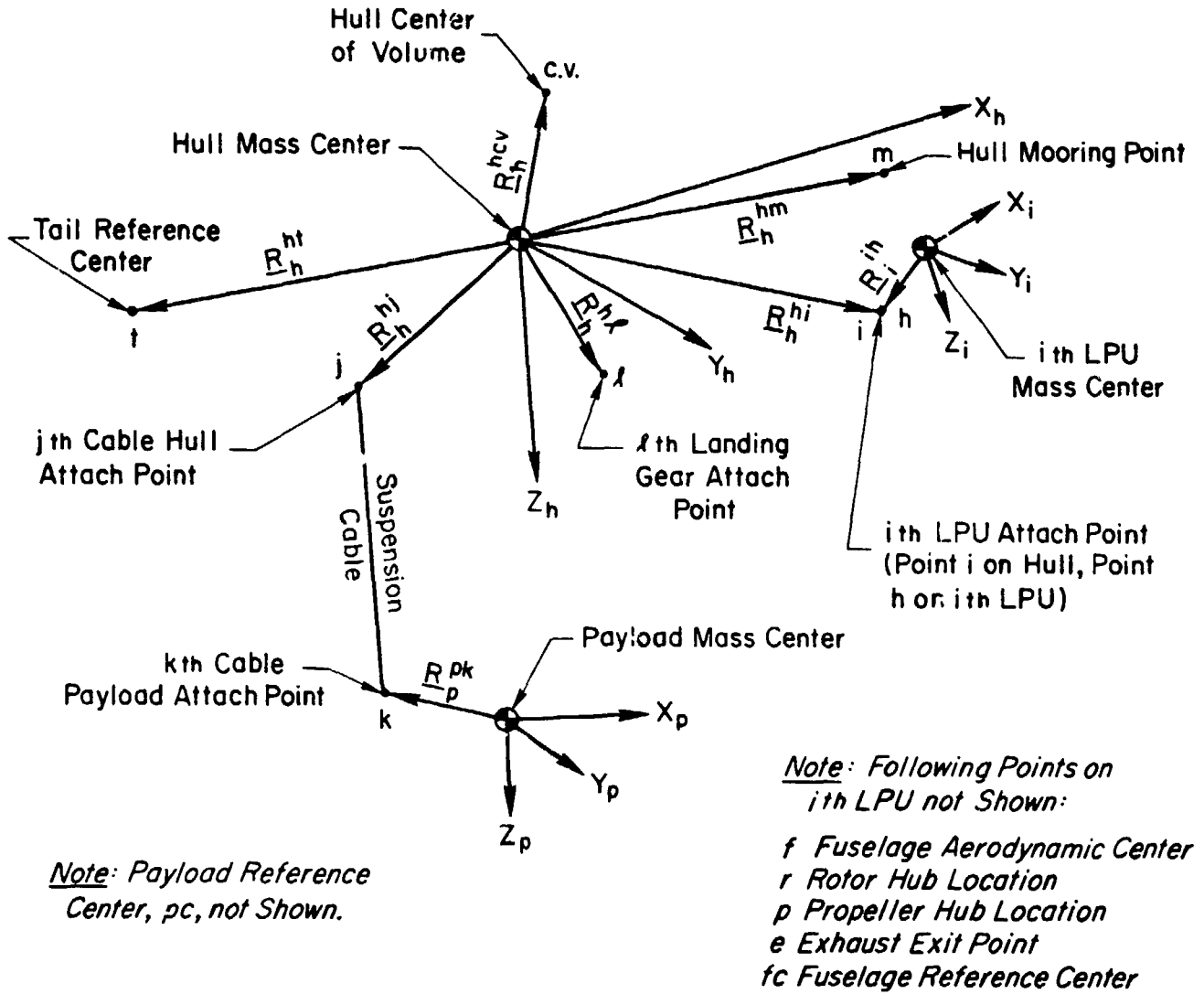


Figure 2-1. Vector Geometry of Hull, Payload and  $i$ th LPU

ORIGINAL PAGE IS  
OF POOR QUALITY

- Hull mass center to jth payload cable attach point (j = 1, 2, 3, 4) on the hull

$$\underline{R}_h^{hj} = \underline{R}_{hcv}^{hj} - \underline{R}_{hcv}^h \quad (2-21)$$

- Hull mass center to lth landing gear attach point (l = 1, 2, 3, 4)

$$\underline{R}_h^{hl} = \underline{R}_{hcv}^{hl} - \underline{R}_{hcv}^h \quad (2-22)$$

- Hull mass center to mooring attach point, m

$$\underline{R}_h^{hm} = \underline{R}_{hcv}^{hm} - \underline{R}_{hcv}^h \quad (2-23)$$

b. Lift Propulsion Unit

The location of the ith LPU center of gravity relative to the reference center of the LPU fuselage (nacelle) is denoted by  $\underline{R}_{ifc}^i$ . The several points of force application are given by:

- ith LPU mass center to fuselage aerodynamic center, f

$$\underline{R}_i^{if} = \underline{R}_{ifc}^f - \underline{R}_{ifc}^i \quad (2-24)$$

- ith LPU mass center to rotor hub, r

$$\underline{R}_i^{ir} = \underline{R}_{ifc}^{ir} - \underline{R}_{ifc}^i \quad (2-25)$$

- ith LPU mass center to propeller hub, p

$$\underline{R}_i^{ip} = \underline{R}_{ifc}^{ip} - \underline{R}_{ifc}^i \quad (2-26)$$

- ith LPU mass center to hull attach point, h

$$\underline{R}_i^{ih} = \underline{R}_{ifc}^{ih} - \underline{R}_{ifc}^i \quad (2-27)$$

- $i$ th LPU mass center to exhaust exit point,  $e$

$$\underline{R}_i^{ie} = \underline{R}_i^{ie} - \underline{R}_i^{ie} \quad (2-28)$$

### c. Payload

The payload is treated as a body having geometric properties such that its aerodynamic center and its reference center are one and the same. The center of gravity location relative to this center is given by  $\underline{R}_{ppc}^p$ . The remaining points are given by:

- Payload mass center to the reference center,  $pc$

$$\underline{R}_p^{ppc} = -\underline{R}_{ppc}^p \quad (2-29)$$

- Payload mass center to  $k$ th cable attach point ( $k = 1, 2, 3, 4$ ) on the payload

$$\underline{R}_p^{pk} = \underline{R}_{ppc}^{pk} - \underline{R}_{ppc}^p \quad (2-30)$$

## 4. Units

The simulation software is designed to operate with English units (1 lbf = 1 slug  $\times$  1 ft/sec<sup>2</sup>) or SI units (1 newton = 1 kg  $\times$  1 m/sec<sup>2</sup>). All angular units are defined in rad, rad/sec, rad/sec<sup>2</sup>, etc. The acceleration due to gravity,  $g$ , is a user-specified value, with units consistent with the input data. The user sets a "units flag" to signal the printing of the appropriate units with the input data listing. This flag also signals the appropriate calculation of power (i.e., kilowatts for SI units; horsepower, hp, for English units), see Section 7, Subsection I. Except for this one calculation, no unit conversions are computed by the program.

### C. KINEMATIC EQUATIONS

The kinematic relationships between velocities and rates of change of angular and linear displacements for the independent degrees of

freedom are given in this subsection. The rates of change are elements of  $\dot{\underline{S}}$ .

### 1. Hull Assembly

The angular velocity of the hull is given in terms of the body-axis rates

$$\underline{\omega}_h = [p \ q \ r]^T \quad (2-31)$$

and the Euler angle rates

$$\dot{\underline{\Pi}}^h = [\dot{\phi} \ \dot{\theta} \ \dot{\psi}]^T \quad (2-32)$$

$$= B_{Ehh} \underline{\omega}_h \quad (2-33)$$

where

$$B_{Ehh} = \begin{bmatrix} 1 & \sin \phi \tan \theta & \cos \phi \tan \theta \\ 0 & \cos \phi & -\sin \phi \\ 0 & \sin \phi / \cos \theta & \cos \phi / \cos \theta \end{bmatrix} \quad (2-34)$$

This is a nonorthogonal matrix whose inverse (not equal to the transpose) is given by

$$B_{hEh} = \begin{bmatrix} 1 & 0 & -\sin \theta \\ 0 & \cos \phi & \cos \theta \sin \phi \\ 0 & -\sin \phi & \cos \theta \cos \phi \end{bmatrix} \quad (2-35)$$

These relationships are the standard ones for an aircraft, have been derived elsewhere (e.g., Ref. 2-1), and will not be repeated here.

---

\*The vector notation  $[ ]^T$  is used for ease of printing.

Note that the ordering of the Euler angle rates in Eq. 2-32 is such that, for small angles, the first angle represents a rotation about the x-axis, the second about the y-axis, and the third about the z-axis. The ordering does not imply the Euler angle rotation sequence. This convention results in the nonorthogonal B transformation matrices being identity matrices when all Euler angles are zero.

The rate of change of the linear displacement of the hull is given by:

$$\dot{\underline{R}}_I^h = L_{Ih} \underline{V}_h \quad (2-36)$$

## 2. Lift-Propulsion Unit

The body axis rates of the ith LPU are given by:

$$\begin{aligned} \underline{\omega}_i &= L_{ih} \underline{\omega}_h^i \\ &= L_{ih} L_{hI} \underline{\omega}_I^i \\ &= [p_i \quad q_i \quad r_i]^T \end{aligned} \quad (2-37)$$

The Euler angle (gimbal angle) rates are:

$$\dot{\underline{\eta}}_h^i = [\dot{\phi}_i \quad \dot{\theta}_i \quad \dot{\psi}_i]^T \quad (2-38)$$

$$= B_{Eih} (\underline{\omega}_h^i - \underline{\omega}_h) \quad (2-39)$$

The gimbal angles of the ith LPU and the Euler angles (relative to the hull) are identical. The corresponding rates are related to the angular rates of the LPU less those of the hull expressed in a common vector basis, in the above equation, the hull.

The nonorthogonal transformation matrix  $B_{Eih}$  is derived as follows. First the relative angular rates are expanded in terms of their components (see Fig. 2-2):

$$L_{hI} \underline{\omega}_I^i - \underline{\omega}_h = \underline{l}_3 \dot{\phi}_1 + \underline{j}_1 \dot{\theta}_1 + \underline{k}_2 \dot{\psi}_1 \quad (2-40)$$

ORIGINAL PAGE IS  
OF POOR QUALITY

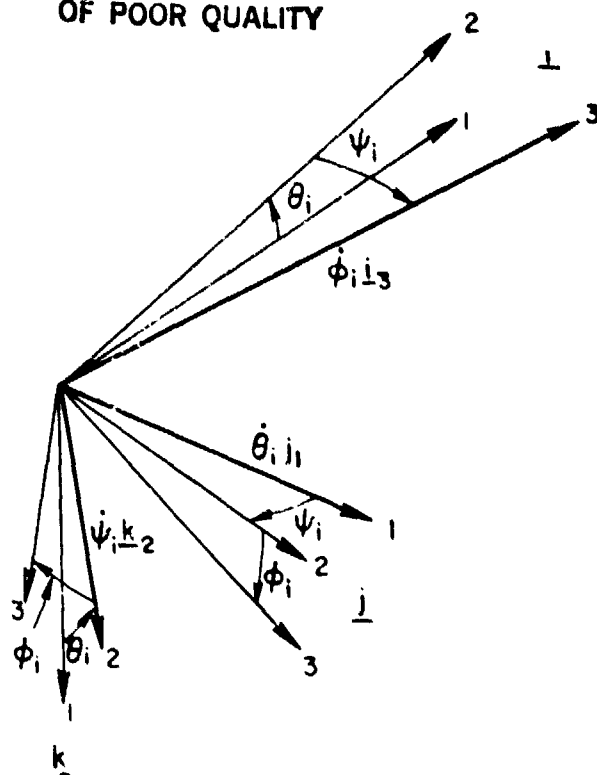


Figure 2-2. Gimbal Angle Rates for  $i$ th LPU

here  $\underline{j}_3$ ,  $\underline{j}_1$ , and  $\underline{k}_2$  are unit vectors along the axes of the LPU in its successive positions in the Euler angle sequence,  $\theta_1$ ,  $\psi_1$ , and  $\phi_1$ . When expressed in the  $X_h Y_h Z_h$  vector basis these unit vectors lead to:

$$\begin{aligned}
 L_{h1}\underline{\omega}_1 - \underline{\omega}_h &= L_{h1} \begin{bmatrix} 1 \\ 0 \\ 0 \end{bmatrix} \dot{\theta}_1 + L_{\theta_1}^{-1} \begin{bmatrix} 0 \\ 1 \\ 0 \end{bmatrix} \dot{\psi}_1 + L_{\theta_1}^{-1} L_{\psi_1}^{-1} \begin{bmatrix} 0 \\ 0 \\ 1 \end{bmatrix} \dot{\phi}_1 \\
 &= \begin{bmatrix} \cos \theta_1 \cos \psi_1 & 0 & \sin \theta_1 \\ \sin \psi_1 & 1 & 0 \\ -\sin \theta_1 \cos \psi_1 & 0 & \cos \theta_1 \end{bmatrix} \begin{bmatrix} \dot{\phi}_1 \\ \dot{\theta}_1 \\ \dot{\psi}_1 \end{bmatrix} \quad (2-41)
 \end{aligned}$$

Thus

$$B_{hEi} = \begin{bmatrix} \cos \theta_i \cos \psi_i & 0 & \sin \theta_i \\ \sin \psi_i & 1 & 0 \\ -\sin \theta_i \cos \psi_i & 0 & \cos \theta_i \end{bmatrix} \quad (2-42)$$

The inverse is given by

$$B_{Eih} = \begin{bmatrix} \cos \theta_i / \cos \psi_i & 0 & -\sin \theta_i / \cos \psi_i \\ -\cos \theta_i \tan \psi_i & 1 & \sin \theta_i \tan \psi_i \\ \sin \theta_i & 0 & \cos \theta_i \end{bmatrix} \quad (2-43)$$

A similar analysis leads to transformation matrices relating  $\dot{\eta}_h^i$  to the difference between the LPU and hull rates expressed in the  $i$ th LPU vector basis. Thus

$$\begin{aligned} \dot{\eta}_h^i &= B_{Eii}(\dot{\omega}_i^i - \dot{\omega}_i^h) \\ &= B_{Eii}L_{ih}(\dot{\omega}_h^i - \dot{\omega}_h) \\ &= B_{Eih}(\dot{\omega}_h^i - \dot{\omega}_h) \\ &= B_{Eih}(L_{hi}\dot{\omega}_i - \dot{\omega}_h) \end{aligned} \quad (2-44)$$

So

ORIGINAL PAGE IS  
OF POOR QUALITY

$$B_{E11} = B_{E1h}L_{h1}$$

$$= \begin{bmatrix} 1 & -\cos \phi_1 \tan \psi_1 & \sin \phi_1 \tan \psi_1 \\ 0 & \cos \phi_1 / \cos \psi_1 & -\sin \phi_1 / \cos \psi_1 \\ 0 & \sin \phi_1 & \cos \phi_1 \end{bmatrix} \quad (2-45)$$

The inverse is

$$B_{1E1} = \begin{bmatrix} 1 & \sin \psi_1 & 0 \\ 0 & \cos \phi_1 \cos \psi_1 & \sin \phi_1 \\ 0 & -\sin \phi_1 \cos \psi_1 & \cos \phi_1 \end{bmatrix} \quad (2-46)$$

### 3. Payload

The angular velocity of the payload is given in terms of its body axis rates:

$$\underline{\omega}_p = [p_p \quad q_p \quad r_p]^T \quad (2-47)$$

and in terms of its Euler angle rates

$$\dot{\underline{n}}_1^p = [\dot{\phi}_p \quad \dot{\theta}_p \quad \dot{\psi}_p]^T \quad (2-48)$$

$$= B_{Epp} \underline{\omega}_p \quad (2-49)$$

The sequence of payload Euler angle rotations relative to the inertial reference frame is the same as for the hull. Thus  $B_{Epp}$  and its inverse,  $B_{pEp}$ , are the same as for the hull (Eqs. 2-34 and 2-35) except for changes in subscript.

The payload position of interest is its position relative to the hull. The rate of change of this position, expressed in the hull vector basis, is equal to the difference in velocities. Thus,

$$\dot{\underline{R}}_h^p = L_{hp} \underline{V}_p - \underline{V}_h \quad (2-50)$$

#### D. PAYLOAD EQUATIONS OF MOTION

The translational motion of the payload is written in terms of its own vector basis:

$$\underline{F}_p = M^p (\dot{\underline{V}}_p^o + \underline{\omega}_p \times \underline{V}_p) \quad (2-51)$$

where  $\underline{F}_p$  is the total external force rating on the payload (body p) written in the pth vector basis,  $M^p$  is the diagonal mass matrix,  $\underline{\omega}_p$  is the angular velocity of the payload relative to inertial space expressed in the pth vector basis,  $\underline{V}_p$  is the linear velocity of the payload relative to inertial space expressed in the pth vector basis, and  $\dot{\underline{V}}_p^o$  is the time derivative of  $\underline{V}_p$  relative to the pth vector basis.

## DYNAMIC ANALYSIS OF FOOT QUALITY

The body axis forces and velocities can be expressed in the inertial vector basis by premultiplying by the direction cosine matrix,  $L_{Ip}$ , e.g.,  $\underline{V}_I^p = L_{Ip}\underline{V}_p$ . The inertial acceleration of the payload is given by:

$$\dot{\underline{V}}_I^p = L_{Ip}(\dot{\underline{V}}_p^o + \underline{\omega}_p \times \underline{V}_p) \quad (2-52)$$

The rotational equation of motion for the payload is likewise written in terms of its own body-fixed vector basis having its origin at the payload center of mass:

$$\underline{T}_p = \dot{\underline{H}}_p^o + \underline{\omega}_p \times \underline{H}_p \quad (2-53)$$

where  $\underline{T}_p$  is the total external moment vector acting on the payload (body p) expressed in the pth vector basis,  $\underline{H}_p$  is the angular momentum of the payload about its mass center expressed in the pth vector basis, and  $\dot{\underline{H}}_p^o$  is the time derivative of  $\underline{H}_p$  relative to the pth vector basis.

The angular momentum is given by:

$$\underline{H}_p = [I^p]_p \underline{\omega}_p \quad (2-54)$$

where  $[I^p]_p$  is the payload's inertia tensor about its center of mass in its body-fixed vector basis. The time derivative of  $\underline{H}_p$  is given by:

$$\dot{\underline{H}}_p^o = [I^p]_p \dot{\underline{\omega}}_p \quad (2-55)$$

where the time derivative of the inertia tensor is zero because the body is rigid and because the derivative is defined relative to the vector basis of the body.

The translational and rotational equations of motion can be rearranged as follows:

$$M^P \underline{\dot{V}}_p = -M^P (\underline{\omega}_p \times \underline{V}_p) + \underline{F}_p \quad (2-56)$$

$$[I^P]_p \underline{\dot{\omega}}_p = (-\underline{\omega}_p \times [I^P]_p \underline{\omega}_p) + \underline{T}_p \quad (2-57)$$

The external forces and moments acting on the payload are discussed in Sections 3 (non-aerodynamic) and 9 (aerodynamic).

#### E. MULTIBODY SOLUTION ALGORITHM

This subsection describes the solution algorithm for the accelerations of the hull and attached LPUs. As indicated at the outset of this section, the algorithm involves the simultaneous solution of motion equations and constraint equations.

The equations of motion for each body making up the HLA are written as if the body were in isolation. These equations are identical in form to Eqs. 2-56 and 2-57 for the payload with changes in subscript (h = hull; i = ith LPU, i = 1, 2, 3, 4). Among the forces acting on each body are the constraint forces acting at the attach point between the one body and the next. Because these forces are not necessarily expressed in the vector basis of the body and produce moments about the body's center of mass, coordinate transformations and cross products involving radius vectors to the attach points are involved in accounting for the constraints. When the equations of motion for all bodies are collected and arranged, there results a vector matrix equation of the form:

$$M \underline{\dot{V}} = \underline{F} + T_{VC} \underline{F}_C \quad (2-58)$$

where

$M$  = Inertia matrix including true inertia terms and aerodynamic acceleration derivatives for the hull\*

$\underline{\overset{0}{V}}$  = Acceleration vector

$\underline{F}$  = Applied force vector excluding those acceleration derivative dependent terms which are accounted for by certain elements in  $\underline{\overset{0}{MV}}$

$T_{VC}$  = Matrix relating the constraint force vector to the acceleration vector

$\underline{F}_C$  = Constraint force vector expressing the forces and moments acting between component bodies due to ideal constraints\*\*

The fact that the bodies are fastened together at the attach points means that there exist functional relationships between the motions of one body and the motions of the body to which it is attached. These relationships are constraint equations. When all such relationships are expressed in terms of the accelerations of the several bodies and appropriately arranged, there results a second vector matrix equation of the form:

$$T_{CV}\underline{\overset{0}{V}} = \underline{E} + \underline{\dot{V}}_{rel} \quad (2-59)$$

where

---

\*Certain of the aerodynamic forces are dependent upon elements of  $\underline{\overset{0}{V}}$ . These terms are moved to the left-hand side of the equation to facilitate the solution, see Section 8.

\*\*Non-ideal constraints arise out of modeling the forces between the bodies as being dependent on, e.g., flexibility and damping effects. Such forces are included in  $\underline{F}$ .

**ORIGINAL PAGE IS  
OF POOR QUALITY**

$T_{CV}$  = Matrix relating the acceleration vector to the relative and required acceleration vectors

$\underline{E}$  = Required acceleration vector needed to establish the constraint forces (depends upon various body velocities)

$\dot{\underline{V}}_{rel}$  = Relative acceleration vector allowed (or specified) by the constraint

To solve these equations for  $\underline{\overset{0}{V}}$  and  $\underline{F}_C$  one starts by eliminating  $\dot{\underline{V}}$ . Equation 2-58 is premultiplied by the inverse of the inertia matrix  $M^{-1}$  to yield an expression for the acceleration vector:

$$\underline{\overset{0}{V}} = M^{-1}\underline{F} + M^{-1}T_{VC}\underline{F}_C \quad (2-60)$$

This expression is substituted into Eq. 2-59 to give:

$$T_{C,M^{-1}}\underline{F} + T_{CVM^{-1}}T_{VC}\underline{F}_C = \underline{E} + \dot{\underline{V}}_{rel} \quad (2-61)$$

This is arranged to give:

$$T_{CVM^{-1}}T_{VC}\underline{F}_C = \underline{E} - T_{CVM^{-1}}\underline{F} + \dot{\underline{V}}_{rel} \quad (2-62)$$

which is an equation of the form

$$A\underline{F}_C = \underline{B} \quad (2-63)$$

where the matrix  $A = T_{CVM^{-1}}T_{VC}$  is known, as is the vector

$$\underline{B} = \underline{E} - T_{CVM^{-1}}\underline{F} + \dot{\underline{V}}_{rel} \quad (2-64)$$

Equation 2-63 is solved numerically for  $\underline{F}_C$ . The result is substituted back into Eq. 2-60 to obtain a numerical evaluation for  $\underline{\overset{0}{V}}$ .

Those elements of  $\underline{\overset{0}{V}}$  which represent constrained motions need not be integrated for the corresponding elements of  $\underline{V}$ . This is because they are motions completely determined (by virtue of the constraints) on the

remaining elements of  $\underline{V}$ . Thus  $\underline{\dot{V}}^0$  is appropriately truncated to form part of the state vector rate of change.

#### F. HULL AND LPU EQUATIONS OF MOTION

Expansion of Eq. 2-58, using equations of the forms given by Eqs. 2-56 and 2-57 (with a change in subscripts) is straightforward. The external forces and moments acting on the five bodies are discussed in Section 3 (non-aerodynamic) and Sections 5 through 8 (aerodynamic). Figure 2-3 shows the vector matrix expansion where the acceleration-dependent aerodynamic force terms of the hull have been accounted for in the  $6 \times 6$  inertia matrix in the upper left-hand corner of  $M$ . These aerodynamic terms are not present in the hull external force and moment terms,  $\underline{F}_h$  and  $\underline{T}_h$ , on the right-hand side of the equation. To complete the motion equations requires expansion of  $T_{VC}EC$ .

The constraint force acting on the hull at the  $i$ th LPU attach point is written in the hull vector basis as  $\underline{F}_{Ch}^{hi}$ . For the mooring simulation there is an additional constraint force,  $\underline{F}_{Ch}^{hm}$ . With four LPUs assumed, the constraint forces can be written as follows:

- On the hull:  $\left( \sum_{i=1}^4 \underline{F}_{Ch}^{hi} \right) + \underline{F}_{Ch}^{hm}$

- On the  $i$ th LPU:  $-L_{ih} \underline{F}_{Ch}^{hi}$

In the latter equation, the equal and opposite (hence the minus sign) constraint forces are resolved into the  $i$ th vector basis using the direction cosine matrix  $L_{ih}$ .

The constraint moment acting at the  $i$ th LPU attach point is written in the hull vector basis as  $\underline{T}_{Ch}^{hi}$ . The moments acting at the hull center of gravity also include those due to the constraint forces acting on the moment arm  $\underline{R}_h^{hi}$ ,  $i = 1, 2, 3, 4$ ; and on the moment arm  $\underline{R}_h^{hm}$ . The constraint moments can now be written:

ORIGINAL PAGE IS  
OF POOR QUALITY

$$\begin{bmatrix} \bar{V}_h \\ \bar{\omega}_h \\ \bar{V}_1 \\ \bar{\omega}_1 \\ \bar{V}_2 \\ \bar{\omega}_2 \\ \bar{V}_3 \\ \bar{\omega}_3 \\ \bar{V}_4 \\ \bar{\omega}_4 \end{bmatrix} \begin{bmatrix} I^h \\ \vdots \end{bmatrix} = \begin{bmatrix} -M^h \bar{\omega}_h \times \bar{V}_h + \bar{F}_h \\ -\bar{\omega}_h \times [I^h]_h \bar{\omega}_h + \bar{T}_h \\ -M^1 \bar{\omega}_1 \times \bar{V}_1 + \bar{F}_1 \\ -\bar{\omega}_1 \times [I^1]_1 \bar{\omega}_1 + \bar{T}_1 \\ -M^2 \bar{\omega}_2 \times \bar{V}_2 + \bar{F}_2 \\ -\bar{\omega}_2 \times [I^2]_2 \bar{\omega}_2 + \bar{T}_2 \\ -M^3 \bar{\omega}_3 \times \bar{V}_3 + \bar{F}_3 \\ -\bar{\omega}_3 \times [I^3]_3 \bar{\omega}_3 + \bar{T}_3 \\ -M^4 \bar{\omega}_4 \times \bar{V}_4 + \bar{F}_4 \\ -\bar{\omega}_4 \times [I^4]_4 \bar{\omega}_4 + \bar{T}_4 \end{bmatrix} + T_{vc} \bar{F}_c$$

Figure 2-3. Equations of Motion for Hull and Lift-Propulsion Units (Eq. 2-65)

ORIGINAL PAGE IS  
OF POOR QUALITY

- On the hull: 
$$\sum_{i=1}^4 (\underline{T}_{Ch}^{hi} + \underline{R}_h^{hi} \times \underline{F}_{Ch}^{hi}) + \underline{R}_h^{hm} \times \underline{F}_{Ch}^{hm}$$
- On the *i*th LPU: 
$$-\underline{L}_{ih} \underline{T}_{Ch}^{hi} - \underline{R}_i^{ih} \times \underline{L}_{ih} \underline{F}_{Ch}^{hi}$$

In the latter equation the sign is negative because the constraint force on the *i*th LPU has the opposite sign from that acting on the hull.

The constraint forces and moments are arranged as shown in Fig. 2-4. To expand the  $T_{VC}$  matrix the following identities are used:

$$\underline{A} \times \underline{B} = -\underline{B} \times \underline{A} \quad (2-66)$$

$$\underline{A} \times \underline{B} = [\underline{A} \times] \underline{B} \quad (2-67)$$

where

$$\underline{A} = [a_1 \quad a_2 \quad a_3]^T \quad (2-68)$$

and

$$[\underline{A} \times] = \begin{bmatrix} 0 & -a_3 & a_2 \\ a_3 & 0 & -a_1 \\ -a_2 & a_1 & 0 \end{bmatrix} \quad (2-69)$$

#### G. HULL AND LPU CONSTRAINT EQUATIONS

The hull and the *i*th LPU are both rigid bodies which are fastened together at a single point; point *h* on the *i*th LPU and point *i* on the hull are coincident. The translational motion of the LPU is a dependent variable in the sense that the position and attitude of the hull and the LPU gimbal angles, i.e., angular orientation of the LPU relative to the hull, determine the motion of the LPU center of mass.

In particular, the LPU position relative to the hull can be expressed in the hull vector basis as:

ORIGINAL PRINTING  
OF POOR QUALITY

$$\begin{bmatrix}
 \underline{F}_{Ch}^{h1} & \underline{I}_{Ch}^{h1} & \underline{F}_{Ch}^{h2} & \underline{I}_{Ch}^{h2} & \underline{F}_{Ch}^{h3} & \underline{I}_{Ch}^{h3} & \underline{F}_{Ch}^{h4} & \underline{I}_{Ch}^{h4} & \underline{I}_{Ch}^{hm} \\
 1 & 1 & 1 & 1 & 1 & 1 & 1 & 1 & 1 \\
 [R_h^{h1} \times] & 1 & [R_h^{h2} \times] & 1 & [R_h^{h3} \times] & 1 & [R_h^{h4} \times] & 1 & [R_h^{hm} \times] \\
 -L_{1h} & & & & & & & & \\
 -[R_1^{1h} \times] L_{1h} & -L_{1h} & & & & & & & \\
 & & -L_{2h} & & & & & & \\
 & & -[R_2^{2h} \times] L_{2h} & -L_{2h} & & & & & \\
 & & & & -L_{3h} & & & & \\
 & & & & -[R_3^{3h} \times] L_{3h} & -L_{3h} & & & \\
 & & & & & & -L_{4h} & & \\
 & & & & & & & -[R_4^{4h} \times] L_{4h} & -L_{4h}
 \end{bmatrix}$$

$\underline{F}_C$

$\underline{T}_{VC}$

Figure 2-4. Constraint Force Terms,  $\underline{T}_{VCFC}$ , in Equations of Motion for Hull and LPUs (Eq. 2-70)

$$\underline{R}_h^i = \underline{R}_h^{hi} - L_{hi} \underline{R}_i^{ih} \quad (2-71)$$

It can also be expressed in terms of positions relative to the inertial reference frame:

$$L_{IH} \underline{R}_h^i = \underline{R}_I^i - \underline{R}_I^h \quad (2-72)$$

When  $\underline{R}_h^i$  is eliminated between these two expressions, the LPU center of mass position relative to the inertial reference frame is defined in terms of the independent variables — hull position and two direction cosine matrices (note that  $L_{Ih} L_{hi} = L_{II}$ ):

$$\underline{R}_I^i = \underline{R}_I^h + L_{Ih} \underline{R}_h^{hi} - L_{II} \underline{R}_I^{ih} \quad (2-73)$$

The velocity of the LPU center of gravity is likewise constrained. Taking the time derivative of Eq. 2-73 yields:

$$\underline{V}_I^i = \underline{V}_I^h + \left( L_{Ih} \underline{\omega}_h \times \underline{R}_h^{hi} \right) - \left( L_{II} \underline{\omega}_I \times \underline{R}_I^{ih} \right) \quad (2-74)$$

The linear velocities can be expressed in the vector bases of each body by noting that  $\underline{V}_I^i = L_{II} \underline{V}_I$  and  $\underline{V}_I^h = L_{Ih} \underline{V}_h$ . Making the substitutions and premultiplying by  $L_{II}$  gives:

$$\underline{V}_I = L_{ih} \left( \underline{V}_h + \underline{\omega}_h \times \underline{R}_h^{hi} \right) - \left( \underline{\omega}_I \times \underline{R}_I^{ih} \right) \quad (2-75)$$

This expression, made possible by the existence of the translational constraint at the LPU attach point to the hull, allows determination of  $\underline{V}_I$  in the simulation without integration of an acceleration.

However, the constraint equations required for simultaneous solution with the equations of motion must be stated in terms of accelerations. Accordingly, the time derivative of Eq. 2-75 is taken, the derivative being relative to the vector bases of the individual bodies:

$$\begin{aligned} \overset{o}{V}_i + \omega_i \times \underline{V}_i &= L_{ih} [\overset{o}{V}_h + \omega_h \times \underline{V}_h + \overset{o}{\omega}_h \times \underline{R}_h^{hi} \\ &+ \omega_h \times (\omega_h \times \underline{R}_h^{hi})] - \omega_i \times \underline{R}_i^{ih} - \omega_i \times (\omega_i \times \underline{R}_i^{ih}) \end{aligned} \quad (2-76)$$

This equation is premultiplied by  $L_{hi}$  and rearranged to place all the acceleration terms on the left-hand side:

$$\begin{aligned} \overset{o}{V}_h + \omega_h \times \underline{R}_h^{hi} - L_{hi} \overset{o}{V}_i - L_{hi} \overset{o}{\omega}_i \times \underline{R}_i^{ih} \\ = -\omega_h \times (\underline{V}_h + \omega_h \times \underline{R}_h^{hi}) + L_{hi} [\omega_i \times (\underline{V}_i + \omega_i \times \underline{R}_i^{ih})] \end{aligned} \quad (2-77)$$

This is the desired translational motion constraint equation pertaining to the attach point between the hull and the  $i$ th LPU. The right-hand side is an element of  $\underline{E}$  in Eq. 2-59. No relative acceleration is allowed and the contribution to  $\dot{\underline{V}}_{rel}$  is a zero element.

The angular motion of the hull relative to the LPU is treated as constraint motion. Again the constraint is expressed in terms of accelerations. Thus taking the derivative of Eq. 2-44 yields

$$\overset{-1}{\dot{\eta}}_h = B_{Eih} (L_{hi} \overset{o}{\omega}_i - \overset{o}{\omega}_h) \quad (2-78)$$

The desired equation is obtained by premultiplying by  $B_{hEi}$  and placing the body-axis acceleration terms on the left-hand side:

$$\overset{o}{\omega}_h - L_{hi} \overset{o}{\omega}_i = -B_{hEi} \overset{-1}{\dot{\eta}}_h \quad (2-79)$$

The right-hand side of the equation is an element of  $\dot{\underline{V}}_{rel}$ ; the contribution to  $\underline{E}$  is a zero element.

In the HILAMOR program the moored flight condition is simulated by adding an additional constraint between a point on the hull and the inertial reference frame. The position of the hull mass center is given by:

ORIGINAL PAGE IS  
OF POOR QUALITY

$$\underline{R}_I^h = \underline{R}_I^{Ih} - L_{Ih} \underline{R}_h^{hm} \quad (2-80)$$

where  $\underline{R}_I^{Ih}$  is the location of the mooring mass attach point, h, in the inertial reference frame.

The velocity of the mass center is obtained by taking the derivative with respect to time (note that  $\underline{R}_I^{Ih}$  is a constant):

$$\underline{V}_I^h = -L_{Ih} \underline{\omega}_h \times \underline{R}_h^{hm} \quad (2-81)$$

Noting that  $\underline{V}_I^h = L_{Ih} \underline{V}_h$  gives:

$$\underline{V}_h = -\underline{\omega}_h \times \underline{R}_h^{hm} \quad (2-82)$$

This expression and Eq. 2-80 are used to determine the hull's velocity and position, respectively, in the mooring simulation.

Taking the time derivative of Eq. 2-82 relative to the hull vector basis gives:

$$\overset{o}{V}_h + (\underline{\omega}_h \times \underline{V}_h) = \left( \overset{o}{-\underline{\omega}_h} \times \underline{R}_h^{hm} \right) - \underline{\omega}_h \times (\underline{\omega}_h \times \underline{R}_h^{hm}) \quad (2-83)$$

The desired constraint equation is obtained by placing the accelerations on the left-hand side, all other terms on the right:

$$\overset{o}{V}_h + (\underline{\omega}_h \times \underline{R}_h^{hm}) = -\underline{\omega}_h \times (\underline{V}_h + \underline{\omega}_h \times \underline{R}_h^{hm}) \quad (2-84)$$

The term on the right is an element of  $\underline{E}$ ; there is no contribution to  $\dot{\underline{V}}_{rel}$ .

The constraint equations are arranged in vector-matrix form as shown in Fig. 2-5 (Eq. 2-85). The constraint associated with mooring is partitioned from the remaining terms by a dotted line as it is only present in HLAMOR.



**ORIGINAL PAGE IS  
OF POOR QUALITY**

Careful examination of  $T_{CV}$  reveals that this matrix is the transpose of  $T_{VC}$  shown in Fig. 2-4 (Eq. 2-70). The same storage array can be used for both matrices.

**H. FORCE AND MOMENT SUMMATIONS**

This subsection summarizes the external forces and moments acting on the several bodies making up the HLA.

**1. Hull Assembly**

The hull-tail assembly external forces originate in gravity, the landing gears, the payload suspension cables, and aerodynamics. The force summation is:

$$\underline{F}_h = \underline{F}_{G_h} + \underline{F}_{g_h} + \underline{F}_{c_h} + (\underline{F}_{A_h} - \underline{F}_{HAD_h}) \quad (2-86)$$

2-65      3-1    3-19   3-33            8-298

where the designations under each term note the equation where the term is defined. This practice is repeated throughout this subsection.

The external moments acting on the hull assembly are:

$$\underline{T}_h = \underline{T}_{g_h} + \underline{T}_{c_h} + (\underline{T}_{A_h} - \underline{T}_{HAD_h}) \quad (2-87)$$

2-65      3-20   3-34            8-299

In these two equations the  $\underline{F}_{HAD_h}$  and  $\underline{T}_{HAD_h}$  terms are the hull acceleration-dependent portion of the total hull aerodynamic force and moment vectors,  $\underline{F}_{A_h}$  and  $\underline{T}_{A_h}$ , which have been moved to the left hand side, thereby augmenting the hull inertia matrix,  $[\underline{I}^h]_h$ , see Sec. 8, Subsection I.

**2. LPU**

Each LPU ( $i = 1, 2, 3, 4$ ) has gravitational, aerodynamic and direct thrust forces rating on it. The force summation is:

$$\underline{F}_i = \underline{F}_{G_i} + \underline{F}_{A_i} + \underline{F}_{e_i} \quad \text{ORIGINAL PAGE IS OF POOR QUALITY} \quad (2-88)$$

2-65      3-2      7-95    3-41

The moment summation is:

$$\underline{T}_i = \underline{T}_{A_i} + \underline{T}_{e_i} \quad (2-89)$$

2-65      7-96    3-42

### 3. Payload

The payload has gravitational, aerodynamic and payload suspension cable forces acting on it. The force summation is:

$$\underline{F}_p = \underline{F}_{G_p} + \underline{F}_{c_p} + \underline{F}_{A_p} \quad (2-90)$$

2-56      3-3      3-35    9-13

The moment summation is:

$$\underline{T}_p = \underline{T}_{c_p} + \underline{T}_{A_p} \quad (2-91)$$

2-57      3-36    9-14

### I. STATE VECTOR RATE OF CHANGE

The elements making up the state vector rate of change,  $\dot{\underline{S}}$ , differ for each of the three simulation programs, as do the set of dependent variables which come about because of the constraints. Table 2-2 lists the vector elements of  $\dot{\underline{S}}$  in order in the left-hand column together with their sources (MSA = Multibody Solution Algorithm) for the HLASIM program. The column of dependent vector variables on the right falls out of the translational constraints between the LPUs and the hull. This version of the program has 42 integrated quantities plus spares; each vector element has three components.

The number increases to 54 plus spares for the HLPAY program. The added elements in  $\dot{\underline{S}}$  are listed with their source equations in Table 2-3.

TABLE 2-2. INTEGRATED AND DEPENDENT VARIABLES,  
HLASIM PROGRAM

INTEGRATED VARIABLES	SOURCE OR EQUATION	DEPENDENT VARIABLES	SOURCE OR EQUATION
$\overset{o}{V}_h$	MSA	$\overset{h1}{E}C_h$	MSA
$\overset{o}{\Delta}h$	MSA	$\overset{h1}{T}C_h$	MSA
$\overset{\cdot}{R}I^h$	2-36	$\underline{V}_1$	2-75
$\overset{\cdot}{\Delta}I^h$	33	$\underline{R}_h^1$	2-71
$\overset{o}{\omega}_1$	MSA	$\overset{h2}{E}C_h$	MSA
$\overset{\cdot}{\Delta}h^1$	2-44	$\overset{h2}{T}C_h$	MSA
$\overset{o}{\omega}_2$	MSA	$\underline{V}_2$	2-75
$\overset{\cdot}{\Delta}h^2$	2-44	$\underline{R}_h^2$	2-71
$\overset{o}{\omega}_3$	MSA	$\overset{h3}{E}C_h$	MSA
$\overset{\cdot}{\Delta}h^3$	2-44	$\overset{h3}{T}C_h$	MSA
$\overset{o}{\omega}_4$	MSA	$\underline{V}_3$	2-75
$\overset{\cdot}{\Delta}h^4$	2-44	$\underline{R}_h^3$	2-71
$\overset{\cdot}{V}INT$	Sec. 4	$\overset{h4}{E}C_h$	MSA
$\overset{\cdot}{\Delta}INT$	Sec. 4	$\overset{h4}{T}C_h$	MSA
Spares	--	$\underline{V}_4$	2-75
Spares	--	$\underline{R}_h^4$	2-71

ORIGINAL FILED  
OF POOR QUALITY

TABLE 2-3. ADDED INTEGRATED VARIABLES, HLPAY PROGRAM

INTEGRATED VARIABLES	EQUATION
$\overset{o}{V}_p$	2-56
$\overset{o}{\omega}_p$	2-57
$\overset{\cdot}{R}_h^p$	2-50
$\overset{\cdot}{\Delta I}^p$	2-49

TABLE 2-4. CHANGES TO INTEGRATED AND DEPENDENT VARIABLES, HLAMOR PROGRAM

DELETED INTEGRATED VARIABLES	SOURCE OR EQUATION	ADDED DEPENDENT VARIABLES	EQUATION
$\overset{o}{V}_h$	MSA	$\overset{hm}{F}_{C_h}$	MSA
$\overset{\cdot}{R}_I^h$	2-36	$\overset{\cdot}{V}_h$	2-82
$\overset{\cdot}{V}_{INT}$	Sec. 4	$\overset{h}{R}_I$	2-80
Spares	--		

The mooring simulation has no active control. This removes the flight control system variables,  $\dot{V}_{INT}$  and  $\dot{\omega}_{INT}$  from  $\dot{S}$  in HLASIM. The addition of the mooring mast constraint makes  $V_h$  and  $R_h^h$  dependent variables and further adds the mooring mast constraint force vector,  $F_{Ch}^{hm}$ . These changes are listed in Table 2-4. HLAMCR has only 30 integrated quantities.

A final modification was made to the program structure as a result of changes in the simulation requirements. Specifically, controlled or flexible joints between the LPUs and the hull were no longer required. The following changes were made in the program code:

- The gimbale angle accelerations are set to zero in Eq. 2-85 (Fig. 2-3), i.e.,

$$\ddot{\theta}_h^i = 0 \quad , \quad i = 1, 2, 3, 4 \quad (2-92)$$

- The value of  $\omega_i$  returned by the integrator is ignored. Instead the following equation, obtained from Eq. 2-40 by setting the gimbale rates to zero, is used:

$$\omega_i = L_{ih}\omega_h \quad , \quad i = 1, 2, 3, 4 \quad (2-93)$$

- The gimbale angle rates in  $\dot{S}$  are likewise set to zero to avoid drift in the gimbale angles which could conceivably occur due to, for example, roundoff errors in the coordinate resolution. Thus,

$$\dot{\theta}_h^i = 0 \quad , \quad i = 1, 2, 3, 4 \quad (2-94)$$

The result makes the multibody system composed of hull and central LPUs behave like a single rigid body. However, the simulation still calculates  $F_{Ch}^{hi}$  and  $T_{Ch}^{hi}$ , which are internal loads in the structure of the HLA. Reversing these changes and incorporating an appropriate model for the LPU gimbals is all that is required to model the flexible five-body system envisioned at the outset.

## SECTION 3

### NON-AERODYNAMIC EXTERNAL FORCES AND MOMENTS

#### A. SCOPE

This section describes all of the external forces acting on the several bodies making up the HLA and its slung payload except for those due to aerodynamics (to be described later in Sections 5 through 9) or already accounted for in the ideal constraint forces and moments described in Section 2. These external forces originate in the following sources:

- Gravitational acceleration
- Landing gear
- Payload suspension cables
- Direct thrust

The following subsections contain the mathematical models for these four types of external forces.

#### B. GRAVITATIONAL FORCES

The gravitational forces act at the center of mass of the respective bodies, the center of mass being regarded as fixed within the body. In the case of the hull, the center of gravity depends upon the structure and the distribution of the lifting gas and ballonet-contained air within the envelope. The gravitational torques are zero.

The gravitational force is expressed in the vector basis of each body. Thus:

1) Hull

$$\underline{F}_{G_h} = m_h g L_{hI} [0 \ 0 \ 1]^T \quad (3-1)$$

ORIGINAL PAGE IS  
OF POOR QUALITY

2)  $i$ th LPU

$$\underline{E}_{G_i} = m_i g L_{ih} L_{hi} [0 \ 0 \ 1]^T \quad (3-2)$$

where  $m_i$  is the mass of the  $i$ th LPU.

3) Payload

$$\underline{E}_{G_p} = m_p g L_{pI} [0 \ 0 \ 1]^T \quad (3-3)$$

### C. LANDING GEAR FORCES AND MOMENTS

Landing gear forces act on the hull when the hull position relative to the ground is such as to bring one or more landing gears in ground contact. The model is a simplified representation of the dominant forces associated with a landing gear having a swiveled wheel in ground contact. The forces are due to landing gear strut compression, compression rate, and rolling friction over the ground.

The landing gear strut is vertically oriented with respect to the hull vector basis and located at a point  $l$  (= landing gear) on the hull. The location of this point in the inertial reference frame is given by:

$$\underline{R}_I^{hl} = \underline{R}_I^h + L_{Ih} \underline{R}_h^{hl} \quad (3-4)$$

$$= \begin{bmatrix} x_I^{hl} & y_I^{hl} & -h_l \end{bmatrix} \quad (3-5)$$

where  $h_l$  is the altitude of point  $l$  above the ground plane, see Fig. 3-1.

The distance,  $l_l$ , between point  $l$  and the ground plane measured parallel to the hull  $z$ -axis is given by:

$$l_l = \frac{h_l}{\cos \theta \cos \phi} \quad (3-6)$$

The bottom-most portion of the wheel or skid is located at point  $g$  (= ground contact), a distance  $l_g$  below point  $l$  when measured in the hull vector basis. When fully relaxed or extended,  $l_g = l_{og}$ . Thus a

ORIGINAL PAGE IS  
OF POOR QUALITY

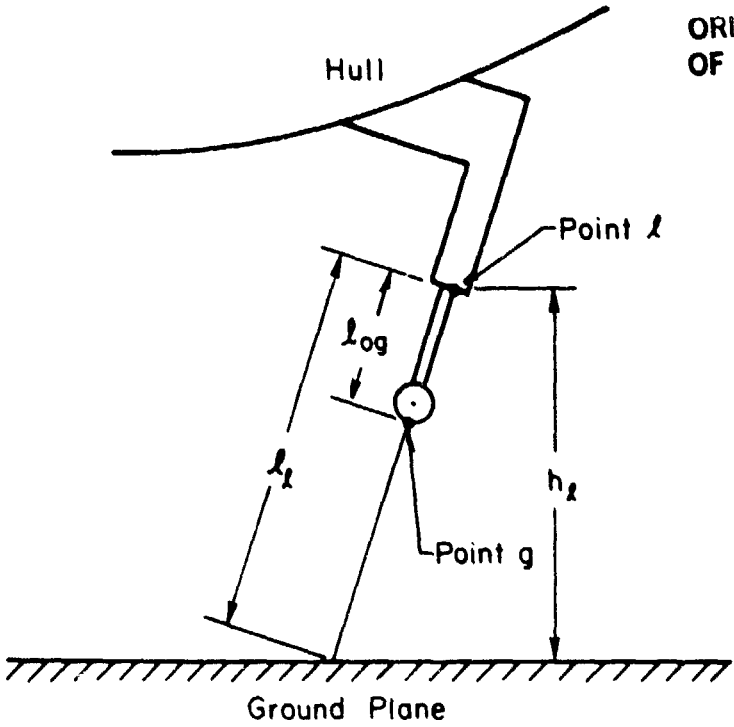


Figure 3-1. Landing Gear Model Geometry

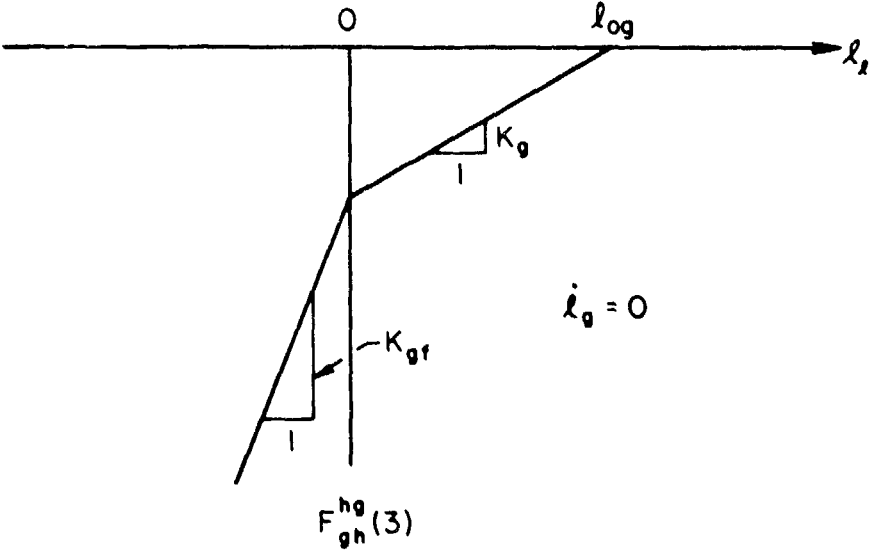


Figure 3-2. Landing Gear Static Force Model

ORIGINAL PAGE IS  
OF POOR QUALITY

comparison between  $l_l$  and  $l_{og}$  determines whether or not the landing gear has contacted the ground:

$$l_g = \begin{cases} l_{og} & , \quad l_l > l_{og} \\ l_l & , \quad l_l < l_{og} \end{cases} \quad (3-7)$$

In the latter case, point g lies in the ground plane.

The axial forces in the strut depend upon the compression length and the compression rate. The spring force has two gradients (positive sign). The smaller of the two,  $K_g$ , corresponds to the strut spring force; the larger,  $K_{gf}$ , corresponds to deflection of the hull structure itself. Figure 3-2 plots force versus deflection for zero deflection rate. The force is negative because it acts in the negative z-axis direction on the hull.

The total axial (z-direction) force acting on the hull at point g includes a damping term and is given by:

$$F_{gh}^{zh}(3) = \begin{cases} 0 & ; \quad l_l > l_{og} \\ K_g(l_g - l_{og}) + C_g \dot{l}_g < 0 & ; \quad 0 < l_g < l_{og} \\ K_f l_g - K_g l_{og} + C_g \dot{l}_g < 0 & ; \quad l_g < 0 \end{cases} \quad (3-8)$$

The rate of change of landing gear deflection,  $\dot{l}_g$ , is zero for  $l_l > l_{og}$  and equal to  $\dot{l}_g = \dot{l}_l$  for  $l_l < l_{og}$ .  $\dot{l}_l$  is obtained by differentiating Eq. 3-6 with respect to time and rearranging terms. Thus the compression rate for  $l_l < l_{og}$  is given by:

$$\dot{l}_g = \frac{1}{\cos \theta \cos \phi} [\dot{h}_l + l_g \sin \theta \cos \phi \dot{\theta} + l_g \cos \theta \sin \phi \dot{\phi}] \quad (3-9)$$

**ORIGINAL PAGE IS  
OF POOR QUALITY**

There are other forces acting at point g originating in the interaction of the landing gear with the ground. In the inertial reference frame, these interaction forces consist of a normal force, acting perpendicular to the plane of the ground, and a friction force, acting in the plane of the ground. The friction force is modeled as a Coulomb friction force proportional to the normal force and acting against the direction of motion. The total force vector is given by:

$$\underline{F}_{gI}^{hg} = \begin{bmatrix} \hat{e}_{Ix}^{hg} \mu_k & \hat{e}_{Iy}^{hg} \mu_k & 1 \end{bmatrix}^T F_{gI}^{hg}(3) \quad (3-10)$$

where  $\mu_k$  is the proportionality constant (positive sign), and

$$\hat{e}_I^{hg} = \begin{bmatrix} \hat{e}_{Ix}^{hg} & \hat{e}_{Iy}^{hg} & 0 \end{bmatrix}^T$$

is the unit vector in the direction of the velocity of point g, and  $F_{gI}^{hg}(3)$  is the z-axis or normal component of the force.  $F_{gI}^{hg}(3)$  is always negative ( $l_l < l_{og}$ ) or zero ( $l_l > l_{og}$ ).

The location of point g in the inertial reference frame is given by:

$$\underline{R}_I^{hg} = \underline{R}_I^h + L_{Ih} [\underline{R}_h^{hl} + \underline{R}_{hl}^{hg}] \quad (3-11)$$

where  $\underline{R}_{hl}^{hg} = [0 \quad 0 \quad l_g]^T$ . The velocity is obtained by taking the first time derivative:

$$\dot{\underline{R}}_I^{hg} = \underline{V}_I^h + L_{Ih} [\underline{\omega}_h \times \underline{R}_h^{hl} + \dot{\underline{R}}_{hl}^{hg} + \underline{\omega}_h \times \underline{R}_{hl}^{hg}] \quad (3-12)$$

$$= L_{Ih} [\underline{V}_h + [0 \quad 0 \quad \dot{l}_g]^T + \underline{\omega}_h \times (\underline{R}_h^{hl} + \underline{R}_{hl}^{hg})] \quad (3-13)$$

$$= \begin{bmatrix} \dot{V}_I^{hg}(1) & \dot{V}_I^{hg}(2) & 0 \end{bmatrix}^T \quad (3-14)$$

The unit vector,  $\hat{e}_I^{hg}$ , is the norm of the velocity vector:

$$\hat{e}_I^{hg} = \frac{\dot{R}_I^{hg}}{|\dot{R}_I^{hg}|} \quad (3-15)$$

All that remains now is to determine the normal force. This is accomplished by resolving  $F_{gI}^{hg}$  into the hull vector basis where the third component,  $F_{gh}^{hg}(3)$ , is known and given by Eq. 3-8. The resolution is:

$$F_{gh}^{hg} = L_{hI} F_{gI}^{hg} \quad (3-16)$$

The third component in terms of the normal force is:

$$\begin{aligned} F_{gh}^{hg}(3) = & [\hat{e}_{Ix}^{hg} \mu_k (\cos \phi \sin \theta \cos \psi + \sin \phi \sin \psi) \\ & + \hat{e}_{Iy}^{hg} \mu_k (\cos \phi \sin \theta \sin \psi - \sin \phi \cos \psi) \\ & + \cos \phi \cos \theta] F_{gI}^{hg}(3) \end{aligned} \quad (3-17)$$

When this expression is solved for  $F_{gI}^{hg}(3)$ , and the result substituted into Eq. 3-10, the total force acting at point g is defined. Equation 3-16 then defines the force acting at point g. The moment acting on the hull is given by:

$$\underline{T}_{gh}^{hg} = \underline{R}_h^{hg} \times \underline{F}_{gh}^{hg} \quad (3-18)$$

The forces and moments are summed for the four landing gears as follows:

$$\underline{F}_{gh} = \sum_{g=1}^4 \underline{F}_{gh}^{hg} \quad (3-19)$$

$$\underline{T}_{gh} = \sum_{g=1}^4 \left( \underline{R}_g^{hg} \times \underline{F}_{gh}^{hg} \right) \quad (3-20)$$

D. SLING FORCES AND MOMENTS

The payload is suspended below the hull on a series of cables, as many as four. These cables are attached at points  $j$  on the hull and points  $k$  on the payload. The cable force acts between points  $j$  and  $k$  and is modeled as a combination of tensile and damping forces. The tensile forces are proportional to cable stretch from its relaxed length and to stretch rate.

The vector distance between point  $j$  on the hull and point  $k$  on the payload in the hull vector basis is:

$$\underline{R}_{hj}^{pk} = \underline{R}_h^{pk} - \underline{R}_h^{hj} \quad (3-21)$$

where the first term on the right-hand side is given by:

$$\underline{R}_h^{pk} = \underline{R}_h^p + L_{hp} \underline{R}_p^{pk} \quad (3-22)$$

The distance between points  $j$  and  $k$  is given by the absolute value of the vector distance:

$$l_{jk} = \left| \underline{R}_{hj}^{pk} \right| \quad (3-23)$$

$$= \sqrt{(x_{hj}^{pk})^2 + (y_{hj}^{pk})^2 + (z_{hj}^{pk})^2} \quad (3-24)$$

The unit vector directed from  $j$  to  $k$  is given by the norm:

$$\hat{e}_{hj}^{pk} = \frac{1}{l_{jk}} \underline{R}_{hj}^{pk} \quad (3-25)$$

The rate of change of  $l_{jk}$  is given by the dot product of the unit vector and the time derivative of the vector distance:

$$\dot{l}_{jk} = \dot{R}_{hj}^{pk} \cdot \dot{e}_{hj}^{pk} \quad (3-26)$$

$$= \dot{x}_{hj}^{pk} \dot{e}_{hjx}^{pk} + \dot{y}_{hj}^{pk} \dot{e}_{h jy}^{pk} + \dot{z}_{hj}^{pk} \dot{e}_{hjz}^{pk} \quad (3-27)$$

where  $\dot{R}_{hj}^{pk}$  is obtained by taking the time derivative of Eq. 3-21:

$$\dot{R}_{hj}^{pk} = \dot{R}_h^{pk} - \dot{R}_h^{pk} \quad (3-28)$$

$$= L_{hp}(\dot{V}_p + \omega_p \times R_p^{pk}) - (\dot{V}_h + \omega_h \times R_h^{hj}) \quad (3-29)$$

The cable force is given by:

$$F_{jk} = \begin{cases} K_C(l_{jk} - l_{o_{jk}}) + C_C \dot{l}_{jk} > 0 & ; \quad l_{jk} > l_{o_{jk}} \\ 0 & ; \quad l_{jk} < l_{o_{jk}} \end{cases} \quad (3-30)$$

where  $l_{o_{jk}}$  is the relaxed length of the cable and  $K_C$  and  $C_C$  are the spring and damping constants, respectively.

This force magnitude is converted into a vector by taking the dot product with the unit vector:

$$\underline{F}_{ch}^{hj} = F_{jk} \cdot \underline{e}_{hj}^{pk} \quad (3-31)$$

The equal and opposite force acting at point k on the payload is:

$$\underline{F}_{cp}^{pk} = -L_{ph} \underline{F}_{ch}^{hj} \quad (3-32)$$

The total cable force acting on the hull is:

$$\underline{F}_{ch} = \sum_{j=1}^4 \underline{F}_{ch}^{hj} \quad (3-33)$$

The moment about the hull center of mass is:

$$\underline{T}_{ch} = \sum_{j=1}^4 \underline{R}_{hj} \times \underline{F}_{ch} \quad (3-34)$$

The total cable force acting on the payload center of gravity is:

$$\underline{F}_{cp} = \sum_{k=1}^4 \underline{F}_{cp}^{pk} \quad (3-35)$$

The moment about the payload center of mass is:

$$\underline{T}_{cp} = \sum_{k=1}^4 \underline{R}_p^{pk} \times \underline{F}_{cp}^{pk} \quad (3-36)$$

#### E. DIRECT THRUST FORCES AND MOMENTS

Each lift-propulsion unit is acted upon by direct thrust forces due to the jet exhaust of its turboshaft (or equivalent) engine(s). The thrust acts at a point e (= exhaust) and is directed along the negative z-axis of a coordinate reference frame which is oriented with respect to the LPU reference axes by a negative pitch angle,  $B_{1e}$ , and a subsequent positive roll angle,  $A_{1e}$ . This peculiar choice is made for compatibility with similar definitions for propeller shaft orientation and for rotor control or swashplate axes discussed in Section 7.

The pitch angle,  $B_{1e}$ , is in the negative sense about the LPU y-axis; the roll angle,  $A_{1e}$ , is in the positive sense about the new x-axis location (Figure 3-3). The pitch transformation matrix is given by:

$$L_{B_{1e}} = \begin{bmatrix} \cos B_{1e} & 0 & \sin B_{1e} \\ 0 & 1 & 0 \\ -\sin B_{1e} & 0 & \cos B_{1e} \end{bmatrix} \quad (3-37)$$

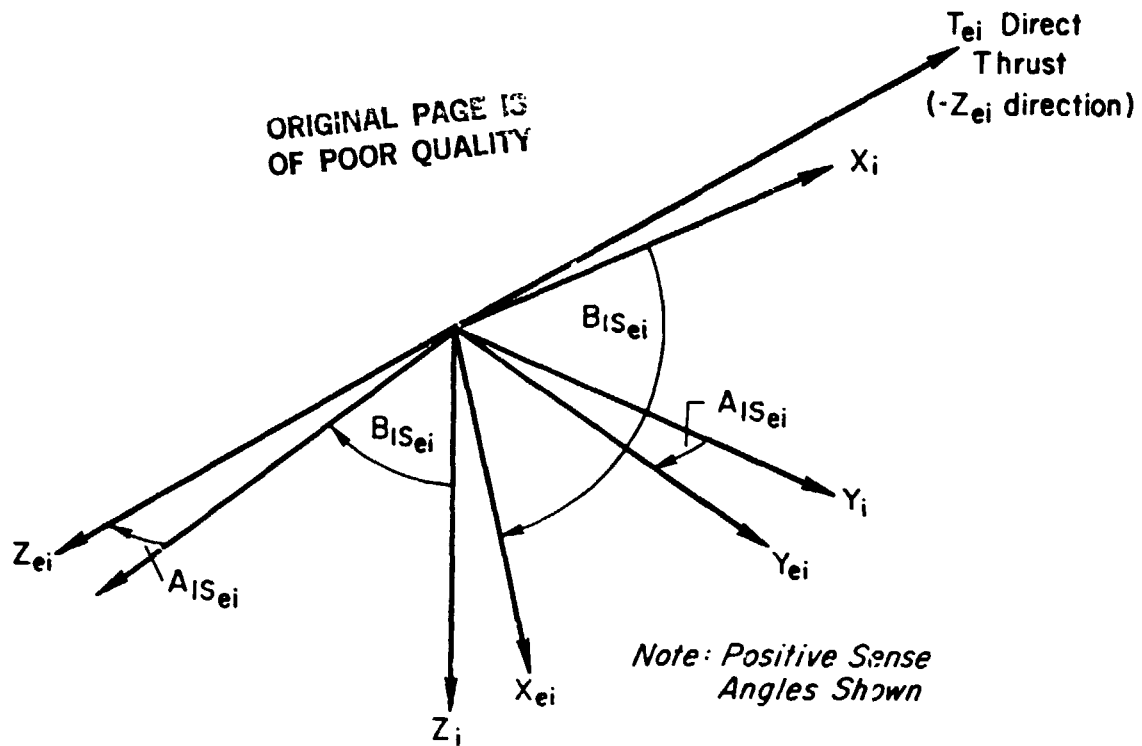


Figure 3-3. Orientation of Direct Thrust Vector Relative to LPU Reference Axes

The roll transformation matrix is:

$$L_{A_{1e}} = \begin{bmatrix} 1 & 0 & 0 \\ 0 & \cos A_{1e} & \sin A_{1e} \\ 0 & -\sin A_{1e} & \cos A_{1e} \end{bmatrix} \quad (3-38)$$

so that

$$L_{ei} = L_{A_{1e}}^{-1} B_{1e} = \begin{bmatrix} \cos B_{1e} & 0 & \sin B_{1e} \\ -\sin B_{1e} \sin A_{1e} & \cos A_{1e} & \cos B_{1e} \sin A_{1e} \\ -\sin B_{1e} \cos A_{1e} & -\sin A_{1e} & \cos B_{1e} \cos A_{1e} \end{bmatrix} \quad (3-39)$$

This is an orthogonal transformation whence:

$$L_{ie} = L_{ei}^{-1} = L_{ei}^T \quad (3-40)$$

The force acting on the LPU is given by:

$$F_{e1}^{ie} = L_{ie} [0 \quad 0 \quad -T_e]^T \quad (3-41)$$

The corresponding moment about the LPU center of mass is:

$$T_{e1} = R_{e1}^{ie} \times F_{e1}^{ie} \quad (3-42)$$

#### F. CAUTIONARY REMARKS

The running costs for the simulation can increase dramatically if the integration routine is forced to small step sizes by the presence of high-frequency modes in the system structure. Operation of the trim routine (Section 10) is also adversely affected. Among the nonaerodynamic forces there are two potential sources of such high-frequency modes:

- 1) Landing gear
- 2) Payload sling

The user is therefore cautioned to err on the side of low frequencies when working up a data set that includes landing gear and ca

spring forces. Verify the approximate frequencies associated with the spring constants chosen so as to not call for very high frequencies inadvertently. Testing of the simulation to date has shown both of these potential sources of difficulty to be manageable without violating physical reality for such structures.

**SECTION 4**  
**FLIGHT CONTROL SYSTEM**

**A. OVERVIEW**

The flight control system implemented in the simulation is a highly simplified representation of an automatic feedback control system that exercises control over all six degrees of hull motion freedom. It functions to maintain trimmed flight conditions in the presence of disturbances and can execute maneuver commands. However, its design does not attempt to anticipate the needs of all users or all possible HLA configurations. Rather, the goal was to allow source code changes with minimal difficulty to suit the requirements of individual users.

The generalized loop structure for all six control loops is typified by the longitudinal velocity control loop shown in Fig. 4-1. The system is of the proportional-integral-derivative (PID) type incorporating limiters at three points in the loop. It is responsive to commands from a command generator at the extreme left and a test input generator at the right. Control is exercised through a mixer box at the extreme right. The resulting control surface deflections are inputs to the remainder of the simulation, the block labeled HLA Dynamics. The simulated motion outputs are modified by the flight control sensors whose outputs are the feedbacks to the control loop. In certain loops a position feedback can be substituted for the velocity command in the command generator, thereby creating a position hold system.

The remainder of this section discusses the various elements of Fig. 4-1 that make up the flight control system.

**B. MIXER BOX**

The mixer box functions to link the numerous control surfaces into six equivalent and approximately orthogonal control points, one for each degree of hull motion freedom. The simulation trim state calculations

ORIGINAL PAGE IS  
OF POOR QUALITY

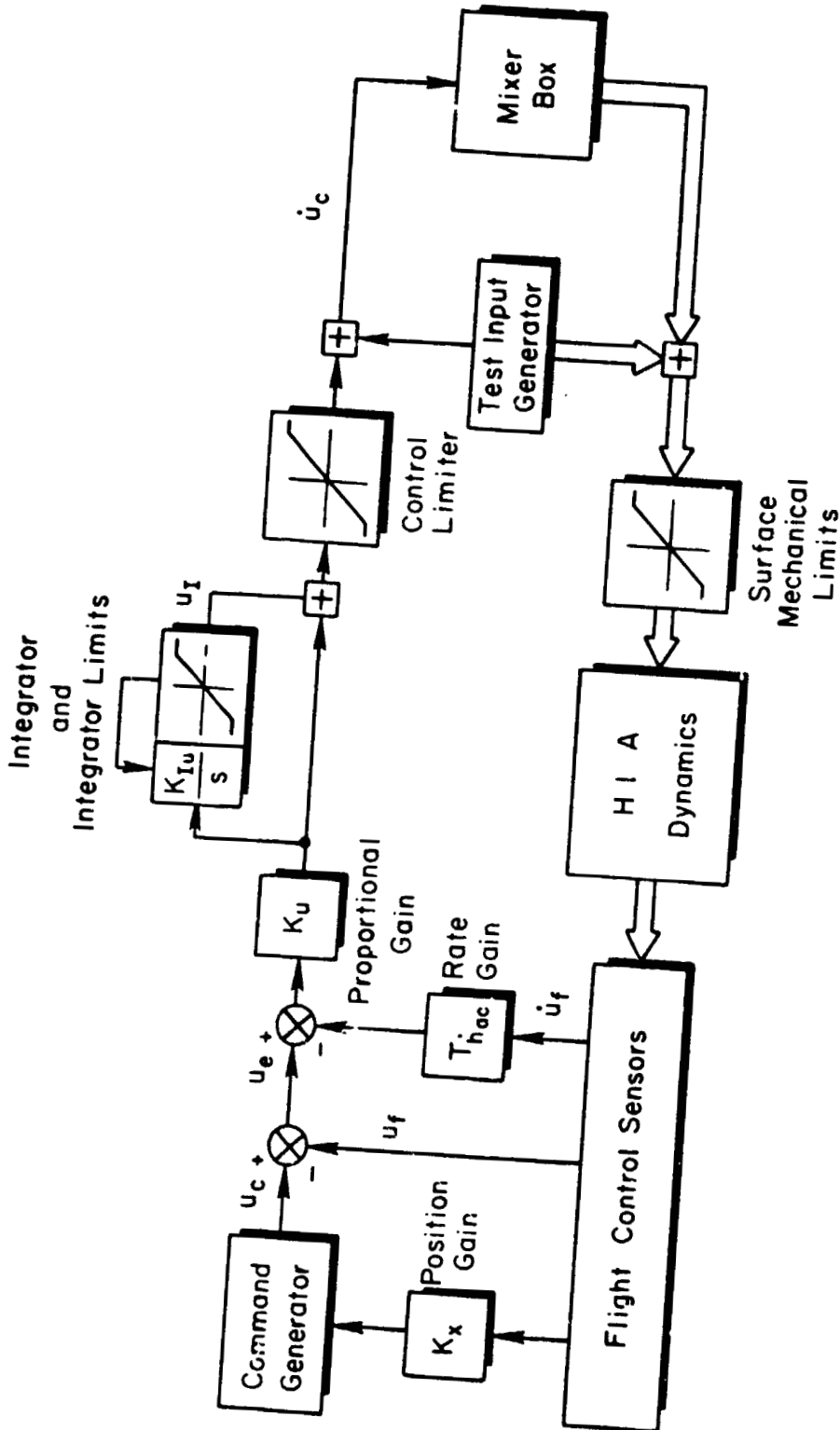


Figure 4-1. Control System Loop Structure

(Section 10) also operate through these six control points. Changes made to this part of the system must therefore be made with care because both flight control and trim functions are affected. On the other hand, such changes are relatively easy, being confined to a single routine, SUMCON, in the source code; the linking is not alterable through input data changes.

The present code is appropriate for an HLA having four LPUs, two on either side of a central buoyant hull located ahead and behind the center of gravity. The LPUs have fore-and-aft thrusting propellers in addition to the lifting rotors. The rotors have longitudinal and lateral cyclic controls; both rotors and propellers have collective controls. Hull-mounted fins have three controls corresponding to the conventional airplane's elevator, aileron, and rudder surfaces. There are no links to the LPU gimbal angle accelerations,  $\ddot{\theta}_h^i$ , the LPU direct forces,  $T_e$ , or to the rotor and propeller speeds,  $\Omega_r$  and  $\Omega_p$ . These variables, while fixed by input data specification in the current simulation, represent additional control possibilities in future developments.

The link equations were chosen to provide approximately orthogonal responses and adequate control power for the HLA configuration described. The individual LPUs are identified by the number in parentheses. The numbering convention has all odd numbers on the left and even on the right; lower numbers forward, larger numbers aft.

- Propeller Collectives. These are controlled by acceleration commands  $\dot{u}_c$  and  $\dot{r}_c$  from the longitudinal velocity and yawing velocity control loops:

$$\theta_{op}(1) = \dot{u}_c + \dot{r}_c \quad (4-1)$$

$$\theta_{op}(2) = \dot{u}_c - \dot{r}_c \quad (4-2)$$

$$\theta_{op}(3) = \dot{u}_c + \dot{r}_c \quad (4-3)$$

$$\theta_{op}(4) = \dot{u}_c - \dot{r}_c \quad (4-4)$$

**ORIGINAL PAGE IS  
OF POOR QUALITY**

- Rotor Collectives. These are controlled by acceleration commands,  $\dot{w}_c$ ,  $\dot{p}_c$ , and  $\dot{q}_c$ , from the vertical velocity, roll attitude, and pitch attitude control loops, respectively:

$$\theta_{or}(1) = -\dot{w}_c + \dot{p}_c + \dot{q}_c \quad (4-5)$$

$$\theta_{or}(2) = -\dot{w}_c - \dot{p}_c + \dot{q}_c \quad (4-6)$$

$$\theta_{or}(3) = -\dot{w}_c + \dot{p}_c - \dot{q}_c \quad (4-7)$$

$$\theta_{or}(4) = -\dot{w}_c - \dot{p}_c - \dot{q}_c \quad (4-8)$$

- Lateral Cyclics. These are controlled by acceleration commands from the lateral velocity control loop with no other mixing; control power is most limited in this axis:

$$A_{lsr}(1) = \dot{v}_c \quad (4-9)$$

$$A_{lsr}(2) = \dot{v}_c \quad (4-10)$$

$$A_{lsr}(3) = \dot{v}_c \quad (4-11)$$

$$A_{lsr}(4) = \dot{v}_c \quad (4-12)$$

- Longitudinal Cyclics. These controls operate in parallel with the propellers to increase the control power for longitudinal and yawing acceleration:

$$B_{lsr}(1) = (1/2)\dot{u}_c + 2\dot{r}_c \quad (4-13)$$

$$B_{lsr}(2) = (1/2)\dot{u}_c - 2\dot{r}_c \quad (4-14)$$

$$B_{lsr}(3) = (1/2)\dot{u}_c + 2\dot{r}_c \quad (4-15)$$

$$B_{lsr}(4) = (1/2)\dot{u}_c - 2\dot{r}_c \quad (4-16)$$

- Tail Fin Deflections. These are controlled by acceleration commands from the attitude loop:

$$\delta_a = -\dot{p}_c \quad (4-17)$$

$$\delta_e = -\dot{q}_c \quad (4-18)$$

$$\delta_r = -\dot{r}_c \quad (4-19)$$

**C. TEST INPUT FEATURES**

The simulation allows the user to increment any of the six linked control points or any of the control surfaces for simulation test

purposes. These increments are added to the six control loop outputs or to the mixer box outputs, respectively. The user specifies a starting time, an ending time, and the size of the increment. The result is to place a finite width pulse on the particular control during the time interval.

These capabilities are summarized in Table 4-1. Note that the starting and ending times for a particular set of controls apply to all the possible inputs of this set. For the rotor controls, there are twelve input points all governed by the starting and ending times  $t_{1r}$  and  $t_{2r}$ .

TABLE 4-1. TEST INPUT CAPABILITIES

CONTROL POINT	START	END	TEST INPUTS
Linked controls	$t_{1lc}$	$t_{2lc}$	$\Delta \dot{u}_c, \Delta \dot{v}_c, \Delta \dot{w}_c, \Delta \dot{p}_c, \Delta \dot{q}_c, \Delta \dot{r}_c$
Rotor controls	$t_{1r}$	$t_{2r}$	$\Delta \theta_{or}(i); i = 1, 2, 3, 4$ $\Delta A_{1sr}(i); i = 1, 2, 3, 4$ $\Delta B_{1sr}(i); i = 1, 2, 3, 4$
Propeller controls	$t_{1p}$	$t_{2p}$	$\Delta \theta_{op}(i); i = 1, 2, 3, 4$
Tail surface	$t_{1t}$	$t_{2t}$	$\Delta \delta_a, \Delta \delta_e, \Delta \delta_r$

#### D. CONTROL LOOPS

The structure of all six control loops is the same as shown in Fig. 4-1. Commands from the Command Generator (subscript c) are differenced with the state feedback (subscript f) to give the state error (subscript e). The derivative, or rate feedback (also subscript f) is passed through a rate gain (symbol T) and subtracted from the state error. The result passes through the proportional gain (symbol K) and through a parallel combination of a straight-through path and an integral path (gain symbol  $K_I$ ). The sum becomes the acceleration command

ORIGINAL PAGE IS  
OF POOR QUALITY

(also subscript c) in the absence of any additive test inputs to the limited control point.

The control loop signals for all six control loops are listed in Table 4-2. With the exception of the yaw rate loop, where there is no rate feedback, all elements are present in all loops.

The parameters for all six control loops are listed in Table 4-3. Here the limits are symbolized the same as in the computer code.

TABLE 4-2. CONTROL LOOP SIGNALS

CONTROL LOOP	INPUT COMMAND	STATE FEEDBACK	STATE ERROR	RATE FEEDBACK	INTEGRATOR OUTPUT	CONTROL OUTPUT
Longitudinal Velocity	$u_c$	$u_f$	$u_e$	$\dot{u}_f$	$u_I$	$\dot{u}_c$
Lateral Velocity	$v_c$	$v_f$	$v_e$	$\dot{v}_f$	$v_I$	$\dot{v}_c$
Vertical Velocity	$h_c$	$h_f$	$h_e$	$-\dot{w}_f$	$h_I$	$\dot{h}_c$
Roll Attitude	$\phi_c$	$\phi_f$	$\phi_e$	$p_f$	$\phi_I$	$\dot{\phi}_c$
Pitch Attitude	$\theta_c$	$\theta_f$	$\theta_e$	$q_f$	$\theta_I$	$\dot{\theta}_c$
Yaw Rate	$\dot{\psi}_c$	$\dot{\psi}_f$	$\dot{\psi}_e$	--	$\dot{\psi}_I$	$\dot{r}_c$

TABLE 4-3. CONTROL LOOP PARAMETERS

CONTROL LOOP	RATE GAIN	PROPORTIONAL GAIN	INTEGRAL GAIN	INTEGRATOR LIMIT	CONTROL
Longitudinal Velocity	$T_{\dot{u}_{ac}}$	$K_u$	$K_{I_u}$	UILM	ULLM
Lateral Velocity	$T_{\dot{v}_{ac}}$	$K_v$	$K_{I_v}$	VILM	VLLM
Vertical Velocity	$T_{\dot{w}_{ac}}$	$K_h$	$K_{I_h}$	HDTILM	HDTLLM
Roll Attitude	$T_p$	$K_\phi$	$K_{I_\phi}$	PHIILM	PHILLM
Pitch Attitude	$T_q$	$K_\theta$	$K_{I_\theta}$	THEILM	THELLM
Yaw Rate	0	$K_{\dot{\psi}}$	$K_{I_{\dot{\psi}}}$	RILM	RLLM

## 1. Control Loop Activation and Trim Control

The user has the option of deactivating one or more of the control loops. This can be viewed as setting the proportional gain to zero. However, the integrator remains, as it serves to provide the trim command to the control surface. In the longitudinal velocity control loop, for example, the computed trim value of  $\dot{u}_c$  (see Section 10) is the initial condition placed on the integrator. With the longitudinal velocity loop inactive, the output of the integrator remains invariant.

## 2. Limiter Function

There are three kinds of limiting available to the user. There are mechanical limits on each control surface denoted by, for example,  $(\theta_{or})_{max}$  for the limit value on rotor collective deflection. There are also limits operating on the output of each of the six control loops, and integrator limits (see Table 4-3 for symbology).

The mechanical limits are symmetric for all controls. For investigations of trim control power under various flight conditions, these limits are typically opened up to physically unrealistic values to insure that a trim condition will exist (see Section 10). For other kinds of investigations, more realistic limits might be chosen.

With realistic levels of mechanical limiting, the choice of control limit can become important. It generally should be so chosen as to not completely saturate all affected control surfaces when these controls are also used for control about some other axis. For example, operation of the longitudinal velocity control loop should not saturate the propeller collective and the rotor longitudinal cyclics, for if this were to occur the only yaw control capability remaining around zero would reside in the rudder. On the other hand, the control limit must be large enough to allow a trim to be achieved. Note that this limit is active in the trim function (Section 10); if it is set too low a trim may not be achievable.

The third limit in the control loop is on the integrator output. The operation of this limit is different from the others. When an

integrator output limit is encountered, the limiter functions to remove the integrator input until the input changes sign. When this occurs, the integrator will promptly begin to decrease below the limit, and prolonged "hangup" at the integrator limit is avoided.

Choice of limit level is important here as elsewhere. Generally, it must be smaller than the control limit, but should be large enough to accommodate any realistic control trim condition. In particular, for trim control power studies, it might be set to unrealistically high levels to insure that a mathematical trim exists. Of course, in this case the remaining limits should likewise be set to very large values.

#### E. SENSORS -- CHOICE OF STATE FEEDBACKS

The actual states being controlled depend upon the sensors chosen. Here too a limited number of options has been provided, as listed in Table 4-4.

TABLE 4-4. SENSOR SIGNALS

CONTROL LOOP	STATE FEEDBACK	MOTION VARIABLE	RATE FEEDBACK	MOTION VARIABLE
Longitudinal Velocity	$u_f$	$V_h(1)$ or $u_{as}$	$\dot{u}_f$	$a_{x_{ac}}$
Lateral Velocity	$v_f$	$V_h(2)$ or $v_{as}$	$\dot{v}_f$	$a_{y_{ac}}$
Vertical Velocity	$\dot{h}_f$	$-V_h(3)$	$\ddot{h}_f$	$-a_{z_{ac}}$
Roll Attitude	$\phi_f$	$\phi$	$p_f$	$p$
Pitch Attitude	$\theta_f$	$\vartheta$	$q_f$	$q$
Yaw Rate	$\dot{\psi}_f$	$\dot{\psi}$ or $r$	--	--

ORIGINAL PAGE IS  
OF POOR QUALITY

In particular, the user can select inertial speed or airspeed for translational velocity control. In the former case the speed is that measured at the hull center of gravity. In the latter case, the airspeed sensor location affects the signal. Thus:

$$[u_{as} \quad v_{as} \quad w_{as}]^T = \underline{V}_h^{a \text{ cv}} + (\underline{\omega}_h \times \underline{R}_{hcv}^{has}) - \left( \frac{\partial \underline{V}_h^{am \text{ cv}}}{\partial R} \cdot \underline{R}_{hcv}^{has} \right) \quad (4-20)$$

where  $\underline{R}_{hcv}^{has}$  is the location of the airspeed sensor relative to the hull's center of volume.  $\underline{V}_h^{a \text{ cv}}$  is the speed relative to the air mass as measured at the hull center of volume;  $(\partial \underline{V}_h^{am \text{ cv}} / \partial R)$  accounts for certain density gradient effects, see Section 8.

The user can also select between the body  $\dot{\phi}$  rate,  $r$ , and the Euler angle rate,  $\dot{\psi}$ , in the yaw rate loop.

The altitude rate signal is that measured at the hull center of gravity.

The acceleration signals are given by:

$$[a_{xac} \quad a_{yac} \quad a_{zac}]^T = \underline{V}_h^o + (\underline{\omega}_h \times \underline{V}_h) + \left( \underline{\omega}_h \times \underline{R}_h^{hac} \right) + \underline{\omega}_h \times (\underline{\omega}_h \times \underline{R}_h^{hac}) \quad (4-21)$$

where

$$\underline{R}_h^{hac} = \underline{R}_{hcv}^{hac} - \underline{R}_{hcv}^h \quad (4-22)$$

is the accelerometer location relative to the hull center of gravity.

#### F. COMMANDS

The control loop commands (subscript c) are a user-defined table of data points (subscript COM) which establish the command time history in each control axis. This input capability allows execution of simple maneuvers by the simulated HLA.

The user also has a position hold option that can be used to determine system performance in this mode of operation. The user selects starting ( $t_{PH1}$ ) and ending ( $t_{PH2}$ ) times for the position loop to be closed. During the time interval the command table is replaced by a

ORIGINAL PAGE IS  
OF POOR QUALITY

position signal in four control axes where the position is measured relative to the point where the accelerometer was located in inertial space at the starting time. Following this interval the command table is resumed. This option is summarized in Table 4-5.

TABLE 4-5. COMMAND SIGNALS

CONTROL LOOP	VELOCITY COMMAND	POSITION HOLD ( $t_{PH1} < t < t_{PH2}$ )
Longitudinal Velocity	$u_{COM}$	$K_x[x(t_{PH1}) - R_I^{hac}(1)]$
Lateral Velocity	$v_{COM}$	$K_y[y(t_{PH1}) - R_I^{hac}(2)]$
Vertical Velocity	$\dot{h}_{COM}$	$K_h[h(t_{PH1}) + R_I^{hac}(3)]$
Roll Attitude	$\phi_{COM}$	0
Pitch Attitude	$\theta_{COM}$	0
Yaw Rate	$\dot{\psi}_{COM}$	$K_\psi[\psi(t_{PH1}) - \psi]$

As can be seen from Table 4-5, when the position hold feature is activated the HLA control loops are commanded to hold the existing heading, to zero the pitch and roll attitude, and to restore the position to that existing at time  $t_{PH1}$ . The dynamics of this position hold feature depend, of course, on the position gains chosen,  $K_x$ ,  $K_y$ ,  $K_h$ , and  $K_\psi$ .

When the position hold feature is inactive, the system is a velocity command system in the three translational degrees of freedom and in yaw; an attitude command system in pitch and roll.

## G. CAUTIONARY REMARKS

The integration routine used in the simulation program will automatically reduce its step size to satisfy its error criterion. Running costs for time histories are sensitive to this step size, which can become quite small under the following circumstances:

- 1) Encountering a limit.
- 2) Accommodating high acceleration loop gains.

The latter will be recognized as an effective "algebraic loop." The simulation has been tested with these loops closed. However, for the configurations examined thus far, they are not necessary for system stability and response.

**SECTION 5**  
**AERODYNAMICS OVERVIEW**

**A. INTRODUCTION**

This section presents an overview of the aerodynamic computational approach, and an outline of the aerodynamic disturbance and interference models. The detailed descriptions and equation summaries for specific models are presented in Sections 6 through 9. Due to the nonlinearities and complexity inherent in the aerodynamics of the various elements (i.e., rotors, hull, tail, etc.), the previous vector notation is often dropped in favor of scalar equations. Computer implementation of the aerodynamic models is in scalar form. A somewhat cumbersome notation is adopted to preserve important distinctions between relative velocity  $[ ]^a$ , air-mass velocity  $[ ]^{am}$ , air-mass input source  $[ ]^{sam}$ , discrete air-mass input  $[ ]^{dam}$ , uniform steady wind  $[ ]^w$ , and among vehicle elements (e.g., hull center-of-volume  $[ ]^{a cv}$ , tail reference center  $[ ]^{sam t}$ , etc.)

The simulation provides the capability to investigate problems generic to the HLA concept. This includes the evaluation of basic vehicle characteristics and the importance of aerodynamic and dynamic nonlinearities relative to the more familiar linear phenomena. Emphasis was placed on determining dominant effects and obtaining gross loads and motions, using aerodynamic models based on uniformly valid first approximations to a variety of effects. Input data requirements are minimized to facilitate these design tradeoff studies.

Analytical functions are used for the hull and tail loads that allow simulation over wide ranges of incidence, speed, and acceleration without recourse to lookup tables. Apparent mass effects are calculated for both hull and tail. The rotors and propellers on the lift/propulsion units (LPUs) are treated with combined momentum and blade element theories in the power-on condition. In the power-off (moored) condition, they are modeled by simple cross-flow drag relations. Various higher order terms in the descriptions of the hull, tail, LPUs, and slung load have been omitted.

ORIGINAL PAGE IS  
OF POOR QUALITY

The aerodynamic model equations do not "self-estimate" the basic aerodynamic properties from vehicle geometry; they are used only to fit estimated or measured aerodynamic data. For example, it will be shown that the basic hull-alone axial force model has the form:

$$X_h = -\frac{1}{2} \rho S_h C_{A_h} u_h^{a \text{ cv}} \left| u_h^{a \text{ cv}} \right| \quad (5-1)$$

In the simulation several parameters which are constant for a given run are lumped and entered as one precomputed constant. Thus Eq. 5-1 is implemented as:

$$X_h = \sigma X_{u|u|_h} \cdot u_h^{a \text{ cv}} \left| u_h^{a \text{ cv}} \right| \quad (5-2)$$

where

$u_h^{a \text{ cv}}$  = Hull x-axis components of relative airspeed at hull center-of-volume

$X_{u|u|_h}$  =  $-(\rho_0/2)S_h C_{A_h}$  is the input constant determined by the user

$\sigma$  =  $\rho/\rho_0$ , relative air density correction

To make clear the basic aerodynamic models involved the derivations use the format of Eq. 5-1, while the simulation employs the more efficient format of Eq. 5-2. The methodology for estimating these constants is presented in Appendix A.

## B. COMPUTATIONAL FLOW

In keeping with the generic multibody formulation of the equations of motion, the aerodynamic loads are modeled separately for each of the LPUs, the hull-tail-structure assembly, and the slung payload. Figure 5-1 shows the computational flow at each time step:

- 1) The vehicle states are accessed from the current time step; these include translational and rotary motions of each element, local air mass motions at each element (steady and turbulent wind inputs), and several control inputs.

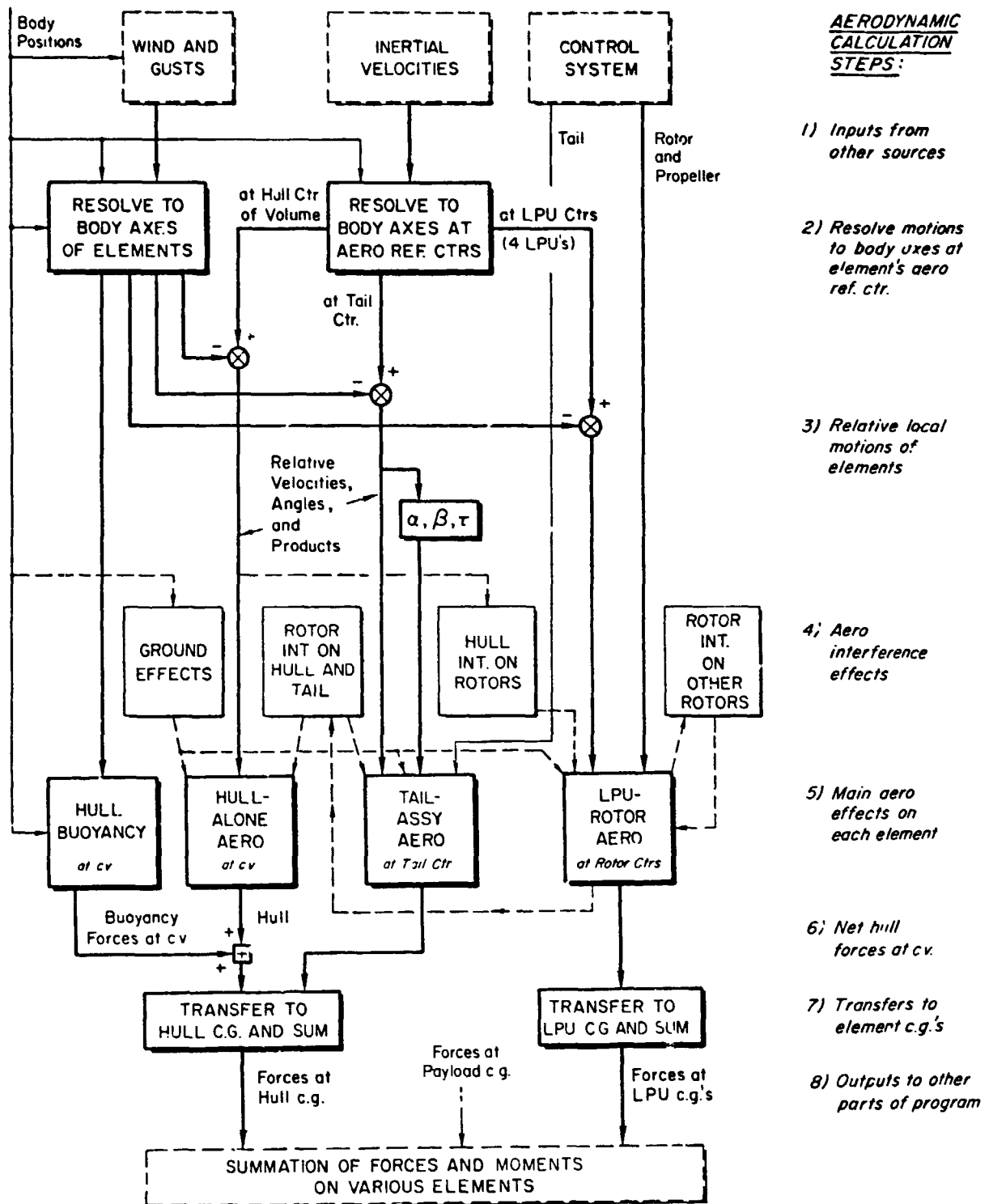


Figure 5-1. Computational Flow of Aerodynamic Model

- 2,3) These are resolved into relative air-to-element velocity components at each rotor and propeller hub, the LPU aerodynamic center, the hull center of volume (c.v.), the tail reference center (usually the aerodynamic center of effective tail-plus-fuselage ensemble), and the slung payload aerodynamic center, when the payload is present.
- 4) These kinematic relative velocities are adjusted by various factors or increments to account for local velocity interference due to: a) hull on rotors and propellers; b) rotors and propellers on hull and tail; c) rotors on propellers and LPU fuselage (nacelles); and d) ground proximity to the hull, tail, rotors, and propellers.

Thus the net relative or apparent air velocities are the vector sum:<sup>\*</sup>

$$\underline{v}_{\text{relative}} = \underline{v}_{\text{inertial motion}} - \underline{v}_{\text{interference}} \\ - \underline{v}_{\text{local airmass}}$$

- 5) Analytically efficient formulas are used to fit and evaluate the variation of aerodynamic forces and moments with each element's velocity and/or angle relative to the local air mass and to rotor and propeller speed. Interference effects which arise from changes in the nature of local flow (e.g., rotors introduce turbulence into the hull local flow) are accounted for in the respective element's equations. Buoyant forces are computed at the c.v. from the normal atmospheric pressure gradient, and horizontal pressure gradients due to changing wind velocities or convergent wind fields.
- 6) Net hull forces at the c.v. are summed and transferred to the hull center of gravity (c.g.) along with the tail-on-hull forces. Only at this stage are the major pitch, yaw and roll stability characteristics of the hull and fin assembly manifested.

---

<sup>\*</sup>We define a positive interference or local airmass state (e.g., linear or angular velocity, etc.) as one which causes atmospheric motion along the positive body axis direction.

- 7) The rotor, propeller, and LPU fuselage forces are transferred to forces and moments at each LPU c.g. for use in the multibody equations of motion.
- 8) Outputs of the loads on the several bodies are inputs to other parts of the program.

### C. ATMOSPHERIC ENVIRONMENT

This subsection briefly reviews the background and structure of the aerodynamic disturbance model. The detailed development is presented in Section 6.

The local air mass velocity (superscript "am") is represented at each of several locations by a constant mean wind (superscript "w") plus varying components (superscript "sam"), superimposed in inertial coordinates to give the power spectra and rms levels characteristic of turbulent winds:

$$\underline{v}_{am} = \underline{v}_w + \underline{v}_{sam}(x,y,t) \quad (5-3)$$

Local air mass motions are required at each LPU's c.g., at the tail reference center, and at the hull c.v. and at the slung load reference center. These locations are far enough apart that extrapolation of point gust values and gradients from a single point gives inaccurate results (Ref. 5-1).

As originally noted by Skelton (Ref. 5-2) and thoroughly developed by Holley and Bryson (Ref. 5-3) and Etkin (Ref. 5-1), the degree of gust component correlation between any pair of locations drops off as the space between them increases, so that at a hundred feet apart the correlations among turbulent components nearly vanishes. At smaller distances (on the order of aircraft wing chords, spans, and lengths) the correlations may be significant, but at the larger separations between HLA rotors, hull lengths, and cables, such correlations are considered negligible. For a conventional aircraft the approach is to put in gust inputs at wing and tail locations which are carefully chosen to yield "effective" gust magnitudes and gradients about the c.g., as best

explained by Etkin (Ref. 5-1). In the basic approach, both correlated and uncorrelated components must be included to retain the isotropic properties of atmospheric turbulence.

Here, a simpler extension of these concepts was adopted; the hull is treated as a spatial averager of gusts which are input at four points around a meridional plane (Fig. 5-2). The point locations are selected as a compromise to be close to the rotor hubs, tail reference center, and hull's effective length (like the effective span of a lifting wing). The hull, tail, and each LPU effective local air mass velocity is taken as the mean wind plus appropriate weighted average among the four input locations. Hull and tail air mass time derivatives are computed from numerical differentiation of these velocities.

The effective gradients ( $\partial u^{am}/\partial x$ , etc.) along and across the hull are computed as the linear gradients among the four input points; this gives a lower "effective" hull gradient than the local gust gradient at a point, as it should (Ref. 5-1). The four-point meridional gust model yields six planar spatial gradients at the hull c.v. (none with respect to height), which give rise to effective gust rotation terms and air mass acceleration terms. There are six more at the tail reference center. The air mass acceleration terms (spatial and time dependent) give rise to unsteady ("apparent mass") loads on both the hull and tail and to buoyancy terms on the hull. The atmospheric velocity inputs must not include steps as these generate extremely large accelerations in the simulation when the derivative is computed; the velocity rate of change is theoretically infinite.

For simplicity, the atmospheric disturbances are calculated at the LPU center of gravity and are not modified to account for the various spatial velocity gradients across the individual LPU components. This point approximation is justified because of the small dimensions of the LPU compared with the large dimensions of the gust source distribution and the hull. This assumption allows considerable simplification of the aerodynamic models of the individual LPU elements, as well as a reduction in the number of required aerodynamic disturbance input states.

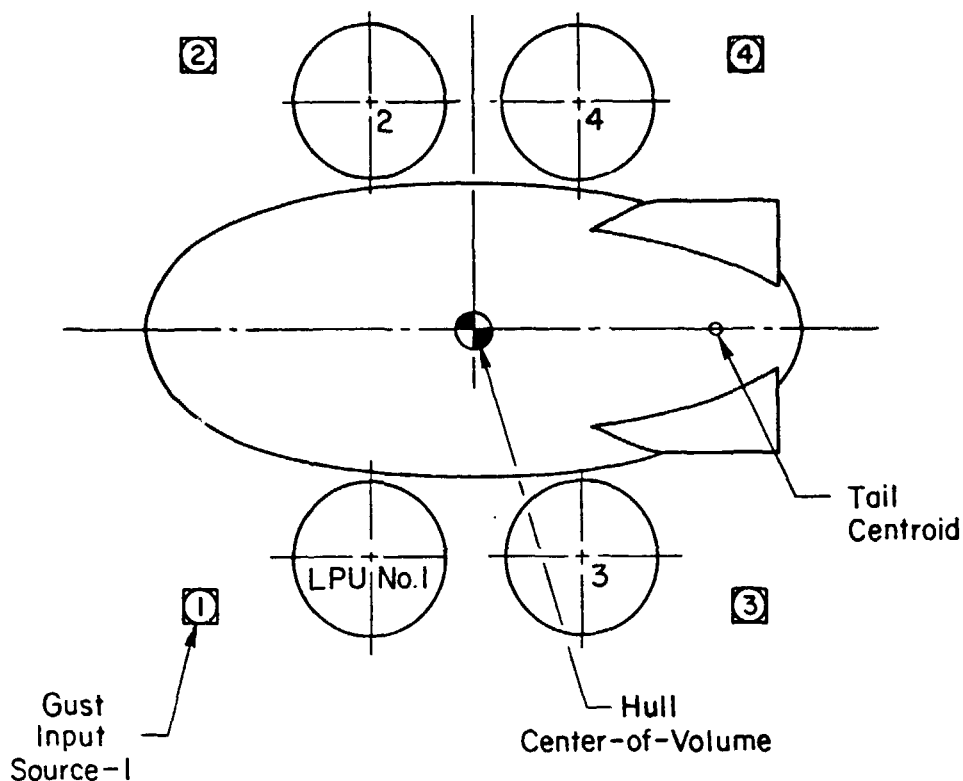


Figure 5-2. Atmospheric Input Model

The vehicle atmospheric model requires a set of twelve inertial velocity component time histories ( $u^{sam}$ ,  $v^{sam}$ ,  $w^{sam}$  at the four input source locations) to be defined ahead of time. For computational convenience, the input points translate (but do not rotate) with the hull. This scheme allows the use of actual recorded gust records (e.g., from ground-based meteorological towers) in order to simulate more precisely the peculiar patchiness which is characteristic of ground winds but is otherwise difficult to simulate realistically (Ref. 5-4). The precomputed inputs can contain both correlated and uncorrelated gust velocity components. They may also emulate discrete disturbances or steady gradient conditions (converging wind field) by appropriate user input selection.

The local air mass velocities at the slung load are input as an additional separate set of linear velocity components and velocity gradients

ORIGINAL PAGE IS  
OF POOR QUALITY

at a fifth source point. These are similarly expressed in inertial coordinates, which are then resolved into payload coordinates.

User-selected scale factors allow the defined wind velocities at the five source locations to be amplified or attenuated to arbitrary intensities.

The time dependency of the gust inputs (Eq. 5-3), which gives rise to the important (hull and tail) airmass acceleration effects, is not common to conventional aircraft analysis. For example, neglecting higher order terms, the total relative axial airmass acceleration may be written as (Ref. 5-1):

$$\frac{Du^{am}}{Dt} = \frac{\partial u^{am}}{\partial t} + u^a \frac{\partial u^{am}}{\partial x} + v^a \frac{\partial u^{am}}{\partial y} \quad (5-4)^*$$

where the relative velocities with respect to the airmass are given by:

$$u^a = u - u^{am}$$

$$v^a = v - v^{am}$$

The so called "frozen field" or "Taylor's Hypothesis" assumes that the time partial derivative ( $\partial/\partial t$ ) may be neglected compared to the spatial dependency ( $\partial/\partial x$ ,  $\partial/\partial y$ ) for most flight conditions under the restriction (Ref. 5-1):

$$u^a/u^{am} > 1/3$$

However, for low-speed LTA vehicles, where "nearly convected" flight is possible ( $u \approx u^{am}$ ), so  $u^a \approx 0$ , the frozen field assumption is inappropriate. Therefore, both time and spatial dependencies are retained in Eq. 5-3.

This multiple-point gust source approach is much more correct and versatile than the conventional aerodynamic disturbance input scheme (single-point gust source with extrapolated gradients). The omission of some small terms (e.g. second order terms in Eq. 5-4) should not deter

---

\*The z-gradients are missing due to the assumed planar (two dimensional spectrum) model and are felt to be of small effect (Ref. 5-1).

its usefulness. It is felt that this four (five if the payload is present) point wind input model can effectively simulate nearly all of the wind conditions faced in normal hovering and cruising operations.

There is also a provision in the simulation for discrete (test) inputs to be applied to specific isolated vehicle elements (e.g., hull, tail, LPUs). These inputs are of a  $(1 - \cosine)$  form and allow the user to excite the vehicle elements with disturbances of known magnitude and direction (i.e., no spatial interpolation is computed). This is especially helpful in preliminary assessment of closed loop response to vehicle (and payload) excitations.

#### **D. AERODYNAMIC INTERFERENCE EFFECTS**

A major objective of the present effort was to represent the various aerodynamic interference effects. Some limited wind tunnel data Ref. 5-5 suggest significant nonlinear rotor/hull interactions, not considered a problem in classic airships. Additional hull/ground and rotor/ground interactions have been documented in a number of references (e.g., Refs. 5-8 and 5-9).

The effort focused on reviewing the available literature, completing additional numerical experiments, and finally formulating models which could capture adequately the first order effects. Extrapolation and generalization, based on first principles (e.g. potential flow solutions, linear single dependency models, etc.), allows simulation over all ranges of speed and incidence without recourse to look-up tables or iterative algorithms. The resulting models are simple analytic functions of the dominant parameters (e.g. ground height, rotor thrust, etc.) All equation constants are input data in the simulation to allow incorporation of configuration dependent experimental data.

The interference effects may be categorized according to two basic types:

- A) Velocity Interference - The physical mechanism is a change in local air mass mean velocity magnitude and/or direction.

B) Flow Property Interference - The physical mechanism is a change in the nature of the local flow (e.g., turbulence level, wake distortion).

The various interference effects are tabulated below according to these two types with references to available wind tunnel data. Some of these effects generate both kinds of interference.

A) VELOCITY INTERFERENCE	B) FLOW PROPERTY INTERFERENCE	REFERENCES
1) Hull on Rotor, Propeller, LPU-fuselage	Hull on Rotor and Propeller	5-5, 5-6
2) Rotor and Propeller on Hull and Tail	Rotor and Propeller on Hull	5-5, 5-6
3) Rotor on Propeller		5-7
4) Rotor and Propeller on LPU-Fuselage		5-7
5) Ground on Hull, Tail, Rotor, Propeller	Ground on Hull	5-8, 5-9, 5-10, 5-11

A brief explanation of the dominant source for each interference effect follows:

1. Hull on Rotor, Propeller, LPU-Fuselage (Section 7). The immersion of LPU within the hull wake causes a reduction in the local velocity of the rotor, propeller and LPU-fuselage (Type A). In addition, the local hull wake turbulence causes a reduction in the rotor and propeller blade lift effectiveness (lift curve slope) which tends to reduce thrust capability (Type B).
2. Rotor and Propeller on Hull and Tail (Section 8). The main effects are due to the hull and tail being sucked toward the rotors' and propellers' effective "sink." If all are thrusting equally, a net downward force (for LPUs below hull centerline) will result from the sinks' downward induced velocity (Type A). There will also be a forward and downward velocity increment at the tail due to this "sink" effect (Type A).

In addition, the shedding of rotor and propeller vortices into the hull relative free-stream causes an increase in local turbulence, realized by an associated increase in the hull crossflow drag coefficient (Type B). The typical HLA geometry makes this latter effect negligible in the case of the tail.

3. Rotor on Propeller (Section 7). The operation of the propeller within the downwash field of the rotor causes changes in the propeller local free-stream velocity (Type A).
4. Rotor and Propeller on LPU-Fuselage (Section 7). The rotor and propeller wash over the LPU-fuselage, as above, changes the relative free-stream velocity (Type A) increasing the power requirements for most flight conditions.
5. Ground Effects on All Elements (Sections 7, 8). Several complex ground interactions affect the performance of the hybrid airship. The dominant effects include hull flow rotation (Type A), hull wake contraction (Type B), ground induced (reflection) velocities on the rotors and propellers (Type A), tail downwash restriction (Type A), and tail lift curve slope improvement (Type B).

## SECTION 6

### ATMOSPHERIC ENVIRONMENT

This section describes the models of the atmospheric environment and presents the pertinent equations.

#### A. MODEL TYPES AND BASIC ASSUMPTIONS

Three distinct models of the atmospheric environment are used simultaneously in order emulate a variety of conditions:

- 1) Steady wind
- 2) Discrete (1 - cosine) gust inputs
- 3) Multiple-source interpolation model

There are several fundamental differences in the assumptions associated with each of the above models. The following discussion outlines these basic differences as an overview for the detailed discussion of each of the three models.

1. Steady Wind. The steady wind is specified by the user according to its three components in the inertial reference axes. The steady wind is assumed to be constant with respect to the inertial (nonrotating) frame and is continually transformed into the coordinate systems of the various elements (e.g., hull, tail, LPUs, and slung load). This model is used in calculations for all phases of the simulation (trim, stability derivatives, and time history calculations). The steady wind contributes to the air mass acceleration, relative to the hull and tail, due to the inertial rotation of the vehicle. This relative acceleration contributes significantly to the unsteady ("apparent mass") loads on the hull and tail.
2. Discrete (1 - cosine) Inputs. These inputs, which are intended for test purposes, act on isolated vehicle elements (e.g., hull only, tail only, load only, etc.). They provide a means to excite specific vehicle elements without spatial interpolation to the remaining elements. These test inputs are assumed to translate and rotate with the vehicle. In this way, the value of the air mass velocities relative to a specific element is directly specifiable by a user. Unlike the steady wind or 4 point model, these inputs are given in coordinates of each element's

local reference axis system. Analytical time derivatives of the (1 - cosine) gust velocities are calculated in order to obtain body axis (i.e., relative to the rotating frame) linear and angular accelerations. The (1 - cosine) function is also used in order to specify test values of the spacial gradients ( $\partial u/\partial x$ ,  $\partial v/\partial y$ , etc.), allowing for the excitation of individual buoyancy and unsteady ("apparent mass") terms.

3. Multiple-Source Atmospheric Input Model. The justification for this model was described in Section 5, Subsection C. As noted, the user inputs groups of three linear velocities at each of four vehicle input locations, and three linear and three angular velocities at the fifth (payload) location when the payload is present. These input data are interpolated for the current simulation time and are multiplied by user-provided scale factors. The four vehicle input points form a rectangle whose dimensions are also user selected. This four-point grid is laterally symmetric with respect to the hull x-z plane of symmetry. The fifth gust input point is located at the payload dynamic center and is distinct from the four point veh model.

All of the velocity inputs in the Multiple Source Point Atmospheric Input Model are in coordinates of a non-rotating inertially oriented frame, which translates but does not rotate with the vehicle. Spatial and time interpolation is used to obtain all the necessary velocity gradients and accelerations at the various aerodynamic reference centers (e.g., hull center volume, tail reference center, LPU centers of gravity, slung payload aerodynamic reference center). Since the gust input velocities in this model are assumed to be in a frame which is non-rotating, the calculated time derivatives will be with respect to the inertial reference frame. All of the resulting velocities and gradient vectors are transformed in to the local element axis systems (i.e., hull, LPU, and payload).

The following subsections present detailed discussions and equation derivations for the three atmospheric environment models outlined above.

#### B. STEADY WIND MODEL EQUATIONS

The user selected steady wind vector,  $V_I^W$ , is inertially referenced. The various locally referenced vectors are:

$$\underline{V}_h^w = L_{hI} \underline{V}_I^w \quad (6-1)$$

$$\underline{V}_i^w = L_{iI} \underline{V}_I^w \quad (6-2)$$

$$\underline{V}_p^w = L_{pI} \underline{V}_I^w \quad (6-3)$$

The time derivative of  $\underline{V}_h^w$ , with respect to the rotating hull body axes (needed later for unsteady aerodynamic calculations) is:

$$\underline{\dot{V}}_h^w = \dot{\underline{V}}_h^w - (\underline{\omega}_h \times \underline{V}_h^w) \quad (6-4)$$

Since the steady wind is fixed in magnitude and direction,

$$\dot{\underline{V}}_h^w = 0$$

so,

$$\underline{\dot{V}}_h^w = - \underline{\omega}_h \times \underline{V}_h^w \quad (6-5)$$

We note that  $\dot{\underline{\omega}}_h^w = 0$  (inertially fixed) so

$$\underline{\dot{\omega}}_h^w = 0 \quad (6-6)$$

### C. DISCRETE TEST INPUT MODEL

The discrete test input model allows the isolated excitation of local airmass states, without spatial interpolation to the remaining vehicle states. These discrete test inputs have the common (1 - cosine) form (shown in Fig. 6-1):

$$g = (g_{\max}/2)(1 - \cos[2\pi(t - t_1)/(t_2 - t_1)]) \quad (6-7)$$

ORIGINAL PAGE 19  
OF POOR QUALITY

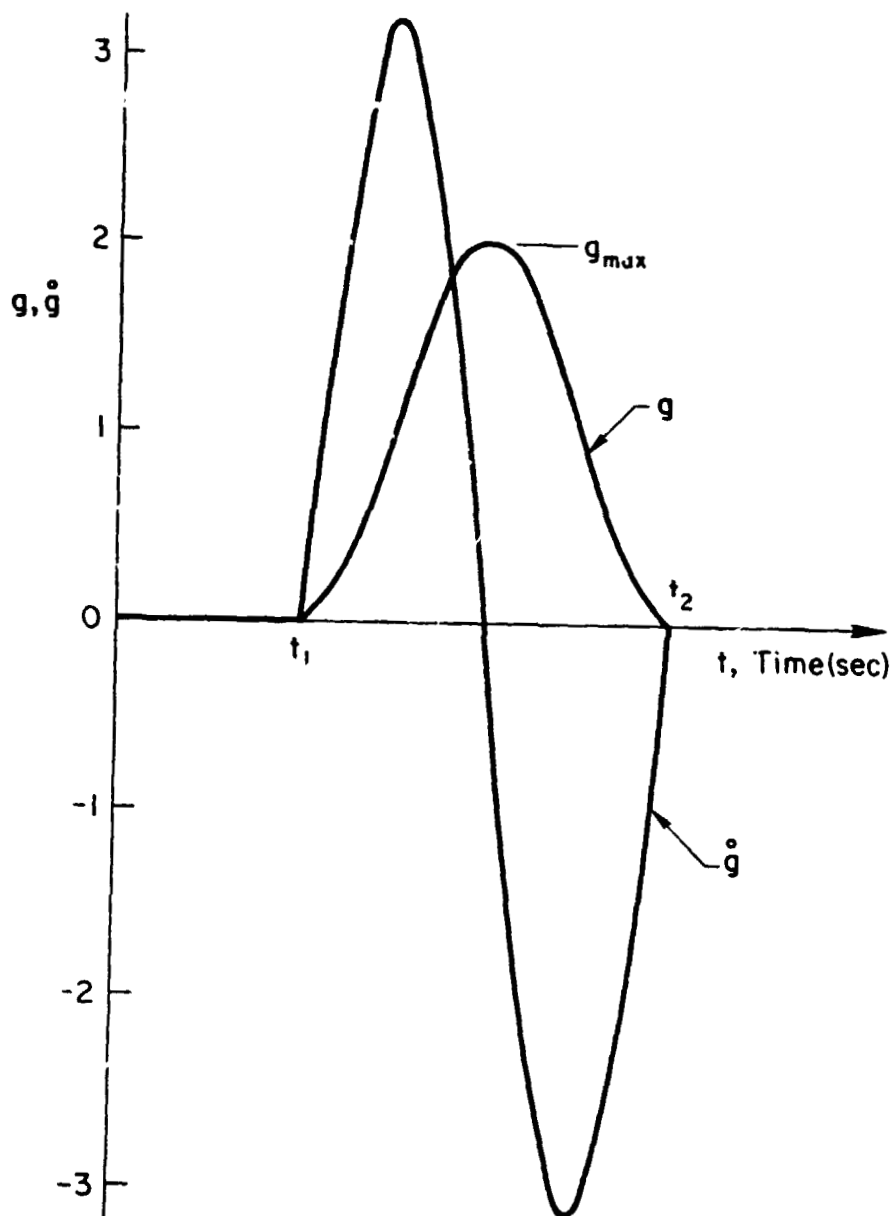


Figure 6-1. Discrete Test Input ( $g$ ) and Input Derivative ( $\dot{g}$ ) Forms

where

$g$  = one of the 48 discrete local airmass input states (all are denoted by the superscript "dam" = discrete airmass)

$g_{\max}$  = maximum value of  $g$

$t$  = present simulation time

$t_1$  = start of (1 - cosine) disturbance

$t_2$  = end of (1 - cosine) disturbance

The following 36 local airmass states accessible by the discrete input model are as follows:

1) Hull States (9)

Linear and angular local air-  
mass velocity vectors at the  
hull center of volume (cv)

$$\underline{v}_h^{\text{dam cv}}, \underline{\omega}_h^{\text{dam cv}}$$

Auxiliary\* hull gradients

$$\frac{\partial u_h^{\text{dam cv}}}{\partial x}, \frac{\partial u_h^{\text{dam cv}}}{\partial y}, \frac{\partial v_h^{\text{dam t}}}{\partial y}$$

2) Tail States (9)

Linear and angular local air-  
mass velocity vectors at the  
tail aerodynamic reference  
center (t)

$$\underline{v}_h^{\text{dam t}}, \underline{\omega}_h^{\text{dam t}}$$

Auxiliary tail gradients

$$\frac{\partial u_h^{\text{dam t}}}{\partial x}, \frac{\partial u_h^{\text{dam t}}}{\partial y}, \frac{\partial v_h^{\text{dam t}}}{\partial y}$$

3) LPU-States (12)

Linear local airmass velocity  
vector at the LPU-center of  
gravity locations (i), for each  
of the LPUs;  $i = 1, 2, 3,$  and  $4$

$$\underline{v}_i^{\text{dam i}}$$

---

\*The term "auxiliary" is adopted when referring to the nonstandard airmass gradients  $\partial u/\partial x, \partial u/\partial y, \partial v/\partial y$ .

ORIGINAL FROM THE  
OF POOR QUALITY

4) Payload States (6)

Linear and angular local velocity vectors at the payload aerodynamic reference center (pc)  $\underline{v}_p^{dam pc}$ ,  $\underline{\omega}_p^{dam pc}$

An additional 12 inputs arise from the hull and tail local airmass linear and angular acceleration vectors

$$\left( \underline{v}_h^{o dam cv}, \underline{\omega}_h^{o dam cv}, \underline{v}_h^{o dam t}, \underline{\omega}_h^{o dam t} \right)$$

These are needed for the aerodynamic calculations (unsteady and buoyancy effects), and are calculated using:

$$\underline{g}^o = [\pi g_{max} / (t_2 - t_1)] \sin [2\pi(t - t_1) / (t_2 - t_1)] \quad (6-8)$$

A plot of Eq. 6-8 for a typical  $g(t)$  is shown in Fig. 6-1.

D. MULTIPLE SOURCE ATMOSPHERIC INPUT MODEL

The geometric orientation of the four point vehicle (rectangular) input grid is shown in Fig. 6-2. The vehicle input sources (s1-s4) are located relative to the hull center-of-volume (c.v.) by the user supplied scalar quantities  $R_x^f$ ,  $R_x^a$ ,  $R_y^r$ . The sources are assumed to be positioned in a laterally symmetrical fashion so,  $R_y^l \equiv -R_y^r$ . The payload input source is located at the user selected payload aerodynamic reference center ( $\underline{R}_p^{pc}$ ).

The tail aerodynamic reference center is located relative to the hull c.v. by the scalar quantity  $R_x^t (\equiv \underline{R}_h^{hl}(1) - \underline{R}_h^{hcv}(1))$ , shown in Fig. 6-2. Finally, the center-of-gravity of each LPU is located relative to the hull center of volume by the two scalar quantities  $R_x^i$ ,  $R_y^i$ ; where

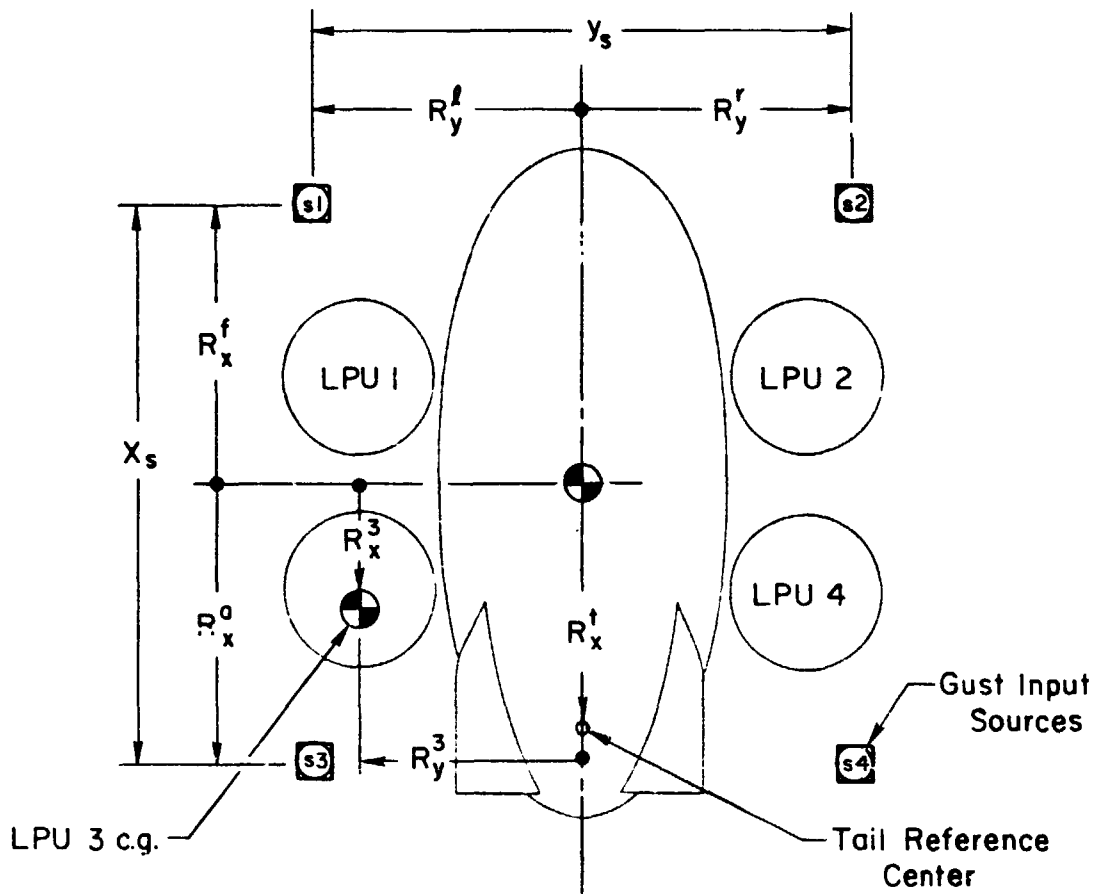


Figure 6-2. Geometry for Atmospheric Input Model

$$R_x^i \equiv \underline{R}_h^{hi}(1) - L_{hi} \underline{R}_i^{ih}(1) - \underline{R}_h^{hcv}(1)$$

$$R_y^i \equiv \underline{R}_h^{hi}(2) - L_{hi} \underline{R}_i^{ih}(2) - \underline{R}_h^{hcv}(2)$$

and  $i = 1, 2, 3,$  and  $4.$

The spatial interpolation scheme outlined below allows the calculation of the (3G) local airmass, vehicle states and (6) local airmass payload states (all with superscript "sam" = stationary airmass). The 4

ORIGINAL PAGE IS  
OF POOR QUALITY

vehicle input sources are denoted by superscripts ("s1-s4") and the payload input source by superscript ("s5").

- 1) Four vehicle input source vectors in hull coordinates  
( $\underline{v}_h^{s1}, \underline{v}_h^{s2}, \underline{v}_h^{s3}, \underline{v}_h^{s4}$ ).

The four vehicle input source vectors appropriate to the current simulation time (t) are obtained by time interpolation, amplitude scaling, and coordinate transformation of the user supplied data files. For example,

$$\underline{v}_h^{s1} = L_{hI} \underline{v}_I^{s1} \quad (6-9)$$

where \*\*\*

$$\underline{v}_I^{s1} = M_h \left[ \underline{v}_I^{s1} \Big|_{t_0} + (t - t_0) \left( \frac{\underline{v}_I^{s1} \Big|_{t_1} - \underline{v}_I^{s1} \Big|_{t_0}}{t_1 - t_0} \right) \right] \quad (6-10)$$

and

$$\underline{v}_I^{s1} \Big|_{t_0}, \underline{v}_I^{s1} \Big|_{t_1}$$

denote the user supplied vectors for input source s1 appropriate to simulation time  $t_0, t_1$ ; respectively.

$M_h$  is the user supplied scale factor. Equations 6-9 and 6-10, similarly, are used to calculate  $\underline{v}_h^{s2}, \underline{v}_h^{s3}, \underline{v}_h^{s4}$ .

- 2) Hull local air mass linear velocity vector at the center of volume ( $\underline{v}_h^{sam\ cv}$ )

$$\underline{v}_h^{sam\ cv} = \underline{v}_h^f + (\hat{x}_h)(\underline{v}_h^a - \underline{v}_h^f) \quad (6-11)$$

where,

$$\underline{v}_h^f = (\underline{v}_h^{s1} + \underline{v}_h^{s2})/2.0 \quad (6-12)$$

$$\underline{v}_h^a = (\underline{v}_h^{s3} + \underline{v}_h^{s4})/2.0 \quad (6-13)$$

$$\hat{x}_h = [-R_x^f / (R_x^a - R_x^f)] \quad (6-14)$$

- 3) Hull local airmass angular velocity vector at the center-of-volume

$$\underline{\omega}_h^{\text{sam cv}} \equiv \begin{bmatrix} \frac{\partial w_h^{\text{sam cv}}}{\partial y} \\ -\frac{\partial w_h^{\text{sam cv}}}{\partial x} \\ \frac{\partial v_h^{\text{sam cv}}}{\partial x} \end{bmatrix}^* \quad (6-15)$$

where,

$$\frac{\partial w_h^{\text{sam cv}}}{\partial y} = (w_h^l - w_h^r)/y_s \quad (6-16)$$

$$\frac{\partial w_h^{\text{sam cv}}}{\partial x} = (w_h^f - w_h^a)/x_s \quad (6-17)$$

$$\frac{\partial v_h^{\text{sam cv}}}{\partial x} = (v_h^f - v_h^a)/x_s \quad (6-18)$$

\*The interposed rotary airmass components each have two terms theoretically<sup>(6-1)</sup>, viz.,

$$\underline{\omega}_h^{\text{sam cv}} \text{ (3rd component)} \equiv r_h^{\text{sam cv}} \equiv \frac{\partial v_h^{\text{sam cv}}}{\partial x} - \frac{\partial u_h^{\text{sam cv}}}{\partial y}$$

The  $\partial u/\partial y$  term has negligible effect on the yaw rate quasi-steady aerodynamics (Section 8) and is dropped from the yaw gust Eq. 6-15 (third component), but is retained explicitly for lateral buoyancy calculations. The z-gradients are missing due to the assumed planar input model and are felt to be of small effect.

and

$$\underline{V}_h^l \equiv \begin{bmatrix} l \\ u_h \\ v_h \\ w_h \end{bmatrix}, \quad \underline{V}_h^r \equiv \begin{bmatrix} r \\ u_h \\ v_h \\ w_h \end{bmatrix}$$

$$\underline{V}_h^f \equiv \begin{bmatrix} f \\ u_h \\ v_h \\ w_h \end{bmatrix}, \quad \underline{V}_h^a \equiv \begin{bmatrix} a \\ u_h \\ v_h \\ w_h \end{bmatrix}$$

where

$$\underline{V}_h^l = \underline{V}_h^{s1} + \hat{x}_h(\underline{V}_h^{s3} - \underline{V}_h^{s1}) \quad (6-19)$$

$$\underline{V}_h^r = \underline{V}_h^{s2} + \hat{x}_h(\underline{V}_h^{s4} - \underline{V}_h^{s2}) \quad (6-20)$$

$\underline{V}_h^f, \underline{V}_h^a$  are given in Eqs. 6-12, 6-13, respectively and,

$\hat{x}_h$  is given in Eq. 6-14.

$$y_s \equiv 2R_y^l \quad (6-21)$$

$$x_s \equiv R_x^c - R_x^a \quad (6-22)$$

as shown in Fig. 6-2.

4) Hull local airmass auxiliary gradients

ORIGINAL PRICES  
OF POOR QUALITY

$$\frac{\partial u_h^{\text{sam cv}}}{\partial x} = (u_h^f - u_h^a)/x_s \quad (6-23)$$

$$\frac{\partial u_h^{\text{sam cv}}}{\partial y} = (u_h^r - u_h^l)/y_s \quad (6-24)$$

$$\frac{\partial v_h^{\text{sam cv}}}{\partial y} = (v_h^r - v_h^l)/y_s \quad (6-25)$$

5) Tail local airmass linear velocity vector at the reference center

$$\underline{v}_h^{\text{sam t}} = (\underline{v}_t^l + \underline{v}_t^r)/2.0 \quad (6-26)$$

where

$$\underline{v}_t^l = \underline{v}_h^{s1} + (\hat{x}_t)(\underline{v}_h^{s3} - \underline{v}_h^{s1}) \quad (6-27)$$

$$\underline{v}_t^r = \underline{v}_h^{s2} + (\hat{x}_t)(\underline{v}_h^{s4} - \underline{v}_h^{s2}) \quad (6-28)$$

and

$$\hat{x}_t = (R_x^t - R_x^f)/(R_x^a - R_x^f) \quad (6-29)$$

6) Tail local airmass angular velocity vector at the reference center

ORIGINAL PAGE  
OF POOR QUALITY

$$\underline{u}_h^{\text{sam t}} \equiv \begin{bmatrix} \frac{\partial w_h^{\text{sam t}}}{\partial y} \\ -\frac{\partial w_h^{\text{sam t}}}{\partial x} \\ \frac{\partial v_h^{\text{sam t}}}{\partial x} \end{bmatrix}^* \quad (6-30)$$

where

$$\frac{\partial w_h^{\text{sam t}}}{\partial y} = (w_t^l - w_t^r) / y_s \quad (6-31)$$

$$\frac{\partial w_h^{\text{sam t}}}{\partial x} = \frac{\partial w_h^{\text{sam cv}}}{\partial x} \quad \text{From Eq. 6-17} \quad (6-32)$$

$$\frac{\partial v_h^{\text{sam t}}}{\partial x} = \frac{\partial v_h^{\text{sam cv}}}{\partial x} \quad \text{From Eq. 6-18} \quad (6-33)$$

and

$$\underline{v}_t^l \equiv \begin{bmatrix} u_t^l \\ v_t^l \\ w_t^l \end{bmatrix}, \quad \underline{v}_t^r \equiv \begin{bmatrix} u_t^r \\ v_t^r \\ w_t^r \end{bmatrix}$$

\*As in Eq. 6-15, only the first order terms are retained.

ORIGINAL PAGE IS  
OF POOR QUALITY

where

$\underline{v}_t^l, \underline{v}_t^r$  are given in Eqs. 6-27, 6-28 respectively.

7) Tail local airmass auxiliary gradients

$$\frac{\partial u_h^{\text{sam } t}}{\partial x} = \frac{\partial u_h^{\text{sam } cv}}{\partial x} \quad (6-34)$$

$$\frac{\partial u_h^{\text{sam } t}}{\partial y} = (u_t^r - u_t^l)/y_s \quad (6-35)$$

$$\frac{\partial v^{\text{sam } t}}{\partial y} = (v_t^r - v_t^l)/y_s \quad (6-36)$$

8) Local airmass linear velocity vector at the LPUs' centers of gravity ( $\underline{v}_i^{\text{sam } i}$ ,  $i = 1, 2, 3, 4$ ).

For illustrative purposes, the equations pertaining to LPU-3 are given below. Equations for the remaining LPUs are obtained by direct resymboling (i.e., replace sub and superscript "3" with the appropriate LPU number) of the following equations.

$$\underline{v}_3^{\text{sam } 3} = L_{3h} \underline{v}_h^{\text{sam } 3} \quad (6-37)$$

where

$$\underline{v}_h^{\text{sam } 3} = \underline{v}_3^l + (\hat{y}_3)(\underline{v}_3^r - \underline{v}_3^l) \quad (6-38)$$

and

ORIGINAL PAGE IS  
OF POOR QUALITY

$$\underline{v}_3^l = \underline{v}_h^{s1} + (\hat{x}_3)(\underline{v}_h^{s3} - \underline{v}_h^{s1}) \quad (6-39)$$

$$\underline{v}_3^r = \underline{v}_h^{s2} + (\hat{x}_3)(\underline{v}_h^{s4} - \underline{v}_h^{s2}) \quad (6-40)$$

where

$$\hat{x}_3 = (R_x^3 - R_x^f) / (R_x^a - R_x^f) \quad (6-41)$$

$$\hat{y}_3 = (R_y^3 - R_y^a) / (R_y^r - R_y^a) \quad (6-42)$$

- 9) Local air mass linear and angular velocity vectors at the payload aerodynamic reference center

$$\underline{v}_p^{sam\ pc} = L_{pI} \underline{v}_I^{s5} \quad (6-43)$$

$$\underline{\omega}_p^{sam\ pc} = L_{pI} \underline{\omega}_I^{s5} \quad (6-44)$$

where

$\underline{v}_I^{s5}$ ,  $\underline{\omega}_I^{s5}$  are the payload input source vectors, appropriate to the current simulation time,  $t$ . These are obtained from Eq. (6-10) with  $\underline{v}_I^{s1}$  replaced by  $\underline{v}_I^{s5}$  and  $\underline{\omega}_I^{s1}$ , and  $M_{I_i}$  replaced by  $M_{v_p}$  and  $M_{\omega_p}$ , respectively.

ORIGINAL [REDACTED]  
OF POOR QUALITY

- 10) The linear and angular acceleration vectors for the hull and tail (required for the aerodynamic calculations) are evaluated numerically with the following central difference approximation:

$$\dot{\underline{v}}_h^{sam\ cv} = \frac{1}{2(\Delta t)} \left[ \underline{v}_h^{sam\ cv} \Big|_{t+\Delta t} - \underline{v}_h^{sam\ cv} \Big|_{t-\Delta t} \right] \underline{hI} \Big|_t \quad (6-45)$$

$$\dot{\underline{\omega}}_h^{sam\ cv} = \frac{1}{2(\Delta t)} \left[ \underline{\omega}_h^{sam\ cv} \Big|_{t+\Delta t} - \underline{\omega}_h^{sam\ cv} \Big|_{t-\Delta t} \right] \underline{LhI} \Big|_t \quad (6-46)$$

where  $\Delta t = 0.0001$ , and similarly for  $\dot{\underline{v}}_h^{sam\ t}$ ,  $\dot{\underline{\omega}}_h^{sam\ t}$

**E. SUPERPOSITION OF THE STEADY WIND, DISCRETE,  
AND MULTIPLE SOURCE MODELS**

The three atmospheric models described above are superimposed to allow flexibility of disturbance scenarios. The 36 local air mass velocity states are given by:

- 1) Hull States (9)

$$\underline{v}_h^{am\ cv} = \underline{v}_h^w + \underline{v}_h^{dam\ cv} + \underline{v}_h^{sam\ cv} \quad (6-47)$$

$$\underline{\omega}_h^{am\ cv} = \underline{\omega}_h^{dam\ cv} + \underline{\omega}_h^{sam\ cv} \quad (6-48)$$

$$\frac{\partial \underline{u}_h^{am\ cv}}{\partial x} = \frac{\partial \underline{u}_h^{dam\ cv}}{\partial x} + \frac{\partial \underline{u}_h^{sam\ cv}}{\partial x} \quad (6-49)$$

$$\frac{\partial \underline{u}_h^{am\ cv}}{\partial y} = \frac{\partial \underline{u}_h^{dam\ cv}}{\partial y} + \frac{\partial \underline{u}_h^{sam\ cv}}{\partial y} \quad (6-50)$$

$$\frac{\partial \underline{v}_h^{am\ cv}}{\partial y} = \frac{\partial \underline{v}_h^{dam\ cv}}{\partial y} + \frac{\partial \underline{v}_h^{sam\ cv}}{\partial y} \quad (6-51)$$

ORIGINAL PAGE IS  
OF POOR QUALITY

2) Tail States (9)

$$\underline{v}_h^{am t} = \underline{v}_h^w + \underline{v}_h^{dam t} + \underline{v}_h^{sam t} \quad (6-52)$$

$$\underline{\omega}_h^{am t} = \underline{\omega}_h^{dam t} + \underline{\omega}_h^{sam t} \quad (6-53)$$

$$\frac{\partial \underline{u}_h^{am t}}{\partial x} = \frac{\partial \underline{u}_h^{dam t}}{\partial x} + \frac{\partial \underline{u}_h^{sam t}}{\partial x} \quad (6-54)$$

$$\frac{\partial \underline{u}_h^{am t}}{\partial y} = \frac{\partial \underline{u}_h^{dam t}}{\partial x} + \frac{\partial \underline{u}_h^{sam t}}{\partial x} \quad (6-55)$$

$$\frac{\partial \underline{v}_h^{am t}}{\partial y} = \frac{\partial \underline{v}_h^{dam t}}{\partial y} + \frac{\partial \underline{v}_h^{sam t}}{\partial y} \quad (6-56)$$

3) LPU-States (12),  $i = 1, 2, 3, 4$ .

$$\underline{v}_i^{am i} = \underline{v}_i^w + \underline{v}_i^{dam i} + \underline{v}_i^{sam i} \quad (6-57)$$

4) Payload States (6)

$$\underline{v}_p^{am pc} = \underline{v}_p^w + \underline{v}_p^{dam pc} + \underline{v}_p^{sam pc} \quad (6-58)$$

$$\underline{\omega}_p^{am pc} = \underline{\omega}_p^{dam pc} + \underline{\omega}_p^{sam pc} \quad (6-59)$$

C-2

The 12 hull and tail local air mass acceleration states are more complex. As will be shown later, the aerodynamic loads on the hull and tail due to air mass acceleration may be categorized according to two types:

- Hull and tail unsteady ("apparent mass") loads — these depend on body axis (i.e., relative to rotating reference frame) acceleration:

$$\underline{V}_h^{0am\ cv}, \underline{\omega}_h^{0am\ cv}, \underline{V}_h^{0am\ t}, \underline{\omega}_h^{0am\ t}$$

- Hull "buoyancy" loads — these depend on the inertial (i.e., relative to non-rotating reference frame) linear acceleration,  $\dot{\underline{V}}_h^{sam\ cv}$ .

The correspondence between time derivatives calculated in rotating and non-rotating frames of reference is:

$$\dot{\underline{A}}_h = \underline{\dot{A}}_h^c + (\underline{\omega}_h \times \underline{A}_h) \quad (6-60)$$

where

$\underline{A}_h$  is a general vector (e.g.,  $\underline{V}_h^{am\ cv}$ ,  $\underline{\omega}_h^{am\ t}$ ) in hull coordinates

$\dot{\underline{A}}_h$  denotes time derivative calculated with respect to inertial (non-rotating axes)

$\underline{\dot{A}}_h^o$  denotes time derivative calculated with respect to rotating (i.e., hull reference) axes

$\underline{\omega}_h$  is the body axis angular velocity vector

Recall that the steady wind and multiple source input model are inertially based, while the discrete test input model is body axis based. Making use of Eq. 6-60 and the previous results, the required linear acceleration vectors are:

$$\underline{V}_h^{0am\ cv} = -(\underline{\omega}_h \times \underline{V}_h^w) + \underline{V}_h^{0dam\ cv} + \dot{\underline{V}}_h^{sam\ cv} - (\underline{\omega}_h \times \underline{V}_h^{sam\ cv}) \quad (6-61)$$

ORIGINAL PAGE IS  
OF POOR QUALITY

so,

$$\underline{\overset{0}{V}}_h^{am\ cv} = - \underline{\omega}_h \times (\underline{V}_h^w + \underline{V}_h^{sam\ cv}) + \underline{\overset{0}{V}}_h^{dam\ cv} + \underline{\dot{V}}_h^{sam\ cv} \quad (6-62)$$

$$\underline{\dot{V}}_h^{am\ cv} = \underline{\overset{0}{V}}_h^{dam\ cv} + (\underline{\omega}_h \times \underline{V}_h^{dam\ cv}) + \underline{\dot{V}}_h^{sam\ cv} \quad (6-63)$$

Likewise, the required tail acceleration vector is:

$$\underline{\overset{0}{V}}_h^{am\ t} = - \underline{\omega}_h \times (\underline{V}_h^w + \underline{V}_h^{sam\ t}) + \underline{\overset{0}{V}}_h^{dam\ t} + \underline{\dot{V}}_h^{sam\ t} \quad (6-64)$$

The required angular accelerations are similarly obtained:

$$\underline{\overset{0}{\omega}}_h^{am\ cv} = \underline{\overset{0}{\omega}}_h^{dam\ cv} + \underline{\dot{\omega}}_h^{sam\ cv} - (\underline{\omega}_h \times \underline{\omega}_h^{sam\ cv}) \quad (6-65)$$

$$\underline{\overset{0}{\omega}}_h^{am\ t} = \underline{\overset{0}{\omega}}_h^{dam\ t} + \underline{\dot{\omega}}_h^{sam\ t} - (\underline{\omega}_h \times \underline{\omega}_h^{sam\ t}) \quad (6-66)$$

The higher order angular terms for the tail are ignored compared to the hull, giving:

$$\underline{\overset{0}{\omega}}_h^{am\ t} = \underline{\overset{0}{\omega}}_h^{dam\ t} + \underline{\dot{\omega}}_h^{sam\ t} \quad (6-67)$$

## SECTION 7

### LIFT PROPULSION UNIT AERODYNAMIC FORCES AND MOMENTS

#### A. BASIC ASSUMPTIONS

Each Lift Propulsion Unit (LPU) can be considered as a modified helicopter having a main lifting rotor, a horizontally thrusting propeller, and a fuselage (nacelle). The rotors and propellers are driven by one or more turboshaft or functionally equivalent engines. The engines are assumed to maintain constant (user selected) shaft angular speed, separately specified for each rotor and propeller.

Without loss of generality, the main rotor shaft is assumed to be directly parallel to the LPU z-axis. When the LPU gimbal angles are zero, the LPU reference axes are parallel to the corresponding axes of the hull, and the main rotor shaft (the nominal rotor thrust vector) is directed vertically upward. The propeller shaft and turbine exhaust axis (Sec. 3E) are oriented at arbitrary angles relative to the LPU reference axis system.

This section presents models for calculating forces acting on the LPU due to the main rotor aerodynamics, propeller aerodynamics, and the LPU fuselage (nacelle) aerodynamics. A variety of important aerodynamic interference effects among the hull, ground, rotors, propellers, and LPU fuselages are modeled. Additional equations model the forces and moments on the LPU for a power off mooring condition.

The organization of the following subsections follows that of the calculation sequence in the simulation program. First the relative velocities with respect to local airmass at the LPU center of gravity, rotor hub, propeller hub, and LPU-fuselage aerodynamic reference center are all calculated based on the kinematic motion of the vehicle and the local airmass velocity as determined from the atmospheric environment model. These elemental velocity vectors are adjusted for hull blockage of the LPU relative free stream according to a  $(1 - \cosine)$  function of the local flow angle at each element. The elemental velocities are then

resolved into the coordinates appropriate to each element, e.g., rotor control-wind axes.

The rotor thrust is determined from the collective pitch setting and relative flow conditions, including the effect of ground proximity and hull wake turbulence interferences. An auxiliary calculation of the rotor mean lift coefficient and angle of attack is completed in order to check the validity of the linearized aerodynamic assumptions employed throughout the rotor and propeller models. The rotor flapping and coning angles are calculated from the thrust coefficient, blade collective pitch, and remaining dependent rotor states. These angles allow the calculation of the horizontal force, lateral force, and torque coefficients and required engine power, thereby completing the rotor calculations for one LPU. This procedure is then repeated for the remaining three LPUs.

As earlier noted, propeller operation with the downwash field of the rotor causes changes in the propeller local freestream velocity. At this stage, corrections are made to the propeller local velocity based on the rotor operating conditions. The propeller thrust and related operating conditions are calculated using the rotor algorithm. As with the rotor, the propeller thrust calculations include the effects of ground and hull interference. The coning and flapping equations are ignored because the propeller is rigid and nonarticulated. The propeller calculations are repeated for the remaining three LPUs.

The results of the rotor and propeller calculations are used to adjust the relative freestream velocity of the LPU fuselages to account for rotor and propeller interference effects. Once the adjusted freestream velocity vectors for each of the LPU fuselages have been determined, the associated forces and moments are calculated based on simple cross flow models.

The final set of equations in this section model the forces and moments on the LPUs for the power-off moored flight condition. Here all interference effects are neglected except those due to hull blockage of the relative freestream velocity.

ORIGINAL COPY  
OF PROGRAM QUALITY

The rotor transformations, force and moment equations, and computational algorithms are presented in the following subsections in detail. The propeller calculations reuse the identical rotor equations with minor simplifying exceptions; so the propeller equations will not be explicitly presented in the text. The rotor variables in the output listing carry the subscript, r; the propeller variables carry the subscript p. Neither subscript is used in the development except where necessary to differentiate between rotor and propeller.

**B. VELOCITIES RELATIVE TO LOCAL AIRMASS**

The main rotor, propeller, and fuselage (nacelle) aerodynamics all depend upon the LPU velocity relative to local airmass. This local relative airmass velocity is determined from the kinematic motion of the particular LPU as well as outputs from the atmospheric disturbance models.

The basic (non-interference) local airmass velocity at the *i*th LPU center-of-gravity,  $\underline{V}_i^{am}$ , is given by Eq. 6-57. Following the sign convention adopted for air mass velocities (Section 5, Subsection B), the basic LPU c.g. velocity relative to the local airmass is given by:

$$\underline{V}_i^a = \underline{V}_i - \underline{V}_i^{am} \quad (7-1)$$

$$= [u_a, v_a, w_a]_i^T \quad (7-2)$$

The angular velocity relative to the local airmass is given by:

$$\underline{\omega}_i^a = \underline{\omega}_i - \underline{\omega}_i^{am} \quad (7-3)$$

Recalling that the angular velocities and gradients of the local airmass at the LPUs are neglected ( $\underline{\omega}_i^{am} \equiv 0$ ):

$$\underline{\omega}_i^a = \underline{\omega}_i \quad (7-4)$$

ORIGINAL PAGE IS  
OF POOR QUALITY

The position vectors, locating the rotor hub ( $\underline{R}_i^{ir}$ ), propeller hub ( $\underline{R}_i^{ip}$ ), and fuselage (nacelle) aerodynamic center ( $\underline{R}_i^{if}$ ), with respect to the LPU c.g. reference axis, are shown in Fig. 7-1. The relative velocities of each isolated LPU element are determined from this figure and Eqs. 7-2 and 7-4:\*

$$\underline{V}_i^{ar} = \underline{V}_i^a + (\underline{\omega}_i \times \underline{R}_i^{ir}) \quad (7-5)$$

$$\underline{\omega}_i^r = \underline{\omega}_i \quad (7-6)$$

$$\underline{V}_i^{ap} = \underline{V}_i^a + (\underline{\omega}_i \times \underline{R}_i^{ip}) \quad (7-7)$$

$$\underline{\omega}_i^p = \underline{\omega}_i \quad (7-8)$$

$$\underline{V}_i^{af} = \underline{V}_i^a + (\underline{\omega}_i \times \underline{R}_i^{if}) \quad (7-9)$$

$$\underline{\omega}_i^f = \underline{\omega}_i \quad (7-10)$$

### C. HULL ON LPU VELOCITY INTERFERENCE

The hull interferes with the various LPU elements (rotor, propeller, and LPU fuselage) due in part to the blockage (shadowing) of the LPU relative freestream. Experimental data on this interference effect is limited and somewhat anomalous, but seems to bear out thrust decreases related to the blockage (shadowing) of the LPU freestream due to the effective hull wake (Refs. 5-8, 7-5). A major problem in modeling this interference effect is the definition of the wake region and its blockage effect because of the complex three dimensional flow geometry. This problem is especially complicated for combined translational and rotational motions of the vehicle.

---

\*In order to retain the precision of the basic (nondisturbance) LPU models, the kinematic effects due to LPU angular velocity and LPU element spatial separation are retained.

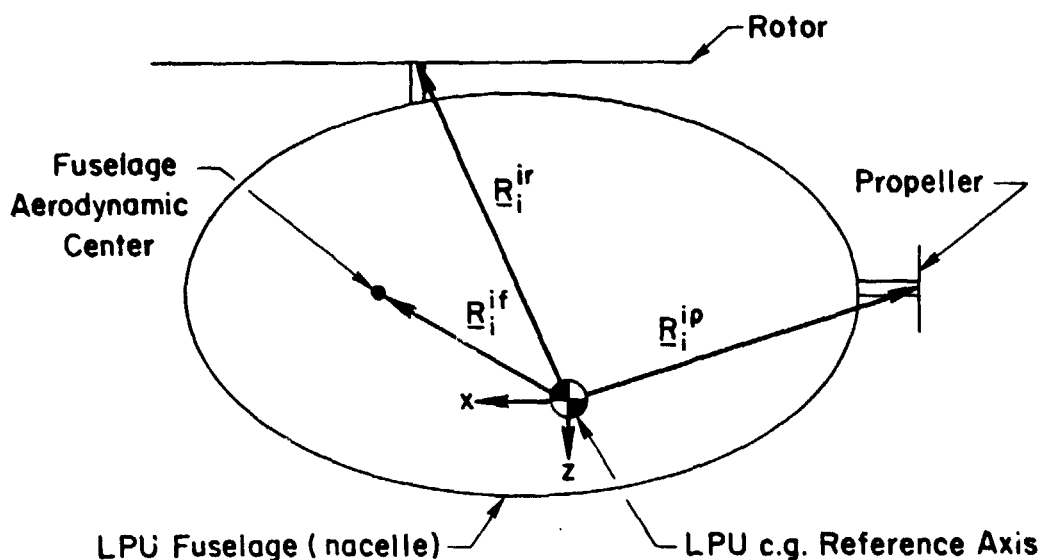


Figure 7-1. Geometry for Lift Propulsion Unit (LPU)

The basic model for hull on LPU velocity interference is presented first. This model is applicable to pure vehicle translation with no inertial or relative rotational velocity effects. All of the vehicle elements experience the relative freestream from the same direction, thereby simplifying the wake geometry. This model is then elaborated to account for translational and rotational motion. Here, the hull wake can be shed in different directions along the length of the vehicle.

#### 1. Wake Model for Pure Translational Motion

Here it is assumed that the hull wake is shed in a downstream direction colinear with the hull center-of-volume freestream velocity vector ( $\underline{v}_h^{a\ cv}$ ). The wake geometry for pure translational motion is shown in Fig. 7-2. The orientation of the hull shed wake is determined by the two relative flow angles,  $\beta$  and  $\lambda$ . The first angle ( $\beta$ ) locates the effective hull direction in the  $x$ - $y$  plane of symmetry of the hull. The second angle ( $\lambda$ ) locates the relative direction of the effective hull wake in the  $y$ - $z$  plane of symmetry of the hull. For pure translational motion with uniform atmospheric conditions (uniform wind with no turbulent components), these wake angles define the relative

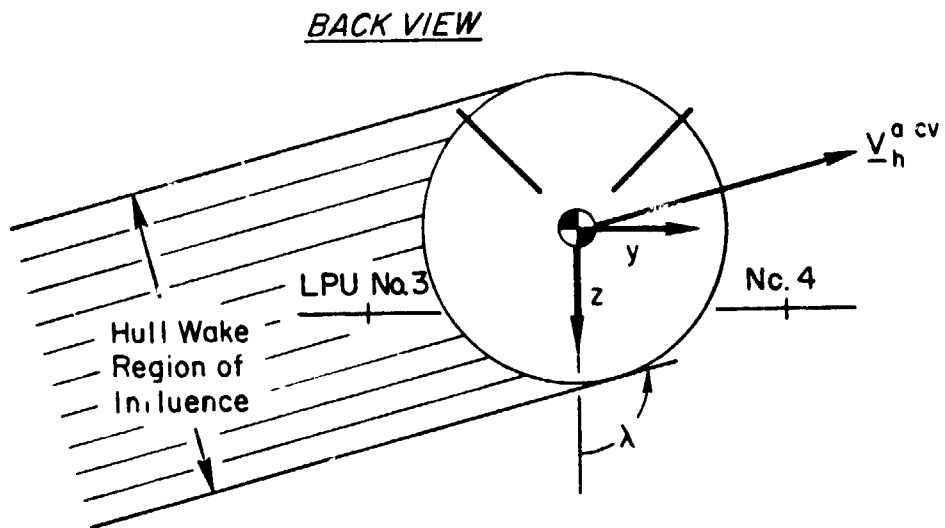
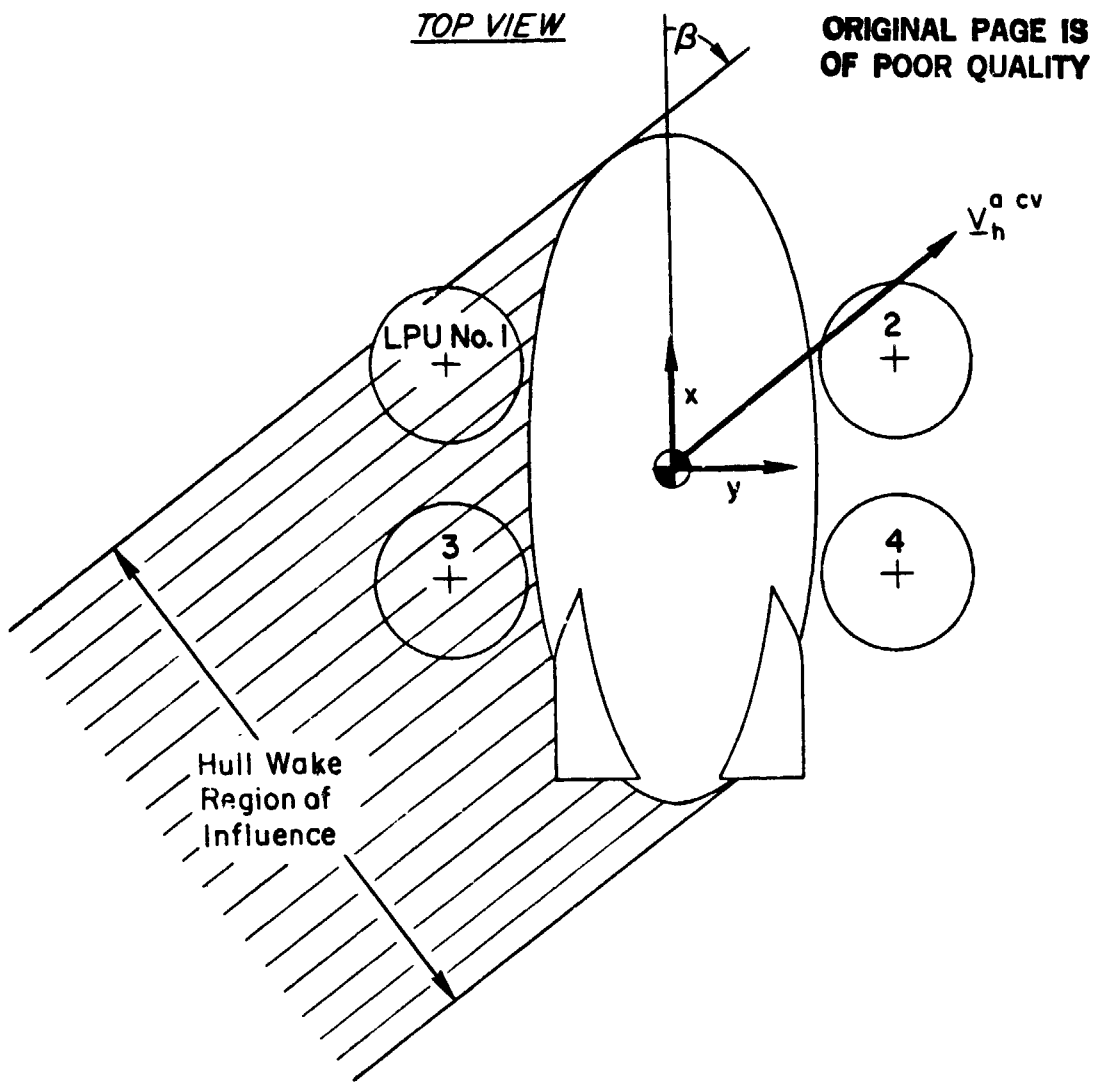


Figure 7-2. Hull Wake Geometry for Pure Translational Motion

ORIGINAL PAGE IS  
OF POOR QUALITY

downstream flow direction for the hull and all of the LPU elements. They are, in that sense, analogous to the conventional aircraft angle-of-sideslip and angle-of-attack parameters. However, unlike their aircraft counterparts, these wake angles are defined over the positive range of  $0 < \beta, \lambda < 2\pi$  rad. These definitions reduce the complexity of the wake geometry calculations.

Attenuation of the relative free stream velocity at one or more of the LPUs occurs when they are blanketed by the shed wake of the hull. Experimental results can be used to define wake angle regions ( $\beta$  and  $\lambda$ ) for each LPU within which significant velocity attenuation for that LPU occurs. In the absence of adequate experimental data, these regions are approximated from geometrical considerations of the relative orientation of the LPUs and the hull. The region of blockage is denoted separately for each LPU according to the user supplied values of the blockage region wake angles ( $\beta_1, \beta_2$  and  $\lambda_1, \lambda_2$ ). An LPU is considered to be within the wake of the hull when the values of the wake angles ( $\beta$  and  $\lambda$ ) are within the specified region for the LPU.

When an LPU is within the wake blockage (shadow) region of the hull, an attenuation of local free-stream velocity at each of the LPU's elements results. This blockage is modeled according to a (1 - cosine) function of the wake angle of the specific LPU within the shadow (blockage) region as follows:

$$(\underline{V}_1^a)' = M(\beta_1)M(\lambda_1)\underline{V}_1^a \quad (7-11)$$

where  $(\underline{V}_1^a)'$  denotes the LPU velocity relative to the local air mass after the hull wake blockage correction has been made and  $M$  is the (1 - cosine) defect function.

The defect function is given by:

$$\begin{aligned} M(\zeta) &= 1. + [(M_{\max} - 1.)(1. - \cos \psi)/2.] , \quad \zeta_1 < \zeta < \zeta_2 & (7-12) \\ M(\zeta) &= 1 , \quad \zeta < \zeta_1 \text{ or } \zeta > \zeta_2 \end{aligned}$$

ORIGINAL PAGE IS  
OF POOR QUALITY

where

$$v = 2\pi(\zeta - \zeta_1)/(\zeta_2 - \zeta_1) \quad (7-13)$$

and

$$\zeta = \beta_1 \text{ or } \lambda_1$$

Here  $\zeta_1$  and  $\zeta_2$  are the starting and ending wake angles for each  $\zeta$  and  $M_{\max}$  is the maximum velocity (blockage) defect for each  $\zeta$  wake region ( $0 < M_{\max} < 1.$ ). Thus,  $M_{\max} = 1.$  implies no blockage and  $M_{\max} = 0.$  implies complete blockage.

The defect function,  $M(\zeta)$ , defined in Eqs. 7-12 and 7-13 is shown in Fig. 7-3 for typical values of  $\zeta_1$ ,  $\zeta_2$  and  $M_{\max}$ . When the local flow angle ( $\zeta$ ) is outside of the assumed shadow region, the defect function is equal to 1 (no defect). When the LPU is completely within the shadow of the hull's wake, and the user input maximum defect ( $M_{\max}$ ) is equal to 0, the LPUs will be operating in an effective zero relative velocity condition (i.e., hover). The defect functions for the  $\beta$  wake region and  $\lambda$  wake regions are multiplicative (Eq. 7-11).

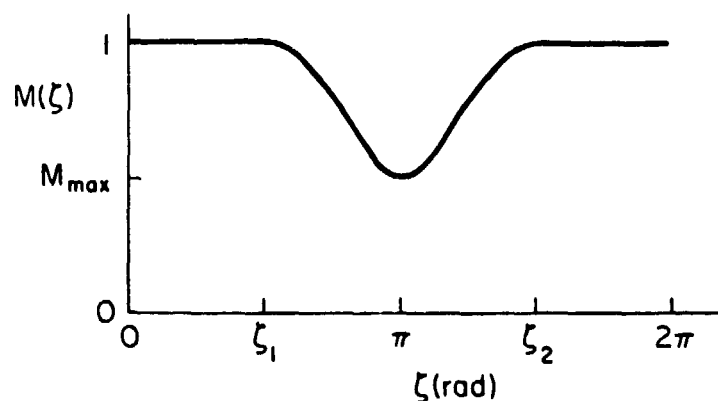


Figure 7-3. Hull Wake Defect Function

## 2. Wake Model for Arbitrary Vehicle and Airmass Motions

ORIGINAL PAGE IS  
OF POOR QUALITY

The previous model assumed that the vehicle was in pure translation, and that the ambient atmospheric conditions were constant over the entire vehicle (i.e., uniform relative wind). Modifications to this model are required to account for arbitrary translational and rotational motion. For instance, consider the case when the vehicle is experiencing pure positive yaw rotation with no relative wind velocity at the hull center of volume ( $\underline{V}_h^{a\ cv} = \underline{0}$  and  $\underline{\Omega}_h^{a\ cv} > \underline{0}$ ). During such motion, LPU-1 and LPU-4 will be operating in the cross flow wake of the hull. Unlike the previous study translational case, the hull wake is shed in opposite directions at the front and rear of the vehicle. To account for arbitrary motions which are combinations of the pure translation case treated above and the pure rotational example, we define local wake angles for the eth element of the LPU as:

$$\beta_i^e = \tan^{-1}(v_i^{a\ e}/u_i^{a\ e}) \quad 0 < \beta_i^e < 2\pi \quad (7-14)$$

$$\lambda_i^e = \tan^{-1}(v_i^{a\ e}/w_i^{a\ e}) \quad 0 < \lambda_i^e < 2\pi \quad (7-15)$$

where  $\beta_i^e$ ,  $\lambda_i^e$  are the wake angles at the eth element of each LPU, e.g., rotor (e = r), propeller (e = p), fuselage (e = f) and,

$$\underline{v}_i^{a\ e} = \begin{bmatrix} u \\ v \\ w \end{bmatrix}_i^{a\ e} \equiv \begin{bmatrix} v_i^{a\ e}(1) \\ v_i^{a\ e}(2) \\ v_i^{a\ e}(3) \end{bmatrix} \quad (7-16)$$

where  $\underline{v}_i^{a\ e}$  is given by Eqs. 7-5, 7-7, and 7-9 as applicable.

This model requires the specification of 72 input parameters, e.g.,  $\lambda_1$ ,  $\lambda_2$ ,  $\beta_1$ ,  $\beta_2$ ,  $M_{\max}(\beta)$ ,  $M_{\max}(\lambda)$  for each of 12 LPU elements.

For pure translational motion (i.e., uniform relative wind), the results of Eqs. 7-14 and 7-15 will be the same for all elements. In that case the model reduces to that of Eq. 7-11, as it should.

The corrected velocities,  $(\underline{V}_1^a e)'$ , are used in the computation of the element aerodynamic forces and moments. For notational efficiency, the prime ( )' is dropped. However, the corrected vector (Eq. 7-11) is implied in the following subsections.

**D. ROTOR AXIS TRANSFORMATIONS AND VECTOR RESOLUTIONS**

The rotor forces and moments are calculated in the "control-wind" axis system which is oriented by the axis of no feathering and the relative wind.

The control or swashplate axes are oriented relative to the LPU axes by a pitch angle,  $B_{1s}$ , in the negative sense about the LPU y-axis; and by a subsequent roll angle,  $A_{1s}$ , in the positive sense about the x-axis. The pitch transformation matrix is given by:

$$L_{B_{1s}} = \begin{bmatrix} \cos B_{1s} & 0 & \sin B_{1s} \\ 0 & 1 & 0 \\ -\sin B_{1s} & 0 & \cos B_{1s} \end{bmatrix} \quad (7-19)$$

The roll transformation matrix is:

$$L_{A_{1s}} = \begin{bmatrix} 1 & 0 & 0 \\ 0 & \cos A_{1s} & \sin A_{1s} \\ 0 & -\sin A_{1s} & \cos A_{1s} \end{bmatrix} \quad (7-20)$$

ORIGINAL PAGE IS  
OF POOR QUALITY

so that

$$L_{A_{1s}} L_{B_{1s}} = \begin{bmatrix} \cos B_{1s} & 0 & \sin B_{1s} \\ -\sin B_{1s} \sin A_{1s} & \cos A_{1s} & \cos B_{1s} \sin A_{1s} \\ -\cos A_{1s} \sin B_{1s} & -\sin A_{1s} & \cos B_{1s} \cos A_{1s} \end{bmatrix} \quad (7-21)$$

$$= L_{ci} \quad (7-22)$$

The usual practice in formulating helicopter forces and moments is to replace this matrix by its small angle equivalent (sines replaced by angles, cosines by unity), in which case the order of rotation is immaterial. The large angle form is retained here because the same matrix formulation is also used to describe the orientation of the propeller -- much larger angles, in general.

The LPU body axis relative wind linear and angular components are transformed into control axes by

$$\begin{bmatrix} u & v & w \end{bmatrix}_c^T = L_{ci} V_i^a r \quad (7-23)$$

$$\begin{bmatrix} p & q & r \end{bmatrix}_c^T = L_{ci} \omega_i^a r \quad (7-24)$$

where the superscript "a" on the relative velocity components has been dropped for economy in notation.

The azimuth angle of the relative wind in the plane of no feathering is given by

ORIGINAL PAGE IS  
OF POOR QUALITY

$$\beta_{cw} = \tan^{-1} \left( \frac{v_c}{u_c} \right) \quad (7-25)$$

where the subscript c has been attached to the relative velocity components to indicate the control axis coordinate system. The azimuth angle defines the in-plane component of the rotor hub velocity relative to the air mass. It also defines the orientation of the "control-wind" axis system (subscript "cw") where

$$\begin{aligned} u_{cw} &= \sqrt{u_c^2 + v_c^2} \\ v_{cw} &= 0 \\ w_{cw} &= w_c \end{aligned} \quad (7-26)$$

and

$$\begin{aligned} \cos \beta_{cw} &= u_c / u_{cw} \\ \sin \beta_{cw} &= v_c / u_{cw} \end{aligned} \quad (7-27)$$

The appropriate transformation matrix is given by:

$$L_{cwc} = \begin{bmatrix} \cos \beta_{cw} & \sin \beta_{cw} & 0 \\ -\sin \beta_{cw} & \cos \beta_{cw} & 0 \\ 0 & 0 & 1 \end{bmatrix} \quad (7-28)$$

ORIGINAL PAGE IS  
OF POOR QUALITY

The transformation of a vector expressed in the  $i$ th LPU reference basis to the same vector expressed in control-wind axes is denoted by:

$$\underline{u}_{cw} = L_{cwi}\underline{u}_i \quad (7-29)$$

where

$$L_{cwi} = L_{cwc}L_{ci} \quad (7-30)$$

As with other orthogonal transformations:

$$L_{cwi}^{-1} = L_{cwi}^T \equiv L_{icw} \quad (7-31)$$

The forces and moments produced by the rotor on the LPU are computed in the control-wind axis system. Figure 7-4 illustrates the several axis systems centered on the hub. The rotor thrust,  $T$ , is directed oppositely to  $w_{cw}$  and the rotor horizontal force,  $H$ , is directed oppositely to  $u_{cw}$ ; the definitions are analogous to the usual definitions of lift and drag on an airplane's wing. The rotor side force,  $Y$ , lies in the direction of  $T \times H$ . The torques produced by the rotor on the helicopter,  $L$ ,  $M$ , and  $Q$ , are in the positive sense about  $u_{cw}$ ,  $y_{cw}$ , and  $w_{cw}$ .

The control-wind axis forces are expressed in LPU coordinates by:

$$\underline{F}_{A_1}^{ir} = L_{icw}[-H \ Y \ -T]_{cw}^T \quad (7-32)$$

The torques are resolved into LPU coordinates by:

$$\underline{T}_{A_1}^{ir} = L_{icw}[L \ M \ Q]_{cw}^T \quad (7-33)$$



ORIGINAL PAGE IS  
OF POOR QUALITY

- Rigid, planar blades. The rotor blades are of untwisted rectangular planform, are rigid, and have a tip loss factor of unity. The flapping hinge is assumed located at the rotor hub, thereby setting the rotor torques L and M to zero.
- Linear blade aerodynamics. Stall and compressibility effects are ignored.
- Hull wake turbulence interference on rotor. As previously noted, this causes a decrease in the lifting efficiency of the rotor blades. This effect is modeled by an adjustment of the blade lift curve slope according to a thrust loading dependency.
- Quasi-steady flapping. Only the zeroth (coning) and first-order flapping effects are considered on a quasi-steady basis, i.e., no flapping dynamics.
- Flat-plate drag in vortex-ring state. When the flow through the rotor disk approaches zero, the model is replaced by one which represents the actuator disk as a flat plate.

The rotor speed is assumed constant.

The control inputs for the rotor are the collective deflection,  $\theta_0$ , and the longitudinal,  $B_{1S}$ , and lateral,  $A_{1S}$ , cyclic deflections of the "axis of no feathering." The remaining influences are the relative wind,  $[u, v, w]_{cw}^T$ , the relative angular rate,  $[p, q, r]_{cw}^T$ , and rotor hub height above the ground.

The rotor forces and torques are defined in terms of dimensionless coefficients:

$$\begin{bmatrix} H \\ Y \\ T \end{bmatrix}_{cw} = \rho A (\Omega R)^2 \begin{bmatrix} C_H \\ C_Y \\ C_T \end{bmatrix} \quad (7-34)$$

ORIGINAL PAGE IS  
OF POOR QUALITY

$$\begin{bmatrix} L \\ M \\ Q \end{bmatrix}_{cw} = \rho A (\Omega R)^2 R \begin{bmatrix} 0 \\ 0 \\ C_Q \end{bmatrix} \quad (7-35)$$

#### F. THRUST COEFFICIENT AND INDUCED FLOW

This subsection and the one following it present the basic equations for thrust coefficient and rotor induced velocities with the necessary corrections for ground effects. These equations parallel those of Bramwell (Ref. 7-1), with ground effect corrections due to Heyson (Ref. 7-2). The lift curve slope ( $a$ ), which is affected by the hull proximity and thrust loading (thrust loading = thrust/disk area), is assumed known a priori in the following development. Subsection G presents an algorithm for making this hull turbulence correction, as well as a model for non-hover ground effects.

The equations which follow represent the aerodynamics of a single rotor without reference to the LPU numbering system. The subscript  $i$  used previously is dropped.) Scalar equation forms are adopted for notational convenience. The subscript "in" signifies rotor "self-induced" velocity.

The thrust coefficient is given by:

$$C_T = \frac{\sigma a}{4} \left[ \frac{2}{3} \theta_0 \left( 1 + \frac{3}{2} \mu^2 \right) + \lambda \right] \quad (7-36)$$

where the several constants are defined below:

- $\rho$  = Air density
- $A$  =  $\pi R^2$ , actuator disk area
- $R$  = Effective blade radius (accounts for tip loss factor if desired)
- $\sigma$  =  $bc/\pi R$ , solidity ratio;  $b$  is the number of blades and  $c$  the chord length
- $a$  = Lift curve slope

The remaining variables in Eq. 7-36 are:

a) Advance ratio,  $\mu$

$$\mu = \frac{u_{cw}}{\Omega R} \quad (7-37)$$

b) Inflow ratio,  $\lambda$

$$\lambda = \frac{w_{cw} - (w_{in} + \Delta w)}{\Omega R} \quad (7-38)$$

where

$w_{in}$  is the rotor self induced velocity,  $w_{in} > 0$  for  $C_T > 0$  (i.e., thrust direction collinear with the negative control axis direction, Fig. 7-4).

$\Delta w$  ground induced velocity,  $\Delta w < 0$  for  $C_T > 0$  and LPU upright.

Dividing and multiplying by  $w_{in}$ ,

$$\lambda = \frac{w_{cw} - (GEF)w_{in}}{\Omega R} \quad (7-39)$$

where

$$GEF \equiv 1 + (\Delta w/w_{in})$$

Heyson (Ref. 7-2) has determined the dependency of  $\Delta w/w_{in}$  on non-dimensional rotor height,  $\hat{h}$  ( $\hat{h} \equiv$  rotor height/rotor diameter) from momentum considerations. Figure 7-5 presents a plot of GEF (= ground effect) versus  $\hat{h}$  based on Heyson's results for hovering flight. Corrections for non-hovering flight conditions are made later in Subsection G. The data presented in Fig. 7-5 can be described analytically by the function:

$$GEF = 1 - e^{\hat{h}KGR} \quad (7-40)$$

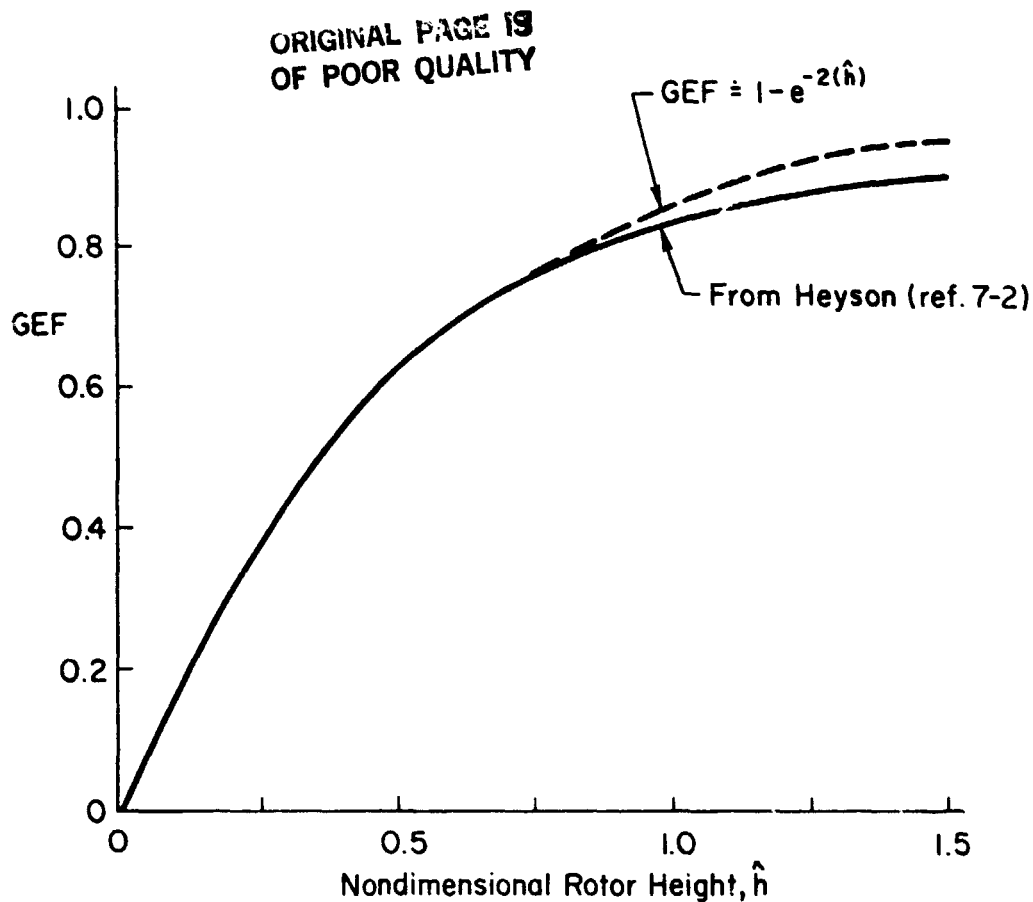


Figure 7-5. Rotor Ground Effect in Hovering Flight

where

KGR = A user-supplied curve fit constant derived from Fig. 7-5 or other available data.

The equation for the thrust coefficient neglects the effects of the angular velocity of the control-wind reference frame with respect to the air mass.\* This approximation is very good for the low speed, low angular rate flight conditions anticipated for the HLA where  $\mu p_{cw}/\Omega \ll 1$ . The inertial gyroscopic effects are retained, as discussed later in Subsection I.

The induced velocity,  $w_{in}$ , is given by (Ref. 7-3):

$$w_{in} = \frac{T}{2\rho AV_R} \quad (7-41)$$

\*The earlier omission of the air mass angular (gradient) states at the LPU locations is consistent with this approximation.

## CORRECTED VALUES OF POOR QUALITY

where  $V_R$  is the resultant velocity of the rotor hub given by:

$$V_R = \sqrt{u_{cw}^2 + (w_{cw} - (GEF)w_{in})^2} \quad (7-42)$$

These equations form the basis of an iterative procedure for determining the thrust coefficient to be described in the following paragraphs.

### 1. Iterative Solution for $w_{in}$

The algorithm is somewhat more complex than that usually employed because  $C_T$  and  $\lambda$  frequently approach zero in the HLA application. Rotor operation near zero thrust is typical for the thrusting rotors near hover and for the lifting rotors when operating in a neutral buoyancy condition. The procedure involves application of a Newton-Raphson procedure to define  $w_{in}$  with a check to verify that the proper solution has been found. The initial guess to start the procedure is determined from a simpler set of equations applicable to the hover flight condition. Along the way the flow conditions implied by the successive iterations are monitored for proximity to the vortex ring state where the equations are no longer valid. In this event, the algorithm branches to a separate calculation of  $C_T$  and  $\lambda$  based on approximating the zero flow condition by flat plate drag.

The equations for the Newton-Raphson iteration are formulated as follows. Equations 7-33 (thrust coefficient) and 7-41 are combined to yield an expression for the thrust coefficient in terms of  $V_R$ ,  $w_{in}$  and  $\Delta w$ :

$$C_T = \frac{2w_{in}V_R}{(\Omega R)^2} \quad (7-43)$$

The previous expression for  $C_T$  and Eqs. 7-38 and Eq. 7-41 are substituted into Eq. 7-36 on the left- and right-hand sides. When all terms are moved to the left-hand side there results:

ORIGINAL PAGE IS  
OF POOR QUALITY

$$V_R w_{in} - \frac{a\sigma\theta_0}{12} (\Omega R)^2 - \frac{a\sigma\theta_0 \mu^2}{8} (\Omega R)^2 - \frac{a\sigma w_{cw}}{8} (\Omega R) + \frac{a\sigma(\text{GEF})w_{in}}{8} (\Omega R) = F(w_{in}) = 0 \quad (7-44)$$

The function  $F(w_{in})$  is to be driven to zero by the Newton-Raphson procedure. This requires the derivative of  $F(w_{in})$  with respect to  $w_{in}$ , given by:

$$\frac{\partial F(w_{in})}{\partial w_{in}} = V_R + w_{in} \frac{\partial V_R}{\partial w_{in}} + \frac{a\sigma(\text{GEF})\Omega R}{8} \quad (7-45)$$

The partial derivative on the right-hand side is obtained from Eq. 7-42 as:

$$\frac{\partial V_R}{\partial w_{in}} = - \frac{w_{cw} - (\text{GEF})w_{in}}{V_R} \quad (7-46)$$

Upon substitution into Eq. 7-45:

$$\frac{\partial F(w_{in})}{\partial w_{in}} = V_R + \frac{(\text{GEF})[(\text{GEF})w_{in} - w_{cw}]w_{in}}{V_R} + \frac{a\sigma(\text{GEF})\Omega R}{8} \quad (7-47)$$

Equations 7-44 and 7-47 are evaluated at the chosen value of  $w_{in}$  to estimate the change in  $w_{in}$  required to set  $F(w_{in})$  to zero. The iteration is repeated until the change in  $w_{in}$  is reduced to some appropriately low level. The iteration requires a beginning value for  $w_{in}$ . The initial guess is obtained as follows.

## 2. Starting Value for $v_1$

Assume the hover flight condition where  $u_{cw} = w_{cw} = 0$ . From Eqs. 7-38 and 7-41 the thrust coefficient is determined to be:

ORIGINAL QUALITY  
OF POOR QUALITY

$$\begin{aligned}
 C_T &= 2\lambda_{\text{hover}}^2 && \text{for } C_T, \theta_0 > 0 \\
 &= -2\lambda_{\text{hover}}^2 && \text{for } C_T, \theta_0 < 0
 \end{aligned}
 \tag{7-48}$$

where

$$\lambda_{\text{hover}} = \frac{-(GEF)w_{in}}{\Omega R}$$

Upon substitution into Eq. 7-36, two conditions are obtained depending upon the sign of  $\theta_0$  and  $C_T$ :

$$\lambda_{\text{hover}}^2 - \frac{a\sigma(GEF)}{8} \lambda_{\text{hover}} - \frac{a\sigma(GEF)\theta_0}{12} = 0 \quad C_T, \theta_0 > 0$$

(7-49)

$$\lambda_{\text{hover}}^2 + \frac{a\sigma(GEF)}{8} \lambda_{\text{hover}} + \frac{a\sigma(GEF)\theta_0}{12} = 0 \quad C_T, \theta_0 < 0$$

For  $\theta_0 > 0$ , the first of these equations applies and takes the negative root. For  $\theta_0 < 0$ , the second equation is solved for the positive root. The initial guess for  $w_{in}$  is then given by:

$$w_{in} = \frac{-\Omega R \lambda_{\text{hover}}}{(GEF)}$$

(7-50)

This guess is used to start the iteration procedure for determining the induced velocity using Eqs. 7-44 and 7-47 with Eq. 7-37 (for  $\mu$ ) and 7-42 (for  $V_R$ ).

The procedure can result in convergence on the wrong root for  $w_{in}$ . To check for this possibility, another equation for  $w_{in}$  is solved using the thrust coefficient implied by the iterative solution. The check solution is developed as follows.

3. Check Solution for  $v_1$

Define a normalizing velocity,  $U_T$ , as follows:

$$\begin{aligned} U_T &= \Omega R \sqrt{C_T/2} & C_T > 0 \\ &= -\Omega R \sqrt{-C_T/2} & C_T < 0 \end{aligned} \quad (7-51)$$

$= (w_{in})_{\text{hover}}$ , out of ground effect

Then define normalized values of  $w_{in}$ ,  $w_{cw}$ , and  $\sqrt{u_{cw}^2 + w_{cw}^2}$  as follows:

$$\begin{aligned} \bar{w}_{in} &= w_{in}/U_T \\ \bar{w}_{cw} &= w_{cw}/U_T \\ \bar{v} &= \sqrt{u_{cw}^2 + w_{cw}^2}/U_T \end{aligned} \quad (7-52)$$

Equations 7-42 and 7-43 can be combined to eliminate  $C_T$  and normalized to yield the following fourth-order equation in  $\bar{w}_{in}$ :

$$(\text{GEF})^2 \bar{w}_{in}^4 - 2(\text{GEF}) \bar{w}_{cw} \bar{w}_{in}^3 + \bar{v}^2 \bar{w}_{in}^2 - 1 = 0 \quad (7-53)$$

The coefficients of this equation are evaluated using the thrust coefficient implied by the converged solution for  $w_{in}$  obtained previously.

Figure 7-6 shows a sketch of the positive solutions for Eq. 7-53 for the zero forward speed case and no ground effect (i.e.,  $\text{GEF} = 1$ ). Positive  $\bar{w}_{cw}$  is to the left, thereby maintaining the same orientation of the plot as shown in the usual texts (e.g., Refs. 7-1, 7-3, and others) where the sign convention for  $\bar{w}_{cw}$  is in the opposite sense. An experimental solution is also sketched to indicate the differences between theory and experiment in region,  $2 > \bar{w}_{cw} > 0$ , nominally identified as the "vortex ring state."

The smallest positive root is the correct one. As can be seen from the sketch, solving for this root can break down in the region near  $\bar{w}_{cw} = 2$  as the slope of the curve becomes infinite. Further, in solving for  $w_{in}$  using Eqs. 7-44 and 7-47, the iterative procedure can converge on the wrong root if the flow conditions place the root in the windmill brake state.

The sketch also shows that the difference between the theoretical and experimental curves in that portion of the vortex ring state where  $0 < \bar{w}_{cw} < 1.5$  is not serious. Consequently, the theoretical solution is taken as the true one outside the crosshatched region where departure from the experimental curve is relatively large and/or there are numerical difficulties in solving for  $w_{in}$ . When  $GEF = 1$ , this region marks the condition where:

$$2.1 < \bar{w}_{cw} < 1.5 \quad (7-54)$$

When ground effects are present ( $GEF < 1$ ), the crosshatched region of Fig. 7-6 (vortex ring state) shifts to the right with decreasing ground height ( $GEF$  decreasing). Therefore, as the ground height decreases, the vortex ring state will be encountered with smaller descent rates than for the rotor operating out of ground effect operation. An analysis of the shift of the vortex ring state region (Eq. 7-54) with ground effect constant ( $GEF$ ) yields the following approximate expression defining the "vortex ring state."

$$1.1 + GEF < \bar{w}_{cw} < 0.5 + GEF \quad (7-55)$$

When the criterion of Eq. 7-55 is satisfied, a change is made to an alternate means of calculating the induced flow and thrust coefficient based on flat plate drag.

In using the smallest positive root of Eq. 7-53 as a check on the iterative solution of Eq. 7-44, the procedure is as follows. If the two roots agree, the correct root has been obtained and both  $C_T$  and  $w_{in}$  have been determined. If they disagree, the iterative procedure is restarted

using the smallest positive root of Eq. 7-53 (which is not the correct answer because of the incorrect thrust coefficient used in computing the polynomial coefficients). Throughout the procedure the value of  $\bar{w}_{cw}$  is monitored against the criterion of Eq. 7-55. If this condition occurs, the program branches as indicated in the preceding paragraph, and prints a message to the user.

#### 4. Flat Plate Drag Solution

This solution approximates for the thrust coefficient and induced flow in the crosshatched region of Fig. 7-6 by assuming that:

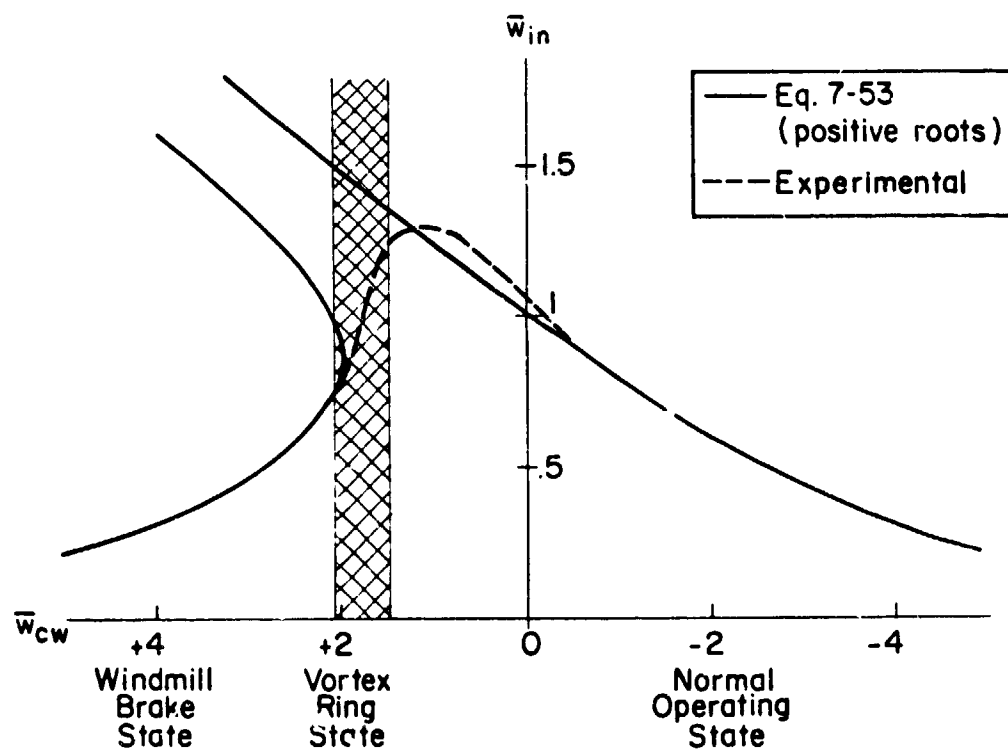


Figure 7-6. Sketch of Normalized Inflow Velocity vs. Normalized Vertical Speed for Zero Forward Speed  
GEF = 1 (No Ground Effect)

$$(GEF)w_{in} = w_{cw} \quad (7-56)$$

meaning that there is zero total flow through the actuator disk. Because there is zero flow, the disk is modeled as a flat plate having area equal to that of the actuator disk. The thrust is given by:

$$T = \frac{1}{2} \rho A C_D w_{cw}^2 = \rho A (\Omega R)^2 C_T \quad (7-57)$$

The thrust coefficient is therefore:

$$C_T = \frac{1}{2} C_D |\lambda_C| \lambda_C \quad (7-58)$$

where

$$\lambda_C = \frac{w_{cw}}{\Omega R} \quad (7-59)$$

and from Eq. 7-56

$$w_{in} = \frac{w_{cw}}{(GEF)} \quad (7-60)$$

This equation provides the correct limiting case (autorotation) result for  $C_D = 1.23$ . For accelerated or non-axial motion, errors are introduced by the approximation.

##### 5. Rotor Mean Lift Coefficient and Angle-of-Attack

An indication of the operating regime of the rotor may be gained from the following approximate expression (Ref. 7-3) for the rotor mean lift coefficient ( $\bar{C}_L$ ):

$$\bar{C}_L = 6 \frac{C_T}{\sigma} \quad (7-61)$$

where

$C_T$  is the converged thrust coefficient result of Eq. 7-36.

The rotor mean angle-of-attack is determined by:

$$\bar{\alpha} = \bar{C}_L/a \quad (7-62)$$

The assumption of linear aerodynamics employed in the blade element theory result of Eq. 7-36, requires:

$$\bar{C}_L < \bar{C}_{L\text{STALL}} = 1$$

The calculated values of  $\bar{C}_L$  and  $\bar{\alpha}$  provide important information on the validity of the rotor (and propeller) models in various flight regimes. The results of Eqs. 7-61 and 7-62 are invalid for "vortex ring state" operation.

#### G. ADDITIONAL INTERFERENCE EFFECTS

This section presents models for rotor ground effects in a non-hovering flight condition and hull wake turbulence interference on the rotor operation. These models are first be presented individually, then followed by a discussion of the algorithm which permits the simultaneous calculation of these effects within the simulation.

##### 1. Rotor Ground Effect in Non-Hovering Flight Conditions

The problem of determining the multitude of ground/rotor vortex interactions in non-hovering flight conditions has been thoroughly treated by Heyson (Refs. 7-2, 7-4). His results show a significant decrease in rotor ground effect with small forward speed (or effective relative wind). Such reductions in ground effect also occur in hovering flight with non-vertical wake orientation due to vehicle pitch or roll. In the present model, these effects are largely reflected\* by changes in the ground induced velocity ( $\Delta w$ ), through its defining relations (Eq. 7-39 and 7-40).

---

\*We neglect the remaining small ground induced velocities about the other axes.

ORIGINAL PAPER  
OF POOR QUALITY

An approximate expression for GEF is obtained from the theory of Ref. 7-4 which yields\*:

$$GEF = 1 - (\cos^2 \chi_e)^{\hat{h}} KGR \quad (7-63)$$

where

$\hat{h}$ , KGR have been previously defined (Eq. 7-40)

and

$\chi_e$  the effective wake orientation angle with respect to the inertial vertical axis.

This effective wake angle accounts for the distortion of the geometric wake angle ( $\chi$ ) at the rotor due to wake roll-up effects. It may be calculated from the following equation (Ref. 7-2):

$$\tan \chi_e = \frac{\pi^2}{4} \tan \chi \quad (7-64)$$

where

$$\tan \chi = \frac{\left( u_I^{aw^2} + v_I^{aw^2} \right)^{1/2}}{w_I^{aw}}$$

as in Figure 7-7 (taken from Ref. 7-2). Whence,

$$\chi_e = \tan^{-1} \left[ \frac{\pi^2}{4} \frac{\left( u_I^{aw^2} + v_I^{aw^2} \right)^{1/2}}{w_I^{aw}} \right] \quad (7-65)$$

The inertially referenced rotor wake velocities ( $u_I^{aw}$ ,  $v_I^{aw}$ ,  $w_I^{aw}$ ) of Eq. 7-65 are determined from:

$$\underline{V}_I^{aw} = \begin{bmatrix} u_I^{aw} \\ v_I^{aw} \\ w_I^{aw} \end{bmatrix}_I \quad (7-66)$$

\*For upright hover ( $\chi_e = 0$ ), Eq. 7-63 reduces to Eq. 7-40 as it should.

ORIGINAL PAGE IS  
OF POOR QUALITY

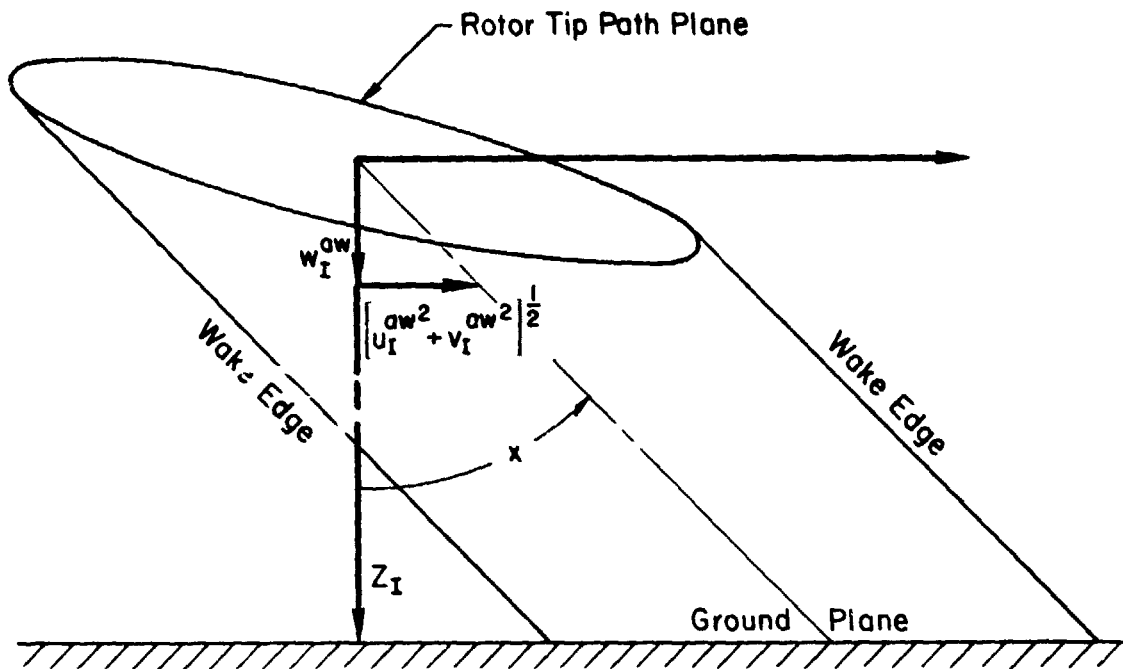


Figure 7-7. Rotor Wake Geometry for Non-Hovering Flight; from Ref. 7-2

where

$$\underline{v}_I^{aw} = L_{IcW} \underline{v}_{cW}^{aw}$$

$$L_{IcW} = L_{Ii} L_{icW}$$

and

$$\underline{v}_{cW}^{aw} = \begin{bmatrix} 0 \\ 0 \\ (GEF)w_{in} \end{bmatrix} - \begin{bmatrix} u_{cW} \\ v_{cW} \\ w_{cW} \end{bmatrix} \quad (7-67)$$

where

$u_{cW}$ ,  $v_{cW}$ ,  $w_{cW}$ , are determined from Eq. 7-26

$w_{in}$  is determined from the iterative process of Eqs. 7-44 and 7-47.

## ORIGINAL EQUATIONS OF POOR QUALITY

The computational implementation of Eq. 7-63 presents an iterative problem:

- a)  $GEF = f(\chi_e)$  , Eq. 7-63
- b)  $\chi_e = f(w_{in}, GEF)$  , Eqs. 7-64, 7-67
- c)  $w_{in} = f(GEF)$  , Eqs. 7-44, 7-47

While it would be possible to incorporate the iterative computation of GEF within the previous Newton Raphson procedure (Subsection F) the following approximate scheme was implemented:

- a) Set  $GEF = 1$  (out of ground effect)
- b) Iteratively calculate  $w_{in}$ ,  $C_T$ , Eqs. 7-44, 7-47, 7-43
- c) Calculate  $\chi_e$ ,  $GEF$ , Eqs. 7-65, 7-63
- d) Iteratively recalculate  $w_{in}$ ,  $C_T$ , Eqs. 7-44, 7-47, 7-43

This "two pass" solution has proven to be within the overall level of accuracy of the simulation.

### 2. Hull Wake Turbulence Interference on the Rotor

Wind tunnel tests on HLA configurations have shown a significant decrease in rotor thrust (at constant collective pitch setting) due to hull proximity in both hovering and forward flight conditions (Ref. 7-5). This effect is most significant (20 percent thrust decrease) at lower thrust levels, and less important at the higher thrust levels where rotor induced flows become better defined. The rotor placements are defined by the non-dimensional parameter,  $\hat{l}_r \equiv$  (lateral separation between rotor hub and hull centerline)/hull diameter. As expected, hull/wake turbulence interference decreases with increased separation between the hull and rotor (increasing  $\hat{l}_r$ ).

The data of Ref. 7-5 are replotted in Fig. 7-8 to show the dependence of thrust ratio (rotor thrust in the presence of the hull/isolated

ORIGINAL PAGE IS  
OF POOR QUALITY

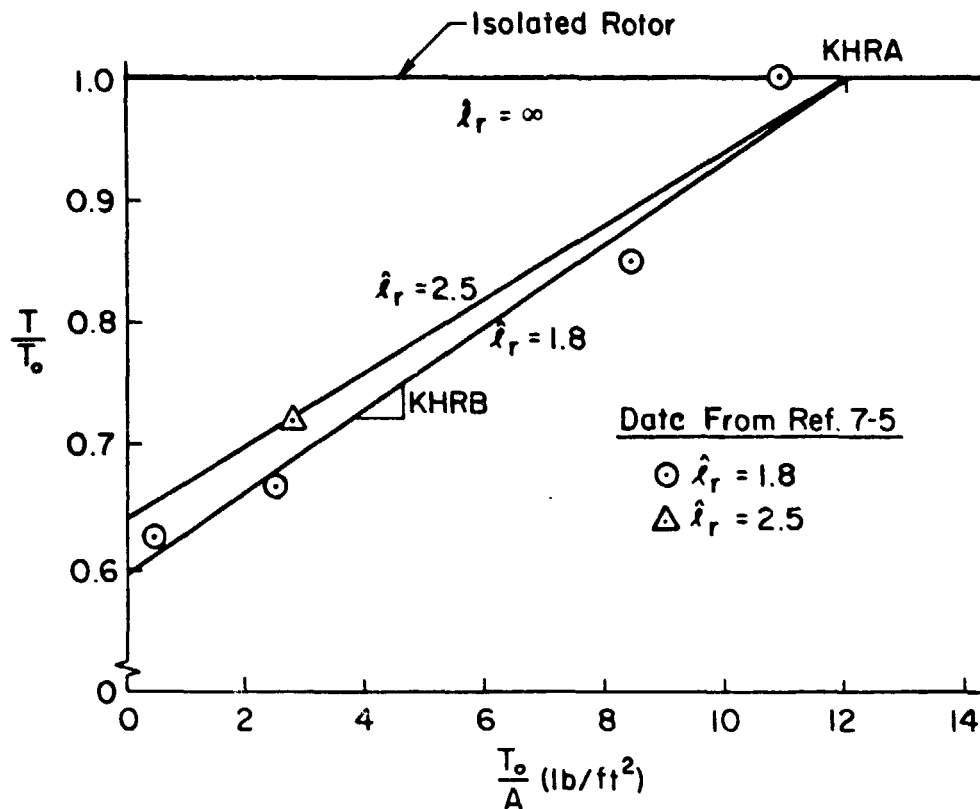


Figure 7-8. Hull Wake Turbulence Effect on Rotor Thrust

rotor thrust) on rotor disk loading (isolated rotor thrust/disk area) for three rotor locations ( $\hat{\lambda}_r$ ). The trends demonstrated in this figure suggest the following form for thrust ratio based on isolated disk loading:

$$\frac{T}{T_0} = 1 - (KHRA - |T_0|/A)KHRB, \quad |T_0|/A < KHRA$$

$$\frac{T}{T_0} = 1, \quad |T_0|/A > KHRA$$

(7-68)

where

T = the rotor thrust in the presence of the hull interference

ORIGINAL PAGE IS  
OF POOR QUALITY

$T_0$  = the isolated rotor thrust

A = rotor disc area

KHRA, KHRB = input constants (separate values for each rotor)

The data of Fig. 7-8, applied to the model form of Eq. 7-68, show the parameter KHRA to be constant with rotor placement, while KHRB decreases with increasing hull/rotor separation. The dependence of KHRB on hull/rotor separation ( $\hat{\lambda}_r$ ) is shown in Fig. 7-9.

The exact cause of the interference effect of the hull on the rotor at zero sideslip has not been established. Calculations have shown that the mean velocity magnitude and direction of the rotor freestream is not

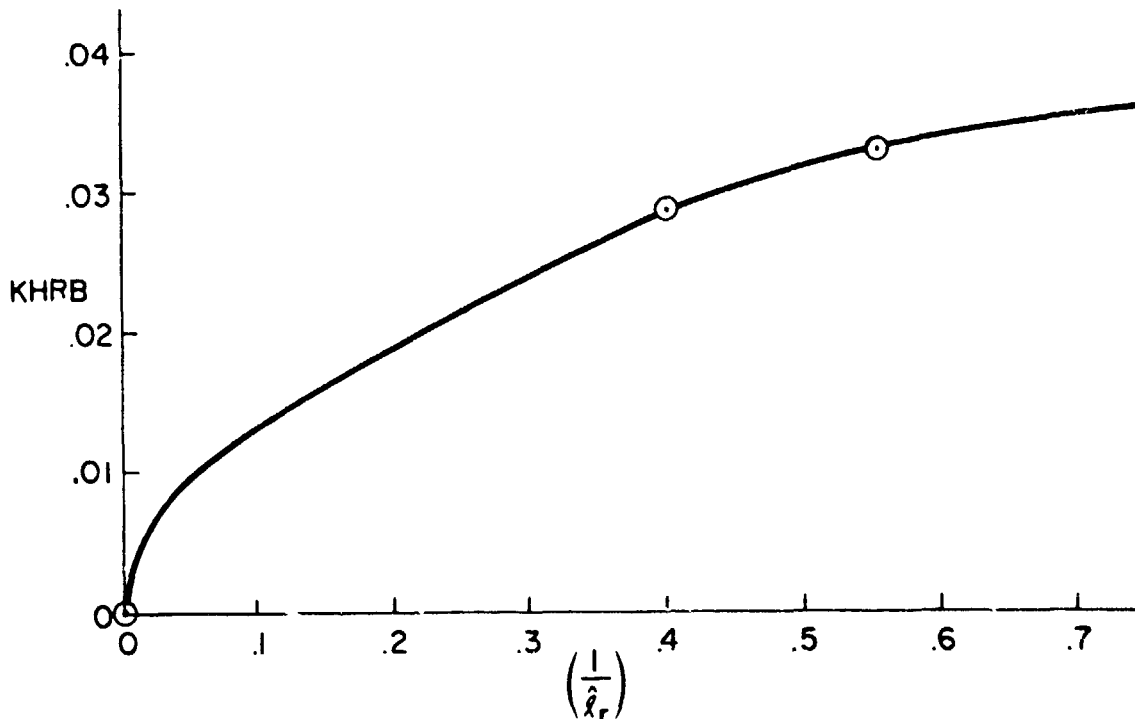


Figure 7-9. Variation of Hull Interference Parameter KHRB with Rotor Placement

significantly distorted by the hull for the rotor locations which were investigated during the wind tunnel test program, Ref. 7-5. The significant decrease in rotor thrust capability (at a constant collective pitch setting) may therefore be related to the impinging of the hull wake on the rotor inflowing freestream. The influx of hull/wake turbulence, as in the case of free stream turbulence effects on a wing, causes a reduction in the rotor blade lift curve slope ( $a$ ). We may, therefore, interpret Eq. 7-68 to be an interference correction on the isolated rotor lift curve slope ( $a_0$ ).\*

The calculation of the rotor blade effective lift curve slope from Eq. 7-68 requires a knowledge of the isolated rotor thrust loading ( $T_0/A$ ). Once the isolated rotor conditions are calculated, the lift curve slope interference correction can be made, and the solution for rotor conditions including interference effects can be determined:

- a) Set  $a = a_0$
- b) Iteratively calculate isolated rotor conditions  $w_{in}$ ,  $C_T$ , Eqs. 7-44, 7-47
- c)  $a = a_0(T/T_0)$ , Eq. 7-68
- d) Iteratively recalculate  $C_T$ ,  $w_{in}$ , Eqs. 7-44, 7-47

As in the case of the algorithm for calculating non-hover ground effects, the present scheme for hull and rotor interference calculations requires a two pass process. Also, the rotor calculations including non-hover ground effects should be evaluated before the hull on rotor interference effects are determined. Such a process would require four passes through the Newton-Raphson algorithm for each rotor (and each propeller). In order to reduce the computational requirements and still retain a sufficient overall level of accuracy, the following two pass algorithm is implemented:

- a) Set  $GEF = 1$   
Set  $a = a_0$

---

\*The symbol for the isolated rotor lift curve slope ( $a_0$ ) should not be confused with that for the rotor coning angle (Eq. 7-69).

ORIGINAL PAGE IS  
OF POOR QUALITY

- b) Iteratively calculate  $w_{in}$ ,  $C_T$ , Eqs. 7-44, 7-47
- c) Calculate  $\chi_e$ , GEF, Eqs. 7-65, 7-63
- d) Calculate  $a = a_0(T/T_0)$ , Eq. 7-68
- e) Iteratively recalculate  $w_{in}$ ,  $C_T$ , Eqs. 7-44, 7-47

#### H. ROTOR FLAPPING COEFFICIENTS

The rotor coning and flapping angles are needed in the calculation of the remaining force and torque coefficients.

The rotor flapping angle,  $\beta$ , is positive for blade deflections above the plane of no feathering.  $\beta$  is a function of  $\psi$ , the azimuthal position of the blade as it advances around the rotor disk (see Fig. 7-1), starting at the downwind position. Thus:

$$\beta(\psi) = a_0 - a_1 \cos \psi - b_1 \sin \psi \quad (7-68)$$

where the flapping coefficients are given by the following:

##### 1. Coning Angle, $a_0$

$$a_0 = \frac{\gamma}{8} \theta_0 (1 + \mu^2) + \frac{4}{3} \lambda \quad (7-69)$$

This expression, like that for the thrust coefficient, neglects the dependency on  $p_{cw}$  (Ref. 7-1). It also neglects the influence of gravity acting on the blade mass (tends to reduce  $a_0$  for lifting rotors). The variable  $\gamma$  is the Lock number, given by:

$$\gamma = \frac{\rho a c R^4}{I_B} \quad (7-70)$$

where  $I_B$  is the blade moment of inertia about the hub.

2. Longitudinal Flapping Angle,  $a_1$  (Ref. 7-6)

$$a_1 = \frac{1}{1 - (\mu^2/2)} \left[ \mu \left( \frac{8}{3} \theta_0 + 2\lambda \right) + \frac{P_{cw}}{\Omega} - \frac{16}{\gamma} \frac{q_{cw}}{\Omega} \right] \quad (7-71)$$

where  $a_1$  is defined as positive for tip path plane tilting backwards (positive sense rotation about Y, see Fig. 7-1).

3. Lateral Flapping Angle,  $b_1$  (Ref. 7-6)

$$b_1 = \frac{1}{1 + (\mu^2/2)} \left[ \frac{4}{3} \mu a_0 - \frac{q_{cw}}{\Omega} - \frac{16}{\gamma} \frac{P_{cw}}{\Omega} \right] \quad (7-72)$$

where  $b_1$  is defined positive for tip path plane tilting to the right (when viewed from the rear); thus a positive rotation about X (Fig. 7-1).  $a_0$  is given in Eq. 7-69.

I. HORIZONTAL FORCE AND TORQUE COEFFICIENTS

The horizontal force coefficient,  $C_H$ , is given by (Ref. 7-1):

$$C_H = \frac{\sigma a}{2} \left[ \frac{\mu \delta}{2a} + \frac{1}{3} a_1 \theta_0 + \frac{3}{4} \lambda a_1 - \frac{1}{2} \mu \theta_0 \lambda + \frac{1}{4} \mu a_1^2 \right] \quad (7-73)$$

The blade drag coefficient,  $\delta$ , is calculated by the following quadratic function (Ref. 7-3) of mean blade angle of attack ( $\bar{\alpha}$ )

$$\delta = \delta_a + \delta_b \bar{\alpha} + \delta_c \bar{\alpha}^2 \quad (7-74)$$

where

$\delta_a, \delta_b, \delta_c$  are input constants

$\bar{\alpha}$  is given in Eq. 7-62

ORIGINAL PAGE IS  
OF POOR QUALITY

This equation neglects terms in  $\mu^2$ ,  $a_0^2$ ,  $b_1$ ,  $p_{cw}$ , and  $q_{cw}$  which are judged in Ref. 7-7 to be negligible. However, there remains an implicit dependence on  $p_{cw}$  and  $q_{cw}$  through  $a_1$ . The resulting dependence on  $q_{cw}$  is exact for hover (Ref. 7-1) and quite adequate for low speed flight. The drag coefficient function is used to allow near-zero thrust levels, where the standard value of  $\delta = 0.012$  is no longer accurate (Ref. 7-3).

The horizontal force coefficient,  $C_Y$ , is given by (Ref. 7-1):

$$C_Y = C_T b_1 \quad (7-75)$$

where  $b_1$  is the lateral flapping coefficient, positive for the tip path plane tilting to the right (positive sense about  $u_{cw}$ ). This equation approximates the lateral force coefficient as being entirely due to lateral flapping and retains the major roll damping effect cited in Ref. 7-6.

The torque coefficient,  $C_Q$ , is given by (Ref. 7-1):

$$C_Q = \frac{\sigma \delta}{8} (1 + 3\mu^2) - \lambda C_T - \mu C_H \quad (7-76)$$

where the first term is the contribution of profile and induced drag and the remaining terms are due to thrust. The torque acts in a positive sense about  $w_{cw}$ , as the direction of rotor rotation is assumed counter-clockwise (as viewed from above).

The power required ( $P_{req}$ ) to maintain a constant rotor angular speed is:

$$P_{req} = Q \Omega \quad (7-77)$$

where

$Q$  is obtained from Eqs. 7-76 and 7-35.

ORIGINAL PAGE IS  
OF POOR QUALITY

The power required is converted to horsepower (English units) by dividing  $P_{req}$  by 550, or to Kilowatts (S.A. Units) by dividing  $P_{req}$  by 1000.

**J. PROPELLER FORCES AND TORQUES**

The equations for the propeller force,  $F_{A_1}^i P$  and torque  $T_{A_1}^i P$  are identical to those used for the rotor except for neglecting flapping and coning degrees of freedom. The assumptions that are outlined in Section E concerning the development of the rotor models apply to the propeller as well. The propeller forces and moments depend on the local relative wind,  $V_1^a P$  at the propeller hub (including hull and rotor interference effects) resolved to "control-wind" axes (e.g., Eq. 7-23 and 7-24) for the propeller. The angles  $A_{1s}$ ,  $B_{1s}$  now define the orientation of the propeller rotation vector ( $\Omega_p$ ) (also the positive thrust direction) relative to the LPU reference axis (Figure 7-10).

An additional step in the calculation of propeller forces and torques, is to correct the local relative wind at the propeller (from Eq. 7-16,  $e = p$ ) for rotor interference. The relative local freestream velocity of the propeller hub is adjusted to account for the rotor induced downwash:

$$(V_1^a P)' = V_1^a P - (KRP) L_{icw} V_{cw}^{in r} \quad (7-78)$$

where

$(V_1^a P)'$  denotes  $V_1^a P$  from Eq. 7-7, corrected for hull velocity blockage with Eq. 7-11, and also corrected for rotor interference

KRP is an input constant for each LPU that accounts for the relative proximity of the rotor and propeller ( $0 < KRP < 2.0$ )

ORIENTATION OF PROPELLER SHAFT AXES  
OF POOR QUALITY

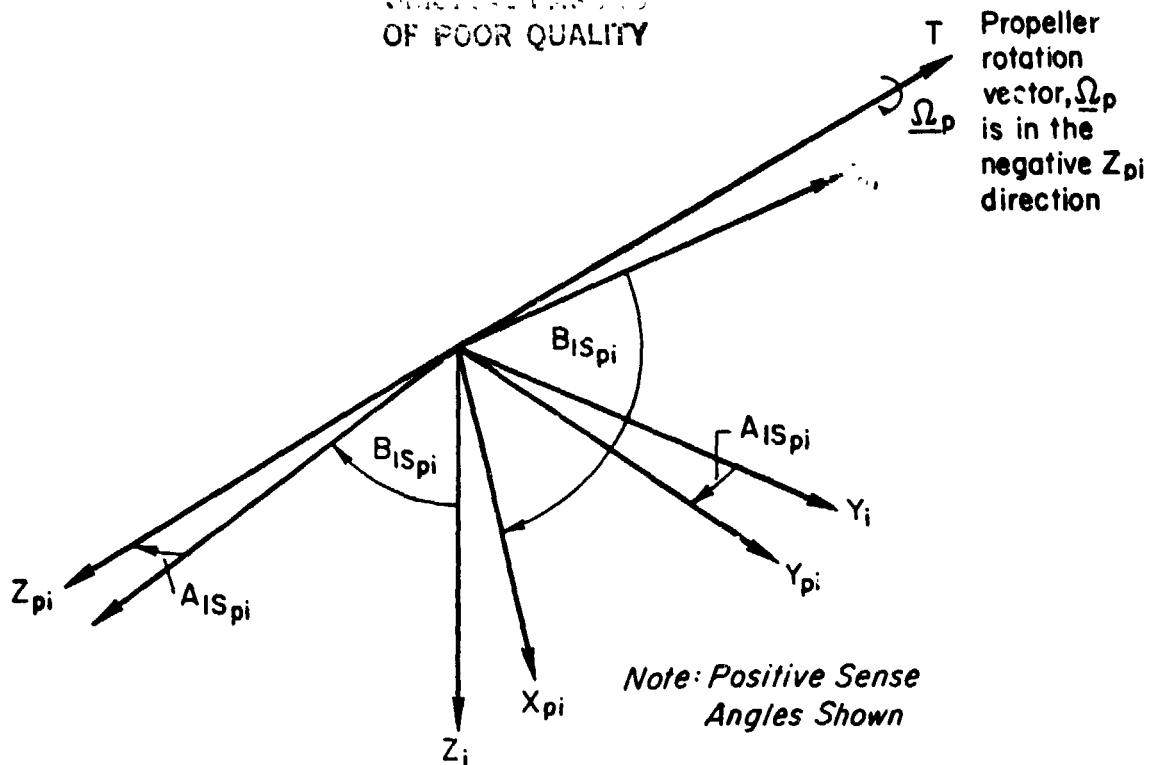


Figure 7-10. Orientation of Propeller Shaft Axes Relative to the LPU Reference Frame

and

$$\underline{v}_{cw}^{in r} \equiv \begin{bmatrix} 0 \\ 0 \\ (GEF_r)w_{in r} \end{bmatrix} \quad (7-79)$$

with  $GEF_r$  and  $w_{in r}$  obtained from the previous rotor calculations for the respective LPU (e.g. rotor 1 for rotor/propeller interference on propeller 1).

Having obtained the relative local flow velocity at each of the propeller hubs in coordinates of the LPU c.g. reference axes,  $(\underline{v}_i^a P)'$ , the rotor equations are entered starting with the axis transformations and velocity resolutions (Eq. 7-19 to 7-31). The calculations of propeller ground effects are retained in order to allow for vertically

oriented propellers. For horizontally thrusting propellers, these effects will be negligible ( $\chi_e \approx 90$  deg,  $GEF \approx 1$ ). The hull wake turbulence interference on the propeller is calculated, as before, with an adjustment on the propeller effective lift curve slope. All second order effects of hull/rotor/propeller wake interaction are neglected. Next the propeller horizontal force is calculated, with the flapping and coning coefficients all equal to zero because the propeller is assumed rigid. Thus, the lateral force coefficient,  $C_y$ , is also neglected (Eq. 7-75). The pitching and rolling moments of the propeller hub are neglected in comparison with the moments generated by the propeller thrust force transfer to the LPU center of gravity. This is consistent with the similar assumption of negligible rotor hub moments (flapping hinge at the rotor hub) in comparison with the rotor thrust transfer moments to the LPU center-of-gravity.

#### K. FUSELAGE (NACELLE) AERODYNAMICS

The forces and moments on the LPU fuselage are calculated from simple models which depend on the relative local air mass velocity of the fuselage aerodynamic reference center. The relative velocity vector, which is calculated from vehicle kinematics, local atmosphere environment states, and hull velocity blockage effects, is corrected for rotor and propeller downwash interference:

$$(\underline{V}_1^a f)' = \underline{V}_1^a f - (KRF)(L_{1cw})^r \underline{V}_{cw}^{in r} - (KPF)(L_{1cw})^p \underline{V}_{cw}^{in p} \quad (7-80)$$

where

$(\underline{V}_1^a f)'$  denotes  $\underline{V}_1^a f$  corrected for rotor and propeller interference

$\underline{V}_1^a f$  is obtained from Eq. 7-9 and corrected for hull velocity blockage with Eq. 7-16

$KRF$ ,  $KPF$  are input constants for each LPU that account for the relative proximity of the rotor, propeller, and fuselage ( $0 < KRF, KPF < 2.0$ )

$(L_{1cw})^r$  is from Eq. 7-31

$(C_{1cw})^p$  is from Eq. 7-31 with the appropriate definition for  $A_{1s}$  and  $B_{1s}$  as given in the previous Subsection

$\underline{v}_{cw}^{in r}$  is from Eq. 7-79

and

$$\underline{v}_{cw}^{in p} \equiv \begin{bmatrix} u \\ 0 \\ (GEF_p)w_{1np} \end{bmatrix} \quad (7-81)$$

with  $GEF_p$  and  $w_{1np}$  obtained from the previous propeller calculations for the respective LPU.

The relative velocity for LPU-fuselage 1 is corrected only for interference by rotor 1 and propeller 1. Second order effects between LPUs are neglected.

The following fuselage model given here is taken from Ref. 7-6, but assumes no contribution from aerodynamic surfaces on the fuselage. The small fuselage aerodynamic moments are neglected in comparison to those resulting from the rotor and propeller models. The forces act at the fuselage aerodynamic reference center and are oriented in the direction of the LPU reference axes.

The components of  $(\underline{V}_i^{a f})'$  are:

$$(\underline{V}_i^{a f})' \equiv \begin{bmatrix} u \\ v \\ w \end{bmatrix}_i^{a f} \quad (7-82)$$

where the primes on the individual components which denote interference correction have been dropped. The axial force is modeled as crossflow drag:

$$X_A = X_{|u|u} |u|u \quad (7-83)$$

ORIGINAL ...  
OF POOR QUALITY

where the derivative  $X_{|u|u}$  is a function of air density, reference area, and the appropriate drag coefficient.

The vertical and side force have the same form:

$$Y_A = Y_{|v|v} |v|v \quad (7-84)$$

$$Z_A = Z_{|w|w} |w|w \quad (7-85)$$

and we neglect the pure moments,

$$L_A = M_A = N_A = 0 \quad (7-86)$$

The force and moment vectors about the LPU center of gravity due to the fuselage aerodynamic loads are:

$$\underline{F}_{A_1}^{if} = \begin{bmatrix} X_A \\ Y_A \\ Z_A \end{bmatrix} \quad (7-87)$$

$$\underline{T}_{A_1}^{if} = \begin{bmatrix} L_A \\ M_A \\ N_A \end{bmatrix} \quad (7-88)$$

## ORIGINAL EQUATIONS OF POWER QUALITY

These equations, while highly simplified, are felt to be well within the precision required for representing the fuselage aerodynamic contribution.

### L. POWER OFF FORCES AND MOMENTS

This subsection presents the aerodynamic models for the rotors, propellers and LPU fuselages (nacelles) when the vehicle is in a power off (moored) flight condition. In this condition, the various LPU elements contribute mostly to the drag of the vehicle. To retain consistency with the fuselage model, the small circulation lift of stationary rotors and propellers and the pure aerodynamic moments about the hub attachment points are neglected. Typical calculations for the power off condition show the rotor and propeller forces to be exceedingly small. Therefore, the errors introduced by simplifying the power off models are of negligible importance to the overall mooring simulation.

All thrust related interference effects are eliminated for the powered off condition. Only the hull on LPU velocity interference model (Section 7, Subsection C) is retained. The equations for the forces on the stationary rotor are presented first, with additional notes on the calculation of propeller and fuselage forces.

#### 1. Stationary Rotor Aerodynamics

The following simple crossflow model provides the rotor forces in coordinates of the control wind reference axes (cw) based on the relative velocity of the air mass at the rotor hub (Eq. 7-26):

$$X_{cw} = -\frac{1}{2} \rho A \sigma \delta_a u_{cw} |u_{cw}| \quad (7-89)$$

$$Y_{cw} = 0 \quad (7-90)$$

$$Z_{cw} = -\frac{1}{2} \rho A \sigma C_{zr} w_{cw} |w_{cw}| \quad (7-91)$$

ORIGINAL PAGE IS  
OF POOR QUALITY

where

$u_{cw}, w_{cw}$  are from Eq. 7-26

$\delta_a$  defined in Eq. 7-74

$C_{C_{zr}} = 1.2$  (Ref. 7-8)

Note that a fixed value of 1.2 is used for the rotor blade crosswind drag coefficient ( $C_{C_{zr}}$ ) in Eq. 7-89. This value, which is roughly constant for all high aspect ratio surfaces, is sufficiently accurate to preclude the requirement for different inputs for each rotor (and propeller).

The power off rotor force is resolved into the LPU reference axes, giving

$$\underline{F}_{A_1}^{ir} = (L_{icw})^T [X_{cw} Y_{cw} Z_{cw}]^T \quad (7-92)$$

The corresponding moment acting at the rotor hub is zero, thus, for the power off condition:

$$\underline{T}_{A_1}^{ir} = 0 \quad (7-93)$$

where  $L_{icw}$  is obtained from Eq. 7-31, noting:  $A_{1s}, B_{1s} \equiv 0$ .

## 2. Stationary Propeller Forces and Moments

As before, equations for the propeller force,  $\underline{F}_{A_1}^{ip}$ , and moment  $\underline{T}_{A_1}^{ip}$ , are obtained by direct resymboling of the appropriate equations for the rotors. In this case, the propeller equations are identical to Eqs. 7-87 to 7-91 above, except that the earlier definition of propeller shaft orientation angles ( $A_{1s}, B_{1s}$  as in Section 7, Subsection J) is retained. In the power off flight condition, rotor interference on the propeller free-stream velocity is ignored ( $\underline{v}_{cw}^{in} = 0$ ).

### 3. Fuselage Aerodynamics

The description of the fuselage aerodynamic force,  $\underline{F}_{A_i}^{if}$ , and moment,  $\underline{T}_{A_i}^{if}$ , presented in subsection 7-K is retained, noting that the second and third terms of the Eq. 7-80 involving rotor and propeller induced velocities are zero. So,

$$(\underline{V}_i^a f)^{\cdot} = \underline{V}_i^a f \quad (7-94)$$

#### M. SUMMATION OF FORCES AND MOMENTS

The total aerodynamic force acting at the  $i$  th LPU center of gravity ( $i = 1, 2, 3, 4$ ) is given by:

$$\underline{F}_{A_i} = \underline{F}_{A_i}^{ir} + \underline{F}_{A_i}^{ip} + \underline{F}_{A_i}^{if} \quad (7-95)$$

where the individual contributions are for the power on (HLASIM and HLAPAY simulation programs) or power off (HLAMOR simulation program) as appropriate.

The total aerodynamic moment acting on the  $i$  th LPU is given by:

$$\begin{aligned} \underline{T}_{A_i} = & \left( \underline{T}_{A_i}^{ir} + \underline{R}_i^{ir} \right) \times \underline{F}_{A_i}^{ir} + \underline{T}_{A_i}^{ip} + \left( \underline{R}_i^{ip} \times \underline{F}_{A_i}^{ip} \right) \\ & + \underline{T}_{A_i}^{if} + \left( \underline{R}_i^{if} \times \underline{F}_{A_i}^{if} \right) \end{aligned} \quad (7-96)$$

where the various terms are for the power on or power off condition as appropriate.

## SECTION 8

### HULL/TAIL ASSEMBLY AERODYNAMICS

#### A. BASIC ASSUMPTIONS

The hull/tail assembly is composed of a central buoyant hull envelope of quasi-ellipsoidal shape and a tail assembly equipped with movable control surfaces. The tail assembly is laterally centered on the hull x-z plane of symmetry, with longitudinal and vertical location specified by user inputs. This allows for a variety of symmetrical (x-tails) and unsymmetrical configurations (y-tails, v-tails, and t-tails). The central hull envelope is considered to include all external support structure related to the lift propulsion units (LPUs), payload cable attachments, mooring mast attachment, landing gears, and tail.

The approach used in the following development considers the aerodynamic loads (i.e., forces and moments) on the hull assembly and tail assembly separately. The hull assembly models are based on the motion of the hull center of volume (superscript "cv") relative to the local air mass, with corrections for the various rotor, propeller and ground interference effects. The tail assembly aerodynamic models are based upon the motion of the tail reference center (superscript "t") relative to the local air mass, with corrections for rotor, propeller, and ground interference effects.

The hull and tail aerodynamic models consist of analytical functions which allow continuous simulation of vehicle flight dynamics over all ranges of speed and flow incidence without recourse to lookup tables. The methodology for estimating the necessary input parameters is described in Appendix A. Using this methodology, alternative configurations can be studied without requiring additional data. This elemental approach allows for the incorporation of the 4 point atmospheric disturbance input model, and provides a mechanism for changing vehicle geometry without large associated changes in the vehicle data base.

Interference models account for the significant effects of rotor, propeller, and ground proximity to the hull and tail. These models are based on experimental wind tunnel data (Ref. 8-1) and computed aerodynamic results (Ref. 8-2). They have been implemented in a scheme which does not require iterative computation procedures. This is made possible by neglecting second order hull/rotor/propeller/ground wake interaction effects.

The calculation of hull and tail aerodynamic loads uses mathematical models which are largely undocumented elsewhere. In order to make clear the derivation of the many new aerodynamic models, the organization of this section will follow a progression of increasing aerodynamic flow complexity, rather than the computational sequence used in the simulation and reflected in the Section 7 discussion of the lift propulsion unit aerodynamic models. Specifically, the discussion of the quasi-steady aerodynamic models where the loads arise from relative air mass velocities is separated from the discussion of the unsteady aerodynamic models where the loads arise from relative air mass accelerations.

First, the vector equations are presented in Subsection B for all of the pertinent relative air mass velocities and accelerations, including the various velocity interference effects (Type A) due to rotor, propeller and ground proximity. Next, the aerodynamic equations are derived for the hull and tail quasi-steady flow forces and moments. The quasi-steady hull and tail models are compared to published airship experimental data (Ref. 8-3) to show typical aerodynamic characteristics and model limitations.

The proximity of the turbulent wakes of the rotor and propeller to the hull causes an increase in the total hull crossflow drag coefficient. Hull proximity to the ground causes a decrease in the hull crossflow drag force; tail proximity to the ground causes an increase in the tail lift curve slope. Models are presented which correct the respective hull and tail equation parameters for these (Type B) interference effects in Subsection C.

The quasi steady aerodynamics of the hull are presented in Subsection D; of the tail in Subsection E. Their combined effects are illustrated and compared with published data in Subsection F. Certain additional interference effects (Type B) which affect the quasi-steady forces and moments are presented in Subsection G.

Aerodynamic equations for unsteady (accelerated motion) loads on the hull and tail are derived in Subsection H. The loads arising from vehicle unsteady inertial motion are distinguished from those arising from airmass unsteady inertial motion. As will be shown, each of these motions produces different resulting forces and moments.

Due to the dependence of the aerodynamic loads on vehicle inertial acceleration, a problem arises in computing the acceleration needed for numerical solutions. An organization of the steady and unsteady aerodynamic force and moment equations is presented in Subsection I which provides for the calculation of the required accelerations.

By way of summary, Subsection J presents example time histories of the various contributions to the total load experienced by an HLA configuration during a gust encounter.

There is an essential difference between the organization of the equation development and that of the computer program. In the former case, the models are organized according to airmass motion type (e.g., quasi-steady, unsteady), with hull and tail equations considered together. In the latter case, the organization is according to the calculation of hull loads or tail loads, with differing airmass motion types treated together. A more in depth appreciation of the organization of the simulation aerodynamic calculations can be gained by referring to the software manuals.

For clarity of presentation, the figures in this section depict angular quantities in units of degrees and degrees/sec, etc. while all the simulation equations assume angular units of radians and radians/sec, etc.

**B. VELOCITIES AND ACCELERATIONS RELATIVE  
TO LOCAL AIRMASS**

The hull and tail aerodynamic models depend on the velocity and acceleration vectors at the respective reference center locations. The hull reference center location is defined as the hull center-of-volume (cv), which for ellipsoidal configurations is at the intersection of the major and minor axes. The reference center for tail calculations (t) is defined by the user, and typically corresponds to the nominal wind tunnel wing aerodynamic center (e.g., tail 25 percent chord location). The basic (non-interference) relative velocity and acceleration vectors, at the respective reference locations, are determined from the inertial motion of the vehicle and outputs from the atmospheric disturbance model. Following the sign convention adopted for air mass quantities (Subsection 5-B), the hull and tail velocity vectors relative to the local air mass are given by:

$$\underline{V}_h^{a \text{ cv}} = \underline{V}_h^{hcv} - \underline{V}_h^{am \text{ cv}} \quad (8-1)$$

$$\underline{\omega}_h^{a \text{ cv}} = \underline{\omega}_h^{hcv} - \underline{\omega}_h^{am \text{ cv}} \quad (8-2)$$

$$\underline{V}_h^{a \text{ t}} = \underline{V}_h^{ht} - \underline{V}_h^{am \text{ t}} \quad (8-3)$$

$$\underline{\omega}_h^{a \text{ t}} = \underline{\omega}_h^{ht} - \underline{\omega}_h^{am \text{ t}} \quad (8-4)$$

where

$$\underline{V}_h^{am \text{ cv}}, \underline{\omega}_h^{am \text{ cv}}, \underline{V}_h^{am \text{ t}}, \underline{\omega}_h^{am \text{ t}}$$

are given in Eqs. 6-47, 6-48, 6-52, 6-53 respectively. The remaining vectors in the above equations are determined from the rigid body motion of the hull center-of-gravity ( $\underline{V}_h, \underline{\omega}_h$ ) and the vehicle geometry (Fig. 8-1):

LEFT SIDE VIEW

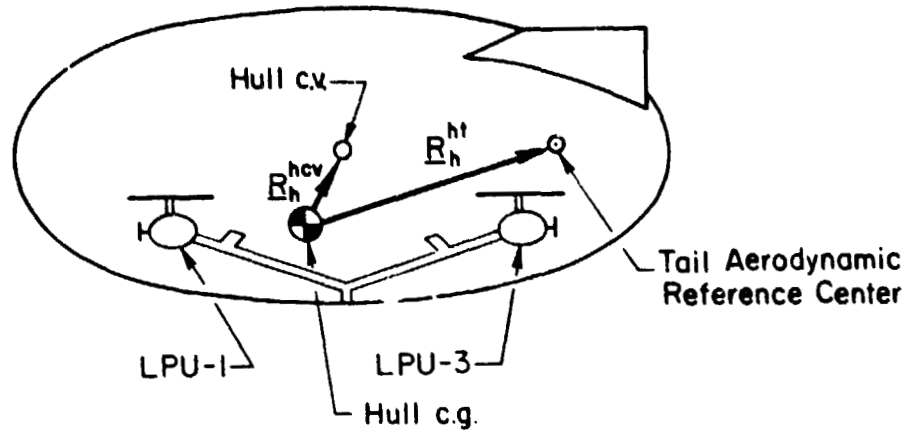


Figure 3-1. Hull Geometry Vectors

$$\underline{v}_h^{hcv} = \underline{v}_h + (\underline{\omega}_h \times \underline{R}_h^{hcv}) \quad (8-5)$$

$$\underline{\omega}_h^{hcv} = \underline{\omega}_h \quad (8-6)$$

$$\underline{v}_h^{ht} = \underline{v}_h + (\underline{\omega}_h \times \underline{R}_h^{ht}) \quad (8-7)$$

$$\underline{\omega}_h^{ht} = \underline{\omega}_h \quad (8-8)$$

The effective acceleration of the hull center-of-volume relative to the local airmass, with respect to rotating body axes is given by:

ORIGINAL PAGE IS  
OF POOR QUALITY

$$\underline{\overset{0}{V}}_h^{a \text{ cv}} = \left[ \underline{\overset{0}{V}}_h^{h \text{ cv}} - \underline{\overset{0}{V}}_h^{a \text{ m cv}} + \left( \frac{\partial \underline{\overset{0}{V}}_h^{a \text{ m cv}}}{\partial \underline{R}} \underline{\overset{0}{V}}_h^{a \text{ cv}} \right) \right] \quad (8-9)$$

where the airmass velocity gradient matrix is given by

$$\frac{\partial \underline{\overset{0}{V}}_h^{a \text{ m cv}}}{\partial \underline{R}} \equiv \begin{bmatrix} \partial u / \partial x & \partial u / \partial y & \partial u / \partial z \\ \partial v / \partial x & \partial v / \partial y & \partial v / \partial z \\ \partial w / \partial x & \partial w / \partial y & \partial w / \partial z \end{bmatrix}_h^{a \text{ m cv}} \quad (8-10)$$

and  $\underline{\overset{0}{V}}_h^{a \text{ m cv}}$ ,  $\underline{\overset{0}{V}}_h^{a \text{ cv}}$  are obtained from Eqs. 6-62 and 8-1, respectively. The elements of matrix Eq. 8-10 are obtained from Eqs. 6-48, 6-49, 6-50, 6-51, and the airmass angular velocity definition Eq. 6-15. Note that the third column terms ( $\partial/\partial z$ ) are all zero according to the assumed planar model (Section 5, Subsection C).

The x-axis terms in the brackets of Eq. 8-9 correspond to Eq. 5-4 and similarly for the y-axis terms. The first term in brackets ( $\underline{\overset{0}{V}}_h^{a \text{ m cv}}$ ) is the time derivative of the local airmass velocity, which corresponds to the first right-hand-side term of Eq. 5-4. The second term in the brackets of Eq. 8-10 is a compact matrix/vector notation form for the relative acceleration of the local airmass due to spatial velocity gradients. These effects are represented (for x-axis terms) by the last two right-hand-side terms of Eq. 5-4.

The first term in Eq. 8-9 is the kinematic acceleration of the hull center-of-volume with respect to the rotating body reference axes ( $\underline{\overset{0}{V}}_h^{h \text{ cv}}$ ), given by

$$\underline{\overset{0}{V}}_h^{h \text{ cv}} = \underline{\overset{0}{V}}_h + (\underline{\omega}_h \times \underline{R}_h^{h \text{ cv}}) \quad (8-11)$$

The angular acceleration vector of the hull center-of-volume relative to the local airmass (with respect to the hull rotating reference axes) is given by:

ORIGINAL PAGE IS  
OF POOR QUALITY

$$\frac{O_a}{\omega_h} cv = \frac{O_{hcv}}{\omega_h} - \frac{O_{am}}{\omega_h} cv \quad (8-12)$$

where

$$\frac{O_{hcv}}{\omega_h} = \frac{O}{\omega_h} \quad (8-13)$$

and

$\frac{O_{am}}{\omega_h} cv$  is given in Eq. 6-65

The corresponding equations for the tail effective acceleration vectors can be obtained by direct resymboling of the preceding results (Eqs. 8-9 to 8-13), viz.,

$$\frac{O_a}{V_h} t = \left[ \frac{O_{ht}}{V_h} - \frac{O_{am}}{V_h} t + \left( \frac{\partial V_h^{am}}{\partial R} V_{ii}^a t \right) \right] \quad (8-14)$$

where  $\frac{O_{am}}{V_h} t$ ,  $V_h^a t$  are obtained from Eqs. 6-64 and 8-3, respectively. The second term in the bracket of Eq. 8-14 is identical to Eq. 8-10 except that the superscript "am t" is implied. The corresponding matrix elements are similarly obtained from Eqs. 6-53, 6-54, 6-55, 6-56 and the angular velocity definition of Eq. 6-30. Again the third column elements ( $\partial/\partial z$ ) are all zero.

The first term of Eq. 8-14 is obtained directly from Eq. 8-11 as:

$$\frac{O_{ht}}{V_h} = \frac{O}{V_h} + \left( \frac{O}{\omega_h} \times R_h^{ht} \right) \quad (8-15)$$

The angular acceleration of the tail reference center relative to the local air mass (with respect to the rotating hull body axes) is:

$$\frac{O_a}{\omega_h} t = \frac{O_{ht}}{\omega_h} - \frac{O_{am}}{\omega_h} t \quad (8-16)$$

where

$$\frac{O_{ht}}{\omega_h} = \frac{O}{\omega_h} \quad (8-17)$$

and  $\frac{O_{am}}{\omega_h} t$  is given in Eq. 6-67.

ORIGINAL PAGE IS  
OF POOR QUALITY

Finally, for hull buoyancy calculations, the acceleration of the local airmass at the hull center-of-volume with respect to non-rotating inertial reference axes is required. Here only the inertial motion of the local airmass is considered, and the inertial motion of the vehicle itself is disregarded. The total effective inertial acceleration of the local airmass is comprised of a time dependent portion and a spatially dependent portion according to the equation:

$$\left(\dot{\underline{V}}_h^{am\ cv}\right)_{Total} = \dot{\underline{V}}_h^{am\ cv} + \frac{\partial \underline{V}_h^{am\ cv}}{\partial \underline{R}} \underline{V}_h^{am\ cv} \quad (8-18)$$

where  $\underline{V}_h^{am\ cv}$ ,  $\dot{\underline{V}}_h^{am\ cv}$  are obtained from Eqs. 6-47 and 6-63, respectively, and  $\partial \underline{V}_h^{am\ cv} / \partial \underline{R}$  is given in Eq. 8-10.

**C. HULL AND TAIL RELATIVE VELOCITY  
INTERFERENCE EFFECTS**

The major sources of velocity (Type A) interference on the hull and tail arise from rotor, propeller, and ground proximity. The rotors and propellers act as aerodynamic sinks which induce interference velocity increments on the hull and tail. This produces a change in the net velocity vectors relative to the local airmass, and causes the hull and tail to be drawn towards the rotors and propellers. The magnitude of the interference velocity increments varies linearly with the rotor and propeller total induce' velocities and inversely with LPU/hull and LPU/tail separation.

Additional velocity interference increments arise from the hull and tail proximity to the ground. In both cases, the close presence of the ground causes a rotation of the local airmass flow direction without attenuating the magnitude of the relative velocity vector.

The model for rotor on hull velocity interference will be presented first with later generalization to account for rotor and propeller on hull and tail interference effects. Then a model for ground on hull velocity interference effects will be presented.

ORIGINAL PAGE IS  
OF POOR QUALITY

Additional ground on hull and tail (Type B) interference effects are discussed in Subsection G.

1. Rotor On Hull Velocity Interference

The operation of one rotor near the hull causes an induction of flow around the hull towards the rotor. A typical flow pattern for the hull with one thrusting rotor is shown in Fig. 8-2 reprinted from Ref. 8-4. In idealized aerodynamic terms, the rotor acts as a 3-dimensional flow sink. The strength (K) is defined as the induced volume flow rate through the rotor:

$$K = \frac{\dot{m}}{\rho} \quad (8-19)$$

where

K = rotor sink strength (induced volume flow rate)

$\dot{m}$  = induced mass flow rate

$\rho$  = ambient air density

and

$$\dot{m} = \rho A |(GEF)w_{in}| \quad (8-20)$$

where A is the rotor actuator disk area and (GEF) $w_{in}$  is as determined in Section 7.

The absolute value function of Eq. 8-20 is necessary because the aerodynamic sink is omnidirectional, and depends only on the flow rate. Therefore, as a model for rotor flow induction, Eq. 8-20 does not distinguish between positive or negative thrust conditions. This assumption is sufficiently accurate for rotor placements which do not cause large direct impingements of the rotor wake on the hull (Ref. 8-2).

The magnitude of the sink induced velocity at the hull center-of-volume  $U_g^h$  due to one rotor is calculated from potential flow theory (Ref. 8-5):

ORIGINAL PAGE IS  
OF POOR QUALITY

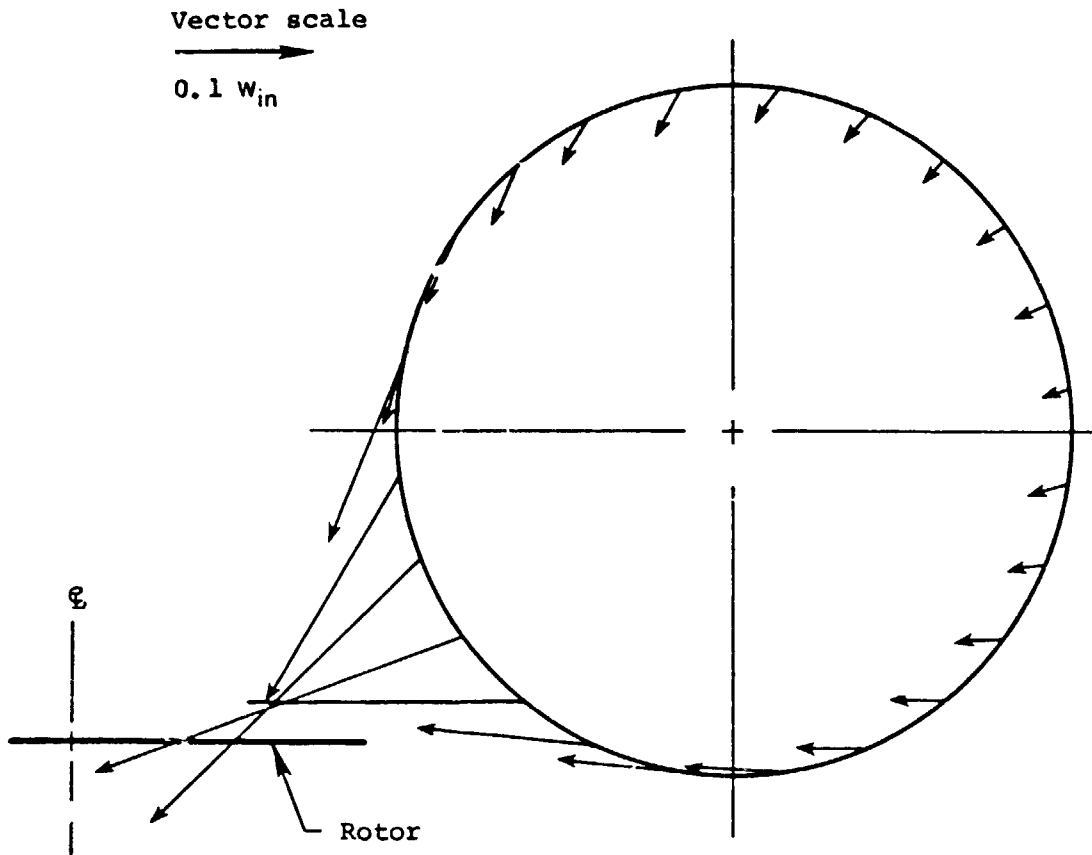


Figure 8-2. Rotor-Induced Velocities on HLA Hull in Hover;  
Thrust Loading  $(T/A) = 8.26 \text{ lb/ft}^2$ ; from Ref. 8-4

$$U_s^h = \frac{K}{4\pi d^2} \quad (8-21)$$

where K is obtained from Eq. 8-19, and d is the radial distance from the hull c.v. to the respective rotor hub. Substituting Eqs. 8-23 and 8-24 into 8-25, and adopting the following definitions:

$$(w_{in})_{TOT} \equiv (GEF)w_{in}, \text{ total rotor induced velocity (self-induced plus ground induced).}$$

$$\bar{d} \equiv d/2R, \text{ nondimensional rotor/hull separation distance; } R = \text{rotor radius.}$$

There results

$$U_s^h = \frac{(w_{in})_{TOT}}{16\bar{d}^2} \quad (8-22)$$

The expression for sink induced interference velocity given in Eq. 8-22 shows the simple theoretical dependency on total rotor induced velocity  $(w_{in})_{TOT}$  and nondimensional rotor/hull separation distance,  $\bar{d}$ . The velocity interference of the rotor sink drops off with the square of the separation distance, becoming a negligible fraction of  $(w_{in})_{TOT}$  for separations greater than three rotor diameters. For a given HLA configuration, this interference effect will be most significant when the rotors are operating at a maximum induced velocity condition (e.g. heavily loaded, hovering flight condition out of ground effect).

The potential flow theory solution for the rotor on hull interference velocity vector,  $\underline{v}_h^{int}$ , is obtained from Eq. 8-22 and the geometry of Fig. 8-2:

$$\left( \underline{v}_h^{int} \right)_{\text{potential theory}} = U_s^h \hat{e}_{hc} \hat{r} \quad (8-23)$$

ORIGINAL PAGE  
OF POOR QUALITY

where  $\hat{e}_{hcv}^{ir}$  is the unit vector locating the respective rotor hub (super-script "ir") from the hull c.v. (subscript "hcv"). From Fig. 8-2:

$$\hat{e}_{hcv}^{ir} = \frac{R_{hcv}^{ir}}{|R_{hcv}^{ir}|} \quad (8-24)$$

and

$$R_{hcv}^{ir} = R_h^{hi} - L_{hi}(R_i^{ir} - R_i^{ih}) - R_h^{hcv} \quad (8-25)$$

$$|R_{hcv}^{ir}| \equiv d \quad (8-26)$$

In terms of its components, the unit vector is given by

$$\hat{e}_{hcv}^{ir} = \begin{bmatrix} \hat{e}_x \\ \hat{e}_y \\ \hat{e}_z \end{bmatrix}_{hcv}^{ir} \quad (8-27)$$

When Eqs. 8-22 and 8-27 are substituted into 8-23, there results,

$$\left( \frac{v_h^{int r}}{l} \right)_{\text{potential theory}} = \frac{1}{16d^2} \begin{bmatrix} \hat{e}_x \\ \hat{e}_y \\ \hat{e}_z \end{bmatrix}_{hcv}^{ir} |(win)_{TOT}| \quad (8-28)$$

ORIGINAL PAGE IS  
OF POOR QUALITY

Extensive analyses using the Nielsen Engineering and Research Aerodynamic Flow Computations Model (Ref. 8-2) suggest the presence of important viscous (non-potential flow) phenomena. In order to accommodate such effects, the following generalized rotor on hull velocity interference model was implemented:

$$\underline{V}_h^{int r} = \begin{bmatrix} KRHC \\ KRHD \\ KRHE \end{bmatrix} |(w_{in})_{TOT}| \quad (8-29)$$

where KRHC, KRHD, KRHE are user supplied constants (for each rotor). These are calculated from Eq. 8-28 and adjusted as necessary for the viscous effects.

So far, consideration has been given only to interference velocity increments at the hull center-of-volume due to the rotors. The effective gradients which arise from differences in the induced velocity of the various rotors are neglected as being second order effects. Sample calculations show the major interference effect to be a trim down load due to roughly uniform rotor induced velocity interference in the vertical direction. For most symmetrical flight conditions, and typical LPU configurations, the velocity interference increments in the axial and lateral directions will approximately cancel, leaving only the vertical interference velocity for rotor locations below the hull x-y plane of symmetry.

## 2. Propeller on Hull Velocity Interference

The propellers like the rotors act as sinks which induce interference velocities at the hull center-of-volume. The model adopted for propeller on hull velocity interference ( $\underline{V}_h^{int P}$ ) is identical to that discussed above for rotor on hull interference. The interference

ORIGINAL PAGE IS  
OF POOR QUALITY

constants of Eq. 8-29 are redefined for each propeller (KPHC, KPHD, KPHE). We note from the potential flow solution of Eq. 8-22 that for rotor and propeller placements in roughly the same location, the propeller interference constants are approximated from the rotor constants and the ratio of propeller and rotor disk areas according to the following relations:

$$KPHC \doteq (KRHC)(\bar{A}) \quad (8-30)$$

$$KPHL \doteq (KRHD)(\bar{A}) \quad (8-31)$$

$$KPHE \doteq (KRHE)(\bar{A}) \quad (8-32)$$

where

$$\bar{A} \equiv \frac{A_{\text{Propeller}}}{A_{\text{Rotor}}} \quad (8-33)$$

### 3. Rotor and Propeller on Tail

It is assumed that the tail is not in the core of the rotor or propeller slipstream. The rotors and propellers again act as aerodynamic sinks and induce interference velocities at the tail reference center ( $\underline{v}_t^{\text{int } r}$  and  $\underline{v}_t^{\text{int } p}$ , respectively). The form of Eq. 8-22 is applicable, with the nondimensional distance,  $\bar{d}$ , now representing the separation between a rotor or propeller and the tail reference center (t). Thus the rotor on tail velocity interference model requires three geometric constants (KRTA, KRTB, KRTC) corresponding to (KRHC, KRHD, KRHE) of Eq. 8-29. The propeller constants (KPTA, KPTB, KPTC) are obtained by appropriate resymboling of Eqs. (8-30, 8-31 and 8-32). In the case of the tail, viscous effects are not very significant, especially in the low angle attack range. Therefore, the potential flow solution of Eq. 8-22 can be applied directly to determine these constants without the need for experimental correction as is the case for the hull.

ORIGINAL FILE IS  
OF POOR QUALITY

Calculations show that velocity interference effects are significant only for rotor and propeller placements within three (rotor or propeller) diameters. Therefore, only rotors 3 and 4 (Fig. 8-2) have significant interference effects on the tail. In general, the propellers do not have dominant velocity interference effects on either the hull or the tail.

**4. Summary of Rotor and Propeller Velocity Interference Effects**

This article summarizes the above results and presents the general equations for the hull and tail relative velocity vectors, including the interference effects of all the rotors and propellers. These general equations are obtained from the superposition of the various sink induced interference velocities. Second order effects due to interaction among the various sinks are ignored. The velocities are:

$$(\underline{v}_h^{a\ cv})' = \underline{v}_h^{a\ cv} - (\underline{v}_h^{int\ r})_{Total} - (\underline{v}_h^{int\ p})_{Total} \quad (8-34)$$

$$(\underline{v}_h^{a\ t})' = \underline{v}_h^{a\ t} - (\underline{v}_t^{int\ r})_{Total} - (\underline{v}_t^{int\ p})_{Total} \quad (8-35)$$

where the prime ( )' notation indicates that the relative velocity vectors have been corrected for rotor and propeller interference and  $\underline{v}_h^{a\ cv}$  is given in Eq. 8-1,  $\underline{v}_h^{a\ t}$  is given in Eq. 8-3, and

$$(\underline{v}_h^{int\ r})_{Total} \equiv \sum_{i=1}^4 (\underline{v}_h^{int\ r})^i \quad (8-36)$$

$$(\underline{v}_h^{int\ p})_{Total} \equiv \sum_{i=1}^4 (\underline{v}_h^{int\ p})^i \quad (8-37)$$

ORIGINAL PAGE IS  
OF POOR QUALITY

$$(\underline{v}_t^{int\ r})_{Total} \equiv \sum_{i=1}^4 (\underline{v}_t^{int\ r})^i \quad (8-38)$$

$$(\underline{v}_t^{int\ p})_{Total} \equiv \sum_{i=1}^4 (\underline{v}_t^{int\ p})^i \quad (8-39)$$

where  $\underline{v}_h^{int\ r}$ ,  $\underline{v}_h^{int\ p}$ ,  $\underline{v}_t^{int\ r}$ , and  $\underline{v}_t^{int\ p}$  are calculated for each LPU from the generalized expression in Eq. 8-29.

### 5. Ground on Hull Velocity Interference

In large sideslip flight conditions, hull proximity to the ground causes an upward rotation of the crossflow freestream velocity vector with no attenuation of the velocity magnitude. This upward flow rotation yields a corresponding increment of hull lift which has been shown to be significant for ground handling operations. This section first presents a model for the flow rotation effect due to ground proximity for a 90 deg sideslip flight condition (crossflow). Then a model is presented which accounts for ground on hull interference for arbitrary flow and vehicle orientation angles.

#### a. Flow Rotation Model for Pure Crosswind Flight Conditions

The vehicle is assumed to be stationary in a level attitude ( $\theta = \phi = 0$ ) with the freestream crossflow velocity vector,  $\underline{V}^w$ , directed along the positive y axis of the hull. The rotation of this wind vector due to ground interference is depicted in Fig. 8-3. Based on wind tunnel data of the airship Akron (Ref. 8-3) it is assumed that the free-stream velocity magnitude is not affected. The flow orientation angle ( $\lambda'$ ) is measured relative to the hull z-axis (see Fig. 8-3) and is assumed always to be within a small deviation of 90 deg.

The following equations for the hull longitudinal (x-axis), lateral (y-axis) and vertical (z-axis) aerodynamic forces on the hull are developed in Subsection D:

ORIGINAL [unclear]  
OF POOR QUALITY

HULL FRONT VIEW (TAIL AND LPU'S NOT SHOWN)

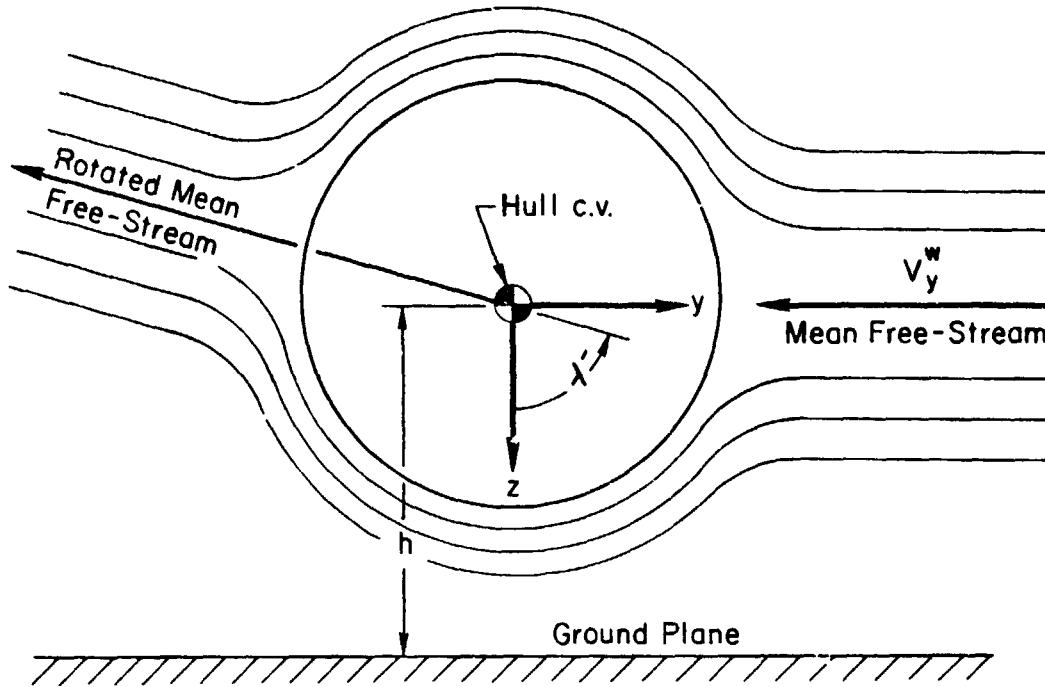


Figure 8-3. Ground-on-Hull Velocity Interference Model

$$X = X_{u|u|_h} u|u| \quad (8-40)$$

$$Y = Y_{v|v|_h} vV_{yz} \quad (8-41)$$

$$Z = Z_{w|w|_h} wV_{yz} \quad (8-42)$$

where from Fig. 8-3 for pure crossflow

$$\begin{aligned} V_{yz} &= V_y^w = \text{relative horizontal crosswind velocity} \\ &= -\underline{V}(2) \end{aligned} \quad (8-43)$$

ORIGINAL PAGE IS  
OF POOR QUALITY

The body-axis components are:

$$u = 0 \quad (8-44)$$

$$v = V_y^w \sin \lambda' \quad (8-45)$$

$$w = V_y^w \cos \lambda' \quad (8-46)$$

For  $\cos \lambda' \approx \pi/2 - \lambda'$  (small angle of ground induced flow rotation,  $\lambda'$  in radians),

$$u = 0 \quad (8-47)$$

$$v = V_y^w \quad (8-48)$$

$$w = V_y^w (\pi/2 - \lambda') \quad (8-49)$$

When substituted into Eqs. 8-40 through 8-42, there results:

$$X = 0 \quad (8-50)$$

$$Y = y_{v|v|h} (V_y^w)^2 \quad (8-51)$$

$$Z = z_{w|w|h} (V_y^w)^2 (\pi/2 - \lambda') \quad (8-52)$$

Equations 8-50 and 8-51 show that the hull x and y forces are unaffected by ground induced velocity rotation effects. Equation 8-52 shows that the hull's z force will increase linearly with the hull flow rotation angle ( $\lambda'$ ).

The dependency of the flow rotation angle ( $\lambda'$ ) on ground proximity is shown in Fig. 8-4, which was obtained by reducing the wind tunnel data of Ref. 8-3. The wind tunnel data was corrected in order to remove the effect of the velocity variation with altitude. The resulting data are referenced to the local freestream velocity at the hull center of volume, instead of the freestream velocity at the reference wind tunnel location. The results of Fig. 8-4 suggest the following form for ground induced flow rotation angle as a function of nondimensional hull height,  $\hat{h}$  ( $\hat{h} \equiv$  height of hull c.v./hull diameter):

$$\lambda' = (\pi/2)(1 - e^{-\hat{h}KGHA}) \quad (8-53)$$

where

KGHA = a user supplied curved fit constant derived from Fig. 8-4 or available wind tunnel data.

The form of Eq. 8-53 is plotted along with the experimental data in Fig. 8-4. The model results compare favorably with the experimental data, and indicates that ground effects will be significant for hull center of volume locations within two hull diameters of the ground plane ( $\hat{h} < 2$ ).

#### b. Arbitrary Vehicle and Freestream Orientations

The previous model is generalized in this subsection. As can be seen from Eq. 8-53 the ground-induced flow rotation angle is dependent only upon the vertical height of the hull center of volume. The angular orientation of the hull is important only to the extent that the velocities used in the force equations of Eqs. 8-40, 8-41, and 8-42 are body axis based. In order to employ the model of the Eq. 8-53, the following

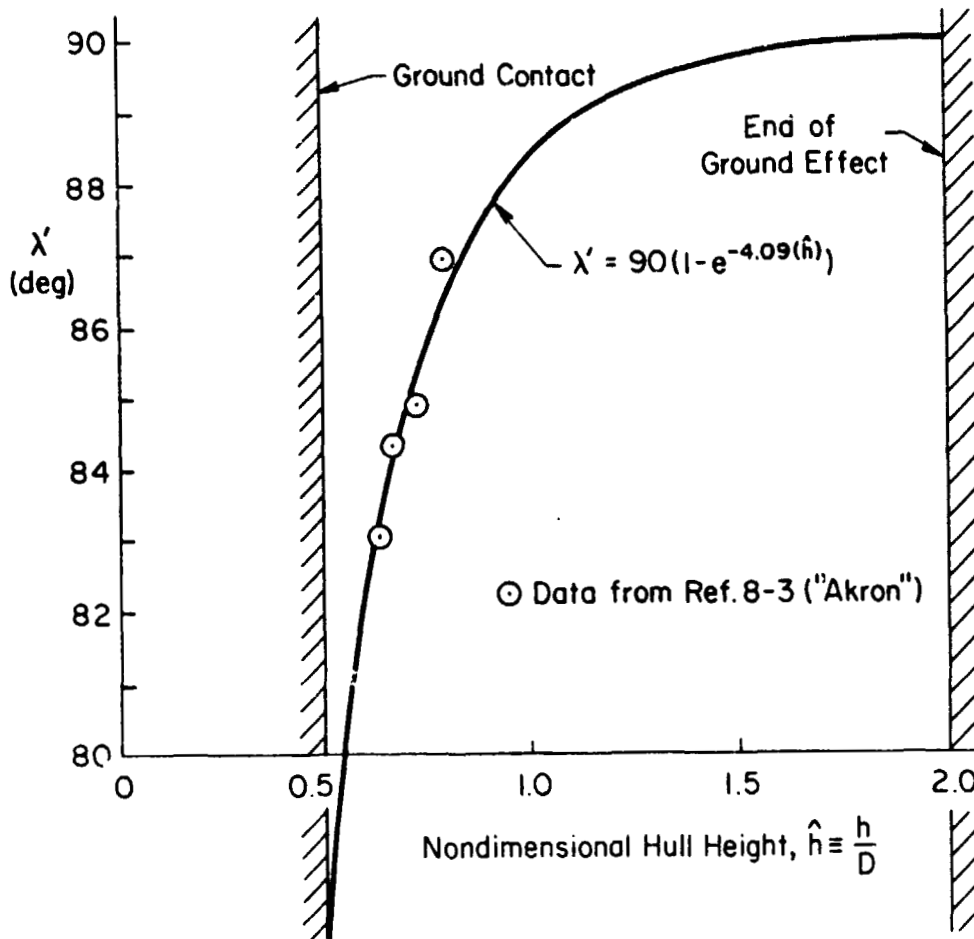


Figure 8-4. Variation in Ground Induced Flow Rotation Angle ( $\lambda'$ ) with Nondimensional Hull Height ( $\hat{h}$ )

transformations are used to calculate the equivalent horizontal cross-wind velocity and coordinates of the vertically oriented HLA heading referenced axis system ( $x_v, y_v, z_v$ ) shown in Fig. 8-3:

$$\underline{v}_v^{a\ cv} = L_{vh}(\underline{v}_h^{a\ cv})' \quad (8-54)$$

where  $(\underline{v}_h^{a\ cv})'$  is the relative velocity vector of the hull center-of-volume relative to the local airmass (eq. 8-34), including the rotor and propeller interference corrections of Subsection 4, above.  $\underline{v}_v^{a\ cv}$  is the relative velocity vector of the hull center-of-volume relative to the local airmass in coordinates of the vertically oriented HLA heading referenced axis system; in terms of Fig. 8-3,

ORIGINAL DOCUMENT  
OF POOR QUALITY

$$\underline{v}_v^a \text{ cv}(2) = -v_y^w \quad (8-55)$$

and

$$L_{vh} = L_\theta^{-1} L_\phi^{-1} = \begin{bmatrix} \cos \theta & \sin \theta \sin \phi & \sin \theta \cos \phi \\ 0 & \cos \phi & -\sin \phi \\ -\sin \theta & \cos \theta \sin \phi & \cos \theta \cos \phi \end{bmatrix} \quad (8-56)$$

where  $\theta$  and  $\phi$  are the pitch and roll Euler angles of the hull. The components of  $\underline{v}_v^a \text{ cv}$

$$\underline{v}_v^a \text{ cv} \equiv \begin{bmatrix} u \\ v \\ w \end{bmatrix}^a \text{ cv} \quad (8-57)$$

where  $v_v^a \text{ cv} = -v_y^w$  of Fig. 8-3.

These components are corrected for the flow rotation as follows:

$$u' = u_v^a \text{ cv} \quad (8-58)$$

$$v' = v_v^a \text{ cv} \quad (8-59)$$

$$w' = |v_v^a \text{ cv}|(\pi/2 - \lambda') + w_v^a \text{ cv} \quad (8-60)$$

where the prime (') superscripts indicate that the relative velocities have been corrected for ground on hull velocity interference.

The equations for the lateral and vertical relative velocities (given above) are consistent with those of Eqs. 8-47, 8-48 and 8-49. The absolute value function in Eq. 8-60 is necessary in order to allow for arbitrary vehicle and wind motion. Equation 8-58 assumes that the axial velocity (parallel with the horizontal plane) is unaffected by ground proximity to the hull. This is consistent with the wind tunnel data of Ref. 8-3, and is sufficiently accurate for most conventional hulls whose fineness ratio (hull length/hull diameter) exceeds two and for small pitch attitude angles  $|\theta| < 25$  deg.

Equations 8-58, 8-59 and 8-60 are transformed back to coordinates of the hull body axes to allow a calculation of the aerodynamic forces on the hull:

$$\left( \underline{v}_h^{a\ cv} \right)'' = L_{hv} \begin{bmatrix} u' \\ v' \\ w' \end{bmatrix} \quad (8-61)$$

The double prime (") denotes correction for the propeller and rotor interference (Eq. 8-34) and for ground proximity. The transformation matrix is given by:

$$L_{hv} = [L_{vh}]^{-1} = [L_{vh}]^T \quad (8-62)$$

Equation 8-61 provides the relative velocity vector at the hull center-of-volume including all rotor, propeller, and ground interference effects. Any second order effects arising from the ground induced flow rotation at the rotors and propeller locations are neglected. These effects are felt to be unimportant.

#### D. QUASI-STEADY HULL AERODYNAMICS

In the next few sections we explain the assumptions and equations used to represent the hull aerodynamics in rectilinear and curvilinear

steady flight. The model for hull rectilinear aerodynamic forces and moments follows that of Allen and Perkins (Ref. 8-12) for a slender body of revolution with zero base area. The discussion of hull forces which originate in combinations of rectilinear and curvilinear motion giving rise to centrifugal accelerations is deferred to Subsection (pending).

The drag parameters used in the hull aerodynamic model are affected significantly by rotor, propeller, and ground interference (Type B) effects. In the discussion that follows, it is assumed that these parameters are known a priori. Corrections for the various Type B interference effects are presented in Subsection G.

### 1. Rectilinear Flight

The aerodynamics of an airship hull may be described in terms of two overlapping angle-of-attack regimes. In the first regime (low incidence, free stream angle of attack less than 5 deg) the flow is largely attached, and the local angle of attack along the hull is twice free-stream value. This local streamline curvature, known as "2-alpha flow," is a result derivable from non-viscous potential flow theory (Ref. 8-6). In the real viscous flow case, the boundary layer separates from the leeward surface, giving rise to small lift forces. The drag force is predominantly due to skin friction even for low fineness ratio hulls (Ref. 8-7).

Curtiss' review (Ref. 8-8) of the literature pertinent to the calculation of low-angle-of-attack hull lift, concluded that presently available techniques inadequately predict hull lift. This may largely be a result of nonlinear separation line movements and strong Reynolds number dependencies. The present simulation model neglects the low-angle-of-attack "2-alpha" lift, resulting in a slight underestimate of the hull-alone lift in that regime. The skin friction drag important for trim and performance calculations is determined from the axial dynamic pressure,  $1/2(\rho u^2)$ , and axial drag coefficient,  $C_{A_h}$ . By using the axial component of velocity (instead of the more usual total velocity) in computing dynamic pressure, the data show that the axial coefficient  $C_{A_h}$

becomes more truly a constant. This approach greatly simplifies the simulation and was used throughout the aerodynamic model development.

The second hull regime (angle of attack greater than 5 deg) is characterized by larger areas of separation which causes a breakdown of the "2-alpha" flow, and the appearance of longitudinal vortices (Ref. 8-9). The resultant aerodynamic force lies virtually normal to the surface. This force is proportional to the perpendicular or "crossflow" dynamic pressure  $[(1/2)\rho w^2$  or  $(1/2)\rho v^2]$  and the "crossflow" drag coefficient ( $C_{C_{zh}}$  or  $C_{C_{yh}}$ ).

The general expressions for the body axis forces, referenced to the hull center of volume, are:

$$X_h = \sigma X_{u|u|_h} u|u| \quad (8-63)$$

$$Y_h = \sigma Y_{v|v|_h} v V_{yz} \quad (8-64)$$

$$Z_h = \sigma Z_{w|w|_h} w V_{yz} \quad (8-65)$$

where, from Eq. 8-61 dropping the double prime notation for simplicity;

$$\begin{bmatrix} u \\ v \\ w \end{bmatrix} \equiv \underline{V}_h^a \quad (8-66)$$

and  $\sigma \equiv \rho/\rho_0$  is the relative air density correction. The velocity perpendicular to the x axis is

$$V_{yz} \equiv \sqrt{v^2 + w^2} \quad (8-67)$$

The coefficients,  $X_{u|u|_h}$ ,  $Y_{v|v|_h}$ , and  $Z_{w|w|_h}$  are input parameters determined by the user. These are related to the conventional aerodynamic quantities according to the defining equations:

$$X_{u|u|_h} \equiv (-\rho_0/2)S_h C_{A_h} \quad (8-68)$$

$$Y_{v|v|_h} \equiv (-\rho_0/2)S_h C_{C_{y_h}} \quad (8-69)$$

$$Z_{w|w|_h} \equiv (-\rho_0/2)S_h C_{C_{z_h}} \quad (8-70)$$

The hull reference area,  $S_h$ , is that which is consistent with the corresponding drag coefficients;  $C_{A_h}$ ,  $C_{C_{y_h}}$ ,  $C_{C_{z_h}}$ . The relative air density correction,  $\sigma$ , is equal to one when the desired air density ( $\rho$ ) corresponds with the reference air density used in the input parameter calculations ( $\rho_0$ ).

The moment characteristics of bare hulls in ideal steady flow have been derived from potential flow theory by Munk, (Ref. 8-10), Zahm, (Ref. 8-11) and others. The theoretical pitching moment has been shown to follow the relation for all  $\alpha_{hcv}$ :

$$M_h = \frac{1}{2} \rho V_0^2 (K_c - K_x) V \sin (2\alpha_{hcv}) \quad (8-71)$$

In this expression,  $V_0$  is the relative free stream velocity magnitude,  $K_a$ ,  $K_b$ ,  $K_c$  are the so-called translational "apparent mass" constants along the hull x, y, and z axes, respectively,  $V$  is the volume of air displaced by the hull, and  $\alpha_{hcv}$  is the hull angle-of-attack at the center of volume, given by:

$$\alpha_{hcv} = \tan^{-1}(w/u) \quad (8-72)$$

For real flow, where leeward separation decreases the theoretical moment obtained from Eq. 8-71, Zahm (Ref. 8-11) suggests a correction factor,  $\eta_m$ , obtainable from wind tunnel results. Generalizing to three

dimensions, the expressions for the hull aerodynamic moments in terms of the hull center-of-volume relative velocities are given by:

$$L_h = \sigma L_{vw_h} vw \quad (8-73)$$

$$M_h = \sigma M_{uw_h} uw \quad (8-74)$$

$$N_h = \sigma N_{uv_h} uv \quad (8-75)$$

where  $L_{vw_h}$ ,  $M_{uw_h}$ , and  $N_{uv_h}$  are input parameters determined by the user. These are related to the conventional aerodynamic quantities according to the defining equations:

$$L_{vw_h} = \rho_0 V (K_b - K_c) \eta_L \quad (8-76)$$

$$M_{uw_h} \equiv \rho_0 V (K_c - K_a) \eta_M \quad (8-77)$$

$$N_{uv_h} \equiv \rho_0 V (K_a - K_b) \eta_N \quad (8-78)$$

and  $\eta_L$ ,  $\eta_M$ ,  $\eta_N$  are the separation correction factors which are typically in the range 0.6-0.8.

## 2. Curvilinear Flight

Classical airships derive 70-90 percent of their total rotary damping, at zero forward speed, from the hull envelope (Ref. 8-13). As the flight speed increases, the relative importance of this contribution is reduced due to the sharp rise in tail damping with velocity. In addition, heavy-lift airships derive considerable rotary damping in pitch from the rotors at cruise conditions. However, rotor damping typically drops to 50 percent of its cruise value in hovering flight (Ref. 8-14). Therefore, the accurate modeling of hull-envelope damping becomes important in hovering and low-speed flight regimes. Beyond the low-speed range ( $V_0 > 20$  fps), the tail and rotor contributions dominate the overall damping characteristics.

A significant consequence of the potential flow theory analysis of airship hulls in curvilinear flight is the conclusion that no resultant moment arises that is proportional to steady angular velocity (Ref. 8-11). As a result, hull rotary damping must arise from viscous flow effects. A "strip theory" solution for hull damping can be obtained by considering the lengthwise variation of "crossflow drag" for pitching motion:

$$M_h(q_{h_a}, w_{h_a}) = -\frac{1}{2} \rho C_{z_h} \int_{-l/2}^{+l/2} x_l (w - qx_l)^2 dS \quad (8-79)$$

where

- $l$  Airship hull length
- $w$  Relative crossflow velocity at the hull center of volume
- $q$  Relative pitching velocity
- $x_l$  Lengthwise coordinate
- $dS$  Section reference area

and for ellipsoids of revolution:

$$dS = D(x) dx_l \quad (8-80)$$

where

$$D(x) = \frac{2}{f} (l^2/4 - x_l^2)^{1/2} \quad (8-81)$$

where

$$f \equiv (\text{hull length/hull diameter}) \equiv \text{hull fineness ratio}$$

The expansion and evaluation of the above integral is an involved procedure, complicated by the need for piecewise (non-closed-form) calculations. An approximate solution that produces sufficiently accurate results can be obtained by considering the superposition of two limiting flight conditions.

ORIGINAL PAGE IS  
OF POOR QUALITY

For hovering flight ( $w = 0$ ), the rotary hull damping is given from Eq. 8-79 as:

$$M_h(q, 0) = \left( \frac{-\rho C_{C_{zh}} l^5}{120 f} \right) q |q| \quad (8-82)$$

When the relative angular rates are small compared to the relative crossflow velocity  $|q| < |w|$ , Eq. 8-79 yields:

$$M_h(q, w) = \left( \frac{-\pi \rho C_{C_{zh}} l^4}{64 f} \right) |w| q \quad (8-83)$$

The combined three-dimensional result for rotary pitching moment is:

$$M_h = M_{q|q|h} q \omega_{yz} + M_{q|w|h} q V_{yz} \quad (8-84)$$

where

$$\omega_{yz} = \sqrt{q^2 + r^2}$$

$M_{q|q|}$  and  $M_{q|w|}$  are user supplied inputs given in the parentheses of Eqs. 8-82 and 8-83, respectively.

and

$$\begin{bmatrix} p \\ q \\ r \end{bmatrix} \equiv \underline{\omega}_h^a \text{ cv given in Eq. 8-2}$$

The remaining moment equations are:

$$L_h = L_{p|p|h} p|p| + L_{p|u|h} p|u| \quad (8-85)$$

$$N_h = N_{r|r|h} r\omega_{yz} + N_{r|v|h} rV_{yz} \quad (8-86)$$

where

$N_{r|r|h}$ ,  $N_{r|v|h}$  are user supplied input constants obtained by replacing  $C_{C_{zh}}$  with  $C_{C_{yh}}$  in Eqs. 8-82 and 8-83

$L_{p|p|}$  and  $L_{p|u|}$  are user supplied input constants which can be calculated by strip theory analysis. Test case calculations show these terms to be of negligible importance when compared to the roll damping from the tail and rotors.

Theoretically, the viscous forces due to rotation of a symmetric hull are zero. However, the simulation code retains terms in  $Y_{r|r|h}$ ,  $Y_{r|v|h}$ ,  $Z_{q|q|h}$  and  $Z_{q|w|h}$  to account for the small rotary forces which can arise due to asymmetric flow separation. Ordinarily these can be neglected in comparison with the larger unsteady aerodynamic forces (Subsection H) and the tail forces arising from vehicle rotation.

### 3. Summary of Hull-Only Quasi-Steady Aerodynamics

The force vector acting at the hull center of volume due to quasi-steady aerodynamic effects is comprised of the three components given in Eq. 8-63 to 8-65 as well as rotary force terms normally neglected:

$$\underline{F}_{QS_h}^{h\ cv} = \sigma \begin{bmatrix} X_{u|u|h} u|u| \\ Y_{v|v|h} v V_{yz} + Y_{r|r|h} r\omega_{yz} + Y_{r|v|h} rV_{yz} \\ Z_{w|w|h} w V_{yz} + Z_{q|q|h} q\omega_{yz} + Z_{q|w|h} qV_{yz} \end{bmatrix} \quad (8-87)$$

This force includes velocity interference effects (Type A) and the Type B interference effects to be discussed subsequently in Subsection G.

The moment vector acting at the hull center of volume due to quasi-steady aerodynamic effects is given by:

$$\underline{I}QSh^{h\ cv} = \sigma \begin{bmatrix} L_{vw_h}vw + L_{p|p|h}p|p| + L_{p|u|h}p|u| \\ M_{uw_h}uw + M_{q|q|h}q\omega_{yz} + M_{q|w|h}qV_{yz} \\ N_{uv_h}uv + N_{r|r|h}r\omega_{yz} + N_{r|v|h}rV_{yz} \end{bmatrix} \quad (8-88)$$

Here the relevant equations are Eq. 8-73 to 8-78 and Eq. 8-84 to 8-86. Again, Type A and Type B interference effects are included.

#### E. QUASI-STEADY TAIL (ON HULL) AERODYNAMICS

The calculation of tail-on-hull quasi-steady aerodynamic loads is based on the assumption of steady rectilinear motion of the tail at large local angles of attack and sideslip. These incidence angles are derived from the relative local velocity field at the tail aerodynamic reference center, which includes those kinematic motion effects due to curved flight. Tail loads due to rotation about the tail's reference center are negligible except for rolling effects.

In low incidence flow the fin forces arise from circulation and edge vortex effects; this is called the "pre-stall" regime, wherein forces depend on dynamic pressure, tail local angles of incidence ( $\alpha$  and  $\beta$ ) and tail surface deflections. At high incidences, near  $\pm 90$  deg, the forces arise from separated flow effects. This is called the "crossflow" regime. Between these is the "stall transition" regime.

The forces for aft-quadrant flow directions (e.g., incidences from  $\pm 90$  to  $\pm 180$  deg) are assumed to be mirror images of the forward flow

forces. This assumption is roughly true for low aspect ratio, sharp edged, fins on slender bodies, and it greatly reduces the number of input parameters. Should greater precision be desired about a given angle of attack or sideslip trim condition, the form of the equations is sufficiently flexible to permit fitting it to more localized aerodynamic properties, as obtained by test or semi-empirical methods.

Additional interference effects besides those that were treated in Subsection C arise from ground proximity to the tail. This causes an increase in the tail local angle of attack (Type A interference) and an increase in the tail lifting efficiency (Type B interference). These interference effects can be important in the low incidence regime, but will be less important in the crossflow and stall transition regimes. In the development of the tail force models we assume that the tail lift parameters are known a priori. The corrections for the various hull and tail Type B interference effects will be presented in Subsection G.

Before continuing with the detailed equations for quasi-steady tail loads, we present the definitions for angle of attack and angle of sideslip since they will be needed in the following sections. Here we also present corrections to these local incidence angles arising from ground on tail velocity interference (Type A) and tail control surface deflections.

#### **1. Tail Aerodynamic Incidence Angles**

The definitions for aerodynamic angle of attack and angle of sideslip commonly used in helicopter literature have been adopted in order to allow a continuous description of aerodynamic loads for all angles of incidence. The definition for angle of attack is the standard one which is used in all aircraft applications. However, the angle of sideslip is determined by the projection of the relative flow vector on the x-y plane of the hull. The algebraic equations for these angles are given in terms of the local velocity vector at the tail aerodynamic reference center as:

$$\alpha \equiv \tan^{-1}(w/u) \quad (8-89)$$

$$\beta \equiv \tan^{-1}(v/u) \quad (8-90)$$

where,  $u$ ,  $v$ , and  $w$  are the three components of  $(V_h^a)^t$  given in Eq. 8-35.

The tail rolling moment due to rolling velocity is calculated from the local angle of attack at the nominal tail tip location [also referred to as the non-dimensional roll-rate in the literature (Ref. 8-15)].

$$\alpha_p \equiv \tan^{-1} \left( \frac{p}{2} \frac{b_t}{u} \right) \quad (8-91)$$

where  $b_t$  is the reference tail span and  $p$  is the first component of  $\omega_h^a$ , from Eq. 8-4.

## 2. Tail Surface Deflection and Ground Effect Velocity Interference

The local tail aerodynamic angles of incidence are affected by deflections of the tail control surfaces and ground proximity (Type A interference). The deflection of the tail surfaces causes a change in the local angle of attack (due to elevator), local sideslip (due to rudder), and local rolling angle of attack (due to ailerons), which is calculated by a simple model based on the tail deflection angle ( $\delta$ ) and a control surface effectiveness parameter ( $\tau$ ). Ground proximity causes a reduction in the induced angle of attack at the tail aerodynamic center due to the straightening effect of the ground plane.

For small angles of deflection, the change in local tail incidence due to tail control surface deflection is linearly related to the deflection angle with a correction for movable tail surface geometry. When the deflections become large (greater than 60 deg), the effectiveness of the movable tail surfaces becomes severely limited. The following model accounts for the change in tail surface efficiency with increasing deflection angles and was taken from Ref. 8-6:

ORIGINAL PAGE IS  
OF POOR QUALITY

$$\alpha' = \alpha + \tau_e \sin \delta_e \quad (8-92)$$

$$\beta' = \beta + \tau_r \sin \delta_r \quad (8-93)$$

$$\alpha_p' = \alpha_p + \tau_a \sin \delta_a \quad (8-94)$$

where the primed notation here indicates that the aerodynamic angles have been corrected for tail surface deflections, and

$\delta_e, \delta_r, \delta_a$  are the elevator, rudder, and aileron deflections, respectively

$\tau_e, \tau_r, \tau_a$  are the tail surface effectiveness parameters for the elevator, rudder, and ailerons, respectively

The values for the tail effectiveness parameters are user input constants, determined from the movable surface planform and the area of the respective movable surfaces as percentages of the fixed tail areas.

The calculation of the velocity ground effect (Type A) on a lifting wing is based on a potential flow model of the ground plane as a reflecting vortex system. The strength of this reflecting vortex is dependent upon the lifting efficiency of the tail (lift curve slope) and the nondimensional height of the tail above the ground plane  $\hat{h}_t \equiv$  (vertical location of the horizontal tail/ $b_t$ ). This ground effect decreases with the inverse square of the nondimensional tail height, becoming negligible for tail locations greater than three tail spans above the ground. As a result, this correction will be unimportant except for mooring and rolling takeoff calculations. The following approximate model is based upon the equations given by Etkin (Ref. 8-15):

$$(\alpha)' = (\text{TIAC})\alpha \quad (8-95)$$

**ORIGINAL PAGE IS  
OF POOR QUALITY**

( $\alpha$ )' denotes that the tail angle of attack has been corrected for ground effects, and

$$\text{TIAC} \equiv [(\partial \epsilon_{gi} / \partial \epsilon)(\partial \epsilon / \partial \alpha)] + 1 \quad (8-96)$$

$\partial \epsilon_{gi} / \partial \epsilon$  is the rate of change of the ground-induced downwash angle with respect to the tail-induced downwash angle

$\partial \epsilon / \partial \alpha$  is the rate of change of tail-induced downwash angle with respect to tail freestream angle of attack

and are given by:

$$\frac{\partial \epsilon_{gi}}{\partial \epsilon} = \frac{1}{1 + (\text{KGTB})(\hat{h}_t)} \quad (8-97)$$

$$\frac{\partial \epsilon}{\partial \alpha} = - \left( \frac{2 Z_{\alpha} v_t^2}{\pi \rho_{air} b_t^2} \right) \quad (8-98)$$

In these equations,

KGTB is an input constant

$\hat{h}_t$   $h_t / b_t$ , the height of tail aerodynamic reference center normalized.

$Z_{\alpha} v_t^2$  is a an input parameter defined in Eq. 8-144 of the following subsection

The effects of ground proximity on the local tail angle of sideslip and rolling angle of attack are neglected as being small in comparison with the preceding tail surface deflection and ground-induced downwash corrections.

ORIGINAL DOCUMENT  
OF POOR QUALITY

The equations for the local tail incidence angles, including the effects of tail surface deflections and ground proximity, are given by:

$$(\alpha)' = [\alpha + (\tau_e \sin \delta_e)](\text{TIAC}) \quad (8-99)$$

$$(\beta)' = \beta + (\tau_r \sin \delta_r) \quad (8-100)$$

$$(\alpha_p)' = \alpha_p + (\tau_a \sin \delta_a) \quad (8-101)$$

where the primed ( )' notation now indicates that the tail aerodynamic incidences have been corrected for both tail surface deflection and ground proximity effects.

The rolling angle of attack correction of Eq. 8-101 is used in the model for tail rolling moment due to roll rate. However, aileron deflection does not affect the generation of side force due to roll rate, which is also indexed to the rolling angle of attack. For this case the uncorrected rolling angle of attack ( $\alpha_p$ ) given in Eq. 8-91 is used and will be distinguished from the adjusted value by the second subscript, "o":

$$\alpha_{p_o} = \tan^{-1}\left(\frac{p}{2} \frac{bt}{u}\right) \quad (8-102)$$

In the discussion that follows, the tail local incidence angles refer to the final corrected values of Eqs. 8-99 to 8-102.

### 3. Definitions for Large Angles of Incidence

The following definitions for reflected (supplementary) angles of incidence allow the use of single-quadrant equations in the tail aerodynamic models:

ORIGINAL PAGE IS  
OF POOR QUALITY

$$\alpha' = \begin{cases} \alpha & |\alpha| < \pi/2 \\ \pi[\text{sgn } \alpha] - \alpha & \pi/2 < |\alpha| < \pi \end{cases} \quad (8-103)$$

$$\beta' = \begin{cases} \beta & |\beta| < \pi/2 \\ \pi[\text{sgn } \beta] - \beta & \pi/2 < |\beta| < \pi \end{cases} \quad (8-104)$$

$$\alpha'_p = \begin{cases} \alpha_p & |\alpha_p| < \pi/2 \\ \pi[\text{sgn } \alpha_p] - \alpha_p & \pi/2 < |\alpha_p| < \pi \end{cases} \quad (8-105)$$

$$\alpha'_{p_0} = \begin{cases} \alpha_{p_0} & |\alpha_{p_0}| < \pi/2 \\ \pi[\text{sgn } \alpha_{p_0}] - \alpha_{p_0} & \pi/2 < |\alpha_{p_0}| < \pi \end{cases} \quad (8-106)$$

In these equations, the singles on the right hand side are defined by the primed quantities in Eq. 8-99 to 8-101. Further, the sign function is given by:

$$A = \begin{cases} +1 & A > 0 \\ -1 & A < 0 \end{cases} \quad (8-107)$$

The three tail incidence regimes (i.e., pre-stall, transition, and crossflow) used in each of the aerodynamic force and moment models (except for axial force) are defined in terms of six parameters ( $\alpha_1$ ,  $\alpha_2$ ,  $\beta_1$ ,  $\beta_2$ ,  $\alpha_{p1}$ ,  $\alpha_{p2}$ ) as follows:

TABLE 8-1. TAIL AERODYNAMIC REGIMES

	$\alpha'$	$\beta'$	$\alpha'_p$ (and $\alpha'_{p0}$ )
Pre-Stall	$ \alpha'  < \alpha_1$	$ \beta'  < \beta_1$	$ \alpha'_p  < \alpha_{p1}$
Stall Transition	$\alpha_1 <  \alpha'  < \alpha_2$	$\beta_1 <  \beta'  < \beta_2$	$\alpha_{p1} <  \alpha'_p  < \alpha_{p2}$
Crossflow	$\alpha_2 <  \alpha'  < \pi/2$	$\beta_2 <  \beta'  < \pi/2$	$\alpha_{p2} <  \alpha'_p  < \pi/2$

#### 4. Tail Forces

Tail forces are modeled for the combination of fins on the hull, so lift carryover and mutual hull/fin interference effects are subsumed in the net tail coefficients. For simplicity, the tail forces are assumed to pass through zero at zero incidence. At low angles of incidence (pre-stall) the normal forces (Z and Y) are modeled by a sum of linear effects proportional to  $(\alpha', \beta', \alpha'_p)$  and leading edge vortex effects proportional to  $(\alpha'^2, \beta'^2, \alpha_p'^2)$ .

Instead of the conventional practice of writing Z as a product of total dynamic pressure ( $\propto V_0^2$ ) and coefficients dependent on  $\alpha'$  and  $\beta'$ , we have found it more efficient to use the dynamic pressure perpendicular to the relevant span ( $\sim V_{xz_t}^2$ ). By doing this, the Z-force slope  $C_{Z_\alpha}$  becomes nearly constant for all  $\beta'$ . Similarly for lateral forces, referencing to  $V_{xy_t}^2$  allows the use of a single slope  $C_{Y_\alpha}$ , which is nearly constant for all  $\alpha'$ . This agrees with skewed-wing theory (Ref. 8-6), matches data well, and simplifies the simulation of large incidences. At large angles of attack (post-stall), the tail's normal forces are modeled by an extension of the hull crossflow theory covered above, with  $C_{C_{y_t}}$  and  $C_{C_{z_t}}$  being the crosswind drag coefficients of the tail (on hull) assembly. In the stall transition regime, the tail forces are

linearly interpolated between those at  $\alpha_1$  and  $\alpha_2$ ;  $\beta_1$  and  $\beta_2$ ; and  $\alpha_p$  and respectively.

The tail axial force is closely proportional, over a large angle range, to a constant (predominantly skin friction) coefficient times the axial component of relative velocity ( $u$ ) squared:

$$X_t = \sigma X_{u|u|_t} u|u| \quad (8-108)$$

where  $X_{u|u|_t}$  is an input parameter determined by the user. It is related to the conventional aerodynamic quantities according to the defining equation:

$$X_{u|u|_t} \equiv \frac{-p_0}{2} S_t C_{A_t} \quad (8-109)$$

The tail reference area,  $S_t$ , is that which is consistent with the axial drag coefficient,  $C_{A_t}$ .

The tail static Y-force model shown in Fig. 8-5 is defined by the following equations:

Pre-Stall:  $|\beta'| < \beta_1$ ; all  $\alpha$  and  $\alpha_p$

$$Y_{t_s} = \sigma [Y_{\beta V_t^2} \beta' + Y_{\beta^2 V_t^2} \beta' |\beta'|] v_{xy_t}^2 \quad (8-110)$$

where

$$v_{xy_t} = \sqrt{u^2 + v^2} \quad (8-111)$$

Crossflow:  $\beta_2 < |\beta'| < \pi/2$ ; all  $\alpha'$  and  $\alpha_p'$

$$Y_{t_s} = \sigma Y_{v|v|_t} v v_{yz_t} \quad (8-112)$$

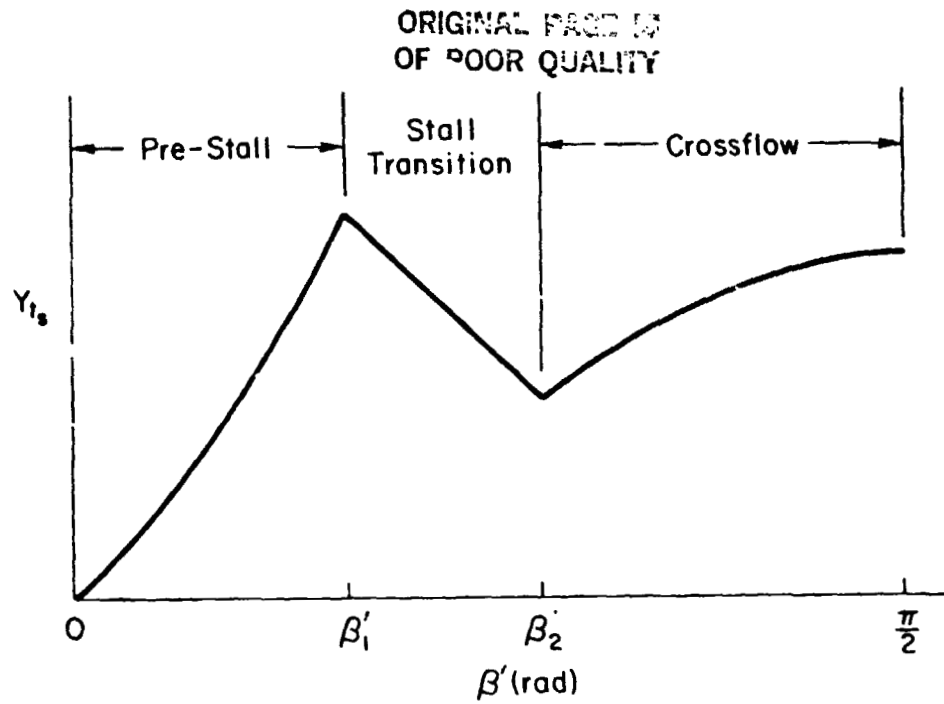


Figure 8-5. Tail Static Y-Force Model

where

$$v_{yz_t} = \sqrt{v^2 + w^2} \quad (8-113)$$

Transition:  $\beta_1 < \beta' < \beta_2$ ; all  $\alpha'$  and  $\alpha_p'$

$$Y_{r_s} = Y_t(\beta_1') + \left[ \frac{Y_t(\beta_2') - Y_t(\beta_1')}{\beta_2' - \beta_1'} \right] (\beta' - \beta_1') \quad (8-114)$$

where  $Y_t(\beta_1')$  is determined from Eq. 8-110 with  $\beta' = \beta_1'$ , and

$$Y_t(\beta_2') = \sigma v_2 v_{yz_2} Y_{v|v|} \quad (8-115)$$

where

$$\beta'_1 \equiv \beta_1 \operatorname{sgn} \beta \quad (8-116)$$

$$\beta'_2 \equiv \beta_2 \operatorname{sgn} \beta \quad (8-117)$$

$$v_2 = v_{xyt} \sin \beta'_2 \quad (8-118)$$

$$v_{v-2} \equiv \sqrt{w^2 + v_2^2} \quad (8-119)$$

Neglecting some higher-order effects of overlapping  $\alpha$ ,  $\beta$ , and  $\alpha_p$  regimes, the dynamic Y-forces (i.e., those due to rolling velocities about the tail aerodynamic reference center) are calculated similarly. Note that  $\alpha_{p_0}$  rather than  $\alpha_p$  is used, since the ailerons do not contribute to the dynamic Y-forces.

Pre-Stall:  $|\alpha'_{p_0}| < \alpha_{p_1}$ ; all  $\alpha'$  and  $\beta'$

$$Y_{td} = \sigma [Y_{\alpha_p} v_t^2 \alpha'_{p_0} + Y_{\alpha_p^2} v_t^2 \alpha'_{p_0} |\alpha'_{p_0}|] v_{xyt}^2 \quad (8-120)$$

Crossflow:  $\alpha_{p_2} < |\alpha'_{p_0}| < \pi/2$ ; all  $\alpha'$  and  $\beta'$

$$Y_{td} = \sigma Y_{p|p|t} |p| \quad (8-121)$$

Transition:  $\alpha_{p_1} < \alpha' < \alpha_{p_2}$ ; all  $\alpha'$  and  $\beta'$

$$Y_{td} = Y_{td}(\alpha'_{p_{1_0}}) + \left[ \frac{Y_{td}(\alpha'_{p_{2_0}}) - Y_{td}(\alpha'_{p_{1_0}})}{\alpha'_{p_{2_0}} - \alpha'_{p_{1_0}}} \right] (\alpha'_{p_0} - \alpha'_{p_{1_0}}) \quad (8-122)$$

and

$Y_{td}(\alpha'_{p_{1_0}})$  is determined from Eq. 8-120 with  $\alpha'_{p_0} = \alpha'_{p_{1_0}}$

$$Y_{td}(\alpha'_{p_{2_0}}) = \sigma p_2 |p_2| Y_{p|p|t} \quad (8-123)$$

ORIGINAL PAGE IS  
OF POOR QUALITY

where

$$\alpha'_{p1_0} = \alpha_{p1} \operatorname{sgn} \alpha_{p_0} \quad (8-124)$$

$$\alpha'_{p2_0} = \alpha_{p2} \operatorname{sgn} \alpha_{p_0} \quad (8-125)$$

$$p_2 = (2V_{p_t}/b_t) \sin \alpha'_{p_0} \quad (8-126)$$

$$V_{p_t} \equiv \sqrt{u^2 + (pb_t/2)^2} \quad (8-127)$$

The tail z-forces are given by:

Pre-Stall:  $|\alpha'| < \alpha_1$ ; all  $\beta'$  and  $\alpha'_p$

$$Z_t = \sigma [Z_{\alpha V^2} \alpha' + Z_{\alpha^2 V^2} \alpha' |\alpha'|] V_{xz_t}^2 \quad (8-128)$$

where

$$V_{xz_t} = \sqrt{u^2 + w^2} \quad (8-129)$$

Crossflow:  $\alpha_2 < |\alpha'| < \pi/2$ ; all  $\beta'$  and  $\alpha'_p$

$$Z_t = \sigma Z_{w|w|_t} w V_{yz_t} \quad (8-130)$$

Transition:  $\alpha_1 < \alpha' < \alpha_2$ ; all  $\beta'$  and  $\alpha'_p$

$$Z_t = Z_t(\alpha'_1) + \left[ \frac{Z_t(\alpha'_2) - Z_t(\alpha'_1)}{\alpha'_2 - \alpha'_1} \right] (\alpha' - \alpha'_1) \quad (8-131)$$

where  $Z_t(\alpha'_1)$  is determined from Eq. 8-128 with  $\alpha' = \alpha'_1$ , and

$$Z_t(\alpha'_2) = \sigma w_2 V_{yz_2} Z_{w|w|_t} \quad (8-132)$$

where

$$\alpha'_1 = \alpha_1 \operatorname{sgn} \alpha \quad (8-133)$$

$$\alpha'_2 = \alpha_2 \operatorname{sgn} \alpha \quad (8-134)$$

$$w_2 = V_{xz_t} \sin \alpha'_2 \quad (8-135)$$

$$V_{yz_2} \equiv \sqrt{v^2 + w_2^2} \quad (8-136)$$

In the preceding equations (Eq. 8-108 to 8-136), the coefficients,  $X_{u|u|_t}$ ,  $Y_{\beta v^2_t}$ ,  $Y_{\beta^2 v^2_t}$ ,  $Y_{p|p|_t}$ ,  $Y_{\alpha_p v^2_t}$ ,  $Y_{\alpha_p^2 v^2_t}$ ,  $Y_{v|v|_t}$ ,  $Z_{\alpha v^2_t}$ ,  $Z_{\alpha^2 v^2_t}$ , and  $Z_{w|w|_t}$  are related to the conventional aerodynamic quantities according to the defining equations:

$$X_{u|u|_t} \equiv (-\rho_0/2) S_t C_{A_t} \quad (8-137)$$

$$Y_{\beta v^2_t} \equiv (-\rho_0/2) S_t C_{Y_{\beta t}} \quad (8-138)$$

$$Y_{\beta^2 v^2_t} \equiv (-\rho_0/2) S_t C_{Y_{\beta^2 t}} \quad (8-139)$$

$$Y_{\alpha_p v^2_t} \equiv (-\rho_0/2) S_t C_{Y_{\alpha_p t}} \quad (8-140)$$

$$Y_{\alpha_p^2 v^2_t} \equiv (-\rho_0/2) S_t C_{Y_{\alpha_p^2 t}} \quad (8-141)$$

$$Y_{p|p|_t} = (-\rho_0/2) S_t C_{Y_{p|p|_t}} \quad (8-142)$$

$$Y_{v|v|_t} = (-\rho_0/2) S_t C_{C_{y_t}} \quad (8-143)$$

$$Z_{\alpha v^2_t} \equiv (-\rho_0/2) S_t C_{Z_{\alpha t}} \quad (8-144)$$

$$Z_{\alpha^2 v^2_t} \equiv (-\rho_0/2) S_t C_{Z_{\alpha^2 t}} \quad (8-145)$$

$$Z_{w|w|_t} \equiv (-\rho_0/2) S_t C_{C_{z_t}} \quad (8-146)$$

The nondimensional parameters of Eq. 8-137 through 8-146 (e.g.,  $C_{A_t}$ ,  $C_{Y_2}$ , etc.) are obtained from available wind tunnel data, see Appendix A.

## 5. Tail Moments

The normal ( $Y_t$  and  $Z_t$ ) and axial ( $X_t$ ) forces computed at the tail's aerodynamic reference center are transferred to the hull c.g. to yield net quasi-steady static aerodynamic forces and moments there. The small pitching and yawing moments which are measured about the tail's own aerodynamic reference center due to pitching and yawing angular velocities are neglected in comparison with the large analogous moments on the hull (Eqs. 8-84 and 8-86). Significant tail rolling moments arise due to static sideslip (dihedral effect) and roll rate ( $\alpha_p$ ). Since the hull static and dynamic rolling moments are typically negligible (Subsection D, articles 1 and 2), the analogous tail moments are retained. The tail rolling moment dependency on roll rate ( $\alpha'_p$ ) is assumed to follow the same model as was used for the tail dynamic side force (i.e., single dependency on  $\alpha'_p$ ). However, the model for tail static rolling moment due to sideslip is more complicated, involving a generalized model which is dependent on both angle of attack and sideslip. This is necessary to account for the inherent asymmetry of the tail static rolling moment characteristics.

The pitching and yawing moments about the tail aerodynamic reference center due to pitching and yawing velocities and the tail X and Z forces due to tail angular velocities are second-order terms and are neglected. However, the tail rolling moment due to rolling angle of attack ( $\alpha_p$ ) is retained, since it contributes the dominant roll damping of the hull/tail system. The model for this moment is directly analogous to that used for the calculation of the dynamic Y-force. Since the tail rolling moment generated by roll rate is the same as that due to an equivalent aileron deflection, the tail rolling angle of attack used in the following calculations is that which was corrected for aileron deflection effects (Eq. 8-101). The resulting model for tail dynamic rolling moment is presented below:

Pre-Stall:  $|\alpha'_p| < \alpha_{p1}$ ; all  $\alpha'$  and  $\beta'$

$$L_{td} = \sigma [L_{\alpha_p} v_t^2 \alpha'_p + L_{\alpha_p^2} v_t^2 \alpha'_p |\alpha'_p|] v_{ty_t}^2 \quad (8-147)$$

Crossflow:  $\alpha_{p2} < |\alpha'_p| < \pi/2$ ; all  $\alpha'$  and  $\beta'$

$$L_{td} = \sigma L_p |p|_t |p| \quad (8-148)$$

Transition:  $\alpha_{p1} < \alpha'_p < \alpha_{p2}$ ; all  $\alpha'$  and  $\beta'$

$$L_{td} = L_{td}(\alpha'_{p1}) + \left[ \frac{L_{td}(\alpha'_{p2}) - L_{td}(\alpha'_{p1})}{\alpha'_{p2} - \alpha'_{p1}} \right] (\alpha'_p - \alpha'_{p1}) \quad (8-149)$$

where  $L_{td}(\alpha'_{p1})$  is determined from Eq. 8-147 with  $\alpha'_p = \alpha'_{p1}$ , and

$$L_{td}(\alpha'_{p2}) = \sigma p_2 |p_2| L_p |p| \quad (8-150)$$

and

$$\alpha'_{p1} = \alpha_{p1} \operatorname{sgn} \alpha_p \quad (8-151)$$

$$\alpha'_{p2} = \alpha_{p2} \operatorname{sgn} \alpha_p \quad (8-152)$$

$$p_2 = \left( \frac{2}{b_t} v_{p_t} \right) \sin \alpha'_p \quad (8-153)$$

with  $v_{p_t}$  given in Eq. 8-127  $L_{\alpha_p} v_t^2$ ,  $L_{\alpha_p^2} v_t^2$ ,  $L_p |p|_t$  are related to the conventional aerodynamic quantities according to the defining equations:

$$L_{\alpha_p} V_t^2 = (-\rho_0/2) S_t b_t C_{L_{\alpha_p}} \quad (8-154)$$

$$L_{\alpha_p^2} V_t^2 = (-\rho_0/2) S_t b_t C_{L_{\alpha_p^2}} \quad (8-155)$$

$$L_{|\beta|} V_t = (-\rho_0/2) S_t b_t C_{L_{|\beta|}} \quad (8-156)$$

The generation of tail static rolling moment due to sideslip (dihedral effect) depends upon both angle of attack ( $\alpha'$ ) and sideslip ( $\beta'$ ). This results from the change in the rolling moment due to sideslip derivative ( $L_{\beta}$ ) with changes in angle of attack, which arises from tails with swept-back quarter chord lines. Even for zero angle of attack, large dihedral effects may exist as a result of tails which are nonsymmetrically disposed on the hull (e.g., vee- or tee-tails). Surveys of a wide range of dihedral effects at large angles of incidence leads to the following five-regime flow model (Fig. 8-6), which is a generalization of the previous three-regime models:

Pre-Stall:  $|\alpha'| < \alpha_1$  and  $|\beta'| < \beta_1$ ; all  $\alpha'_p$

$$L_{t_s} = \sigma [L_{\beta} V_t^2 \beta' + L_{\beta \alpha} V_t^2 \beta' \alpha'] V_{xy_t}^2 \quad (8-157)$$

Crossflow:  $|\alpha'| > \alpha_2$  and/or  $|\beta'| > \beta_2$ ; all  $\alpha'_p$

$$L_{t_s} = \sigma L_{|\beta|} V_t^2 V_{yz_t} \quad (8-158)$$

$\alpha$ -Stall Transit'  $\alpha_1 < |\alpha'| < \alpha_2$  and  $|\beta'| < \beta_1$ ; all  $\alpha'_p$

Linear interpolation between  $\alpha'_1$  and  $\alpha'_2$  along constant  $\beta'$

$$L_{t_s} = L_{t_s}(\alpha'_1, \beta') + \left[ \frac{L_t(\alpha_2, \beta') - L_t(\alpha_1, \beta')}{\alpha_2 - \alpha_1} \right] (\alpha' - \alpha'_1) \quad (8-159)$$

ORIGINAL PAGE IS  
OF POOR QUALITY

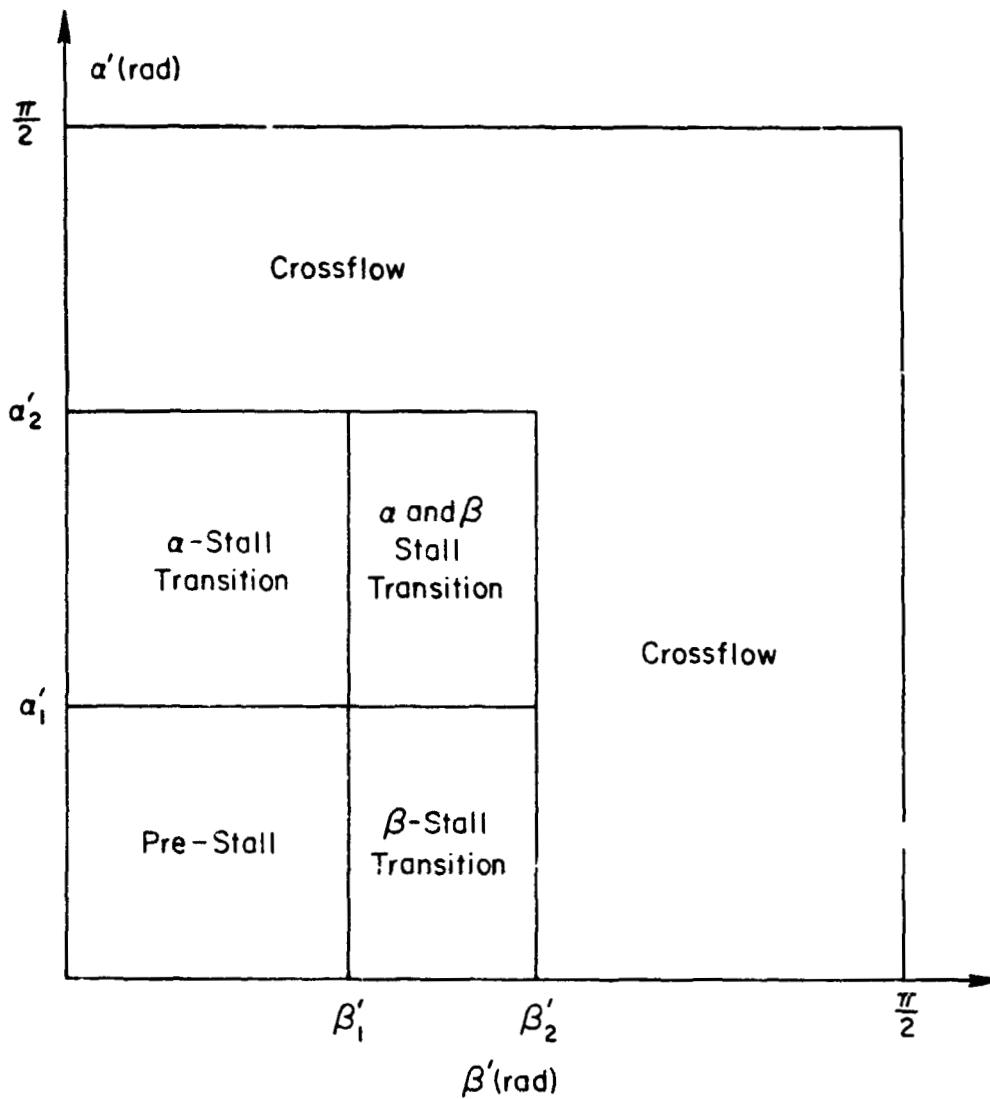


Figure 8-6. Flow Regimes for Tail, Rolling Moment Static Model

ORIGINAL PAGE IS  
OF POOR QUALITY

$\beta$ -Stall Transition:  $|\alpha'| < \alpha_1$  and  $\beta_1 < |\beta'| < \beta_2$ ; all  $\alpha'_p$

Linear interpolation between  $\beta'_1$  and  $\beta'_2$  along constant  $\alpha'$

$$L_{t_s} = L_{t_s}(\alpha', \beta'_1) + \left[ \frac{L_t(\alpha', \beta'_2) - L_t(\alpha', \beta'_1)}{\beta'_2 - \beta'_1} \right] (\beta' - \beta'_1) \quad (8-160)$$

$\alpha$  and  $\beta$  Stall Transition:  $\alpha_1 < |\alpha'| < \alpha_2$  and  $\beta_1 < |\beta'| < \beta_2$ ; all  $\alpha'_p$

Linear interpolation between  $\alpha_1$  and  $\alpha_2$  along constant  $\beta'$

$$L_t = L_t(\alpha'_1, \beta')_2 + \left[ \frac{L_t(\alpha'_2, \beta') - L_t(\alpha'_1, \beta')}{\alpha'_2 - \alpha'_1} \right] (\alpha' - \alpha'_1) \quad (8-161)$$

where  $L_{t_s}(\alpha'_1, \beta')$  is determined from Eq. 8-157 with  $\alpha' = \alpha'_1$ , and

$$L_{t_s}(\alpha'_2, \beta') = \sigma v_{yz_t} L_{v|v|_t} \quad (8-162)$$

$L_{t_s}(\alpha', \beta'_1)$  is determined from Eq. 8-157 with  $\beta' = \beta'_1$ , and

$$L_{t_s}(\alpha', \beta'_2) = \sigma v_2 v_{yz_2} L_{v|v|_t} \quad (8-163)$$

$L_{t_s}(\alpha'_1, \beta'_1)_2$  is determined from Eq. 8-157 with  $\alpha' = \alpha'_1$  and  $v_2$  and  $v_{yz_2}$  are given in Eqs. 8-118 and 8-119, respectively.  $L_{\beta v^2_t}$ ,  $L_{\beta \alpha v^2_t}$ , and  $L_{v|v|_t}$  are related to the conventional aerodynamic quantities according to the defining equations:

$$L_{\beta v^2_t} = \frac{-\rho_0}{2} S_t b_t C_{L_{\beta t}} \Big|_{\alpha=0} \quad (8-164)$$

$$L_{\beta \alpha v^2_t} = \frac{-\rho_0}{2} S_t b_t \frac{\partial C_{L_{\beta t}}}{\partial \alpha} \quad (8-165)$$

$$L_{v|v|_t} = \frac{-\rho_0}{2} S_t b_t C_{L_{v|v|_t}} \quad (8-166)$$

ORIGINAL PAGE IS  
OF POOR QUALITY

The preceding expressions for the dihedral effect may seem complex. However, they are the minimum complexity required to represent the strongly nonlinear variations in rolling moment as a function of angle of attack and sideslip which occur within and beyond the conventional attached flow regime. For example, it is well known (Ref. 8-16) that X-oriented fins give stability (restoring) dihedral effect at large  $\alpha$  and small  $\beta$ , and unstable (divergent) dihedral effect if rolled at  $\sim 5$  deg to give equal  $\alpha$  and  $\beta$ . The above equations correctly model this effect. When the HLA tail operates in the fully separated crossflow regime, the dihedral effect variations become very idiosyncratic functions of particular fin geometry, and the analytical model may not accurately represent specific details.

#### 6. Summary of Tail-Only Quasi-Steady Aerodynamics

The force vector acting of the tail centroid due to the quasi-steady aerodynamic effects discussed in this subsection is given by:

$$\underline{F}_{QS_h}^{ht} = \sigma \begin{bmatrix} X_t \\ Y_{ts} \\ Z_t \end{bmatrix} + \sigma \begin{bmatrix} 0 \\ Y_{td} \\ 0 \end{bmatrix} \quad (8-167)$$

where the various force terms are taken from article 4 (Eq. 8-108 to 8-146).

The moment vector acting at the tail centroid contains only rolling moment contributions for article 5 (Eq. 8-146 to Eq. 8-166):

$$\underline{T}_{QS_h}^{ht} = \sigma \begin{bmatrix} L_{ts} \\ 0 \\ 0 \end{bmatrix} + \sigma \begin{bmatrix} L_{td} \\ 0 \\ 0 \end{bmatrix} \quad (8-168)$$

In both cases the effects of velocity interference (Type A) and tail surface deflection are accounted for; the Type B interference effects are implicit in the coefficients.

## F. TYPICAL HULL/TAIL QUASI-STEADY AERODYNAMIC CHARACTERISTICS

This subsection sums the quasi-steady forces and moments of the hull and tail at the center of gravity of the hull assembly. The resulting model is then correlated with wind tunnel data for a classical airship design. This serves to expose the generic form of airship aerodynamic forces and moments. The aerodynamic force and moment variations of the hull and tail components used in an example HLA configuration are also presented to illustrate further the hull and tail equations developed above. This particular vehicle configuration was used throughout the simulation development.

### 1. Force and Moment Summation

The quasi-steady aerodynamic force acting at the hull center of volume is given by the sum of the hull only force (Eq. 8-87) and the tail-only force (Eq. 8-167).

$$\underline{F}_{QS_h} = \underline{F}_{QS_h}^{h\ cv} + \underline{F}_{QS_h}^{ht} \quad (8-169)$$

The quasi-steady aerodynamic moment is more complex in that allowance is made for the tail center of pressure not at the tail reference center. The result is expressed as a reduction in the tail centroid location relative to the hull center of volume (typically by 10 to 40 percent) is due to the mutual interference effect of the tail and hull (Ref. 8-17). This interference effect is modeled by including correction ratios in the moment arm relative to the center of volume. Thus if the geometric moment arm is given by:

$$\underline{R}_{hcv}^{ht} = [x\ y\ z]^T \quad (8-170)$$

then the modified matrix for expanding the vector cross product is:

$$\begin{bmatrix} \hat{R}_{hcv}^{ht} \times \end{bmatrix} = \begin{bmatrix} 0 & -\lambda_{zp}z & \lambda_{yp}y \\ \lambda_{zq}z & 0 & -\lambda_{xq}x \\ -\lambda_{yr}y & \lambda_{xr}x & 0 \end{bmatrix} \quad (8-171)$$

where the hat (^) denotes the modification and the  $\lambda$ 's are the correction ratios.

In the present model, the lateral offset of the tail centroid from the hull center of volume is assumed zero. Further, the vertical center of pressure correction ratios for rolling and pitching are assumed equal, that is

$$\lambda_{zp} = \lambda_{zq} \quad (8-172)$$

Only the value of  $\lambda_{zq}$  need be specified, whence  $[\hat{R}_{hcv}^{ht} \times]$  is

$$\begin{bmatrix} \hat{R}_{hcv}^{ht} \times \end{bmatrix} = \begin{bmatrix} 0 & -\lambda_{zq}z & 0 \\ \lambda_{zq}z & 0 & -\lambda_{xq}x \\ 0 & \lambda_{xr}x & 0 \end{bmatrix} \quad (8-173)$$

ORIGINAL PAGE IS  
OF POOR QUALITY

The resulting quasi-steady aerodynamic moment about the hull assembly center of gravity is given by:

$$\begin{aligned} \underline{I}QS_h = & \underline{I}QS_h^{hcv} + R_h^{hcv} \times \underline{E}QS_h^{hcv} + \underline{I}QS_h^{ht} + R_h^{hcv} \\ & \times \underline{E}QS_h^{ht} + [\hat{R}_{hcv}^{ht} \times] \underline{E}QS_h^{ht} \end{aligned} \quad (8-174)$$

Implicit in these results (Eq. 8-169 and 8-174) are both Type A and Type B interference effects.

## 2. Validation of Quasi-Steady Model

The hull and tail aerodynamic models were validated against extensive wind tunnel data for the airships "Akron," "Shenandoah," "R101," and the "Goodyear Zeppelins" (Refs. 8-3, 8-13, 8-18, 8-19, 8-20). Static lift, drag, and pitching moment data for the "Akron," with a fineness ratio of 6, are plotted in Fig. 8-7. Also shown are the fitted simulation model equations converted to wind axis components.

The simulation model drag results are within 5 percent of the experimental data over a large range of incidences. As expected, the predicted hull lift is deficient, in comparison to the data. However, the error is less than 10 percent when the hull/tail configuration is considered. Bare hull pitching moment characteristics match fairly well when a separation factor,  $\eta_M$ , of 0.75 is used. Pitching moment correlation with the tail on is not so good, due to the rearward shift of the tail center of pressure. However, the low incidence instability and higher incidence stability so typical of airships are matched. Additional correlations with high incidence and oscillatory (damping) data indicate that the hull and tail aerodynamic forces are generally valid to within about 25 percent accuracy over the entire HLA operational flight envelope. Considering that nearly all of the HLA aerodynamic characteristics requiring control can be simulated, further complexity in this generic model is hard to justify.

ORIGINAL PAGE IS  
CF POOR QUALITY

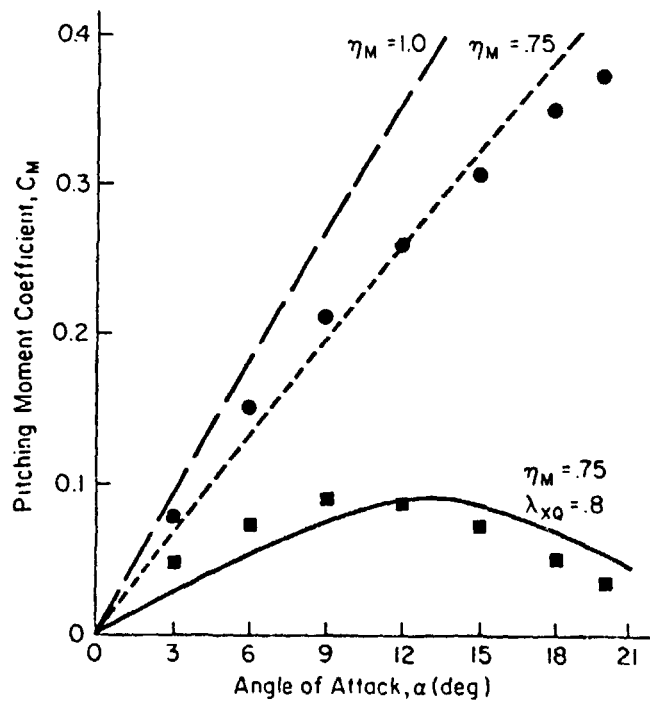
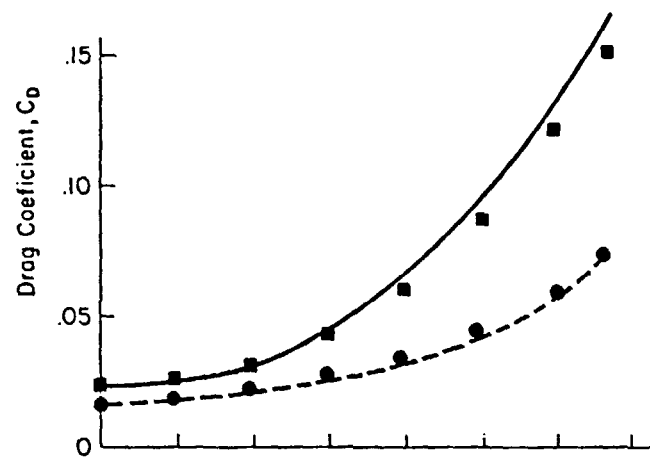
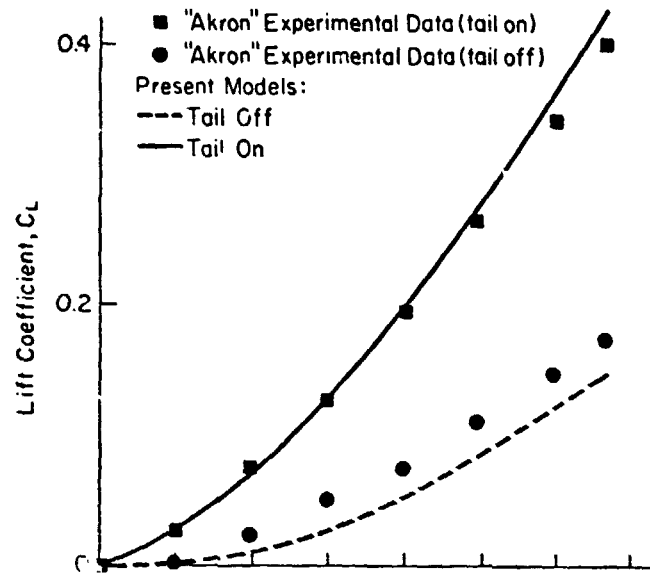


Figure 8-7. Comparison of Akron Airship Data with Quasi-Steady Models

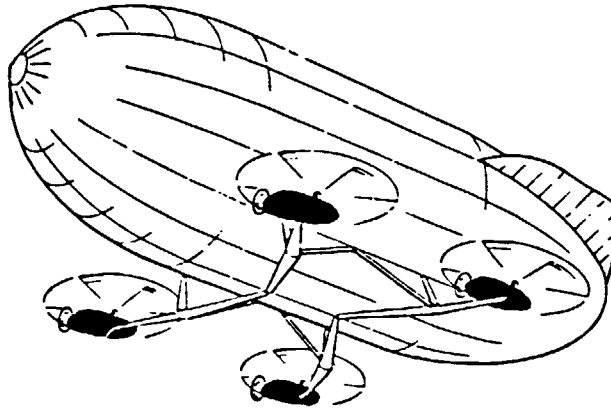
### 3. Steady Aerodynamics Model of Example Configuration

The quasi-steady aerodynamic (model) characteristics for the bare hull and hull/tail assembly of the example simulation test configuration of Fig. 8-8 are presented in Fig. 8-9 for a constant flight speed of 50 ft/sec. The hull properties are assumed equal in pitch or yaw, and the tail-on-hull properties for the 45 deg vee-tail are assumed to be the same in pitch or yaw, except for the rolling moment. Semi-empirical methods (Refs. 8-6, 8-7, 8-21, 8-22) were used to estimate the basic aerodynamic characteristics. The static Z(Y)-force (Fig. 8-9a) is seen to be dominated by the bare hull, as a result of the small tail exposed area. The static pitching (yawing) moment characteristics (Fig. 8-9b) show that the small stable tail contribution is completely overridden by the large unstable hull contribution, thereby rendering the vehicle statically unstable (metacentric stability not included). The present test case, which has a vee-tail, exhibits large negative rolling moments due to sideslip (positive dihedral effect). Figure 8-9c shows significant nonlinearities in the model for angles of attack of +35 and -35 deg, owing to the assumed breakdown of attached flow in the stall transition regimes. The bare hull damping characteristics for axial and non-axial flight are presented in Fig. 8-9d. While the offsets in moments at zero angular rate ( $\dot{q}, \dot{r} = 0$ ) are due to the static hull moment characteristics, the significant increase in damping moment with angular rate results from the  $w_h$  and  $v_h$  dependency in Eqs. 8-84 and 8-86.

#### G. ADDITIONAL INTERFERENCE EFFECTS

Subsections C and E, article 2 treated the various velocity (Type A) interference effects on the hull and tail. Additional important interference effects arise from the proximity of the rotors and propellers to the hull, and the ground to the hull and tail. These effects may significantly alter the drag and lift parameters of the hull and tail (Type B interference). For most standard configurations where the rotor and propeller wakes do not directly impinge on the tail surfaces, the Type B

ORIGINAL PAGE IS  
OF POOR QUALITY



Hull

Length	240 ft
Diameter	103 ft
Volume	$1.5 \times 10^6 \text{ ft}^3$
Tail Area	$2520 \text{ ft}^2$
Weight	$8.89 \times 10^4 \text{ lb}$

Lift Propulsion Unit (LPU)

Rotor Diameter	56 ft
Propeller Diameter	13 ft
Engine Horsepower (One per LPU)	1524 hp
Weight (Each LPU)	$9 \times 10^3 \text{ lb}$

<u>Composite Vehicle</u>	<u>Unloaded</u>	<u>Loaded</u>
Weight (lb)	125,000	165,000
Buoyancy Ratio	0.92	0.70

Figure 8-8. Simulation Test Configuration

ORIGINAL PAGE IS  
OF POOR QUALITY

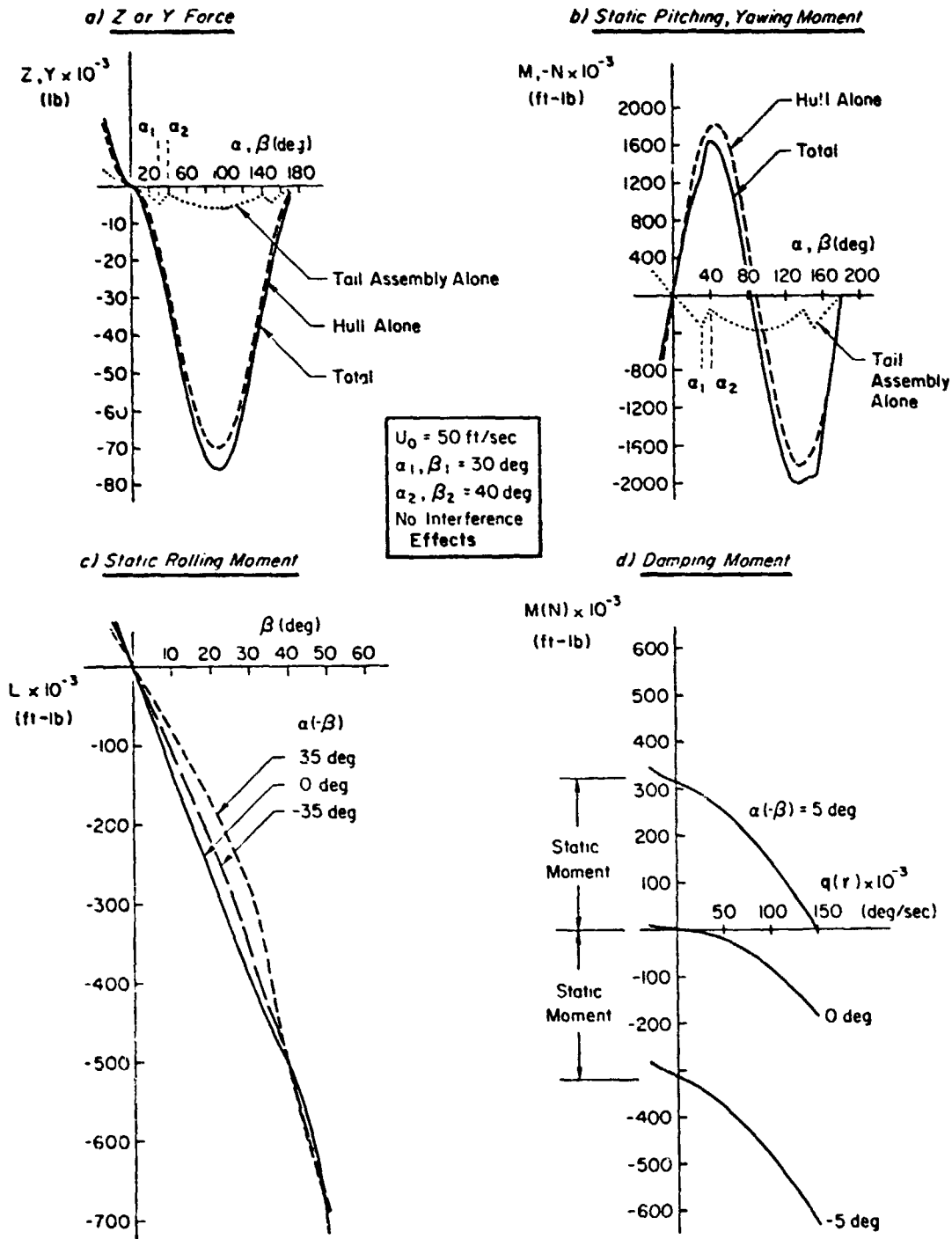


Figure 8-9. Quasi-Steady Aerodynamic Characteristics of the Test Configuration

wake interference effects on the tail crossflow drag coefficients will not be important. In addition, the effect of ground proximity on the tail crossflow drag coefficient is neglected in comparison to the similar effect on the hull.

The rotor-on-hull interference model is based on the HLA wind tunnel data of Ref. 8-1. The model is generalized to represent the similar effects of the propeller interference on the hull. The model of ground effects on the hull is drawn from wind tunnel experiments on a model of the airship Akron, described in Ref. 8-3. The ground-on-tail interference model is based on wind tunnel data (Ref. 8-6) and a potential flow solution (Ref. 8-15).

### 1. Rotor-on-Hull Interference

The data of Ref. 8-1 show a significant increase in hull crossflow drag coefficient ( $C_{Cyh}$ ) with the rotor thrust increase for operations in the large angle of sideslip regime. This is probably due to the interaction of rotor and hull wakes. For the maximum rotor thrust settings, the hull crossflow drag coefficient increases by 80 percent for the nominal rotor spacing, with small reductions for more outward rotor locations.

The rotor thrust-velocity-squared ( $U_T^2$ )<sup>rotor</sup> (with  $U_T$  given Eq. 7-51) is representative of the rotor self-induced flow energy, the dominant source of rotor-on-hull Type B interference. A measure of the induced flow energy from all four rotors is obtained from the following definition of the total thrust-velocity-squared:

$$U_{T_{total}}^2 \equiv \sum_{i=1}^4 (U_T^2)^{rotor\ i} \quad (8-175)$$

The ratio of the hull crossflow drag coefficient with rotors off to that obtained with all rotors on is designated  $(C_{Cyh})'/C_{Cyh}$  where the ( )' notation indicates that the hull crossflow drag coefficient has been corrected for the interference effect of all rotors. The variation of this hull crossflow drag coefficient ratio with total thrust-velocity-squared is shown in Fig. 8-10. The data were obtained from Ref. 8-1 for

ORIGINAL PAGE IS  
OF POOR QUALITY.

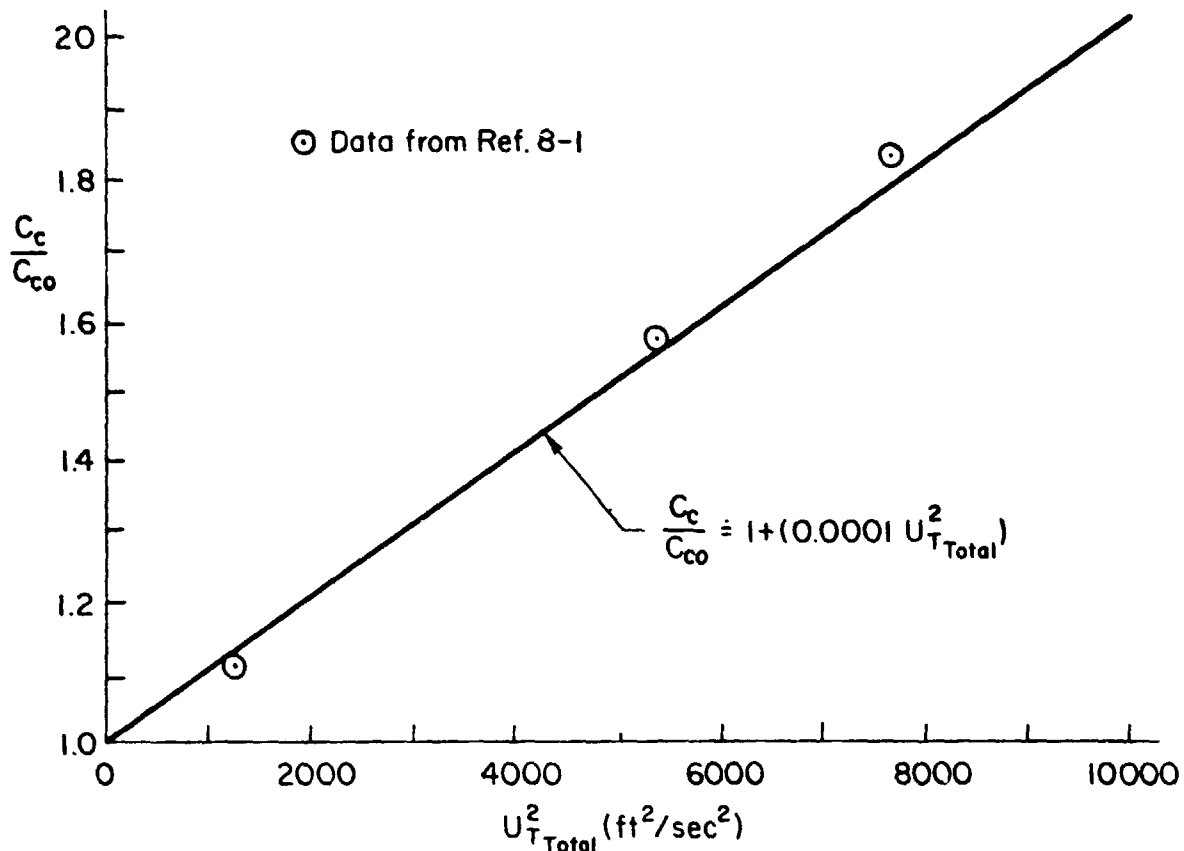


Figure 8-10. Rotor Interference Effect on Hull Crossflow Drag Coefficient for Outward Rotor Locations ( $\bar{d} \approx 1.5$ )

the nominal nondimensional rotor/hull separation distance ( $\bar{d}$  of Subsection C1) equal to 1.47.

As can be seen in Fig. 8-10, the variation of the drag coefficient ratio with thrust velocity follows nearly a square law for this configuration. However, for more outward rotor locations, the wind tunnel data show a more linear dependency on thrust velocity. In order to accommodate arbitrary rotor locations, the following general model has been adopted:

$$\frac{(C_{C_{yh}})' }{C_{C_{yh}}} = 1 + \sum_{i=1}^4 [ (KRHA |U_T|) + (KRHB U_T^2) ]^{\text{rotor } i} \quad (8-176)$$

where  $U_T$  is defined in Eq. 7-51, and KRHA and KRHB are user-supplied constants for each rotor obtained from available wind tunnel data. This hull crossflow drag coefficient correction is reflected in the hull crossflow drag parameter as follows:

$$(Y_{v|v|h})' = \frac{(C_{C_{yh}})'}{C_{C_{yh}}} Y_{v|v|h} \quad (8-177)$$

where  $(Y_{v|v|h})'$  denotes that  $Y_{v|v|h}$  of Eqs. 8-64 and 8-69 has been corrected for rotor interference.

## 2. Propeller-on-Hull Interference

The propellers, like the rotors, can cause significant changes in the hull crossflow drag coefficient due to wake interaction. The model adopted for propeller-on-hull Type B interference is identical to that discussed previously for the rotor-on-hull interference. The interference constants of the Eq. 8-174 are redefined for each propeller (KPHA, KPHB). When the propeller and rotor hubs are in roughly the same location, the propeller interference constants (KPHA, KPHB) are user approximated from the rotor constants and the ratio of the propeller and rotor disk areas according to the following relations:

$$(KPHA)^{prop\ i} \doteq (KRHA)^{rotor\ i} (\bar{A})^i \quad (8-178)$$

$$(KPHB)^{prop\ i} \doteq (KRHB)^{rotor\ i} (\bar{A})^i \quad (8-179)$$

where  $(\bar{A})^i \equiv \frac{A_{propeller}}{A_{rotor}}$ , for the  $i$ th LPU (same as Eq. 8-37)

## 3. Ground-on-Hull Interference

The data of Ref. 8-3 show a significant decrease in the hull crossflow drag coefficient ( $C_{C_{yh}}$ ) for crossflow conditions where the height of the hull above the ground is reduced to within one hull diameter. This decrease in the crossflow drag coefficient with decreasing ground

height is due to changes in the leeward hull wake as the ground is approached. The data of Ref. 8-3 are plotted, in Fig. 8-11, in terms of the drag coefficient ratio  $(C_{Cyh})'/C_{Cyh}$  where the primed ( )' notation denotes that the crossflow drag coefficient has been corrected for ground-on-hull interference. These data are plotted as a function of normalized hull height  $\hat{h}$  (= height of the hull center of volume above the ground/hull diameter). The data of Fig. 8-11 indicate that the crossflow drag coefficient correction becomes negligible when the height of the hull center of volume exceeds one hull diameter. As shown in this figure the wind tunnel data follow an exponential function of normalized hull height, approximated in the following equation:

$$\frac{(C_C)'}{C_C} = 1 - e^{-(K)\hat{h}} \quad (8-180)$$

where K is the curve fit constant. When the hull oriented upright (with  $\phi = \theta = 0$ ), the Y-force model is given by:

$$(Y_h)' = Y_h + (\Delta Y_h)_{ge} \quad (8-181)$$

where ( )' denotes that  $Y_h$  has been corrected for ground interference.  $Y_h$  is given in Eq. 8-64 including the rotor and propeller interference effects on  $Y_{v|v|h}$ , and

$$(\Delta Y_h)_{ge} = -v_y^w |v_y^w| e^{-(K)\hat{h}} Y_{v|v|h} \quad (8-182)$$

with  $v_y^w$  as in Eq. 8-43. When the hull pitch angles are small, the dependency on normalized hull height accounts for differences between the ground interference effects along the length of the hull. The effect of hull roll angle is accounted for by the generalization of the side force corrections of Eqs. 8-181 and 8-182:

$$(X_h)' = X_h \quad (\text{no interference effect}) \quad (8-183)$$

$$(Y_h)' = Y_h + (\Delta Y_h)_{ge} \quad (8-184)$$

$$(Z_h)' = Z_h + (\Delta Z_h)_{ge} \quad (8-185)$$

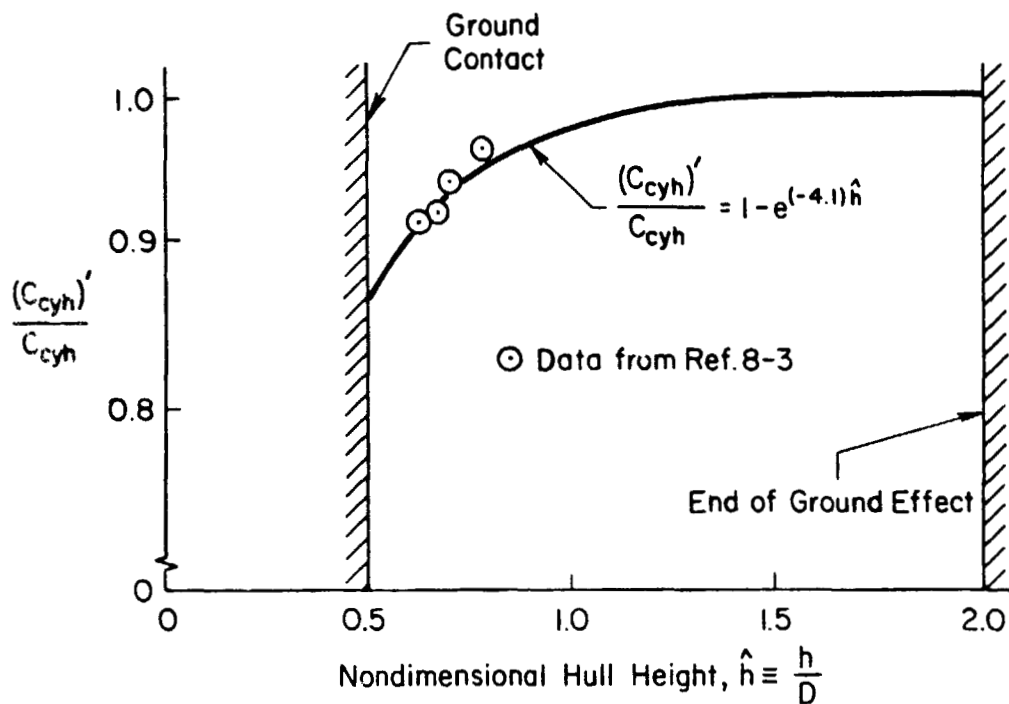


Figure 8-11. Ground Interference Effect on Hull Crossflow Drag Coefficient

and  $X_h$ ,  $Y_h$ ,  $Z_h$  are given in Eqs. 8-58, 8-64, and 8-65 and are corrected for rotor and propeller interference according to Subsection G, Articles 1 and 2.

$$(\Delta Y_h)_{ge} \equiv v_v^a cv |v_v^a cv| (e^{(KGHB)\hat{h}})(\cos \phi_h)(FVVABH) \quad (8-186)$$

$$(\Delta Z_h)_{ge} \equiv -v_v^a cv |v_v^a cv| (e^{(KGHB)\hat{h}})(\sin \phi_h)(FVVABH) \quad (8-187)$$

where

$v_v^a$  is given in Eq. 8-57

$$FVVABH \equiv \sqrt{Y_{v|v|h}^2 \cos^2 \phi_h + Z_{w|w|h}^2 \sin^2 \phi_h} \quad (8-188)$$

#### 4. Ground-on-Tail Interference

The presence of the ground plane causes an increase in the tail circulation and lift effectiveness ( $Z_{\alpha V_t^2}$ ) due to the favorable interference of the ground plane on the three-dimensional flow characteristics of the tail (Ref. 8-6). The following simplified exponential model based on nondimensional height of the tail above the ground  $\hat{h}_t$  (= tail height,  $h_t$ /tail span,  $b_t$ ) was developed from data given in Hoerner (Ref. 8-6):

$$(Z_{\alpha V_t^2})' = Z_{\alpha V_t^2} (\text{TCLC}) \quad (8-189)$$

where ( )' denotes that the tail circulation lift parameter ( $Z_{\alpha V_t^2}$ ) has been corrected for ground effects, and

$$\text{TCLC} = 1/[1 - e^{-(\text{KGTA})\hat{h}_t}] \quad (8-190)$$

In this expression,  $\hat{h}_t \equiv$  tail height above the ground divided by  $b_t \equiv$  user-supplied effective tail span (same value as in Subsection E, Article 1), and KGTA is a user-supplied input constant.

The effects of roll and pitch angles on the tail ground effect calculations are ignored in addition to the unknown effects of ground proximity on the tail vortex lift effectiveness ( $Z_{\alpha^2 V_t^2}$ ).

#### H. UNSTEADY AERODYNAMICS AND BUOYANCY

The airship's low relative density (buoyancy force/weight) makes its static buoyancy force contribution very significant and gives rise to the airship's relative sensitivity to unsteady aerodynamic loads, neither of which are generally of great importance for conventional aircraft. This section presents equations for these effects while making careful distinction among the several categories of loads involved.

The various loads can be classified in three categories. The first category of loads are those which arise from momentum changes in the

local flow due to accelerations of the vehicle or the air mass. These so called "apparent mass" effects impart large forces and moments to the hull and tail.

The second category of loads are those which arise from dependent build up of the bound-vortex patterns accompanying lifting surfaces. The importance of this category of loads, so-called "circulation lag" effects depends upon the lifting characteristics of the individual elements.

Buoyancy loads are in the third category and arise from pressure gradients in the atmosphere surrounding the HLA. The vertical pressure gradient induced by the earth's gravitational field produces the static buoyancy of the airship. Accelerated ambient flow fields also have pressure gradients which give rise to loads which are analogous to the static buoyancy forces. These are often termed "horizontal buoyancy" forces although the surrounding air mass can accelerate vertically as well. More precisely they are termed "buoyancy pressure gradient" forces. These loads depend on the inertial acceleration of the ambient flow, and the displaced volume of the hull. The tail does not experience buoyancy loads since its displaced volume is negligible.

Figure 8-12 taken from Ref. 8-23 shows a typical time history of the forces imparted to a two-dimensional (i.e., infinite span) wing during a step up gust encounter. The initial (infinite) impulsive force arises from the (instantaneous) momentum change in the local flow which accompanies the abrupt alteration of the steady stream lines. This is the "apparent mass" effect. Following this, a bleedoff in the impulsive force occurs with the force level approaching that given by the quasi-steady model. The lag in the bleed-off of the impulsive forces results from the time required for the bound vortex to reach a steady state condition.

The circulation lag effects on an airship hull are very small since it experiences only small circulation lift forces (Subsection D). To be

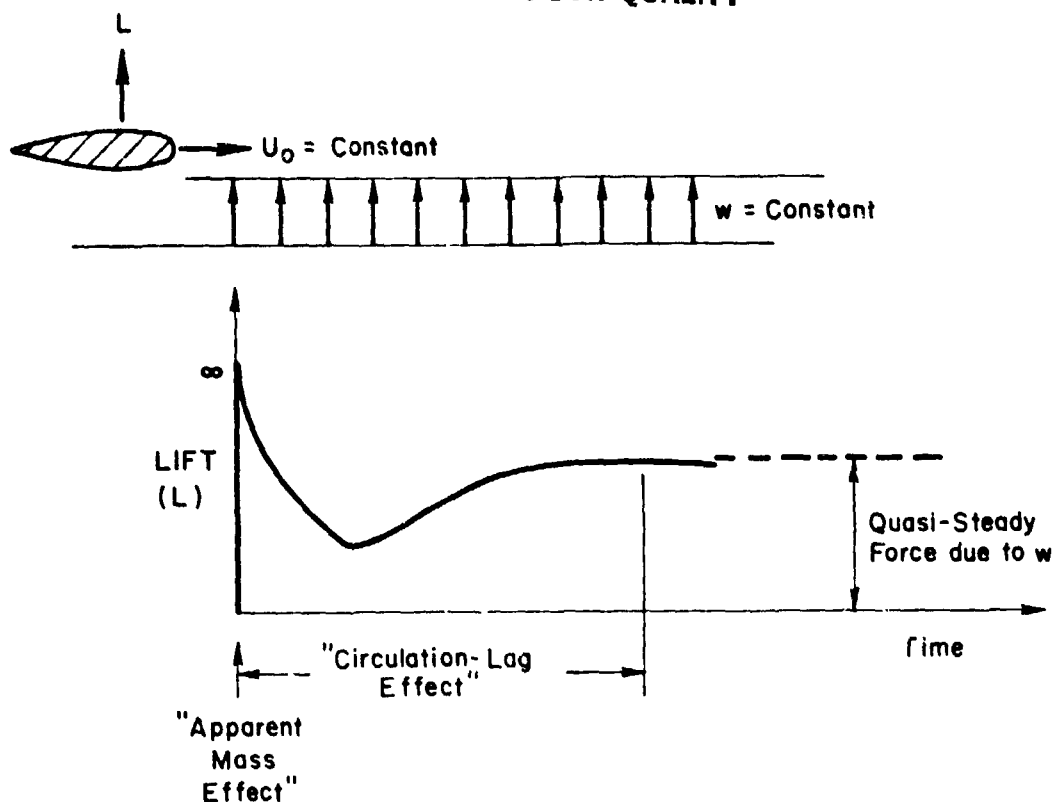


Figure 8-12. Typical Tail Vertical Force Time History During a Step Up-Gust Encounter (From Ref. 8-23)

consistent with the previous omission of the hull lift forces at low angles of attack ( $2\text{-}\alpha$  flow), these associated circulation lag effects are omitted. However, the apparent mass effects are very appreciable for the hull, contributing the dominant source of vehicle loads for unsteady motion.

The tail experiences loads due to both circulation lag and apparent mass effects. The former is highly sensitive to the effective tail aspect ratio ( $b_t^2/S_t$ ), with a value of 1 or 2 being typical of airships. For quasi-steady flow, the tail forces contribute only a small fraction of the total (hull tail) aerodynamic forces due to the typically small relative tail size. This was demonstrated in the quasi-steady results of Subsection F. The circulation lag effects, which are only a small fraction of the typically small quasi-steady tail forces, may be neglected in comparison with the larger tail apparent mass loads.

Inclusion of tail circulation lag effects should be considered for configurations with unusually large tail surfaces of high aspect ratio.

Summarizing the above simplifications, the unsteady aerodynamic effects which are modeled in the simulation are: the apparent mass effects on the hull and tail, and the buoyancy pressure gradient effects on the hull. These models are based on the potential flow solutions of Refs. 8-11, and 8-24 to 8-27. The associated effects of rotor, propeller and ground interference are unknown and therefore neglected. The unsteady aerodynamic forces and moments which arise from flow momentum changes (apparent mass effects) are considered first.

### 1. Momentum Changes

First, a model is presented for determining the unsteady loads on the hull, with later generalizations to allow the calculation of corresponding tail loads.

As outlined above, unsteady loads result from the energy which an accelerating body must impart to the surrounding fluid to cause changes in an otherwise steady flow field, or the energy imparted to a trimmed vehicle by an accelerating flow field (e.g. a gust). The original derivation of accelerated motion forces are due to Kelvin, Ref. 8-24 and Lamb, Ref. 8-25 and were based on equations for imparted fluid kinetic energy. These concepts were accurately applied by many British and American scientists working on the airship problem in the early part of this century. Most notable at a publications by Munk, Ref. 8-26 and Imlay Ref. 8-27.

An alternate approach to the kinetic energy solution is given by Zahn (Ref. 8-11), who considered the time rates of change of the linear and angular momentum of the local flow. Following this approach, the linear momentum vector of the local flow due to hull motion is given by:

$$\underline{p}_h^a = \rho V [K]_h \underline{V}_h^a \quad (8-191)$$

ORIGINAL PAGE IS  
OF POOR QUALITY

where  $\underline{V}_h^{a\ cv}$  is given in Eq. 8-1 (i.e., excluding interference effects), and

$$[K]_h \equiv \begin{bmatrix} K_a & 0 & 0 \\ 0 & K_b & 0 \\ 0 & 0 & K_c \end{bmatrix} \quad (8-192)$$

where  $K_a$ ,  $K_b$ , and  $K_c$  are the so-called hull "apparent mass" constants which are shape factors determined in part by the fineness ratio of the hull (Ref. 8-11). Corrections for separation effects (typically a reduction of less than 20 percent) are discussed in Ref. 8-28.

The hull forces imparted by the surrounding fluid are equal and opposite to the fluid forces imparted by the hull. They act at the hull center of volume and are determined from Newton's Law by the inertial rate of change of the body referenced flow momentum vector:

$$\underline{F}_{MC_h}^{hcv} = - \dot{\underline{P}}_h^a = - \underline{P}_h^a - (\underline{\omega}_h \times \underline{P}_h^a) \quad (8-193)$$

where the subscript MC stands for momentum change and  $\underline{\omega}_h$  is given in Eq. 2-31. Since the matrix  $[K]_h$  is referenced to the body axis, its time derivative relative to rotating body axes is zero. So,

$$\underline{P}_h^a = \rho V [K]_h \underline{V}_h^{a\ cv} \quad (8-194)$$

where  $\underline{V}_h^{a\ cv}$  is given in Eq. 8-9. The relative acceleration is dependent upon the acceleration of the hull center of volume,  $\underline{V}_h^{hcv}$ , given in Eq. 8-16 which in turn contains the unknown quantity  $\underline{V}_h^a$  a function of the external forces in Eq. 2-58. For the present, the quantity  $\underline{V}_h^{a\ cv}$  is assumed to be known a priori; the equations will be rearranged in Sub-section I, following to accommodate the computational difficulty.

ORIGINAL PAGE IS  
OF POOR QUALITY

Expanding Eqs. (8-193) and (8-194) in scalar form yields:

$$X_h = -\rho\psi(K_a \overset{\circ}{u} + K_c q_h w - K_b r_h v) \quad (8-195)$$

$$Y_h = -\rho\psi(K_b \overset{\circ}{v} - K_c p_h w + K_a r_h u) \quad (8-196)$$

$$Z_h = -\rho\psi(K_c \overset{\circ}{w} + K_b p_h v - K_a q_h u) \quad (8-197)$$

where  $\overset{\circ}{u}$ ,  $\overset{\circ}{v}$ , and  $\overset{\circ}{w}$  are components of the relative acceleration vector

$$\begin{bmatrix} \overset{\circ}{u} \\ \overset{\circ}{v} \\ \overset{\circ}{w} \end{bmatrix} \equiv \underline{\overset{\circ}{v}}_h^{a \text{ cv}} \quad (8-198)$$

The angular velocities carrying the subscript h, are components of the angular velocity of the hull relative to the inertial reference frame (repeats Eq. 2-31):

$$\begin{bmatrix} p_h \\ q_h \\ r_h \end{bmatrix} \equiv \underline{\omega}_h \quad (\text{Equation 2 repeated}) \quad (8-199)$$

While the subscripted angular velocities are elements of the angular velocity relative to the air mass, i.e., of  $\underline{\omega}_h^{a \text{ cv}}$  (Eq. 8-2).

Equation 8-195 to Eq. 8-197 can be expressed in the form:

$$X_h = \sigma[X_{u_h}^{\circ} \overset{\circ}{u} + X_{q_h} q_h w + X_{r_h} r_h v] \quad (8-200)$$

$$Y_h = \sigma[Y_{v_h}^{\circ} \overset{\circ}{v} + Y_{p_h} p_h w + Y_{r_h} r_h u] \quad (8-201)$$

$$Z_h = \sigma[Z_{w_h}^{\circ} \overset{\circ}{w} + Z_{p_h} p_h v + Z_{q_h} q_h u] \quad (8-202)$$

ORIGINAL PAGES  
OF POOR QUALITY

where the parameters  $X_{uh}^0$ ,  $X_{qw_h}$ ,  $Z_{qu_h}$ , etc. are simulation input parameters. These are related to the constants of Eqs. 8-195 through (8-197) by the defining equations:

$$X_{uh}^0 \equiv -\rho_0 \sqrt{K_a} \quad (8-203)$$

$$X_{qw_h} \equiv -\rho_0 \sqrt{K_c} \quad (8-204)$$

$$X_{rv_h} \equiv \rho_0 \sqrt{K_b} \quad (8-205)$$

$$Y_{vh}^0 \equiv -\rho_0 \sqrt{K_b} \quad (8-206)$$

$$Y_{pw_h} \equiv \rho_0 \sqrt{K_c} \quad (8-207)$$

$$Y_{ru_h} \equiv -\rho_0 \sqrt{K_a} \quad (8-208)$$

$$Z_{wh}^0 \equiv -\rho_0 \sqrt{K_c} \quad (8-209)$$

$$Z_{pv_h} \equiv -\rho_0 \sqrt{K_b} \quad (8-210)$$

$$Z_{qu_h} \equiv \rho_0 \sqrt{K_a} \quad (8-211)$$

The hull moment equations are obtained by a similar analysis of the angular momentum which is imparted to the surrounding fluid by hull motion. As discussed in Refs. 8-11 and 8-29, linear hull motion gives rise to an angular momentum vector as a result of the curvature of the local streamlines around the hull ellipsoid. The inertial time rate of change of this momentum vector results in quasi-steady aerodynamic hull moments of Subsection D, article 1 (Eqs. 8-73 to 8-75). When the hull experiences angular velocities it imparts angular momentum to the local flow according to the following relation:

ORIGINAL PAGE IS  
OF POOR QUALITY

$$\underline{H}_h^a = \rho V [K']_h \underline{\omega}_h^{a \text{ cv}} \quad (8-212)$$

where  $\underline{\omega}_h^{a \text{ cv}}$  is given in Eq. 8-2 (i.e., excluding interference effects), and

$$[K']_h \equiv \begin{bmatrix} K'_a & 0 & 0 \\ 0 & K'_b & 0 \\ 0 & 0 & K'_c \end{bmatrix} \quad (8-213)$$

where  $K'_a$ ,  $K'_b$ , and  $K'_c$  are the so-called hull "apparent inertia" constants which are shape factors determined by the fineness ratio of the hull (Ref. 8-11).  $K'_a$  is set to zero because of the assumed cylindrical symmetry of the hull.

The moment vector experienced on the hull due to angular motion is obtained from the inertial time of change of the angular momentum vector of the local flow:

$$\underline{T}_{MC_h}^{h \text{ cv}} = - \dot{\underline{H}}_h^a = - \underline{H}_h^a - (\underline{\omega}_h \times \underline{P}_h^a) \quad (8-214)$$

As before, the matrix  $[K']_h$  is body axis referenced; so,

$$\underline{H}_h^{0a} = \rho V [K']_h \underline{\omega}_h^{0a \text{ cv}} \quad (8-215)$$

where  $\underline{\omega}_h^{0a \text{ cv}}$  is given in Eq. 8-12. Again, the relative angular acceleration vector,  $\underline{\omega}_h^{0a \text{ cv}}$ , contains the unknown quantity  $\underline{\omega}_h^0$  (Subsection B), which in turn depends on the external moments as in Eq. 2-58. As before, we assume the quantity  $\underline{\omega}_h^{0a \text{ cv}}$  is known a priori, and defer the computational problem to Subsection I, following.

ORIGINAL PAGE IS  
OF POOR QUALITY

Expanding Eqs. (8-214) and (8-215) in scalar form yields:

$$L_h = -\rho \Psi (K_a^{\circ} p + K_c^{\circ} q_h r - K_b^{\circ} r_h q) \quad (8-216)$$

$$M_h = -\rho \Psi (K_b^{\circ} q + K_a^{\circ} r_h p - K_c^{\circ} p_h r) \quad (8-217)$$

$$N_h = -\rho \Psi (K_c^{\circ} r + K_b^{\circ} p_h q - K_a^{\circ} q_h p) \quad (8-218)$$

where  $\overset{\circ}{p}$ ,  $\overset{\circ}{q}$  and  $\overset{\circ}{r}$  are components of the relative angular acceleration vector

$$\begin{bmatrix} \overset{\circ}{p} \\ \overset{\circ}{q} \\ \overset{\circ}{r} \end{bmatrix} \equiv \overset{\circ}{\omega}_h^{a \text{ cv}} \quad (8-219)$$

and the corresponding relative angular rates are:

$$\begin{bmatrix} p \\ q \\ r \end{bmatrix} \equiv \overset{a \text{ cv}}{\omega}_h$$

Equation 8-216 to 8-218 can be rewritten as:

$$L_h = \sigma [L_{ph}^{\circ} p + L_{qh}^{\circ} q_h r + L_{rh}^{\circ} r_h q] \quad (8-220)$$

$$M_h = \sigma [M_{qh}^{\circ} q + M_{rh}^{\circ} r_h p + M_{ph}^{\circ} p_h r] \quad (8-221)$$

$$N_h = \sigma [N_{rh}^{\circ} r + N_{qh}^{\circ} p_h q + N_{ph}^{\circ} q_h p] \quad (8-222)$$

ORIGINAL PAGE IS  
OF POOR QUALITY

where the subscript ( $\bar{\quad}$ ) denotes the inertial angular velocity within the parameters  $L_{qrh}^-$ , etc. These parameters are simulation inputs which are related to the constants of Eqs. 8-216 to 8-218 by the defining equations:

$$L_{ph}^o \equiv -\rho_o \Psi K'_a \quad (8-223)$$

$$L_{qrh}^- \equiv -\rho_o \Psi K'_c \quad (8-224)$$

$$L_{rgh}^- \equiv \rho_o \Psi K'_b \quad (8-225)$$

$$M_{qh}^o \equiv -\rho_o \Psi K'_b \quad (8-226)$$

$$M_{rph}^- \equiv -\rho_o \Psi K'_a \quad (8-227)$$

$$M_{prh}^- \equiv \rho_o \Psi K'_c \quad (8-228)$$

$$N_{rh}^o \equiv -\rho_o \Psi K'_c \quad (8-229)$$

$$N_{pqh}^- \equiv -\rho_o \Psi K'_b \quad (8-230)$$

$$N_{qph}^- \equiv \rho_o \Psi K'_a \quad (8-231)$$

ORIGINAL PAGE IS  
OF POOR QUALITY

The calculation of tail forces and moments which arise from changes in the local flow momentum directly follows the above development for the hull. Input parameters are related to the circumscribed area of the tail chord and span in lieu of their nonexistent volume. For typical airships, the forces which arise from the tail apparent mass effects are significantly smaller than the analogous hull forces. However, the resulting tail moments about the hull can be important due to the typically long tail arms. Therefore, we retain the first order effects which depend on the linear and angular acceleration terms (the first terms of Eqs. 8-200 to 8-202 and 8-220 to 8-222) and neglect the remaining velocity product terms. This approximation is within the overall level of accuracy of the hull-plus-tail aerodynamic model. The resulting equations for the force,  $\underline{F}_{MC_h}^{ht}$ , and moment,  $\underline{T}_{MC_h}^{ht}$  vectors at the tail aerodynamic reference center are given by:

$$X_t = 0 \quad (8-232)$$

$$Y_t = \sigma Y_{v_t}^o v + \sigma Y_{p_t}^o p \quad (8-233)$$

$$Z_t = \sigma Z_{w_t}^o w \quad (8-234)$$

$$L_t = \sigma L_{p_t}^o p + \sigma L_{v_t}^o v \quad (8-235)$$

$$M_t = \sigma M_{q_t}^o q \quad (8-236)$$

$$N_t = \sigma N_{r_t}^o r \quad (8-237)$$

where  $Y_{v_t}^o$ ,  $Y_{p_t}^o$ ,  $Z_{w_t}^o$ ,  $L_{p_t}^o$ ,  $L_{v_t}^o$ ,  $M_{q_t}^o$ , and  $N_{r_t}^o$  are simulation input parameters which are determined by the tail (on hull) geometry (Refs. 8-23 and 8-28). The  $Y_{p_t}^o$  and  $L_{v_t}^o$  coefficients account for possible vertical separation between the tail centroid for apparent mass effects and the hull centerline. In these equations the relative linear accelerations from Eq. 8-14 are:

ORIGINAL PAGE IS  
OF POOR QUALITY

$$\begin{bmatrix} u \\ v \\ w \end{bmatrix} = \frac{a}{V_h} t \quad (8-238)$$

and (from Eq. 8-16):

$$\begin{bmatrix} p \\ q \\ r \end{bmatrix} = \frac{a}{V_h} t \quad (8-239)$$

## 2. Buoyancy Pressure Gradient Effects

The static buoyancy force, i.e., without air mass acceleration effects, depends upon the geometry and density of the air displaced by the hull. It acts at the center of volume of this displaced air, which is the geometric center of the exterior envelope. The force is given by:

$$\underline{F}_{SB_h}^{h\ cv} = \rho V g L_{hI} [0 \ 0 \ -1]^T \quad (8-240)$$

where  $g$  is the acceleration due to gravity and  $L_{hI}$  is the direction cosine matrix defined in Eq. 2-6.

Dynamic buoyancy forces are imparted by fluid pressure gradients required to accelerate the flow. These forces are in addition to the momentum change forces and moments discussed above. The pressure gradient vector arising from the accelerated flow condition is given in hull reference axes by:

ORIGINAL PAGE IS  
OF POOR QUALITY

$$\underline{P}_h^{am\ cv} \equiv \begin{bmatrix} \partial p / \partial x \\ \partial p / \partial y \\ \partial p / \partial z \end{bmatrix}_h^{am\ cv} = -\rho (\dot{\underline{V}}_h^{am\ cv})_{Total} \quad (8-241)$$

where  $(\dot{\underline{V}}_h^{am\ cv})_{Total}$  is given in Eq. (8-18)

The force vector exerted on the hull is obtained by integrating over the envelope volume,

$$\underline{F}_{DB_h}^{hcv} = - \int\int\int_0^{\Psi} \underline{P}_h^{am\ cv} dx dy dz \quad (8-242)$$

where  $dx dy dz \equiv dV$ . The dynamic buoyancy force vector is therefore given by:

$$\underline{F}_{DB_h}^{hcv} = \rho V (\dot{\underline{V}}_h^{am\ cv})_{Total} \quad (8-243)$$

Because the total effective air mass acceleration consists of both acceleration and gradient terms, the dynamic buoyancy can be written as the sum of a gust acceleration term and a gust gradient term, viz:

$$\underline{F}_{DB_h}^{hcv} = \underline{F}_{GAB_h}^{hcv} + \underline{F}_{GGB_h}^{hcv} \quad (8-244)$$

where the gust acceleration term is:

$$\underline{F}_{GAB_h}^{hcv} = \rho V \dot{\underline{V}}_h^{am\ cv} \quad (8-245)$$

ORIGINAL PAGE IS  
OF POOR QUALITY

and the gust gradient term is:

$$\underline{F}_{GGB_h}^{hcv} = \rho V \frac{\partial \underline{V}_h^{am\ cv}}{\partial R} \underline{V}_h^{am\ cv} \quad (8-246)$$

The total buoyancy force acting at the hull center of volume is the sum of the static and the two gust terms:

$$\underline{F}_h^{hcv} = \underline{F}_{SB_h}^{hcv} + \underline{F}_{GAB_h}^{hcv} + \underline{F}_{GGB_h}^{hcv} \quad (8-247)$$

## I. COMPUTATIONAL CONSIDERATIONS AND EXAMPLE

This subsection collects and summarizes the several contributions to the aerodynamics acting on the hull/tail assembly of the HLA. Certain of these terms are functions of the hull accelerations,  $\underline{\ddot{V}}_h^o$  and  $\underline{\ddot{\omega}}_h^o$ , meaning that these unknowns appear on both sides of the matrix equations of motion. This introduces a computational difficulty which is resolved by moving these terms to the left-hand side, thereby augmenting the hull assembly inertia matrix,  $[\underline{I}^h]_h$ ; see Section 2, Subsection F. The subsection concludes with an illustrative example of the aerodynamic load contributions during a gust encounter, thereby providing an illustrative example of the relative importance of the several load contributors.

### 1. Load Term Summary and Equation Arrangement

#### a. Hull-Only at the Hull Center of Volume, CV

When the quasi-steady and momentum change forces are summed, the result can be separated into a relative acceleration dependent term and a term dependent upon steady flow effects, e.g., products of velocities, etc. For the hull only, the resulting summation yields:

ORIGINAL PAGE IS  
OF POOR QUALITY

$$\underline{E}M_{ch}^{hcv} + \underline{E}QS_h^{hcv} = M_{hF_1} V_h^{o a cv} + \underline{E}SF_h^{hcv} \quad (8-248)$$

where the left hand side terms are defined in Eq. 8-193 and 8-87, and  $M_{hF_1}$  is a diagonal matrix given by:

$$M_{hF_1} = \begin{bmatrix} \sigma X_{uh}^o & 0 & 0 \\ 0 & \sigma Y_{vh}^o & 0 \\ 0 & 0 & \sigma Z_{wh}^o \end{bmatrix} \quad (8-249)$$

The steady flow force vector,  $\underline{E}SH_h^{hcv}$ , is given by:

$$\underline{E}SF_h^{hcv} = \underline{E}QS_h^{hcv} + \begin{bmatrix} X_{qw_h} q_{hw} + X_{rv_h} r_{hv} \\ Y_{pw_h} p_{hw} + Y_{rw_h} r_{hu} \\ Z_{pv_h} p_{hv} + Z_{qw_h} q_{hu} \end{bmatrix} \quad (8-250)$$

where the second vector on the right hand side is taken from the velocity dependent terms in Eq. 8-200 through 8-202.

A similar equation holds for the hull-only moments

$$\underline{I}M_{ch}^{hcv} + \underline{I}QS_h^{hcv} = I_{hT_1} V_h^{o a cv} + \underline{I}SF_h^{hcv} \quad (8-251)$$

where the left hand side terms are given in Eqs. 8-214 and 8-88, and  $I_{hT_1}$  is a diagonal matrix given by:

ORIGINAL PAGE IS  
OF POOR QUALITY

$$I_h T_1 = \begin{bmatrix} \sigma L_{ph}^o & 0 & 0 \\ 0 & \sigma M_{qh}^o & 0 \\ 0 & 0 & \sigma N_{rh}^o \end{bmatrix} \quad (8-252)$$

The steady flow moment vector is given by

$$\underline{T}_{SFh}^{hcv} = \underline{T}_{QSh}^{hcv} + \begin{bmatrix} L_{qrh}^- q_{hr} + L_{rgh}^- r_{hg} \\ M_{rph}^- r_{hp} + M_{prh}^- p_{hr} \\ N_{pqh}^- p_{hq} + N_{qph}^- q_{hp} \end{bmatrix} \quad (8-253)$$

where the second vector on the right hand side is taken from the angular velocity dependent terms in Eq. 8-220 through 8-222. Recall that the velocities carrying the subscript, h, in Eq. 8-250 and 8-253 are relative inertial space; those without a subscript are relative to the moving airmass.

The relative acceleration dependent term in Eq. 8-248 is expanded by substituting Eq. 8-9 for the acceleration at the center of volume:

$$M_{hF1} \underline{V}_h^{a cv} = M_{hF1} \underline{V}_h^{ohcv} - M_{hF1} \underline{V}_h^{oam cv} + M_{hF1} \frac{\partial \underline{V}_h^{am cv}}{\partial R} \underline{V}_h^{a cv} \quad (8-254)$$

$$= \underline{EAD}_h^{hcv} + \underline{EGA}_h^{hcv} + \underline{EGG}_h^{hcv} \quad (8-255)$$

ORIGINAL PAGE IS  
OF POOR QUALITY.

The three terms on the right are respectively the acceleration dependent term, the gust acceleration term, and the gust gradient term. The elements of the  $M_{hF_1}$  matrix have the dimensions of mass. The second two terms in the simulation printout are identified as gust derivative terms:

$$\underline{E}_{GD_h}^{hcv} = \underline{E}_{GA_h}^{hcv} + \underline{E}_{GG_h}^{hcv} \quad (8-256)$$

The steady flow and gust derivative terms are also summed separately in the printout:

$$\underline{E}_{SFGD_h}^{hcv} = \underline{E}_{SF_h}^{hcv} + \underline{E}_{GD_h}^{hcv} \quad (8-257)$$

Finally, all the hull-only aerodynamic forces at the hull center of volume are summed from Eq. 8-257, 8-255, and 8-247 (buoyancy force):

$$\underline{F}_{A_h}^{hcv} = \underline{E}_{SFGD_h}^{hcv} + \underline{E}_{B_h}^{hcv} + \underline{F}_{AD_h}^{hcv} \quad (8-258)$$

A similar development holds for the hull-only moments at the hull center of volume. Thus, the relative acceleration dependent term of Eq. 8-251 is given by

$$I_{hT_1}^{oa\ cv} \omega_h = I_{hT_1}^{ohcv} \omega_h - I_{hT_1}^{oam\ cv} \omega_h \quad (8-259)$$

$$= \underline{T}_{AD_h}^{hcv} + \underline{T}_{GA_h}^{hcv} + \underline{T}_{GG_h}^{hcv} \quad (8-260)$$

ORIGINAL PAGE IS  
OF POOR QUALITY

where the hull only gust gradient dependent moment is identically zero at the center of volume ( $T_{GG_h}^{hcv} \equiv 0$ ). Thus the gust derivative moments are:

$$T_{GD_h}^{hcv} = T_{GA_h}^{hcv} + \cancel{T_{GG_h}^{hcv}} \rightarrow 0 \quad (8-261)$$

The steady flow and gust derivative terms are separately summed:

$$T_{SFGD_h}^{hcv} = T_{SF_h}^{hcv} + T_{GD_h}^{hcv} \quad (8-262)$$

All the hull only aerodynamic torques acting at the hull center of volume are given by:

$$T_{A_h}^{hcv} = T_{SFGD_h}^{hcv} + T_{AD_h}^{hcv} \quad (8-263)$$

b. Tail-Only at the Tail Centroid, t

Equations 8-248 to 8-263 pertain to the aerodynamic forces and moments of the hull alone acting at the hull center of volume. A similar development holds for the tail-only forces and moments rating at the tail centroid. The momentum change and quasi-steady forces are summed:

$$\underline{F}_{MCh}^{ht} + \underline{E}_{QS_h}^{ht} = M_{tF_1}^{Oat} + K_{tF_1}^{Oat} + \underline{E}_{SF_h}^{ht} \quad (8-264)$$

where the left hand side terms are defined in Eq. 8-232 through 8-234 and 8-167. There are two matrices. The first carries the dimensions of mass and is given by:

ORIGINAL PARTS  
OF POOR QUALITY

$$M_{tF1} = \begin{bmatrix} 0 & 0 & 0 \\ 0 & \sigma Y_{v_t}^0 & 0 \\ 0 & 0 & \sigma Z_{w_t}^0 \end{bmatrix} \quad (8-265)$$

The second has the dimension of mass times length and is given by:

$$K_{tF1} = \begin{bmatrix} 0 & 0 & 0 \\ \sigma Y_{p_t}^0 & 0 & 0 \\ 0 & 0 & 0 \end{bmatrix} \quad (8-266)$$

Since there are no velocity dependent terms in the momentum change forces, the steady flow and quasi-steady forces are the same:

$$\underline{E}_{SF_h}^{ht} = \underline{E}_{QS_h}^{ht} \quad (8-267)$$

As for the hull, there is a similar development for the tail-alone moments. The momentum change and quasi-steady moments are summed yielding:

$$\underline{I}_{MC_h}^{ht} + \underline{I}_{QS_h}^{ht} = I_r T_i \omega_h^{0at} + K_t T_i V_h^{0at} + \underline{I}_{SF_h}^{ht} \quad (8-268)$$

ORIGINAL PAGE IS  
OF POOR QUALITY

where the left hand side terms are given in Eq. 8-235 through 8-237 and Eq. 8-168, respectively. The first matrix (moment of inertia dimensions) is given by:

$$I_t T_1 = \begin{bmatrix} \sigma L_{p_t}^0 & 0 & 0 \\ 0 & \sigma M_{q_t}^0 & 0 \\ 0 & 0 & \sigma N_{r_t}^0 \end{bmatrix} \quad (8-269)$$

The second matrix has the dimensions of mass times length:

$$K_t T_1 = \begin{bmatrix} 0 & \sigma L_{v_t}^0 & 0 \\ 0 & 0 & 0 \\ 0 & 0 & 0 \end{bmatrix} \quad (8-270)$$

There are no velocity dependent momentum change terms whence:

$$\underline{I} S_{F_h}^{ht} = \underline{I} Q S_h^{ht} \quad (8-271)$$

The relative acceleration dependent terms in Eq. 8-264 are given by:

$$M_{tF_1} \underline{v}_h^{oat} + K_{tF_1} \underline{\omega}_h^{oat} = (M_{tF_1} \underline{v}_h^{oht} + K_{tF_1} \underline{\omega}_h^{oht}) - (M_{tF_1} \underline{v}_h^{oamt} + K_{tF_1} \underline{\omega}_h^{oamt}) \quad (8-272)$$

$$+ M_{tF_1} \frac{\partial \underline{v}_h^{amt}}{\partial R} \underline{v}_h^{at}$$

$$= \underline{F}_{AD_h}^{ht} + \underline{F}_{GA_h}^{ht} + \underline{F}_{GG_h}^{ht} \quad (8-273)$$

ORIGINAL PAGE IS  
OF POOR QUALITY

As before, the three right hand side terms are defined as the acceleration-dependent, the gust acceleration and gust gradient terms. The second two terms are summed separately in the simulation printout as the gust derivative terms:

$$\underline{E}_{GD_h}^{ht} = \underline{E}_{GA_h}^{ht} + \underline{E}_{GG_h}^{ht} \quad (8-274)$$

The steady flow and gust derivative terms are separately summed as well:

$$\underline{E}_{SFGD_h}^{ht} = \underline{E}_{SF_h}^{ht} + \underline{E}_{GD_h}^{ht} \quad (8-275)$$

Finally, all the tail-only aerodynamic forces are summed at the tail centroid:

$$\underline{E}_{A_h}^{ht} = \underline{E}_{SFGD_h}^{ht} + \underline{E}_{AD_h}^{ht} \quad (8-276)$$

The tail only moments are similarly handled. The relative acceleration dependent terms of Eq. 8-268 are:

$$\underline{I}_{tT_1}^{oat} + K_{tT_1}^{oat} = (\underline{I}_{tT_1}^{oht} + K_{tT_1}^{oht}) \quad (8-277)$$

$$\begin{aligned} & - (\underline{I}_{tT_1}^{oam} + K_{tT_1}^{oam}) + K_{tT_1} \frac{\partial \underline{V}_h^{amt}}{\partial \underline{R}} \underline{V}_h^{at} \\ & = \underline{I}_{AD_h}^{ht} + \underline{I}_{GA_h}^{ht} + \underline{I}_{GG_h}^{ht} \end{aligned} \quad (8-278)$$

ORIGINAL PAGE IS  
OF POOR QUALITY

where the right hand side terms are the acceleration-dependent, gust acceleration and gust gradient dependent terms, respectively. The second two terms are separately summed as the gust derivative terms:

$$\underline{I}_{GD_h}^{ht} = \underline{I}_{GA_h}^{ht} + \underline{I}_{GG_n}^{ht} \quad (8-279)$$

The steady flow and gust derivative terms are also separately summed:

$$\underline{I}_{SFGD_h}^{ht} = \underline{I}_{SF_h}^{ht} + \underline{I}_{GD_h}^{ht} \quad (8-280)$$

All tail only moments are summed at the tail centroid giving:

$$\underline{I}_{A_h}^{ht} = \underline{I}_{SFGD_h}^{ht} + \underline{I}_{AD_h}^{ht} \quad (8-281)$$

c. Hull and Tail at the Hull Center of Gravity, h

In Eq. 8-258, 8-263, 8-276 and 8-281 the acceleration dependent terms (subscript AD) are functions of the hull linear,  $\underline{V}_h$  and angular,  $\underline{\omega}_h$  acceleration. The force summation is:

$$\underline{F}_{HAD_h} = \underline{F}_{AD_h}^{hcv} + \underline{F}_{AD_h}^{ht} \quad (8-282)$$

Upon substituting Eq. 8-11, 8-13, 8-15 and 8-17 for the linear and angular accelerations there results:

ORIGINAL PAGE IS  
OF POOR QUALITY

$$\begin{aligned} \underline{E}_{HAD_h} &= (M_{hF_1} + M_{tF_1}) \underline{V}_h^o \\ &+ \left\{ -M_{hF_1} [R_h^{hcv} \times] - M_{tF_1} [R_h^{ht} \times] + K_{tF_1} \right\} \underline{\omega}_h^o \end{aligned} \quad (8-283)$$

$$= M_{11} \underline{V}_h^o + K_{12} \underline{\omega}_h^o \quad (8-284)$$

where use is made of the identities expressed in Eq. 2-66 through 2-69.

The moment summation about the center-of-gravity is given by:

$$\underline{T}_{HAD_h} = \underline{T}_{AD_h}^{hcv} + \underline{R}_h^{hcv} \times \underline{E}_{AD_h}^{hcv} + \underline{T}_{AD_h}^{ht} + \underline{R}_h^{ht} \times \underline{F}_{AD_h}^{ht} \quad (8-285)$$

Upon substituting in for the angular and linear velocities, the following expression results.

$$\begin{aligned} \underline{T}_{HAD_h} &= \left\{ [R_h^{hcv} \times] M_{hF_1} + [R_h^{ht} \times] M_{tF_1} + K_{tT_1} \right\} \underline{V}_h^o \\ &+ \left\{ I_{hT_1} + I_{tT_1} - [R_h^{hcv} \times] M_{hF_1} [R_h^{hcv} \times] \right. \\ &\quad \left. - [R_h^{ht} \times] M_{tF_1} [R_h^{ht} \times] - K_{tT_1} [R_h^{ht} \times] \right. \\ &\quad \left. + [R_h^{ht} \times] K_{tF_1} \right\} \underline{\omega}_h^o \end{aligned} \quad (8-286)$$

$$= K_{21} \underline{V}_h^o + I_{22} \underline{\omega}_h^o \quad (8-287)$$

ORIGINAL PAGE IS  
OF POOR QUALITY

These contributions to the aerodynamic loads of the hull assembly are subtracted from both sides of the equations of motion for the hull assembly. When coefficients are combined on the left hand side an effective 6 x 6 inertia matrix results:

$$[I^h]_h \begin{bmatrix} \ddot{\theta} \\ \dot{V}_h \\ \ddot{\omega}_h \end{bmatrix} = \underbrace{\begin{bmatrix} \underline{F}_{A_h} - \underline{F}_{HAD_h} \\ \underline{T}_{A_h} - \underline{T}_{HAD_h} \end{bmatrix}}_{\substack{\text{All aero} \\ \text{forces and} \\ \text{moments less} \\ \text{hull acceleration} \\ \text{dependent terms}}} + \begin{bmatrix} \text{All other} \\ \text{forces and} \\ \text{moments} \end{bmatrix} \quad (8-288)$$

where the effective inertia matrix is:

$$[I^h]_h = \begin{bmatrix} M & & & K_w \\ & & & \\ & & & \\ K_v & & & I \end{bmatrix} \quad (8-289)$$

and the individual 3 x 3 partitions are:

$$M = \begin{bmatrix} M_h & 0 & 0 \\ 0 & M_h & 0 \\ 0 & 0 & M_h \end{bmatrix} \quad -M_{11} \quad (8-290)$$

$$K_w = -K_{12} \quad (8-291)$$

$$K_v = -K_{21} \quad (8-292)$$

ORIGINAL PAGE IS  
OF POOR QUALITY

$$I = \begin{bmatrix} I_x & 0 & -I_{xz} \\ 0 & I_y & 0 \\ -I_{xz} & 0 & I_z \end{bmatrix} - I_{22} \quad (8-293)$$

and  $M_{11}$ ,  $K_{12}$ ,  $K_{21}$ , and  $I_{22}$  are given by the coefficients of  $\overset{o}{V}_h$  and  $\overset{o}{\omega}_h$  in Eq. 8-283 and 8-286.

Summarizing the above development, unsteady aerodynamic terms involving kinematic accelerations of the hull assembly do not appear explicitly in the righthand side force summation,  $\underline{F}$ , of Eq. 2-58. They are shifted to the left-hand side of Eq. 2-58 to facilitate solution for the acceleration vector,  $\overset{o}{V}$ . In this sense, these unsteady forces and moment terms appear as "apparent mass" effects because they increase the effective mass characteristics of the hull assembly portion,  $[I^h]_h$ , of the overall inertial mass matrix,  $M$ , in Eq. 258. However, they do not appear in the centrifugal or gravity terms of the applied force vector ( $\underline{F}$ ). Incorrect formulations have at times been obtained when attempts were made to simply augment inertial mass terms in aerodynamic equations of motion. Such a case was reported by Flax, Ref. 8-30, who correctly identified this source of confusion.

The remaining hull-tail assembly aerodynamic terms which do appear in  $\underline{F}$  of Eq. 2-58 are as follows. The hull-only right hand side force terms are given by

$$\underline{F}_{HAB}_h = \underline{F}_{SFGD}_h^{lcv} + \underline{F}_{B}_h^{hcv} \quad (8-294)$$

ORIGINAL PAGE IS  
OF POOR QUALITY

The corresponding moments about the hull center of gravity are:

$$\underline{T}_{HAB_h} = \underline{T}_{SFGD_h}^{hcv} + \underline{R}_h^{hcv} \times \underline{F}_{HAB_h} \quad (8-295)$$

The tail-only right hand side forces are:

$$\underline{F}_{TA_h} = \underline{F}_{SFGD_h}^{ht} \quad (8-296)$$

The corresponding moments (right hand side) are:

$$\underline{T}_{TA_h} = \underline{T}_{SFGD_h}^{ht} + \underline{R}_h^{ht} \times \underline{F}_{GD_h}^{ht} \quad (8-297)$$

$$+ \underline{R}_h^{hcv} \times \underline{F}_{QS_h}^{ht} + [\hat{\underline{R}}_{hcv}^{ht} \times] \underline{F}_{QS_h}^{ht}$$

where the effective moment arm adjustments of Eq. 8-i74 for the quasi-steady tail only forces have been accounted for.

The hull and tail right hand side terms are summed as follows. For the forces:

$$\underline{F}_{A_h} - \underline{F}_{HAD_h} = \underline{F}_{HAB_h} + \underline{F}_{TA_h} \quad (8-298)$$

For the moments:

$$\underline{T}_{A_h} - \underline{T}_{HAD_h} = \underline{T}_{HAB_h} + \underline{T}_{TA_h} \quad (8-299)$$

Equations 8-298 and 8-299 constitute the hull assembly aerodynamic force contribution to  $\underline{F}$  in Eq. 2-5<sup>a</sup>.

#### 4. Typical Hull/Tail Aerodynamic Characteristics During a Gust Encounter

A time history of the force component buildup is shown in Fig. 8-13 in order to illustrate the relative orders of magnitude of the various quasi-steady and unsteady aerodynamic contributions.

The vehicle is trimmed for a 44 ft/sec axial flight condition, with the control system disengaged (open-loop). At the start of the time history ( $t = 0$ ), the vehicle is subjected to an oblique up-gust, tuned to excite the natural oscillatory of pitch and roll motion (see Appendix C for an explanation of the oblique up-gust geometry).

The solid curve (C1) of Fig. 8-13 is the total hull/tail Z-force (excluding hull static buoyancy which is approximately cancelled by the vehicle weight) acting through the hull center of volume. This total force is comprised of the following components, also shown in the figure:

- C2 Quasi-steady hull and tail force; sum of quasi-steady components due to relative vehicle/airmass linear and angular velocities
- C3 Hull unsteady flow force; components due to relative hull/airmass linear and angular acceleration including buoyancy pressure gradient effects
- C4 Tail unsteady flow force; components due to relative tail/airmass linear and angular acceleration.
- C5 Total hull and tail unsteady flow force; sum of C3 and C4 showing the net contribution of vehicle unsteady flow forces to the total Z-force C1.

The results of Fig. 8-13 show that the hull and tail unsteady forces (C5) comprise a major fraction of the total z-force, C1, during the entire time history. In fact, for the present example, the quasi-steady contributions could be neglected entirely without incurring large

ORIGINAL PAGE IS  
OF POOR QUALITY

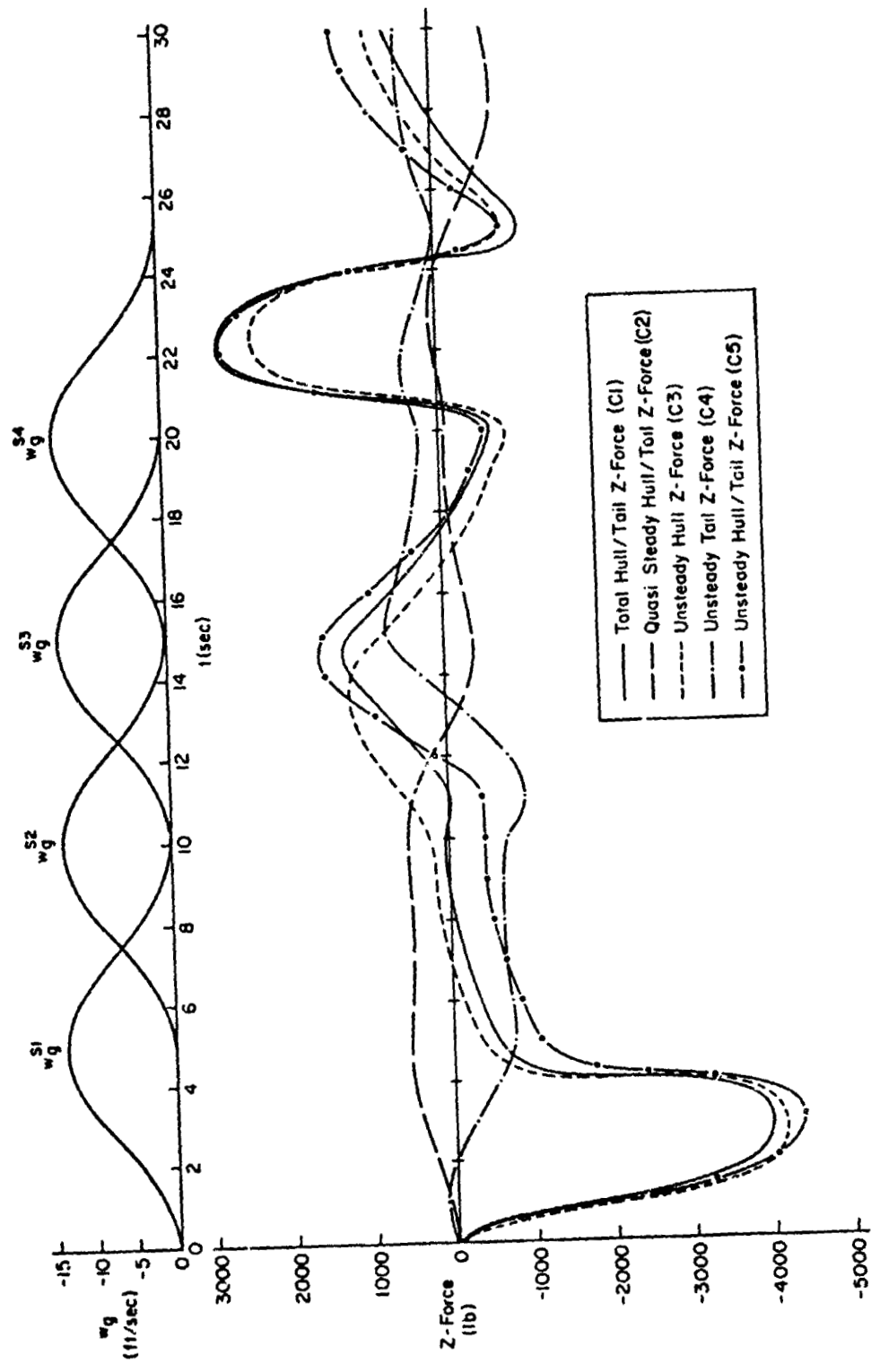


Figure 8-13. Time History of Aerodynamic Terms During an Oblique Up-Gust Encounter

errors. One implication is that, because circulation lag corrections are generally a small percentage of the quasi-steady forces (which are themselves small), the omission of these corrections is probably justified.

More importantly, structural loads are dominated by the unsteady flow forces. Design loads would be significantly underestimated if only quasi-steady force (C2) or gust (i.e., no gust accelerations) models were used. HLAs will be especially susceptible to the unsteady effects during mooring and stationkeeping operations. Previous authors (8-31) incorrectly estimated critical loads due to gusts when they ignored the effects of gust accelerations on vehicle buoyance and "apparent mass" loads.

## SECTION 9

### PAYLOAD AERODYNAMICS

#### A. BASIC ASSUMPTIONS

A review of several references concerning the aerodynamics of payload (cargo) containers and payload models for dynamic simulations was completed (Refs. 9-1, 9-2, and 9-3). References 9-2 and 9-3 describe static wind tunnel results and their use in piloted simulation models. Reference 9-1 discusses in detail static and dynamic payload aerodynamics models and their incorporation in numerical simulations.

The major conclusion to be drawn from the aerodynamic data of Ref. 9-2 is that payload (cargo container) wind tunnel data are highly configuration-sensitive, with strong asymmetries resulting from asymmetric vortex shedding and dependency on corner geometry and construction precision. The generic modeling of the extreme nonlinearity of the data would require many parameters to describe forces in the various flow regimes (analogous to the tail parameters  $\alpha_1$ ,  $\alpha_2$ , etc.). The extensive analyses conducted in Ref. 9-1 suggest that the typical payload limit cycle motion is not obtainable from numerical simulation without the incorporation of complex hysteresis models of the local flow field separation characteristics.

Because of the severe configuration dependency of typical payload aerodynamic data, a simple crossflow model has been adopted. Consistent with this approach, all interference effects on the payload are neglected. However, the software structure allows for the incorporation of more complex aerodynamic models that pertain to a specific payload geometry.

#### B. VELOCITIES RELATIVE TO THE LOCAL AIR MASS

The payload aerodynamic model depends on the linear and angular velocity vectors at the payload aerodynamic reference center (pc).

**ORIGINAL PAGE IS  
OF POOR QUALITY**

These vectors are determined from the inertial motion of the payload and the outputs from the atmospheric disturbance model. Following the sign convention adopted for air mass quantities (Section 5, Subsection B), the payload velocity vectors relative to the local air mass are given by:

$$\underline{v}_p^a \text{ pc} = \underline{v}_p^p \text{ pc} - \underline{v}_p^{\text{am pc}} \quad (9-1)$$

$$\underline{\omega}_p^a \text{ pc} = \underline{\omega}_p^p \text{ pc} - \underline{\omega}_p^{\text{am pc}} \quad (9-2)$$

where  $\underline{v}_p^{\text{am pc}}$ ,  $\underline{\omega}_p^{\text{am pc}}$  are given in Eqs. 6-58 and 6-59, respectively. The remaining unknown vectors in the above equations are determined from the rigid-body motion of the payload center of gravity ( $\underline{v}_p$ ,  $\underline{\omega}_p$ ) and the location of the payload aerodynamic reference center ( $\underline{R}_p^{\text{pc}}$ ):

$$\underline{v}_p^p \text{ pc} = \underline{v}_p + (\underline{\omega}_p \times \underline{R}_p^p \text{ pc}) \quad (9-3)$$

$$\underline{\omega}_p^p \text{ pc} = \underline{\omega}_p \quad (9-4)$$

and  $\underline{R}_p^p \text{ pc}$  is the vector that locates the payload aerodynamic reference center with respect to the payload center of gravity, Eq. 2-29.

### C. PAYLOAD AERODYNAMIC FORCES AND MOMENTS

The simplified payload aerodynamic model is directly analogous to that used for the hull. This model is suitable for payloads where the inertial forces dominate the aerodynamic forces and the x-axis is the slender axis of the payload with an associated low drag coefficient as compared with the y- and z-axis coefficients.

The static aerodynamic forces and moments follow directly from the quasi steady hull aerodynamics given in Section 8, Subsection D. The static aerodynamic forces and moments are given by:

ORIGINAL PAGE IS  
OF POOR QUALITY

$$\underline{I}_{SAp}^{p, pc} = \sigma \begin{bmatrix} X_u |u|_p & u|u| \\ Y_v |v|_p & v|v| \\ Z_w |w|_p & w|w| \end{bmatrix} \quad (9-5)$$

$$\underline{I}_{SAp}^{p, pc} = \sigma \begin{bmatrix} L_{vw} & vw \\ M_{uw} & uw \\ N_{uv} & uv \end{bmatrix} \quad (9-6)$$

where  $V_{yz} = \sqrt{v^2 + w^2}$  and the linear velocities are given by:

$$\begin{bmatrix} u \\ v \\ w \end{bmatrix}_{pc} = V_p^{a, pc} = \begin{bmatrix} v_p^{a, pc(1)} \\ v_p^{a, pc(2)} \\ v_p^{a, pc(3)} \end{bmatrix} \quad (9-7)$$

The dynamic moments are

$$\underline{I}_{DAp}^{p, pc} = \sigma \begin{bmatrix} L_p |p|_p & p|p| \\ M_q |q|_p & q|q| \\ N_r |r|_p & r|r| \end{bmatrix} \quad (9-8)$$

ORIGINAL PAGE IS  
OF POOR QUALITY

where

$$\begin{bmatrix} p \\ q \\ r \end{bmatrix}_{pc} = \omega_p^a pc = \begin{bmatrix} \omega_p^a pc(1) \\ \omega_p^a pc(2) \\ \omega_p^a pc(3) \end{bmatrix} \quad (9-9)$$

$X_u|u|_p$ ,  $Y_v|v|_p$ ,  $Z_w|w|_p$  are input parameters determined by the user. These are related to the conventional aerodynamic quantities according to the defining relations of Eqs. 8-69, 8-70, and 8-71, with the appropriate payload area and the corresponding payload drag coefficients.  $M_q|q|_p$  and  $N_r|r|_p$  are obtained from the analogous equations for the hull dynamic moments (Eq. 8-82), inserting the respective drag coefficients and geometry parameters. The dynamic rolling moment parameter,  $L_p|p|_p$ , can be calculated from strip theory but, like the hull, it is of negligible importance to the payload dynamics.

For typical cable geometries and cargo containers, the static rolling and pitching moments will be negligible in comparison to the cable moments about the payload center of gravity. These parameters have been set to zero in the input subroutines, although they appear in the payload aerodynamic subroutines should their future inclusion be desired. The static aerodynamic payload yawing moment parameter ( $N_{uvp}$ ) has been retained as a user input constant, since it will play an important role in determining the characteristic motion of the payload. This input constant is related to the conventional aerodynamic quantities according to the following defining equation:

$$N_{uv} = -\frac{\rho_0}{2} S_p l_p C N_B \quad (9-10)$$

where

$l_p, S_p$  are payload reference length and reference area, respectively

$C_{N\beta}$  is the payload state yawing moment derivative with respect to sideslip angle ( $\beta$ , radians)

The force and moment vectors at the payload aerodynamic center are summed according to:

$$\underline{F}_{A_p}^{p\ pc} = \underline{F}_{SA_p}^{p\ pc} \quad (9-11)$$

$$\underline{T}_{A_p}^{p\ pc} = \underline{T}_{SA_p}^{p\ pc} + \underline{T}_{DA_p}^{p\ pc} \quad (9-12)$$

They are then transferred to the payload center of mass:

$$\underline{F}_{A_p} = \underline{F}_{A_p}^{p\ pc} \quad (9-13)$$

$$\underline{T}_{A_p} = \underline{T}_{A_p}^{p\ pc} + \left( \underline{R}_{S_p}^{p\ pc} \times \underline{F}_{A_p}^{p\ pc} \right) \quad (9-14)$$

## SECTION 10

### TRIM STATE CALCULATIONS

#### A. OVERVIEW

The purpose of the trim function in the simulation programs is to calculate the required values of certain simulation variables, called controls, which establish a user-specified force and moment balance condition, called a trim state, in the independent degrees of motion freedom of the vehicle. When used as an initial condition in time history calculations, the trim state permits transient-free startup. It also serves as an operating point about which the stability and response derivatives are computed, see Section 11.

The three simulations have three different sets of controls and degrees of motion freedom. In the mooring simulation the controls are the three hull Euler angles; the trim state has zero Euler angle accelerations. This is the simplest trim function. The vehicle-alone simulation uses the six limited control input points as the controls. The trim state consists of specified Euler angles, Euler angle rates, and linear velocities relative to the airmass.

The most complex trim function is used for the vehicle-plus-slung-payload. Here the payload is trimmed first; the controls are the payload Euler angles and its location relative to the hull. The trim state is payload force and moment equilibrium at the specified Euler angles, Euler angle rates and linear velocities relative to the airmass of the hull. This trim establishes the cable tensions acting on the hull which are added to the remaining forces in calculating the six linked control inputs for the hull. The trim algorithm for this two-body simulation is in two stages.

The basic algorithm proceeds from an initial crude estimate of the control values needed for trim, and iteratively solves for the trim solution. Along the way it may encounter various limiting conditions

ORIGINAL PAGE IS  
OF POOR QUALITY

which are flagged to tell the simulation user of trim difficulties. These difficulties are usually of the sort where the trim algorithm runs out of control "power," e.g., calling for excessive rotor collective pitch. Other times they are due to one or another form of numerical difficulty, most typically encountered when spring forces figure prominently in the overall vehicle forces and moments.

**B. TRIM ALGORITHM**

The trim algorithm used in the simulation is a generalization of the second method for the solution of a simultaneous set of nonlinear algebraic equations. It is patterned after that used in Refs. 10-1, 10-2, and elsewhere. Its basic ideas can be illustrated with a single dimension example.

A solution is sought for the nonlinear algebraic equation

$$F(u) = 0 \quad (10-1)$$

for which there already exist two approximations,  $u_1$ , and  $u_2$ . The geometry is sketched in Fig. 10-1. When a secant is projected through the function evaluations  $F(u_1)$  and  $F(u_2)$ , it estimates a better approximation,  $u_{\text{new}}$ , given by:

$$\begin{aligned} u_{\text{new}} &= u_1 + F(u_1) \left( \frac{u_2 - u_1}{F(u_1) - F(u_2)} \right) \\ &= \frac{u_1 F(u_2) - u_1 F(u_1) - u_2 F(u_1) + u_1 F(u_1)}{F(u_1) - F(u_2)} \\ &= \left( \frac{F(u_2)}{F(u_2) - F(u_1)} \right) u_1 + \left( \frac{F(u_1)}{F(u_1) - F(u_2)} \right) u_2 \end{aligned} \quad (10-2)$$

This solution can then be tested for solution improvement, for formulating a new estimate, etc.

ORIGINAL PAGE IS  
OF POOR QUALITY

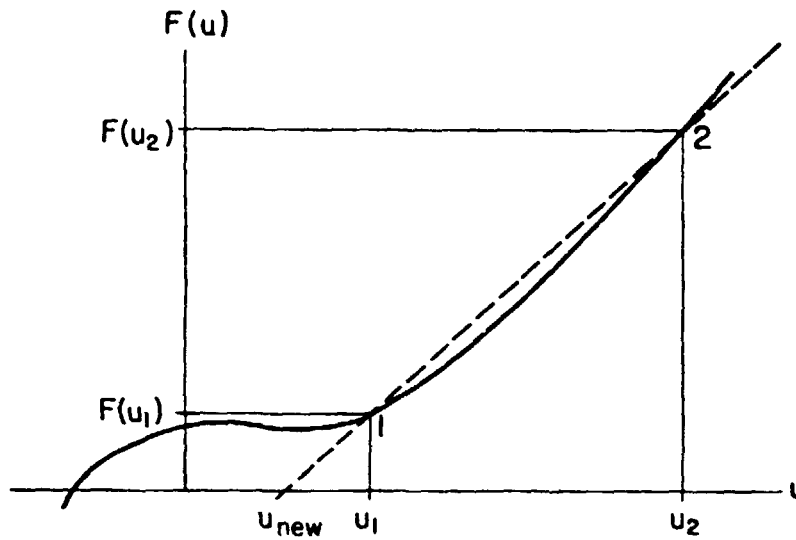


Figure 10-1. Sketch of Secant Approximation

The process can be formalized for the one dimensional case as follows. A solution vector,  $\underline{q} = [q_1 \ q_2]^T$  is sought to satisfy the simultaneous set of linear equations

$$\begin{aligned} q_1 F(u_1) + q_2 F(u_2) &= 0 \\ q_1 + q_2 &= 1 \end{aligned} \tag{10-3}$$

then predicting  $u_{\text{new}}$  according to

$$u_{\text{new}} = q_1 u_1 + q_2 u_2 \tag{10-4}$$

The problem that arises is that  $F(u_{\text{new}})$  may be greater than  $F(u_1)$  or  $F(u_2)$  or both. That is, too large a step is taken and the successive approximation algorithm implied earlier will fail to converge. To get around this, Eq. 10-3 is reformulated as

ORIGINAL PAGE IS  
OF POOR QUALITY

$$\begin{bmatrix} F(u_1) & F(u_2) \\ 1 & 1 \end{bmatrix} \begin{bmatrix} q_1 \\ q_2 \end{bmatrix} = \begin{bmatrix} (1-K)F_{\min} \\ 1 \end{bmatrix} \quad (10-5)$$

where  $F_{\min}$  is the smaller of the two evaluations, and equal to  $F(u_1)$  in the example sketch of Fig. 10-1. The solution vector is given by:

$$\begin{bmatrix} q_1 \\ q_2 \end{bmatrix} = \begin{bmatrix} \frac{(1-K)F_{\min} - F(u_2)}{F(u_2) - F(u_1)} \\ \frac{-(1-K)F_{\min} + F(u_1)}{F(u_2) - F(u_1)} \end{bmatrix} = \begin{bmatrix} \frac{(1-K)F(u_1) - F(u_2)}{F(u_2) - F(u_1)} \\ \frac{-(1-K)F(u_1) + F(u_1)}{F(u_2) - F(u_1)} \end{bmatrix} \quad (10-6)$$

$F_{\min}=F(u_1)$

As  $K$  approaches zero,  $q_1$  approaches 1 and  $q_2$  approaches zero. The resulting value of  $u_{\text{new}}$  (Eq. 10-4) approaches  $u_1$ . Thus the new estimate for  $u$  is close to that estimate,  $u_1$  in this example, which results in the smallest value of  $F(u)$ . The new approximation cannot "jump" far away from the better of the two previous approximations. For small  $K$ , the successive approximations slowly approach the desired answer.

However, the method can still fail if  $F(u)$  has a local minimum which is not a solution, e.g., as in Fig. 10-1. In this event, the iteration procedure must be restarted from a different set of initial approximations,  $u_1$  and  $u_2$ .

The foregoing process is extended to the multidimensional case as follows.  $\underline{F}(\underline{u})$  is now a multidimensional function vector of a multidimensional control vector  $\underline{u}$ ; the number of elements being the same for  $\underline{F}$  and  $\underline{u}$ . For the HLA vehicle-alone simulation  $\underline{F}$  has six elements:

$$\underline{F}(\underline{u}) = \begin{bmatrix} 0 & 0 & 0 & 0 & 0 & 0 \\ u & v & w & p & q & r \end{bmatrix}_h^T \quad (10-7)$$

ORIGINAL PAGE IS  
OF POOR QUALITY

The control vector corresponds to the six linked controls:

$$\underline{u} = [\dot{u}_c \dot{v}_c \dot{w}_c \dot{p}_c \dot{q}_c \dot{r}_c]^T \quad (10-8)$$

For the given trim condition specification (HLA velocity, altitude, attitude, etc.), a value of  $\underline{u}$  is calculated which approximates setting  $\underline{F}$  to zero. In the program this estimate is very crude in order to avoid a requirement for a configuration-dependent or a user-supplied initial estimate. Then six additional  $\underline{u}$ 's are computed by successively multiplying each element of  $\underline{u}$  by a small constant,  $K \ll 1$ . This results in a significant departure from the first estimate along each of the six control "coordinates." If the element is already zero, it is set to  $K$ .\*

For each of the seven values of  $\underline{u}$  which result, the corresponding function vector,  $\underline{F}$  is calculated. To assess the relative magnitude of these vector functions, a modified Euclidean norm is calculated according to:

$$S(\underline{u}) = \frac{F_1(\underline{u})^2}{10} + \frac{F_2(\underline{u})^2}{10} + \frac{F_3(\underline{u})^2}{10} \\ + F_4(\underline{u})^2 + F_5(\underline{u})^2 + F_6(\underline{u})^2 \quad (10-9)$$

where  $F_1$ ,  $F_2$ , and  $F_3$  are the HLA linear accelerations and  $F_4$ ,  $F_5$ , and  $F_6$  are the angular accelerations. The factor of 10 means that 1 ft/sec<sup>2</sup> (or 1 meter/sec<sup>2</sup>) is weighted the same as 1 rad/sec<sup>2</sup> in angular acceleration. The norms,  $S(\underline{u})$  are used to order the  $\underline{F}(\underline{u})$  from  $\underline{F}_{\min}$  to  $\underline{F}_{\max}$ .

---

\*K = 0.001 in the program.

Then a system of equations is set up:

$$\begin{bmatrix} F_1(\underline{u}_1) & F_1(\underline{u}_2) & \dots & F_1(\underline{u}_7) \\ F_2(\underline{u}_1) & F_2(\underline{u}_2) & \dots & F_2(\underline{u}_7) \\ \cdot & \cdot & \dots & \cdot \\ \cdot & \cdot & \dots & \cdot \\ \cdot & \cdot & \dots & \cdot \\ F_6(\underline{u}_1) & F_6(\underline{u}_2) & \dots & F_6(\underline{u}_7) \\ 1 & 1 & \dots & 1 \end{bmatrix} \begin{bmatrix} q_1 \\ q_2 \\ \cdot \\ \cdot \\ \cdot \\ \cdot \\ q_7 \end{bmatrix} = \begin{bmatrix} (1-K)F_{1_{\min}} \\ (1-K)F_{2_{\min}} \\ \cdot \\ \cdot \\ \cdot \\ (1-K)F_{6_{\min}} \\ 1 \end{bmatrix} \quad (10-10)$$

where the elements on the right-hand side are taken from the  $F(\underline{u})$  corresponding to the minimum value of  $S(\underline{u})$ , the modified Euclidean norm. The solution for  $\underline{q}$  is used to estimate a better value of  $\underline{u}$  according to:

$$\underline{u}_{\text{new}} = \sum_{j=1}^7 q_j \underline{u}_j \quad (10-11)$$

The new estimate,  $\underline{u}_{\text{new}}$ , is used to calculate  $F(\underline{u}_{\text{new}})$  and  $S(\underline{u}_{\text{new}})$ . The norm is used to make decisions on how to proceed:

- a) If  $S_{\text{new}} > S_{\text{max}}$ , then the step was too large. Cut  $K$  in half and resolve for  $\underline{q}$ .
- b) If  $S_{\text{new}} < S_{\text{max}}$ , then  $\underline{u}_{\text{new}}$  represents an improvement over  $\underline{u}_{\text{max}}$ . Replace the corresponding column on the left-hand side of Eq. 10-10; replace the right-hand side as well if  $S_{\text{new}} < S_{\text{min}}$ , and resolve for  $\underline{q}$ ; double the value of  $K$  (up to a maximum of 1.0) each time two successive improvements in the trim solution are made.

As the successive approximation process proceeds, the successive values of  $F(\underline{u})$  are tested against a preset tolerance for trim. If  $K$  becomes less than some present  $K_{\text{min}}$ , a local minimum has been found and the process is restarted using the best value of  $\underline{u}$  (corresponds to  $S_{\text{min}}$ ) determined up to the time the restart decision is made.

### C. SPECIAL SITUATIONS

The trim calculation will flag the occurrence of limiting in the control variables. For the vehicle, this corresponds to limiting in the rotor cyclics or collectives, the propeller collectives, or the tail fin deflections. For the payload, it corresponds to cables going slack — a function of the geometry — see the User's Manual, Section 7.

The reader will recognize that the occurrence of one of the conditions does not necessarily mean a physically unrealizable state. What it usually does mean is the close approach to an untrimmable state, certainly a state where it would be impractical to trim the vehicle because of the proximity to control saturation about at least one axis. It also implies a requirement for a configuration-dependent limit-detecting algorithm if partial limiting in the controls is to be allowed. Such complication was not felt to be warranted, besides being impractical in a general, as opposed to specific, vehicle simulation.

The mooring simulation represents a special case in a number of ways. For one thing, there are generally three equilibrium heading angles caused by the fact that most hull configurations are unstable in yaw at zero yaw angle relative to the wind. Zero yaw angle corresponds to a point of unstable equilibrium. The other two points are stable equilibrium points and occur at yaw angles on either side of zero. The program will converge to one or the other of these when the user enters an appropriate initial guess for the yaw angle as part of the trim state specification.

In zero wind mooring there is no yaw constraint, and the user must specify a heading. For this condition the program inserts an artificial yaw spring so that the same three-controller version of the trim algorithm can be used. However, if there is a single, off-center landing gear touching the ground, the vehicle will adopt a yaw deflection against this spring — an artificial trim state. Off-center single landing gear locations are not allowed in the mooring simulation in the no-wind condition.

## SECTION 11

## LINEARIZATION

## A. OVERVIEW

The simulation programs include a set of routines for linearizing the motion equations of the vehicle exclusive of its flight control system feedbacks. These equations describe the open-loop dynamics (i.e., no flight control system loops closed) of small motion perturbations about a selected operating point or trim condition. They are useful for various linear systems analyses, in particular for the synthesis of flight control laws.

The equations consist of a simultaneous set of first-order differential equations of motion and a set of auxiliary equations for certain dependent variables. In addition, the eigenvalues and eigenvectors of the system can be computed as a quick check of the characteristic modes of vehicle response. The primary purpose of the routines is to provide data for the user's own linear systems analysis routines.

## B. EQUATIONS OF MOTION

The linearized equations of motion are given by:

$$\dot{\underline{u}} = A\underline{u} + B'\underline{u}_{lc} + B\underline{u}_c + C\underline{u}_g \quad (11-1)$$

where the various vectors differ for each of the three simulations:

1) State vector,  $\underline{u}$ 

## a) HLASIM

$$\underline{u} = \begin{bmatrix} \underline{V}_h & \underline{\omega}_h & \underline{R}_I^h & \underline{n}_I^h \end{bmatrix}^T \quad (11-2)$$

ORIGINAL PAGE IS  
OF POOR QUALITY

b) HLAPAY

$$\underline{u} = \left[ \underline{v}_h \quad \underline{\omega}_h \quad \underline{R}_I^h \quad \underline{D}_I^h \quad \underline{v}_p \quad \underline{\omega}_p \quad \underline{R}_h^p \quad \underline{D}_I^p \right]^T \quad (11-3)$$

c) HLAMOR

$$\underline{u} = \left[ \underline{\omega}_h \quad \underline{D}_I^h \right]^T \quad (11-4)$$

2) Linked control vector,  $\underline{u}_{\ell c}$  (HLASIM and HLAPAY only)

$$\underline{u}_{\ell c} = \left[ \dot{u}_c \quad \dot{v}_c \quad \dot{w}_c \quad \dot{p}_c \quad \dot{q}_c \quad \dot{r}_c \right]^T \quad (11-5)$$

3) Control vector,  $\underline{u}_c$  (HLASIM and HLAPAY only)

$$\underline{u}_c = \left[ u_c^1 \quad u_c^2 \quad u_c^3 \quad u_c^4 \quad u_c^t \right]^T \quad (11-6)$$

where for  $i = 1, 2, 3, 4$ , (LPU controls):

$$\underline{u}_c^i = \left[ \theta_{or}(i) \quad A_{1s}(i) \quad B_{1s}(i) \quad \Omega_r(i) \quad \theta_{op}(i) \quad \Omega_p(i) \right]^T \quad (11-7)$$

and (tail surface controls):

$$\underline{u}_c^t = \left[ \delta_A \quad \delta_E \quad \delta_R \right]^T \quad (11-8)$$

4) Disturbance vector,  $\underline{u}_g$

a) HLAPAY

$$\underline{u}_g = \left[ \begin{array}{cccccc} \underline{v}_h^{sam \ cv} & \underline{\omega}_h^{sam \ cv} & \dot{\underline{v}}_h^{sam \ cv} & \dot{\underline{\omega}}_h^{sam \ cv} & \underline{\omega}_{hgrad}^{sam \ cv} & \\ \underline{v}_h^{sam \ t} & \underline{\omega}_h^{sam \ t} & \dot{\underline{v}}_h^{sam \ t} & \dot{\underline{\omega}}_h^{sam \ t} & \underline{\omega}_{hgrad}^{sam \ t} & \\ \underline{v}_1^{sam1} & \underline{v}_2^{sam2} & \underline{v}_3^{sam3} & \underline{v}_4^{sam4} & \underline{v}_p^{sam \ pc} & \underline{\omega}_p^{sam \ pc} \end{array} \right]^T \quad (11-9)$$

## ORIGINAL NAME IS OF POOR QUALITY

where the gradient vectors are given by:

$$\underline{\omega}_{\text{grad}}^{\text{sam cv}} = \left[ \begin{array}{ccc} \frac{\partial u_h^{\text{sam cv}}}{\partial x} & \frac{\partial u_h^{\text{sam cv}}}{\partial y} & \frac{\partial v_h^{\text{sam cv}}}{\partial y} \end{array} \right]^T \quad (11-10)$$

$$\underline{\omega}_{\text{grad}}^{\text{sam t}} = \left[ \begin{array}{ccc} \frac{\partial u_h^{\text{sam t}}}{\partial x} & \frac{\partial u_h^{\text{sam t}}}{\partial y} & \frac{\partial v_h^{\text{sam t}}}{\partial y} \end{array} \right]^T \quad (11-11)$$

- b) HLASIM and HLAMOR — same as HLAPAY, deleting payload gust inputs,  $\underline{v}_p^{\text{sam pc}}$  and  $\underline{\omega}_p^{\text{sam pc}}$

In Eq. 11-1, the A matrix is the characteristic matrix of stability derivatives for the vehicle. For the HLAMOR simulation it is a 6 x 6; for HLASIM, 12 x 12; and for HLAPAY, 24 x 24.

The B', B, and C matrices have dimensions corresponding to the size of the state vector, the two control vectors, and the gust vector. Thus the C matrix of response derivatives for the HLAPAY simulation is 24 rows by 48 columns, whereas the B' matrix for HLASIM is 12 rows x 6 columns. The B' and B matrices for HLAMOR are null matrices — no controls in this simulation.

### C. AUXILIARY EQUATIONS

The auxiliary equations relate a selected set of dependent variables to the state vector, the control vectors, and the gust vector. In the three programs, certain of the loads internal to the vehicle are chosen. The load vector is symbolized by  $\underline{F}$ . The auxiliary matrix equation is:

$$\underline{F} = A_a \underline{u} + B'_a \underline{u}_c + B_a \underline{u}_c + C_a \underline{u}_g \quad (11-12)$$

where  $A_a$ ,  $B'_a$ ,  $B_a$ , and  $C_a$  are auxiliary matrices of response derivatives of column dimensions depending on the dimensions of  $\underline{u}$ ,  $\underline{u}_c$ ,  $\underline{u}_c$ , and  $\underline{u}_g$  in the three simulations. The row dimension depends upon the selected elements in  $\underline{F}$ . Thus:

ORIGINAL PAGE IS  
OF POOR QUALITY

1) For HLASIM,

$$\underline{F} = [\underline{F}_{C_h}^{h1} \quad \underline{T}_{C_h}^{h1} \quad \underline{F}_{C_h}^{h2} \quad \underline{T}_{C_h}^{h2} \quad \underline{F}_{C_h}^{h3} \quad \underline{T}_{C_h}^{h3} \quad \underline{F}_{C_h}^{h4} \quad \underline{T}_{C_h}^{h4}]^T \quad (11-15)$$

Here  $\underline{F}$  is the column vector of constraint forces and moments acting on the hull at the four LPU attach points.  $\underline{F}$  has 24 elements for HLASIM.

2) For HLAPAY -- Same as above, adding the cable force magnitude,  $F_{jk}$ ,  $j = k = 1, 2, 3, 4$  (four elements), making 28 elements in all.

3) For HLAMOR -- Same as for HLASIM, adding the landing gear axial force magnitudes,  $F_{gh}^{hg}$  (3), superscript  $g = 1, 2, 3, 4$  (four elements), also making 28 elements in all for  $\underline{F}$ .

For analyzing the vehicle-alone gust response, it is sometimes more useful to use a vector composed of the three gust components at each of the four gust sources -- a twelve-element vector. The relationship between this vector and  $\underline{u}_g$  defined above for HLASIM is obtained through the use of a post-processing routine, see the User's Manual (Vol. III), Section 10.

### 3. DERIVATIVE APPROXIMATION

All of the matrix elements are partial derivatives of a left-hand column vector element (element of  $\underline{u}$  or  $\underline{F}$ ) with respect to an element of the pertinent right-hand side vector (element of  $\underline{u}$ ,  $\underline{u}_{\ell_c}$ ,  $\underline{u}_c$  or  $\underline{u}_g$ ), holding all other variables fixed at the operating point condition. The derivatives are approximated by incrementing the left-hand side vector element forward and backward, differencing these two values, and dividing by two times the increment:

$$\frac{\partial f_i}{\partial u_j} \approx \frac{f_i(u_j + \Delta u) - f_i(u_j - \Delta u)}{2\Delta u} \quad (11-14)$$

where  $f_i$  is an element of  $\dot{\underline{u}}$  or  $\ddot{\underline{x}}$  and  $u_j$  is an element of  $\underline{u}$ ,  $\underline{u}_c$ ,  $\underline{u}_g$ , or  $\underline{u}_g$ ).

The size of the increment is set within the program source codes. The current version increments linear velocities, linear positions, and gust gradient terms by 0.014 ft./sec., ft., or rad. All angular velocities and angles except cyclic deflections are incremented by 0.008 rad/sec or rad. The cyclic deflection,  $A_{1s}$  and  $B_{1s}$ , are incremented by 0.0525 rad.

The program also checks for pronounced nonlinearities in the vicinity of the point about which the derivative is estimated, see the User's Manual, Section 10.

#### **E. EIGENVALUES AND EIGENVECTORS**

An IMSL library routine is used for calculating the eigenvalues and eigenvectors of the A matrix, see the User's Manual, Section 10. The eigenvalues are listed in terms of the real and imaginary parts of a complex number. They correspond to the roots of the characteristic equation of the vehicle. The eigenvectors are also complex numbers, in general, and are listed for each eigenvalue and state variable. These numbers correspond to the modal response coefficients for the system.

REFERENCES

Section 2

- 2-1. Etkin, B., Dynamics of Atmospheric Flight, John Wiley & Sons, Inc., N.Y., 1972.

Section 5

- 5-1. Etkin, B., "The Turbulent Wind and Its Effect on Flight," UTIAS Review No. 44, Aug. 1980 (AIAA 1980 Wright Bros. Lecture; summarized in AIAA Paper 80-1826).
- 5-2. Skelton, G. B., Investigation of the Effects of Gusts on V/STOL Craft in Transition and Hover, AFFDL-TR-68-85, Oct. 1968.
- 5-3. Bryson, A. E., Jr., and W. B. Holley, Wind Modeling and Lateral Aircraft Control for Automatic Landing, Stanford Univ., SUDAAR 489, Jan. 1975.
- 5-4. Heffley, R. K., W. F. Jewell, et al., Atmospheric Disturbance Models and Requirements for the Flying Qualities Military Standard and Handbook, AIAA-81-0302, Nov. 1980.
- 5-5. Nielsen, J. N., O. J. McMillan, S. C. McIntosh, Jr., et al., Feasibility Study of Modern Airships, Phase II, Vol. I: Heavy Lift Airship Vehicle. Book III: Aerodynamic Characteristics of Heavy Lift Airship as Measured at Low Speeds, NASA CR-151919, Sept. 1976.
- 5-6. Unpublished memoranda furnished to Systems Technology, Inc., by Nielsen Engineering Research, Inc.
- 5-7. Keys, C. N., and W. Z. Stephniewski, Rotary-Wing Aerodynamics. Vol. 2: Performance Prediction of Helicopters NASA CR-3083, Jan. 1979.
- 5-8. Silverstein, Abe, and B. G. Gulick, Ground-Handling Forces on a 1/40-Scale Model of the U.S. Airship "Akron", NACA Rept. No. 566, 1936.
- 5-9. Heyson, Harry H., Theoretical Study of the Effect of Ground Proximity on the Induced Efficiency of Helicopter Rotors, NASA TMX-79151, May 1977.
- 5-10. McCormick, B. W. Aerodynamics, Aeronautics, and Flight Dynamics, John Wiley & Sons, Inc., New York, 1979.
- 5-11. Hoerner, Sighard F., and H. V. Borst, Fluid-Dynamic Lift, Hoerner Fluid Dynamics, New Jersey, 1975.

Section 7

- 7-1. Bramwell, A. R. S., Helicopter Dynamics, John Wiley & Sons, New York, 1976.
- 7-2. Heyson, Harry H., Theoretical Study of the Effect of Ground Proximity on the Induced Efficiency of Helicopter Rotors, NASA TM X-71951, May 1977.
- 7-3. Gessow, Alfred and Garry C. Myers, Jr., Aerodynamics of the Helicopter Frederick Ungar Publishing Co., New York, 1952.
- 7-4. Heyson, Harry H., Ground Effect for Lifting Rotors in Forward Flight, NASA TN D-234, May 1960.
- 7-5. Nielsen, J. N., O. J. McMillan, S. C. McIntosh, Jr., et al., Feasibility Study of Modern Airships, Phase II, Vol. I: Heavy Lift Airship Vehicle. Book III: Aerodynamic Characteristics of Heavy Lift Airship as Measured at Low Speeds, NASA CR-151919, Sept. 1976.
- 7-6. Talbot, Peter D., and Lloyd D. Corliss, A Mathematical Force and Moment Model of a UH-1H Helicopter for Flight Dynamics Simulations, NASA TM 73,254, June 1977.
- 7-7. Seckel, Edward Stability and Cont. of Airplanes and Helicopters, Academic Press, New York, 1964.
- 7-8. Hoerner, Sigward F., and H. V. Borst, Fluid-Dynamic Lift, Hoerner Fluid Dynamics, Brick Town, N.J., 1975.

Section 8

- 8-1. Nielsen, J. N., O. J. McMillan, S. C. McIntosh, Jr., et al., Feasibility Study of Modern Airships, Phase II, Vol. I: Heavy Lift Airship Vehicle. Book III: Aerodynamic Characteristics of Heavy Lift Airship as Measured at Low Speeds, NASA CR-151919, Sept. 1976.
- 8-2. Unpublished memoranda furnished to Systems Technology, Inc., by Nielsen Engineering Research, Inc.
- 8-3. Silverstein, Abe, and B. G. Gulick, Ground-Handling Forces on a 1/40-Scale Model of the U.S. Airship "AKRON", NACA Rept. No. 566, 1936.
- 8-4. Spangler, S. B., and C. A. Smith, Theoretical Study of Hull-Rotor Aerodynamic Interference on Semibuoyant Vehicles, NASA CR-152127, Apr. 1978.
- 8-5. Kuethe, A. M., and J. D. Schetzler, Foundations of Aerodynamics, John Wiley & Sons, Inc., New York, Second Edition, 1959.

ORIGINAL PAGE IS  
OF POOR QUALITY

- 8-6. Hoerner, S. F., Fluid Dynamic Lift, published by author, 1975.
- 8-7. Hoerner, S. F., Fluid Dynamic Drag, published by author, 1965.
- 8-8. Curtiss, H. C., Jr., Hazen, D. C., and Putman, W. F., "LTA Aerodynamic Data Revisited," AIAA Paper 75-951, July 1975.
- 8-9. Nielsen, J. N., "Missile Aerodynamics — Past, Present, Future," J. Aircraft, Vol. 17, No. 3, May-June 1980, pp. 165-176.
- 8-10. Munk, M. M., The Aerodynamic Forces on Airship Hulls, NACA Rept. 184, 1924.
- 8-11. Zahm, A. F., Flow and Force Equations for a Body Revolving in a Fluid, NACA Rept. 323, 1929.
- 8-12. Allen, H. Julian, and Edward W. Perkins, A Study of Effects of Viscosity on Flow Over Slender Inclined Bodies of Revolution, NACA TN 2044, 1951.
- 8-13. Zahm, A. F., R. H. Smith, and F. A. Loudon, Air Forces, Moments and Damping on Model of Fleet Airship Shenandoah, NACA Rept. 215, 1925.
- 8-14. Bramwell, A. R. S., Helicopter Dynamics, John Wiley & Sons, New York, 1976.
- 8-15. McCormick, Barnes, W., Aerodynamics, Aeronautics, and Mechanics, Flight Dynamics, John Wiley & Sons, New York, 1979.
- 8-16. Neilsen, Jack N., Missile Aerodynamics, New York, McGraw-Hill, 1960.
- 8-17. Schlichting, Hermann and Erich Truckenbrodt, Aerodynamics of the Airplane, McGraw-Hill, Inc., 1979.
- 8-18. Jones, R., and A. H. Bell, Experiments on a Model of the Airship R.101, ARC R&M 1168, Sept. 1926.
- 8-19. Freeman, H. B., Force Measurements on a 1/40-Scale Model of the U.S. Airship "Akron", NACA Rept. 432, 1982.
- 8-20. Abbott, I. H., Airship Model Tests in the Variable Density Wind Tunnel, NACA Rept. 394, 1931.
- 8-21. Dempsey, E. M., Static Stability Characteristics of a Systematic Series of Stern Control Surfaces on a Body of Revolution, DWT HSRDC Rept. 77-0085, 1977.
- 8-22. Humphreys, D. E., and K. W. Watkinson, Prediction of Acceleration Hydrodynamic Coefficients for Underwater Vehicles from Geometric Parameters, NCSL TR 327-78, Feb. 1978.

- 8-23. Etkin, Bernard, Dynamics of Flight, New York, Wiley, 1959.
- 8-24. Kelvin, Lord, "On the Motion of Rigid Solids Circulating Irrrotationally Through Perforations in Them or in a Fixed Solid," Phil. Mag., May 1873.
- 8-25. Lamb, Sir Horace, Hydrodynamics, Dover, New York, 1945.
- 8-26. Munk, M. M., The Aerodynamic Forces on Airship Models, NACA Rept. 184, 1924.
- 8-27. Imlay, F. H., The Complete Expressions for "Added Mass" of a Rigid Body Moving in an Ideal Fluid, DTMB Rept. 1528, 1961.
- 8-28. Wendel, Kurt, Hydrodynamic Masses and Hydrodynamic Moments of Inertia, David W. Taylor Model Basin Translation 260, July 1956.
- 8-29. Malvestuto, Frank S. Jr., and Lawrence J. Gale, Formulas for Additional-Mass Corrections to the Moments of Inertia of Airplanes, NACA TN 1187, Feb. 1947.
- 8-30. Abbott, I. H., Airship Model Tests in the Variable Density Wind Tunnel, NACA Rept. 394, 1931.
- 8-31. Calligeros, J. M., and McDavitt, P. W., Response and Loads on Airships Due to Discrete and Random Gusts, MIT, ASRL TR 72-1, Feb. 1958.

Section 9

- 9-1. Sampath, Prasad, Dynamics of a Helicopter-Slung Load System, Ph.D. Thesis, U. of Maryland, 1980.
- 9-2. Laub, G. H., and H. M. Kodani, Wind Tunnel Investigation of Aerodynamic Characteristics of Scale Models of Three Rectangular Shaped Cargo Containers, NASA TM S-62,169, 1972.
- 9-3. Shaughnessy, J. D., et al., Development and Validation of a Piloted Simulation of a Helicopter and External Sling Load, NASA TP 1285, 1979.

Section 10

- 10-1. Houck, Jacob A., Lucille H. Gibson, George G. Steinmetz, A Real-Time Digital Computer Program for the Simulation of a Single-Rotor Helicopter, NASA TM X-2872, June 1972.
- 10-2. Burrows, Roger R. and Gary A. McDaniel, "A Method of Trajectory Analysis with Multi-Mission Capability and Guidance Application," AIAA Paper No. 68-844, Aug. 1968.

## APPENDIX A

### REFERENCES FOR AERODYNAMIC INPUTS

This appendix is a cross-reference of experimental and analytical sources for the calculation of the hull and tail aerodynamic inputs. In some cases the cited reference does not relate directly to the specific parameter, but rather provides guidance for estimating an input quantity based on data for other vehicles. An excellent reference which should be consulted for more detailed estimation methods is the Air Force Stability and Control Data, "DATCOM," by D. E. Hook and R. D. Finck. Volume IV contains a table of default input values. These default values are not automatically selected by the computer, but rather are user loaded into the data files as normal inputs to eliminate the otherwise uncertain aerodynamic terms.

CREATED BY  
OF POOR QUALITY

ENGINEERING SYMBOL	VARIABLE NAME	DEFINING EQUATION	REFERENCES
$X_{uh}^o$	XUDOTH	8-203	A-1, A-2, A-3
$Y_{vh}^o$	YVDOTH	8-206	A-1, A-2, A-3
$Z_{wh}^o$	ZWDOTH	8-209	A-1, A-2, A-3
$L_{ph}^o$	LPDOTH	8-213	A-1, A-2, A-3
$M_{qh}^o$	MQDOTH	8-226	A-1, A-2, A-3
$N_{rh}^o$	NRDOTH	8-229	A-1, A-2, A-3
$Y_{vt}^o$	YVDOTT	8-233	A-1, A-2, A-4, A-5
$Z_{wt}^o$	ZWDOTT	8-234	A-1, A-2, A-4, A-5
$L_{vt}^o$	LVDOTT	8-235	A-1
$L_{pt}^o$	LPDOTT	8-235	A-1, A-2, A-4, A-5
$M_{qt}^o$	MQDOTT	8-236	A-1, A-2, A-4, A-5
$N_{rt}^o$	NRDOTT	8-237	A-1, A-2, A-4, A-5
$X_u u h$	XUUABH	8-68	A-6, A-7, A-8, A-9
$X_{qwh}$	XQWH	8-204	A-1, A-2, A-3
$X_{rvh}$	XR VH	8-205	A-1, A-2, A-3
$Y_v v h$	YVVABH	8-69	A-8, A-10

ENGINEERING SYMBOL	VARIABLE NAME	DEFINING EQUATION	REFERENCES
$Y_{r r h}$	YRRABH	8-87	A-1, A-2, A-3
$Y_{ruh}$	YRUH	8-208	A-1, A-2, A-3
$Y_{r v h}$	YRVABH	8-87	A-8, A-10 ORIGINAL PAGE IS OF POOR QUALITY
$Z_{q q h}$	ZQQABH	8-87	
$Z_{pvh}$	ZPVH	8-210	A-1, A-2, A-3
$Z_{quh}$	ZQUH	8-211	A-1, A-2, A-3
$Z_{q w h}$	ZQWABH	8-87	
$L_{p p h}$	LPPABH	8-85	
$L_{p u h}$	LPUABH	8-85	
$L_{vwh}$	LVWH	8-76	A-1, A-2, A-3, A-8, A-11
$L_{qrh}$	LQBRH	8-224	A-1, A-2, A-3
$L_{rqh}$	LRBQH	8-225	A-1, A-2, A-3
$M_{q q h}$	MQQABH	8-84	Eqn. 8-82, A-9
$M_{uwh}$	MUWH	8-77	A-1, A-2, A-3, A-7, A-8, A-9, A-11
$M_{rph}$	MRBPH	8-227	A-1, A-2, A-3

ORIGINAL PAGE IS  
OF POOR QUALITY

ENGINEERING SYMBOL	VARIABLE NAME	DEFINING EQUATION	REFERENCES
$M_{prh}^-$	MPBRH	8-228	A-1, A-2, A-3
$M_{q w h}$	MQWABH	8-84	Eq. 8-83, A-9
$N_{r r h}$	NRRABH	8-86	Eq. 8-82, A-9
$N_{uvh}$	NUVH	8-78	A-1, A-2, A-3, A-7, A-8, A-9, A-11
$N_{p^c h}^-$	NPBQH	8-230	A-1, A-2, A-3
$N_{q^p h}^-$	NQBPH	8-231	A-1, A-2, A-3
$N_{r v h}$	NRVABH	8-86	Eq. 8-83, A-9
$X_{u u t}$	XUUABT	8-137	A-6, A-7, A-8, A-9
$Y_{v v t}$	YVVABT	8-143	A-7, A-8, A-10
$Y_{p p t}$	YPPABT	8-142	A-7, A-8, A-10
$Y_{a_p v_t}^2$	YAPVST	8-140	A-6, A-8, A-10, A-12, A-13
$Y_{B v_t}^2$	YBVSQT	8-138	A-6, A-8, A-10, A-11, A-12, A-13
$Y_{B v_t}^2$	YBSVST	8-139	A-6, A-8, A-10, A-12, A-13
$Y_{a_p v_t}^2$	YAPSVS	8-141	A-6, A-8, A-10, A-12, A-13
$Z_{w w t}$	ZWWABT	8-146	A-7, A-8, A-10

ENGINEERING SYMBOL	VARIABLE NAME	DEFINING EQUATION	REFERENCES
$Z_{\alpha} v_t^2$	ZAVSQT	8-144	A-6, A-8, A-10, A-11, A-12
$Z_{\alpha}^2 v_t^2$	ZASVST	8-145	A-6, A-8, A-10
$L_v  v _t$	LVVABT	8-66	A-7, A-8, A-10
$L_p  p _t$	LPPABT	8-156	A-7, A-8, A-10
$L_{\alpha p} v_t^2$	LAPVST	8-154	A-8, A-10, A-12
$L_{\beta} v_t^2$	LBVSQT	8-164	A-6, A-8, A-10, A-12
$L_{\beta \alpha} v_t^2$	LBAVST	8-165	A-10, A-12
$L_{\alpha p}^2 v_t^2$	LAPSVS	8-155	A-8, A-10, A-12
$\lambda_{xc_t}$	LAMIXQ	8-171	A-6, A-8, A-9, A-10, A-11, A-12, A-13
$\lambda_{xr_t}$	LAMTXR	8-171	A-6, A-7, A-8, A-9, A-10, A-11, A-12, A-13
$\lambda_{zq_t}$	LAMTXQ	8-171	A-6, A-8, A-9, A-10, A-11, A-12, A-13
$\alpha_1$	AL1T	Table 8-1	A-10, A-18
$\alpha_2$	AL2T	Table 8-1	A-10, A-18
$\beta_1$	BETA1T	Table 8-1	A-10, A-18
$\beta_2$	BETA2T	Table 8-1	A-10, A-18

ORIGINAL PAGE IS  
OF POOR QUALITY

ENGINEERING SYMBOL	VARIABLE NAME	DEFINING EQUATION	REFERENCES
$\alpha_{p1}$	ALP1T	Table 8-1	A-10, A-18
$\alpha_{p2}$	ALP2T	Table 8-1	A-10, A-18
$\tau_a$	TAUA	8-94	A-10, A-11, A-12, A-14
$\tau_e$	TAUE	8-92	A-10, A-11, A-12, A-14
$\tau_r$	TAUR	8-93	A-10, A-11, A-12, A-14
$\beta 1^r$	BWK1R1 BWK1R2 BWK1R3 BWK1R4	7-14	A-8, A-15
$\beta 2^r$	BWK2R1 BWK2R2 BWK2R3 BWK2R4	7-14	A-8, A-15
$M_{\max}(\beta^r)$	MXBDR1 MXBDR2 MXBDR3 MXBDR4	7-12	A-8, A-15
$\lambda 1^r$	LWK1R1 LWK1R2 LWK1R3 LWK1R4	7-14	A-8, A-15
$\lambda 2^r$	LWK2R1 LWK2R2 LWK2R3 LWK2R4	7-14	A-8, A-15
$M_{\max}(\lambda^r)$	MXLDR1 MXLDR2 MXLDR3 MXLDR4	7-12	A-8, A-15

ORIGINAL DESIGN  
OF POOR QUALITY

ENGINEERING SYMBOL	VARIABLE NAME	DEFINING EQUATION	REFERENCES
KHRA	KHRA1 KHRA2 KHRA3 KHRA4	7-68	Fig. 7-8, A-15
KHRB	KHRB1 KHRB2 KHRB3 KHRB4	7-68	Fig. 7-9, A-15
KGR	KGR1 KGR2 KGR3 KGR4	7-40	Fig. 7-5, A-16
$\beta 1P$	BWK1P1 BWK1P2 BWK1P3 BWK1P4	7-14	A-8, A-15
$\beta 2P$	BWK2P1 BWK2P2 BWK2P3 BWK2P4	7-14	A-8, A-15
$M_{max}(\beta P)$	MXBDP1 MXBDP2 MXBDP3 MXBDP4	7-12	A-8, A-15
$\lambda 1P$	LWK1P1 LWK1P2 LWK1P3 LWK1P4	7-14	A-8, A-15
$\lambda 2P$	LWK2P1 LWK2P2 LWK2P3 LWK2P4	7-14	A-8, A-15

ORIGINAL PAGE IS  
OF POOR QUALITY

ENGINEERING SYMBOL	VARIABLE NAME	DEFINING EQUATION	REFERENCES
$M_{\max}(\lambda P)$	MXLDP1 MXLDP2 MXLDP3 MXLDP4	7-22	A-8, A-15
KHPA	KHPA1 KHPA2 KHFA3 KHPA4	7-68	Fig. 7-8, A-15
KHPB	KHPB1 KHPB2 KHPB3 KHPB4	7-68	Fig. 7, A-15
KRP	KRP1 KRP2 KRP3 KRP4	7-78	A-17
KGP	KGP1 KGP2 KGP3 KGP4	7-40	Fig. 7-5, A-16
$\beta 1^f$	BWK1F1 BWK1F2 BWK1F3 BWK1F4	7-14	A-8, A-15
$\beta 2^f$	BWK2F1 BWK2F2 BWK2F3 BWK2F4	7-14	A-8, A-15
$M_{\max}(\beta^f)$	MXBDF1 MXBDF2 MXBDF3 MXBDF4	7-12	A-8, A-15

ORIGINAL PAGE IS  
OF POOR QUALITY

ENGINEERING SYMBOL	VARIABLE NAME	DEFINING EQUATION	REFERENCES
$\lambda 1^f$	LWK1F1 LWK1F2 LWK1F3 LWK1F4	7-14	A-8, A-15
$\lambda 2^f$	LWK2F1 LWK2F2 LWK2F3 LWK2F4	7-14	A-8, A-15
$M_{\max}(\lambda^f)$	MXLDF1 MXLDF2 MXLDF3 MXLDF4	7-12	A-8, A-15
$\kappa^f$	KRF1 KRF2 KRF3 KRF4	7-80	A-17
KPF	KPF1 KPF2 KPF3 KPF4	7-80	A-17
KGHA	KGHA	8-53	Fig. 8-4, A-8
KGHB	KGHB	8-186, 8-187	Fig. 8-8, A-11
KRHA	KRHA1 KRHA2 KRHA3 KRHA4	8-176	Fig. 8-10, A-15
KRHB	KRHB1 KRHB2 KRHB3 KRHB4	8-176	Fig. 8-10, A-15

CRITICAL  
OF POOR QUALITY

E. ENGINEERING SYMBOL	VARIABLE NAME	DEFINING EQUATION	REFERENCES
KRHC	KRHC1 KRHC2 KRHC3 KRHC4	8-29	Eq. 8-28, A-15
KRHD	KRHD1 KRHD2 KRHD3 KRHD4	8-29	Eq. 8-28, A-15
KRHE	KRHE1 KRHE2 KRHE3 KRHE4	8-29	Eq. 8-28, A-15
KPHA	KPHA1 KPHA2 KPHA3 KPHA4	8-178	Eq. 8-178, A-15
KPHB	KPHB1 KPHB2 KPHB3 KPHB4	8-179	Eq. 8-179, A-15
KPHC	KPHC1 KPHC2 KPHC3 KPHC4	8-30	Eq. 8-30, A-15
KPHD	KPHD1 KPHD2 KPHD3 KPHD4	8-31	Eq. 8-30, A-15

ORIGINAL RECORD  
OF POOR QUALITY

ENGINEERING SYMBOL	VARIABLE NAME	DEFINING EQUATION	REFERENCES
KPHE	KPHE1 KPHE2 KPHE3 KPHE4	8-32	Eq. 8-30, A-15
KRTA	KRTA1 KRTA2 KRTA3 KRTA4	Tail counter- part of 8-29	Tail counterpart of Eq. 8-29, A-15
KRTB	KRTB1 KRTB2 KRTB3 KRTB4	Tail counter- part of 8-29	Tail counterpart of Eq. 8-29, A-15
KRTC	KRTC1 KRTC2 KRTC3 KRTC4	Tail counter- part of 8-29	Tail counterpart of Eq. 8-29, A-15
KPTA	KPTA1 KPTA2 KPTA3 KPTA4	Tail counter- part of 8-30	Tail counterpart of Eq. 8-30, A-15
KPTB	KPTB1 KPTB2 KPTB3 KPTB4	Tail counter- part of 8-31	Tail counterpart of Eq. 8-31, A-15
KPTC	KPTC1 KPTC2 KPTC3 KPTC4	Tail counter- part of 8-32	Tail counterpart of Eq. 8-32, A-15
KGTA	KGTA	8-190	A-10, A-19, A-20
KGTB	KGTB	8-97	A-10, A-19, A-20

## REFERENCES

- A-1. Humphreys, D. E., and K. W. Watkinson, Prediction of Acceleration Hydrodynamic Coefficients for Underwater Vehicles from Geometric Parameters, NCSL TR 327-78, Feb. 1978.
- A-2. Wendel, Kurt, Hydrodynamic Masses and Hydrodynamic Moments of Inertia, David W. Taylor Model Basin Translation 260, July 1956.
- A-3. Zahm, A. F., Flow and Force Equations for a Body Revolving in a Fluid, NACA Rept. 323, 1929.
- A-4. Malvestuto, Frank S., Jr., and Lawrence J. Gale, Formulas for Additional-Mass Corrections to the Moments of Inertia of Airplanes, NACA TN 1187, Feb. 1947.
- A-5. Gracey, William, The Additional-Mass Effect of Plates as Determined by Experiments, NACA Report No. 707, 1941.
- A-6. Abbott, I. H., Airship Model Tests in the Variable Density Wind Tunnel, NACA Rept. 394, 1931.
- A-7. Hoerner, S. F., Fluid Dynamic Drag, published by author, 1965.
- A-8. Silverstein, A., and B. G. Gulick, Ground-Handling Forces on a 1/40-Scale Model of the U.S. Airship "Akron", NACA Rept. 566, 1936.
- A-9. Zahm, A. F., R. H. Smith and F. A. Loudon, Air Forces, Moments and Damping on Model of Fleet Airship Shenandoah, NACA Rept. 215, 1925.
- A-10. Hoerner, S. F., Fluid Dynamic Lift, published by author, 1975.
- A-11. Ross, S. A., and H. R. Liebert, Stability and Control Characteristics of ZPN-1, ZP2N-1, and ZP2N-1W Airships, Goodyear Aircraft Corp. GER-1909 Rev. D, May 1951.
- A-12. Schlichting, Hermann and Erich Truckenbrodt, Aerodynamics of the Airplane, McGraw-Hill, Inc., 1979.
- A-13. Dempsey, E. M., Static Stability Characteristics of a Systematic Series of Stern Control Surfaces on a Body of Revolution, DWT NSRDC Rept. 77-0085, 1977.
- A-14. Freeman, H. B., Force Measurements on a 1/40-Scale Model of the U.S. Airship "Akron" NACA Rept. 432, 1932.

- A-15. Nielsen, J. N., O. J. McMillan, et al., Feasibility Study of Modern Airships. Phase II, Vol. I: Heavy Lift Airship Vehicle. Book III: Aerodynamic Characteristics of Heavy Lift Airship as Measured at Low Speeds," NASA CR-151919, Sept. 1976.
- A-16. Heyson, Harry H., Ground Effect for Lifting Rotors in Forward Flight, May 1960.
- A-17. Keys, C. N., and W. Z. Stephniewski, Rotary-Wing Aerodynamics. Volume 2: Performance Prediction of Helicopters, NASA CR-3083, Jan. 1979.
- A-18. Abbott, I. H., and A. E. Von Doenhoff, Theory of Wing Sections, Including a Summary of Airfoil Data, Dover Publications, Inc., 1959.
- A-19. McCormick, Barnes W., Aerodynamics, Aeronautics, and Mechanics, Flight Dynamics, John Wiley & Sons, New York, 1979.
- A-20. Etkin, Bernard, Dynamics of Flight, John Wiley & Sons, Inc., New York, 1959.

**APPENDIX B**

SYSTEMS TECHNOLOGY, INC.

13766 SOUTH HAWTHORNE BOULEVARD • HAWTHORNE, CALIFORNIA 90250 • PHONE (213) 679-2281

ORIGINAL PAGE IS  
OF POOR QUALITY

Paper No. 300

HEAVY LIFT AIRSHIP DYNAMICS

Mark B. Tischler  
Robert F. Ringland  
Henry R. Jex

May 1982

For publication in the Journal of Aircraft

## HEAVY LIFT AIRSHIP DYNAMICS

Mark B. Tischler, Robert F. Ringland and Henry R. Jex\*

Systems Technology, Inc.,

Hawthorne, California 90250

Abstract

A nonlinear, multibody, six-degrees-of-freedom digital simulation has been developed to study generic heavy lift airship (HLA) dynamics and control. The slung payload and flight control system models are described, and a review of the aerodynamic characteristics of an example vehicle is presented. Trim calculations show the importance of control mixing selection, and suggest performance deficiencies in crosswind stationkeeping for the unloaded example HLA. Numerically linearized dynamics of the unloaded vehicle exhibit a divergent yaw mode and an oscillatory pitch mode whose stability characteristic is sensitive to flight speed. The vehicle with slung payload shows significant coupling of the payload modes with those of the basic HLA. The accuracy of decoupled linearized models is sensitive to the size of dynamic excursions and the vehicle loading condition. A considerable improvement in the vehicle's stability and response is shown using a simple, multi-axis closed-loop control system operating on the rotor and propeller blade pitch controls.

Nomenclature

h	Altitude
L,M,N	Aerodynamic moments about x,y,z reference axes, respectively

---

\*Staff Engineer, Research, Member AIAA; Principal Specialist, Associate Fellow AIAA, and Principal Research Engineer, Member AIAA; respectively.

- $p, q, r$  Components of angular velocity about  $x, y, z$  reference axes, respectively
- $s$  Laplace transform operator
- $1/T_s, 1/T_h, 1/T_{sy1}, 1/T_{sy2}$  -- Surge, heave, and sway/yaw inverse time constants, respectively (time-to-half-amplitude =  $0.693T$ ;  
 $T = T_s, T_h, T_{sy1}, T_{sy2}$ )
- $u, v, w$  Components of velocity along  $x, y, z$  axes, respectively
- $x, y, z$  Orthogonal, right-hand coordinate axes; positive  $z$  is down
- $X, Y, Z$  Aerodynamic forces along the  $x, y, z$  axes, respectively
- $\alpha$  Tail angle of attack,  $\alpha \equiv \tan^{-1}(w_{t_a}/u_{t_a})$
- $\alpha_1$  Value of  $\alpha$  for stall or vortex breakdown
- $\alpha_2$  Value of  $\alpha$  for start of predominantly crossflow regime
- $\beta$  Tail angle of sideslip,  $\beta \equiv \tan^{-1}(v_{t_a}/u_{t_a})$  (nonstandard definition)
- $\delta_u, \delta_v, \delta_w, \delta_\theta, \delta_\phi, \delta_\psi$  -- Surge, sway, heave, pitch, roll, and yaw control deflections, respectively
- $\zeta_p, \zeta_r$  Pitch and roll mode damping ratios, respectively
- $\zeta_{lat}, \zeta_{lon}$  Lateral and longitudinal slung-payload pendulum mode damping ratios, respectively
- $\zeta_{y_v}$  Yaw vibration slung-payload mode damping ratio
- $\zeta_{h_v}, \zeta_{r_v}, \zeta_{p_v}$  Heave, roll, and pitch slung-payload vibration mode damping ratios, respectively
- $\omega_p, \omega_r$  Pitch and roll mode undamped natural frequencies, respectively
- $\omega_{lat}, \omega_{lon}$  Lateral and longitudinal slung-payload pendulum mode natural frequencies, respectively
- $\omega_{y_v}$  Yaw vibration slung-payload mode natural frequency.
- $\omega_{h_v}, \omega_{r_v}, \omega_{p_v}$  Heave, roll, and pitch slung-payload vibration mode natural frequencies, respectively

Subscripts

a	Apparent, relative to local airmass.
c	Command
c.g.	Center of gravity
c.v.	Center of volume
h	Hull
o	Reference value
p	Payload
t	Tail

Superscript

( <sup>.</sup> )	Time derivative with respect to nonrotating axes
------------------	--

I. Introduction

Recent feasibility studies<sup>(1-3)</sup> have shown that the heavy-lift hybrid airship (HLA) is an efficient and cost-effective vehicle for lifting, transporting over short distances (200 km), and positioning massive loads (typically up to 100 tons). These studies suggest that because of its economic advantages the HLA may serve in an important future role in the areas of logging, container ship offloading, remote site supply and coastal patrol.

While many economic studies are found in the literature, only limited analytical treatment of the engineering problems associated with operation of these vehicles in their intended roles has been published.<sup>(4,5)</sup> The studies of conventional, and more recently heavy lift, airship dynamics and control have used the classical, linearized, small perturbation approaches. However, the validity of using such techniques for the study of the HLA, a relatively new class of vehicle, has yet to be established.

Unlike the lighter-than-air vehicles of the past, the heavy-lift airship will have large thrust-to-weight ratios and low fineness ratios. As a result,

significant nonlinear rotor/hull aerodynamic interactions, not considered a problem in classic airships, have been reported.<sup>(6,7)</sup> Also, unlike its predecessors, the HLA will typically be used in missions requiring precise control through flight regimes encompassing large and rapid changes of speed, incidence, and inertial properties. The response of these vehicles to gusty environments has become an important issue, receiving only limited analytical treatment in the past.<sup>(8-10)</sup> Historically, the lack of control over gust-induced motions has proven the undoing of many dirigibles and blimps. The modern HLA, with its greatly increased control power (rotors and propellers), has the challenge of and potential for solving these traditional problems.

An accurate, nonlinear, non-real-time six-degrees-of-freedom (6 DOF) simulation to investigate the technological problems of the buoyant quadrotor (BQR) concept (Fig. 1). Specific areas of concern already noted are aerodynamics, flight dynamics, and flight controls. The simulation is intended for use as a basic design synthesis and analysis tool for evaluation of competing designs.

The example configuration, used for software development and simulation demonstration, is representative of a class of low fineness ratio, quadrotor HLAs having small fins and designed for efficient low speed cruise and hover flight. The assumed geometric and inertial properties of the loaded and unloaded vehicle are given in Fig. 1.

The simulation provides the capability to investigate generic properties and basic vehicle characteristics. It also permits the evaluation of the relative importance of aerodynamic and dynamic nonlinearities. Throughout the program, emphasis was placed on determining dominant effects and obtaining gross loads and motions, using models based on uniformly valid first approximations to a variety of effects. Also recognized was the need to minimize input data requirements to facilitate design tradeoff studies.

A comprehensive description of the simulation models and typical results was given in an extensive paper at the 1981 AIAA Lighter Than Air (LTA) Conference.<sup>(11)</sup> The present paper highlights the discussion of the flight control system model and example vehicle aerodynamics with emphasis placed on the presentation of performance and dynamic characteristics. The slung payload model is described, and a preliminary analysis of the coupled vehicle/payload dynamics is presented. The vehicle description in Fig. 1 has been corrected from the original paper.<sup>(11)</sup>

## II. Description of Simulation

This section will review the simulation capabilities and describe the aerodynamic, slung payload, and flight control system models. The aerodynamic characteristics of the example configuration are presented to provide insight into the physics of the vehicle dynamics discussed in a later section. The results presented here employ the basic (non-interference) aerodynamic models.

### Simulation Capabilities

The NASA/STI simulation is composed of four computer programs: vehicle, payload, vehicle/payload, and mooring.

Simulation capabilities include the calculation of: trim conditions (operating points) and the associated operating point equations of motion; normal mode response parameters; and large amplitude (nonlinear) motion time histories. The trim solution (unmoored) is an iterative calculation of control positions required to null vehicle (and payload) accelerations at selected orientations, velocities, and local wind directions. This capability is very useful for identifying control power requirements, operational envelopes, and performance tradeoffs. Small perturbations about selected trim points are used to generate numerically the open-loop (i.e., controls-fixed) system characteristic matrix, and the control and gust input matrices for

linear systems analyses. These matrices can be used to evaluate the vehicle open-loop transfer functions for flight control system synthesis, including time and frequency responses.

Fully nonlinear responses of the HLA and payload to a variety of control system commands and gust inputs are generated for open- and closed-loop studies. Control system commands, feedbacks, gains, and limits are determined from user inputs. Over 1000 states, component loads, and other dependent variables can be accessed at each time step and plotted or tabulated as desired. This capability can provide valuable insight into the importance of many nonlinear aerodynamic and dynamic terms.

The following subsections present summaries of the aerodynamic, slung payload and flight control system models. The reader is referred to detailed descriptions<sup>(11,12,13)</sup> of the aerodynamics models, dynamic equation formulation and software architecture.

#### Steady Aerodynamics Model of Example Vehicle

The quasi-steady aerodynamic characteristics for the bare hull and hull/tail assembly of the example configuration of Fig. 1 are presented in Fig. 2 for a constant flight speed of 50 ft/sec. The hull properties are assumed equal in pitch or yaw axes, and the tail-on-hull properties for the 45 deg vee-tail are assumed to be the same in pitch or yaw, except for the rolling moment. Semi-empirical methods<sup>(14,15,16,17)</sup> were used to estimate the basic aerodynamic characteristics. The static Z(Y)-force (Fig. 2a) is seen to be dominated by the bare hull, as a result of the small tail exposed area. The static pitching (yawing) moment characteristics about the center of volume (Fig. 2b) show that the small stabilizing tail contribution is completely overridden by the large unstable hull contribution, thereby rendering the static vehicle aerodynamically unstable (metacentric stability not included). The present test case, which has a "vee-tail," exhibits large negative rolling

moments due to sideslip (positive dihedral effect). Figure 2c shows significant nonlinearities in the mode. for angles of attack of +35 and -35 deg, owing to the assumed breakdown of attached flow in the stall transition regimes. The hull-alone damping characteristics for axial and non-axial flight are presented in Fig. 2d. The offsets in moments at zero angular rate ( $q, r = 0$ ) are due to the static hull moment characteristics. The significant increase in damping moment with angular rate for non-zero  $\alpha$  or  $\beta$  results from the  $w_{h_a}$  and  $v_{h_a}$  dependency in the hull damping model<sup>(11)</sup>.

#### Slung Payload Model

A slung payload model was developed in order to study the generic problems of hull/payload dynamic coupling and performance. A versatile sling geometry was implemented which allows the connection of the payload and hull by four (or less) elastic cables. Attach points on the hull and payload are user selected to facilitate tradeoff studies among various sling configurations (e.g., pendant, "inverted vee," etc.). Each cable is described in terms of spring stiffness and damping constants, with sling mass and aerodynamic properties neglected.

For the present simulation, a simple quasi-steady payload aerodynamics model was implemented which is suitable for trim performance and low speed dynamic analyses of high density containers. This model, which is essentially identical to the hull (tail off) quasi-steady aerodynamic model, accounts for potential flow moments, and viscous drag and damping loads. The model neglects the complex discontinuities (hysteresis, separation bubbles, etc.) and unsteady aerodynamics known to be significant for detailed assessment of stability boundaries and full scale flight correlation<sup>(18)</sup>. Future simulation users can easily adapt the present aerodynamics model for specific payload configurations should a detailed assessment be required.

The payload used as an example is a rectangular cargo container suspended by an "inverted-vee" sling. The container is suspended 3 degrees nose-down for improved dynamic stability characteristics.<sup>(18)</sup> The payload and sling geometry is shown in Fig. 1. The stiffness constant is typical for sling cables and was obtained from Sampath.<sup>(18)</sup> The damping constant was selected to yield a heave vibration mode damping ratio of about 0.2. As indicated in Fig. 1, the payload weight is 20 tons. Aerodynamic parameters were obtained from cargo container wind tunnel data<sup>(18)</sup>.

### Flight Control System

The flight control system implemented in the simulation exercises control over all six degrees of hull motion freedom. It functions to maintain trimmed flight conditions in the presence of disturbances and to execute maneuver commands.

Control Mixing. With four lift-propulsion units (LPUs), each having a rotor and a propeller, and three fin deflection controls, there are a total of 27 possible control points. Sixteen of these are active in the example HLA, four on each of the four LPUs. These are the propeller and rotor collectives, and the rotor lateral and longitudinal cyclics. Each of these is effective between user-set limits corresponding to mechanical limits at the control surface. The remaining control points are the rotor and propeller r\_pms, which are fixed at user-set values in the present simulation. The three fin deflections are fixed at zero.

The simulation incorporates the software equivalent of a "mixer box" to link the active control surfaces into six approximately orthogonal control input points, one for each degree of freedom. An input to one of these points is equivalent to commanding an acceleration in one of the six degrees of freedom. The six linked control points established by the mixer box are used to compute the trim operating points for the vehicle, for calculating linearized

control response derivatives, and for simulation flight control when computing time histories.

In the present model, the six acceleration command points are related to the linked control surfaces as follows:

- Pitch,  $\delta_\theta$  — Fore-and-aft differential rotor collectives
- Roll,  $\delta_\phi$  — Side-to-side differential rotor collectives
- Yaw,  $\delta_\psi$  — Side-to-side differential propeller collectives and differential rotor longitudinal cyclics
- Surge,  $\delta_u$  — Propeller collective and rotor longitudinal cyclics
- Sway,  $\delta_v$  — Rotor lateral cyclics
- Heave,  $\delta_w$  — Rotor collectives

The scheme mixes rotor longitudinal cyclics and propeller collectives to assure adequate control power for hovering with and without a payload, i.e., over a wide range of operating rotor thrust conditions. The mixing ratio is user-selected. The lateral cyclics are used exclusively for side force (sway) control because this axis is most control power limited — i.e., propellers are directed forward in the example HLA.

Flight Control Loops. Upstream of the mixer-box are the individual flight control loops, one for each of the acceleration control points. The pitch control loop, a typical example, is shown in Fig. 3. It incorporates feedback of pitch attitude and body axis pitch rate and contains proportional and integral paths in the forward loop. The attitude and body axis rate feedbacks provide command response and stability augmentation, while the forward loop integrator (initialized by the trim condition calculation at the start of the run) insures zero steady-state attitude error. The user determines the gain choices based upon analysis of the control requirements. The output is limited by a user-set value as is the integral term. The output limit prevents the pitch channel from using all the control authority that might

otherwise be available at one or more of the rotor collectives. The integrator limit similarly prevents the trim term from saturating the pitch control channel; the combined proportional-plus-derivative signal can always influence the pitch control,  $\delta_\theta$ . Upon encountering the limit, the integrator input is removed until it changes sign, when it is restored.

The control-augmented airframe constitutes an attitude-command/attitude-hold system, which is a favorable characteristic for low speed and hovering flight operations.<sup>(19)</sup> Such a system, while not highly maneuverable for "up and away" flying, allows for limited periods of unattended operation in controlling pitch attitude which will likely be required during payload pickup and drop, especially in gusty environments.

The simulation hardware organization is structured so as to confine control system changes to a limited number of subroutines, thereby making it easy for the user to reprogram for a particular HLA configuration under evaluation. Among the parameters suited for study using the flight control system model are: requirements for control power as a function of task and flight condition; control gain and limit schedules; crossfeeds between channels (e.g., for turning flight in cruise); and sensor location and orientation.

### III. Typical Simulation Results

This section presents some results of the simulation to illustrate the program functions and to show the motion dynamics for one class of HLA, the example configuration of in Fig. 1.

#### Trimmed Flight Conditions

A series of trimmed flight conditions covering a wide range of speed and incidences was computed in order to investigate the control authority requirements and flight envelope boundaries for both the unloaded and loaded configurations. The example payload aerodynamic forces are very small compared to

ORIGINAL PAGE IS  
OF POOR QUALITY

its weight, and so the resulting effects on performance were found to be correspondingly small (i.e., less than 2 percent at 44 ft/sec). For the trim analysis given here, the payload aerodynamics were neglected. Payload aerodynamics and sling dynamics are considered in the coupled vehicle/payload analysis discussed later.

Power Requirements. Figure 4 shows the total vehicle power requirements as a function of sea level axial flight speed for the unloaded and loaded configurations. Power is required at hover, even when unloaded, because the buoyancy ratio is less than unity. Based on a total available power rating of 6100 hp, the maximum unloaded cruise speed is 152 ft/sec (103 mph), compared to 145 ft/sec (99 mph) for the loaded vehicle.

These results show the importance of the longitudinal control crossfeed between propeller collective and rotor pitch cyclic. If the longitudinal crossfeed gain is kept the same for the loaded and unloaded configurations, as it was in the present case, rotor thrust contributes a greater proportion of cruise propulsion when the vehicle is loaded. Rotors, as a result of their large disk areas, are inherently more efficient for low speed cruise propulsion than are propellers. Therefore, the power requirements for the loaded and unloaded vehicles are essentially the same at maximum speed. Scheduling the crossfeed gain to optimize rotor and propeller usage for changing loading conditions will greatly improve overall vehicle performance.

The speed for maximum range and speed for maximum endurance, critical design parameters for HLAs, are seen to be 80 and 30 ft/sec for the unloaded and 105 and 75 ft/sec for the loaded vehicle, respectively. These parameters can be tailored to design specification by systematically exercising the simulation trim function for a range of configurations.

Crosswind Hover. The operation of HLAs in crosswind hover conditions is an important design consideration. Figure 5 presents the required uniform rotor lateral cyclic ( $\delta_v$ ) for upright trim (zero roll angle) as a function of

crosswind velocity for the loaded and unloaded vehicle. For a typical lateral cyclic limit of  $\pm 12$  deg, this figure indicates a maximum crosswind capability of 8 ft/sec (4.7 kt) for the unloaded vehicle. The loaded configuration, which trims with larger rotor thrusts, has a crosswind capability of 18 ft/sec (10.7 kt). Trimming at non-zero roll angles would generate larger lateral rotor forces; however, significant roll control ( $\delta_\phi$ ) would be required to offset the vehicle metacentric rolling moment, and/or a more complex load-handling suspension cable control system would be required to allow steady roll angles under load.

#### Small Perturbation Dynamics — Vehicle Alone

The coefficients for the linearized, small perturbation equations of motion were numerically determined for a number of trimmed, controls-fixed, flight conditions without a payload. Additional cases were calculated for a rigidly attached payload, the slung payload alone, and the HLA with slung payload. The characteristic roots of the system, each being associated with a particular dynamic mode of response, were calculated for the various flight conditions.

In describing the characteristic modes of response, we use a shorthand notation for Laplace transform factors. Thus,  $(1/T)$  denotes the factor  $(s + 1/T)$ , while  $[\zeta, \omega]$  denotes  $[s^2 + 2\zeta\omega s + \omega^2]$ . These common metrics in the frequency domain are related to the common time domain metrics as follows:

$$\begin{aligned} \text{Time-to-half-amplitude} &= 0.693T && \text{(real roots)} \\ &= 0.693/\zeta\omega && \text{(complex roots)} \end{aligned}$$

$$\text{Complex root location} = -\zeta\omega \pm j\omega\sqrt{1 - \zeta^2}$$

Table 1 summarizes the characteristic roots for several cases at 44 ft/sec. This condition is representative of blimp-like operations. A discussion of these results is presented below.

The unloaded vehicle (Table 1, Line a) exhibits the following five basic modes:

Surge Subsidence ( $1/T_s$ ). This stable mode is a 1 DOF motion, comprised of variations in axial speed ( $u_{hcg}$ ). About 50 percent of the surge damping arises from vehicle drag, while the remaining portion arises from rotor and propeller effects. This motion is largely decoupled from the other modes because  $M_u$  and  $Z_u$  are small in this flight condition.

Heave Subsidence ( $1/T_h$ ). This stable mode is predominantly composed of vertical motion and derives most of its damping from the rotors. The rotor flapping dynamics induce some coupling between heave, sway, and surge motions, the modal response ratios being:

$$|u_{hcg} : v_{hcg} : w_{hcg}|_{1/T_h} = |0.14 : 0.2 : 1|$$

Significant coupling between the heave and pitch motions, measured in terms of the hull pitch angle to hull angle-of-attack modal ratio:

$$|\theta_h : \alpha_{hcg}|_{1/T_h} = |0.7 : 1|$$

arises from the tail lift response to vertical velocity. Barring this coupling, the HLA heave mode resembles the heave mode exhibited by V/STOL aircraft. (20)

Pitch Oscillation ( $\zeta_p, \omega_p$ ). The oscillatory pitch mode is comprised of variations in  $u_{hcg}$ ,  $w_{hcg}$ , and  $\theta_h$ . The eigenvector phasing shows that  $\theta_h$  variations lead  $w_{hcg}$  and  $u_{hcg}$  by 25 deg and 273.3 deg, respectively. Although somewhat resembling the classical aircraft phugoid mode in frequency and damping, the present motion exhibits large changes in hull angle of attack,

$$|\alpha_{h_{cg}} : \theta_h|_{\omega_p} = |0.55 : 1|$$

Further, the frequency of oscillation ( $\omega_p$ ) is determined by the metacentric height (of c.v. above c.g.), the static aerodynamic pitch instability (effective  $M_x$  of the total vehicle is positive; Fig. 2b), and the total vehicle effective pitch inertia. The light oscillatory damping ( $\zeta_p$ ) is provided by the hull, tail, and rotors. For the 44 ft/sec flight condition, the rotors generate about 70 percent of the vehicle effective pitch damping.

Coupled Swav-Yaw ( $1/T_{sy1}$ ,  $1/T_{sy2}$ ). This mode is comprised of coupled variations in side velocity ( $v_{h_{cg}}$ ) and yaw angle ( $\psi_h$ ). The modal instability arises from the unstable static aerodynamic yawing moment characteristic of the hull/tail assembly (Fig. 2b). The unstable root ( $1/T_{sy1}$ ) and stable root ( $1/T_{sy2}$ ) locations depend on the yawing moment characteristics and the lateral drag and rotor damping. The coupled yaw-sway mode is similar to the unstable spiral mode in conventional aircraft.

Roll Oscillation ( $\zeta_r$ ,  $\omega_r$ ). The stable oscillatory roll mode is a well damped 1 DOF "pendulum motion" composed of variations in side velocity ( $v_{h_{cg}}$ ) and roll angle ( $\phi_h$ ). The modal response ratios indicate that the effective center of rotation is 3 ft below the hull center of volume and above the unloaded vehicle's composite c.g., due largely to apparent mass and inertia effects. The natural frequency ( $\omega_r$ ) is controlled by the metacentric height and effective roll inertia, while the damping ( $\zeta_r$ ) is generated by the rotors and tail.

Dynamic modes of HLAs and classical airships have been calculated by previous authors. The HLA longitudinal analysis completed by Nagabhusan and Tomlinson<sup>(5)</sup> showed the existence of the surge, heave, and pitch oscillatory modes, resembling those presented here. The lateral and longitudinal open-loop results presented by Delaurier and Schenck<sup>(4)</sup> are in correspondence with the five modal responses discussed here. Although specific damping ratios and

frequencies vary (depending on the configuration under study), the mode shapes and relative eigenvalue locations are very similar.

#### Effect of Payload on System Dynamics

The loaded vehicle (rigidly attached payload) has the characteristic roots shown in Table 1, Line b. The added payload weight results in a sizeable increase in the trim rotor thrust and related rotor blade coning and flapping. This produces significant coupling between the longitudinal and lateral-directional degrees of freedom. The surge mode now has substantial sway motion and has become slightly unstable. Except for minor changes in the oscillatory frequencies due to increased metacentric height (above the lowered c.g.) the remaining vehicle modes are essentially unchanged from the unloaded values in Line a.

The vehicle/slung-load configuration has eleven characteristic modes of response. The first five of these correspond to those of the basic vehicle. These basic vehicle modes of response induce in-phase payload motion of almost equal magnitude. For example, the (coupled) vehicle pitch oscillation modal ratios are:

$$|a_{hcg} : \theta_h : \theta_p|_{\omega_p} = |0.57 : 1 : 0.93|$$

This strong coupling into payload motions is due to the sling geometry which with inverted vee slings both forward and aft on the payload (Fig. 1) causes it to move with the hull. The coupled system responds as a single rigid body, with nearly the same modal characteristics as the loaded vehicle (rigidly attached payload) case. The associated coupled system roots are shown in Table 1, Line c, and very closely match those of the loaded vehicle, as expected.

The characteristic roots of the slung payload only system (in isolation) are listed in Table 1, Line d, and reveal six modes of response. The two lowest-frequency modes are associated with longitudinal  $[\zeta_{lon}, \omega_{lon}]$  and lateral  $[\zeta_{lat}, \omega_{lat}]$  pendulum modes. These have very low damping ratios because of the small aerodynamic damping in this flight condition. The next highest frequency mode  $[\zeta_{y_v}, \omega_{y_v}]$  is associated with yawing motions of the payload. Here the arrangement of the sling is such that cable spring force and damping contribute substantially to a higher frequency and damping ratio. The three highest-frequency vibration modes are dominated by the cable spring and damping constants.

The vehicle/slung-load modes, which correspond to the isolated slung payload modes, are presented in Table 1, Line e. A comparison of the results (Lines d and e) shows that the characteristic roots are essentially unaffected. However, the payload motion now induces significant out-of-phase vehicle motions. The magnitude of the vehicle response in each mode is nearly equal to the ratio of the payload mass (or moment-of-inertia) to the appropriate effective vehicle mass or moment-of-inertia (i.e., including hull apparent mass and moment-of-inertia effects) or the dominant degree-of-freedom.

For example, consider the coupled heave vibration mode:

$$\left| \omega_{hcg} : \omega_{pcg} \right|_{\omega_{h_v}} = |0.179 : 1| \hat{=} \frac{\text{Payload Mass}}{\text{Effective Vehicle Mass for z-Axis Motions}} = 0.175$$

These relatively high frequency out-of-phase coupled modes could be important in the design and analysis of inter-element structural members. Also, rotor

ORIGINAL PAGE IS  
OF POOR QUALITY

excitation, including higher-order dynamics not modelled in the present simulation, could be significant at these frequencies.

The present example analysis of the coupled HLA/slung-load dynamics shows that while the characteristic roots of the separated vehicle (Line b) and payload (Line d) modes are essentially unchanged in the combined vehicle (Lines c and e), significant dynamic coupling between the bodies exists. Adequate consideration of the coupled vehicle/slung-payload low frequency modes will be essential for load positioning, and of the high frequency modes for minimizing structural mode excitations. Analogous low frequency problems with heavy-lift-helicopters have required special flight control system characteristics, including feedbacks of the cable angle rates to rotor controls<sup>(21)</sup>. This remains an area for future HLA study.

The coupled vehicle/payload dynamics resemble in character the helicopter/slung load results of Sampath<sup>(18)</sup>. However, the present payload aerodynamic model lacks the detail required to capture the oscillatory nonlinearities and stability sensitivities reported in that reference.

Effect of Flight Speed on Unloaded Vehicle Dynamics

The linearization analysis for the unloaded vehicle was extended over a range of trimmed flight speeds from 0 to 140 ft/sec ( $\alpha = 0$ ). The migration of the 5 modes with axial speed is shown in Fig. 6. The surge ( $1/T_z$ ) and stable sway/yaw ( $1/T_{sy2}$ ) time constants increase fairly linearly with speed. The unstable mode time constant ( $1/T_{y1}$ ) increases due to the increasing hull instability with flight speed.

As expected from helicopter dynamics,<sup>(22)</sup> the heave damping ( $1/T_h$ ) improves with increasing speed. Since both the rotor and tail effectiveness increase with speed, the roll mode becomes more stable, reaching a damping ratio of 0.53 at the flight speed of 140 ft/sec. Forward flight speed reduces the frequency and ultimately destabilizes the pitch oscillation mode, due to

the hull's large aerodynamic instability and the small tail area. However the pitch damping of the rotors improves with increasing airspeed, so the mode is marginally stable up to 60 ft/sec. At this speed, the dominance of the envelope aerodynamics over metacentric stability causes the oscillation to become unstable. Ultimately the mode becomes two aperiodic divergences as the speed further increases.

The sensitivity of the dynamic modes to forward flight speed is a very important consideration in configuration and flight control synthesis. The present analyses show the unaugmented, unloaded example HLA configuration to be best suited for low-speed and hover flight conditions ( $V_0 < 60$  ft/sec). Increased flight speed can be achieved by increasing the tail size and hull fineness ratio, or by incorporating an active stabilizing flight control system.

#### Comparison of Nonlinear and Decoupled Linear Models

Flight mechanics and control analyses commonly are based on the small perturbation, linearized dynamics of vehicle motion where the longitudinal (pitch, surge, and heave) and lateral (roll, yaw, and sway) degrees-of-freedom are assumed decoupled. The validity of employing such assumptions for HLA analyses was checked by comparing the step response of the nonlinear and decoupled linear models for the 44 ft/sec flight condition, with and without a slung payload.

Figure 7 shows the open-loop pitch attitude response of the vehicle to small and large step commands in surge control ( $\delta_u$ ).

The unloaded vehicle pitch angle in response to a small step command of surge control ( $\delta_u = 0.16$  deg) is shown in Fig. 7a. The nonlinear and decoupled linear system responses compare very well, thereby validating the approximations. When the command is increased to  $\delta_u = 2.0$  degrees, Fig. 7b, the discrepancy between the system responses becomes more noticeable, indicating the existence of response nonlinearities for larger motions. However, the

character of the response is well represented for this case where derivative discontinuities in the aerodynamic data for the tail (Fig. 2) are not encountered.

The 6-degree-of-freedom nonlinear and the decoupled 3-degree-of-freedom linear responses of vehicle/slung payload systems are compared for a small command ( $\delta_u = 0.2$  deg) and a large command ( $\delta_u = 10.0$  deg) in Figs. 7c and 7d, respectively. During the first 15 secs, the comparison is good, with the large command response exhibiting some nonlinearity, as before. Thereafter, the response of the linearized system diverges from the nonlinear system. This divergence was traced to the coupling between longitudinal and the lateral-directional degrees of freedom — a factor which is not represented in the decoupled linear model. As previously noted, the loaded vehicle exhibits significantly increased coupling due to the increased rotor flapping associated with the large trim thrust levels.

These results are typical for simulations of rotorcraft where substantial response nonlinearity and coupling between longitudinal and lateral-directional degrees of freedom exists. The comparisons show that control and response coupling characteristics need to be taken into account in the analysis of HLA dynamics and the synthesis of flight control systems for these vehicles.

#### Vehicle Gust Response

The unloaded example configuration was trimmed at the 44 ft/sec flight condition and then subjected to an isolated vertical tail gust in order to study the dynamic responses. The gust input was a one-minus-cosine shaped vertical downdraft with a maximum value of 5 ft/sec and a duration of 4 sec. The selection of an isolated tail gust (no hull gradients) was made in order to excite the vehicle pitch mode with a simple disturbance, not necessarily representative of a realistic gust environment.

Open-Loop Response. The longitudinal response of the open-loop vehicle to the tail gust input is shown in the solid time histories of Fig. 8. (Note that the rate of climb,  $\dot{h}_{h_{CG}}$  not  $w_{h_{CG}}$ , is presented here.) The open-loop behavior is dominated by the pitch mode. The frequency of oscillation, phasing, and relative response ratios correspond very well, as expected, with the previous linearized results.

Closed-Loop Response. The flight control system was closed in all six degrees-of-hull-freedom in order to compare open- and closed-loop unloaded vehicle response to the gust input. Details of the pitch loop closure were presented in Reference 11.

The longitudinal closed-loop response to the tail down gust is plotted (dotted lines) in Fig. 8. The disturbance-suppressing characteristics of the 6 DOF flight control system are clearly apparent. Further studies are needed to determine vehicle response to turbulent environments, utilizing the four-point-gust model<sup>(11)</sup> with realistic turbulence inputs and the aerodynamic interference models.<sup>(13)</sup>

#### IV. Conclusions

An example HLA configuration with a low fineness ratio hull and a small vee-tail was analyzed to expose basic aerodynamic and dynamic properties. Some of the significant conclusions to be drawn from this analysis and a comparison with past airship data, are:

- 1) For the example configuration, the tail size is not sufficient to stabilize the vehicle in cruise flight.
- 2) The choice and scheduling of control mixing between rotors and propellers has a significant effect on vehicle performance. For the example configuration, the loaded and unloaded vehicles exhibited about the same maximum speed because the fixed crossfeed values resulted in higher propulsive efficiency for the loaded condition.

- 3) The trimming capability of the unloaded HLA is severely limited when hovering in crosswinds due to lack of lateral force generation capability.
- 4) Numerically linearized small perturbation dynamic analysis of the unloaded example configuration showed the existence of five characteristic response modes:

- Surge subsidence (stable)
- Heave subsidence (stable)
- Pitch oscillation (stable)
- Coupled sway-yaw (unstable)
- Roll oscillation (stable)

Resemblance of some of the HLA modes to those of classical aircraft and V/STOLs is apparent. The qualitative correlation of these modes with the results of other investigators was noted.

- 5) Analysis of the vehicle/slung-payload dynamics shows significant coupling of the payload dynamics with those of the basic HLA.
- 6) The pitch and unstable sway-yaw (unloaded vehicle) modes were destabilized with increasing axial flight speed, while the other modes became more stable.
- 7) Comparison of nonlinear and decoupled linear solutions for the unloaded vehicle showed close agreement for small motions, with some nonlinear effects for motions larger than a few degrees. The loaded vehicle exhibits strongly coupled characteristics due to the rotor flapping dynamics.
- 8) Open- and closed-loop responses of a 5 fps (one-minus-cosine) down-gust on the tail showed that excellent improvement in the vehicle's dynamic behavior can be attained with the incorporation of simple flight controller having proportional, rate and integral-error feedbacks.

Acknowledgment

The work reported herein was sponsored by the National Aeronautics and Space Administration under Contract NAS2-10330, with Mark Ardema, Alan Faye and Peter Talbot as Contract Technical Monitors.

References

- <sup>1</sup>Ardema, M. D., "Vehicle Concepts and Technology Requirements for Buoyant Heavy-Lift Systems," SAE Paper 791090, 1979.
- <sup>2</sup>Piasecki, F. N., "Ultra Heavy Vertical Lift System -- The 'Helistat,'" Interagency Workshop on Lighter Than Air Vehicles, MIT FTL R75-2, Jan. 1975.
- <sup>3</sup>Goodyear Aircraft Co., "Feasibility Study of Modern Airships. Phase II: Executive Summary," NASA CR-2922, Nov. 1977.
- <sup>4</sup>Delaurier, J., and Schenk, D., "Airship Dynamic Stability," AIAA Paper 79-1591, 1979.
- <sup>5</sup>Nagabhushan, B. L., and Tomlinson, N. P., "Flight Dynamics Analyses and Simulation of Heavy Lift Airships," AIAA Paper 79-1593, 1979.
- <sup>6</sup>Nielsen, J. N., McMillan, O. J., et al., "Feasibility Study of Modern Airships. Phase II, Vol. I: Heavy Lift Airship Vehicle. Book III: Aerodynamic Characteristics of Heavy Lift Airship as Measured at Low Speeds," NASA CR-151919, Sept. 1976.
- <sup>7</sup>Spangler, S. B., and Smith, C. A., "Theoretical Study of Hull-Rotor Aerodynamic Interference on Semibuoyant Vehicles," NASA CR-152127, Apr. 1973.
- <sup>8</sup>Flomenhoft, H. I., "Gust Loads on Airship Fins," McLean Development Labs., E-114, June 1957.
- <sup>9</sup>Calligeros, J. M., and McDavitt, P. W., "Response and Loads on Airships Due to Discrete and Random Gusts," MIT, ASRL TR 72-1, Feb. 1958.
- <sup>10</sup>Curtiss, H. C., Jr., Hazen, D. C., and Putman, W. F., "LTA Aerodynamic Data Revisited," AIAA Paper 75-951, July 1975.
- <sup>11</sup>Tischler, M. B., H. R. Jex, and R. B. Ringland, "Simulation of Heavy Lift Airship Dynamics over Large Ranges of Incidence and Speed," AIAA Paper 81-1335, July 1981.

<sup>12</sup>Ringland, R. F., Tischler, M. B., et al, "Generic Multi-Body Formulation of Heavy-Lift Airship Equations of Motion," Proc. of Joint Automatic Control Conference, Vol. I, San Francisco, Aug. 1980.

<sup>13</sup>Ringland, R. F., Tischler, M. B., et al, "Flight Dynamics Analysis and Simulation of Heavy Lift Airships," Systems Technology, Inc., forthcoming.

<sup>14</sup>Hoerner, S. F., Fluid Dynamic Lift, published by author, 1975.

<sup>15</sup>Hoerner, S. F., Fluid Dynamic Drag, published by author, 1965.

<sup>16</sup>Dempsey, E. M., "Static Stability Characteristics of a Systematic Series of Stern Control Surfaces on a Body of Revolution," DWT HSRDC Rept. 77-0085, 1977.

<sup>17</sup>Humphreys, D. E., and Watkinson, K. W., "Prediction of Acceleration Hydrodynamic Coefficients for Underwater Vehicles from Geometric Parameters," NCSL TR 327-78, Feb. 1978.

<sup>18</sup>Sampath, Prasad, "Dynamics of a Helicopter-Slung Load System," University of Maryland, Ph.D. Thesis, 1980.

<sup>19</sup>Hoh, R. H., and Ashkenas, I. L., "Development of VTOL Flying Qualities Criteria for Low Speed and Hover," NADC 77052-30, Dec. 1979.

<sup>20</sup>McRuer, D., Ashkenas, I., and Graham, D., Aircraft Dynamics and Automatic Control, Princeton Univ. Press, 1973.

<sup>21</sup>Fries, G. H., and J. J. Schneider, "HLH and Beyond," SAE Paper 791086, Dec. 1979.

<sup>22</sup>Bramwell, A. R. S., Helicopter Dynamics, New York, Wiley, 1976.

C-4

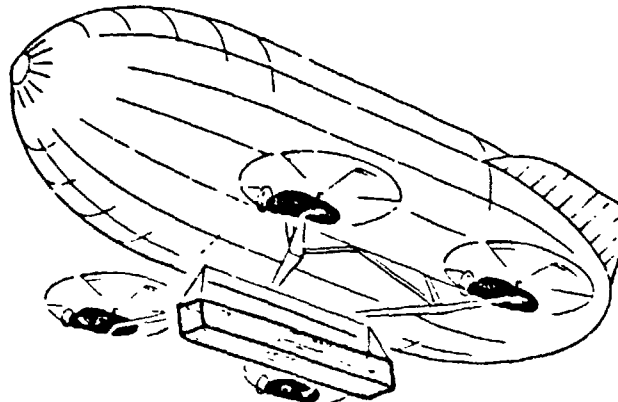
TABLE 1. CHARACTERISTIC ROOTS FOR THE UNLOADED AND LOADED VEHICLE  
AT 44 FT/SEC (30 MPH)

A) Vehicle Modes		Surge	Heave	Pitch	Sway-Yaw	Roll
		$(1/T_s)$	$(1/T_h)$	$[\zeta_p, \omega_p]$	$(1/T_{sy1})$ $(1/T_{sy2})$	$[\zeta_R, \omega_R]$
a) Vehicle Unloaded		(0.0245)	(0.253)	[0.107, 0.273]	(-0.175) (0.279)	[0.371, 0.447]
b) Vehicle Loaded		(-0.0076)	(0.220)	[0.137, 0.340]	(-0.167) (0.267)	[0.298, 0.498]
c) Coupled Vehicle/ Slung Load		(-0.0035)	(0.220)	[0.142, 0.330]	(-0.167) (0.266)	[0.320, 0.524]

ORIGINAL PAGE IS  
OF POOR QUALITY

B) Payload Modes		Lateral Pendulum	Longitudinal Pendulum	Yaw Vibration	Heave Vibration	Roll Vibration	Pitch Vibration
		$[\zeta_{lat}, \omega_{lat}]$	$[\zeta_{lon}, \omega_{lon}]$	$[\zeta_{yy}, \omega_{yy}]$	$[\zeta_{hy}, \omega_{hy}]$	$[\zeta_{ry}, \omega_{ry}]$	$[\zeta_{py}, \omega_{py}]$
d) Slung Load Only		[0.003, 1.112]	[0.008, 1.285]	[0.084, 5.004]	[0.187, 9.338]	[0.304, 15.600]	[0.332, 16.592]
e) Coupled Vehicle/ Slung Load		[-0.004, 1.180]	[0.007, 1.429]	[0.085, 5.059]	[0.200, 10.803]	[0.306, 15.632]	[0.335, 16.798]

ORIGINAL PAGE IS  
OF POOR QUALITY

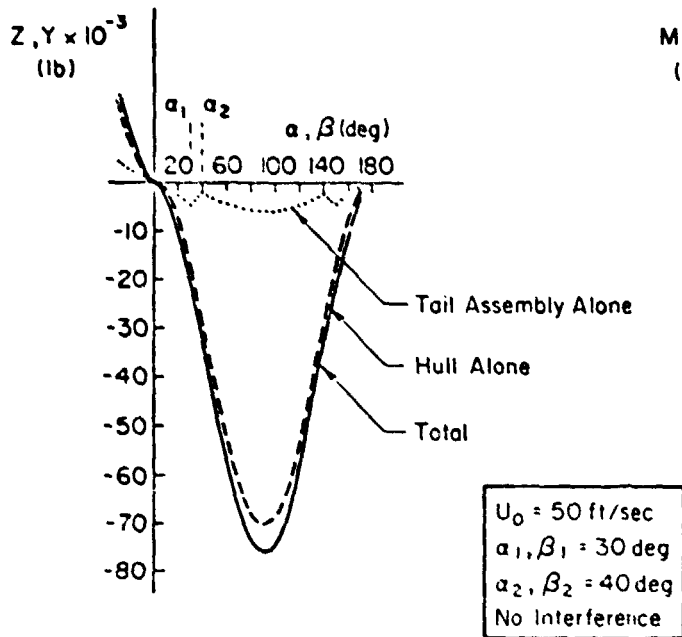


<u>Hull</u>		
Length		240 ft
Diameter		103 ft
Volume		$1.5 \times 10^6 \text{ ft}^3$
Tail Area		$2520 \text{ ft}^2$
Weight		$8.89 \times 10^4 \text{ lb}$
<u>Lift Propulsion Unit (LPU)</u>		
Rotor Diameter		56 ft
Propeller Diameter		13 ft
Engine Horsepower (One per LPU)		1524 hp
Weight (Each LPU)		$9 \times 10^3 \text{ lb}$
<u>Composite Vehicle</u>	<u>Unloaded</u>	<u>Loaded</u>
Weight (lb)	125,000	165,000
Buoyancy Ratio	0.92	0.70

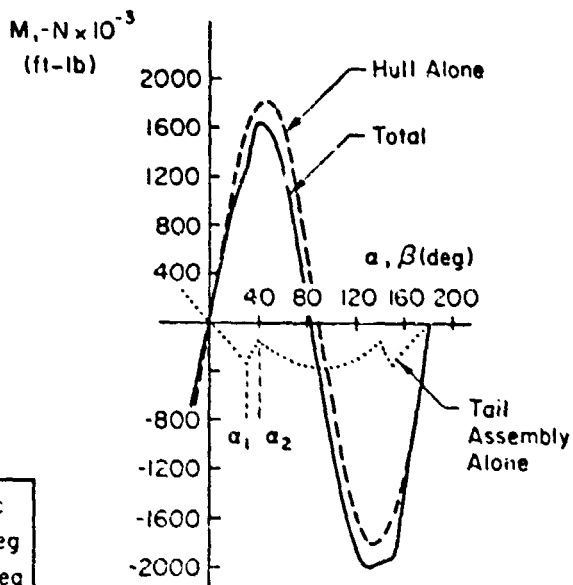
Figure 1. Example Quadrotor HLA and Slung Payload  
Used in Present Simulation

ORIGINAL PAGE IS  
OF POOR QUALITY

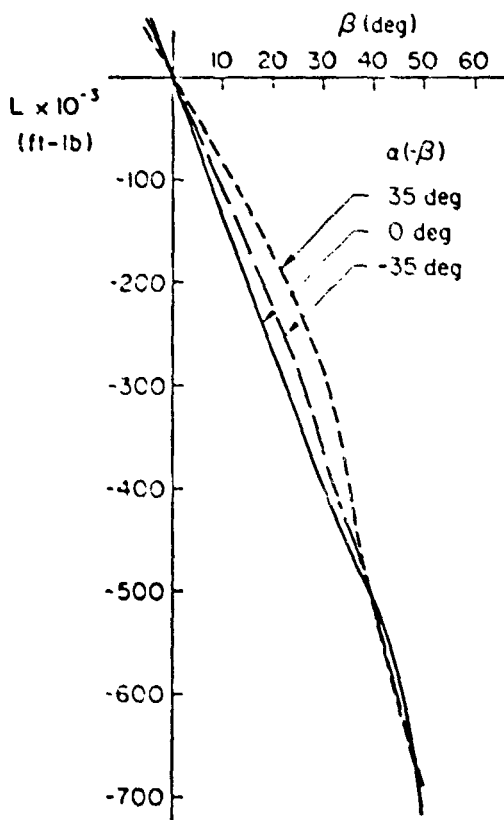
a) Z or Y Force



b) Static Pitching, Yawing Moment



c) Static Rolling Moment



d) Damping Moment, Hull Alone

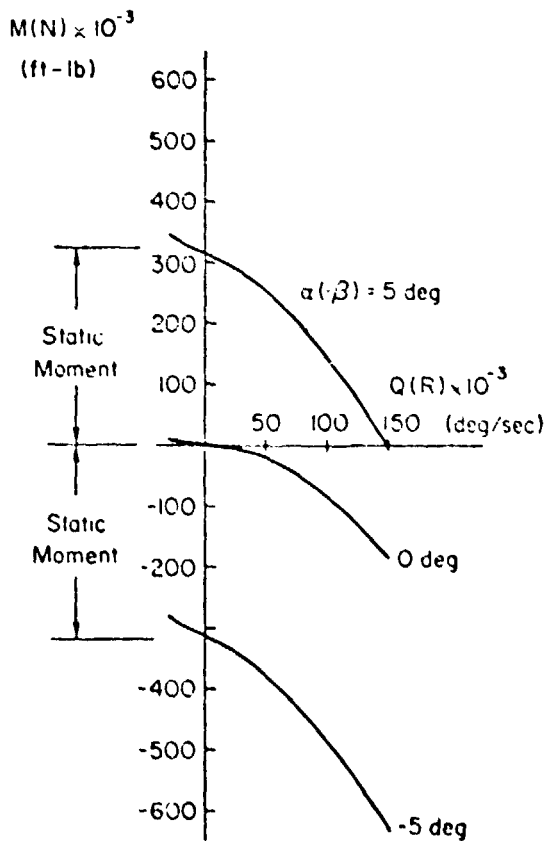


Figure 2. Samples of Simulated Forces and Moments for Example Case of Fig. 1

ORIGINAL PAGE IS  
OF POOR QUALITY

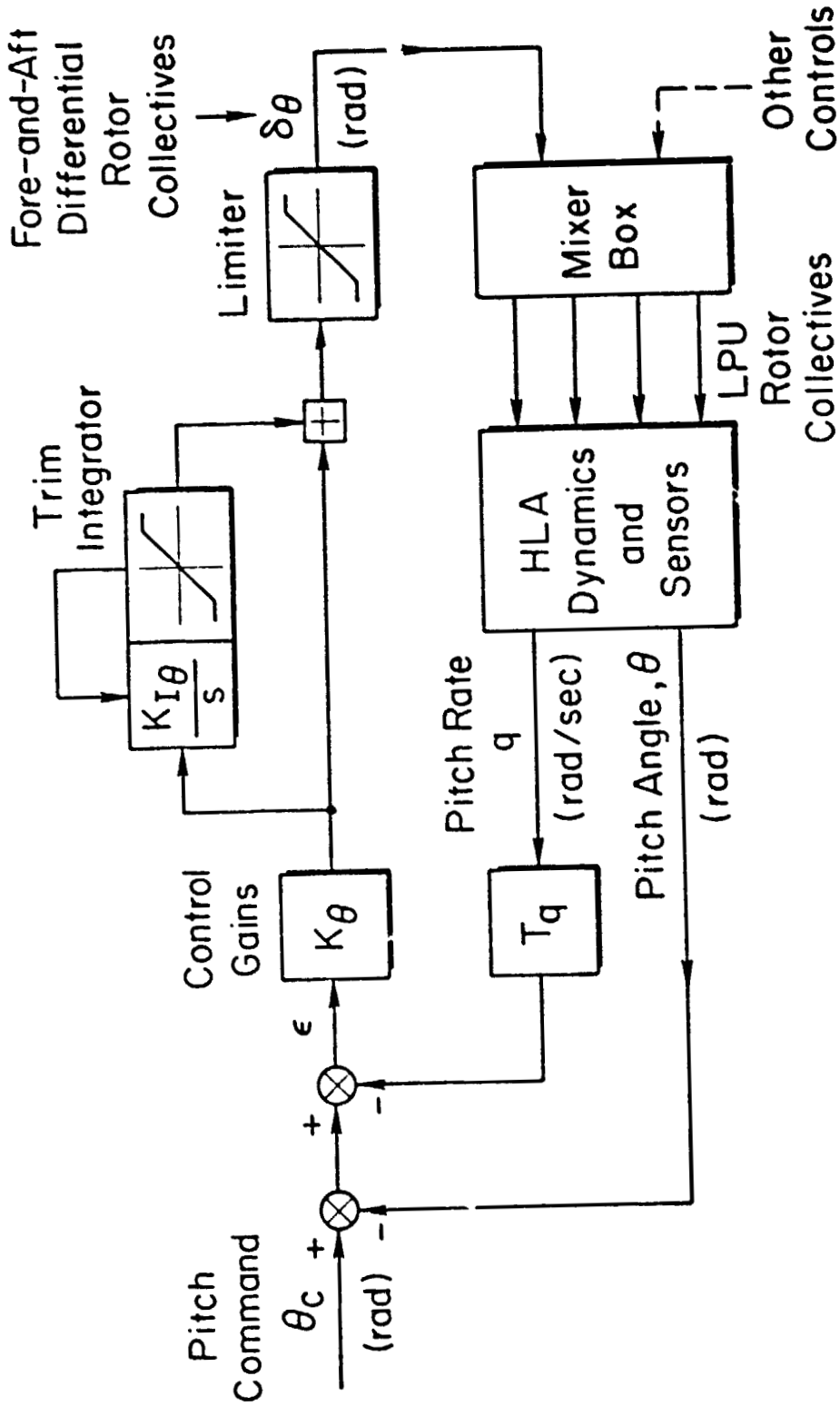


Figure 3. Block Diagram for Pitch Control Loop

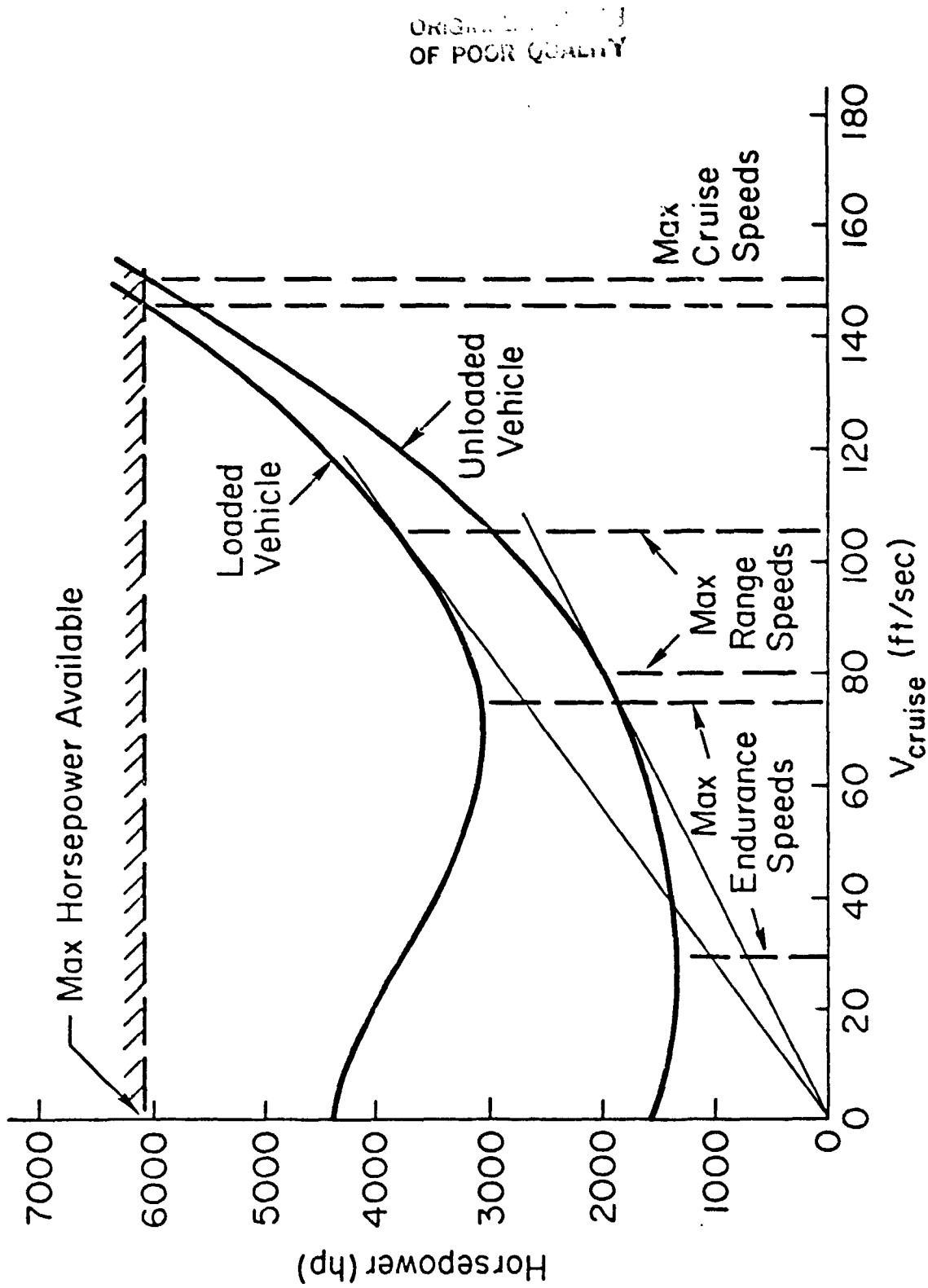


Figure 4. Power Requirements for Trimmed Forward Flight

ORIGINAL PAGE IS  
OF POOR QUALITY

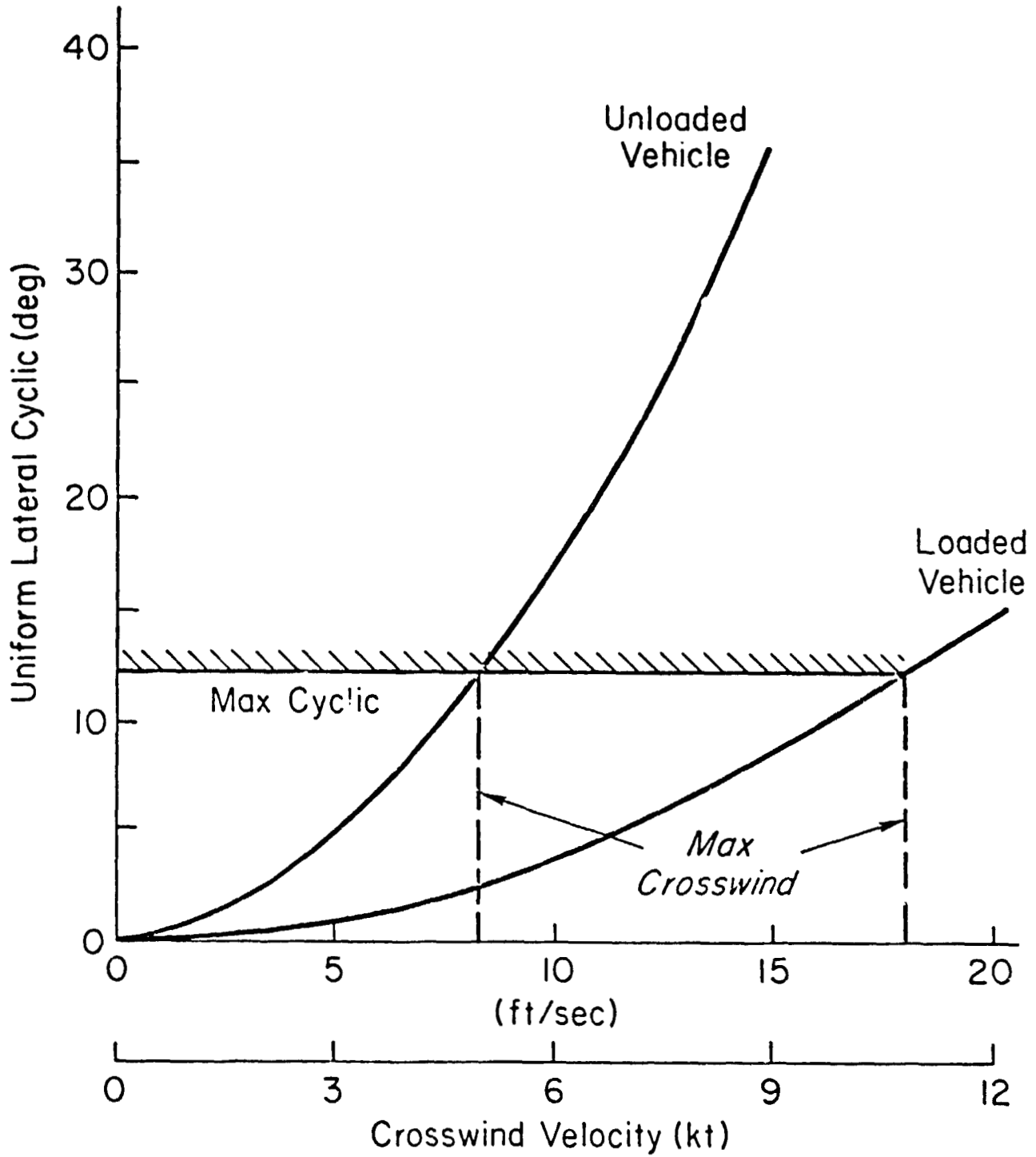


Figure 5. Trimming for Hover in a Steady Crosswind

ORIGINAL PAGE IS  
OF POOR QUALITY

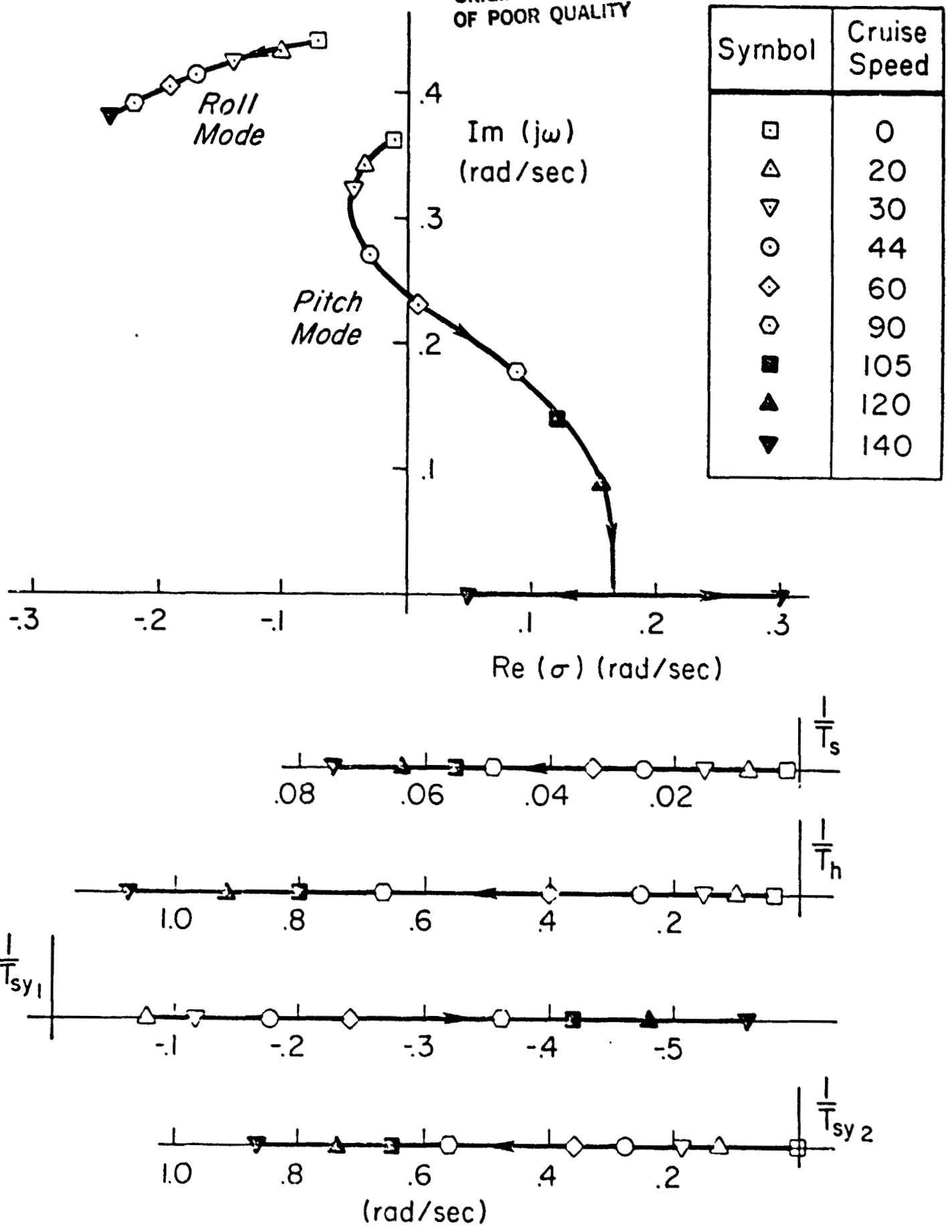
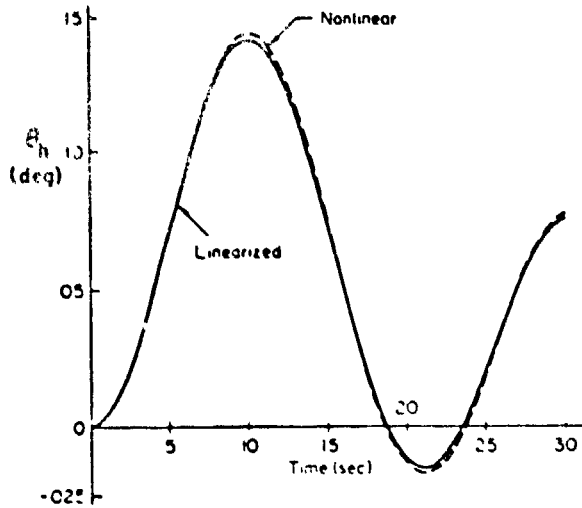


Figure 6. Migration of Unloaded HLA Modes with Cruise Speed

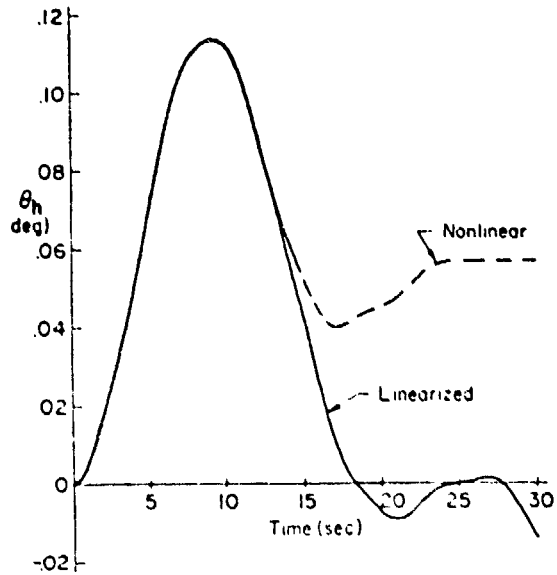
UNLOADED VEHICLE

VEHICLE / SLUNG - LOAD SYSTEM

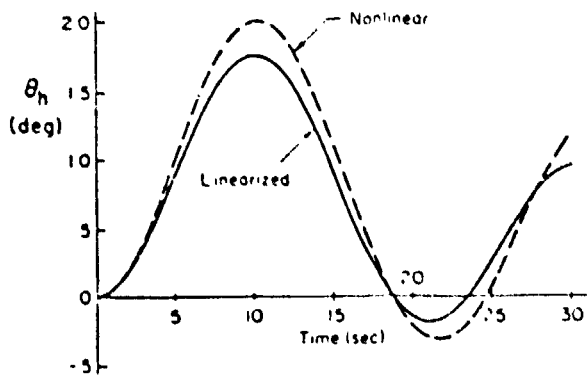
a) Small Step ( $\delta_y = 0.16$  deg)



c) Small Step ( $\delta_y = 0.2$  deg)



b) Large Step ( $\delta_y = 2.0$  deg)



d) Large Step ( $\delta_y = 10$  deg)

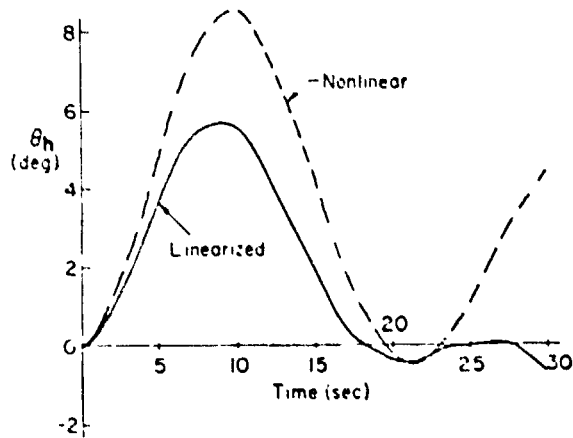
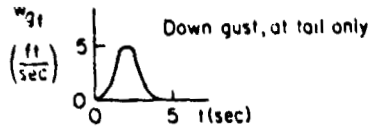


Figure 7. Comparison of 6-Degree-of-Freedom Nonlinear and Decoupled 3-Degree-of-Freedom Linear Open-Loop Responses to Axial Control Steps



ORIGINAL P  
OF POOR QUALITY

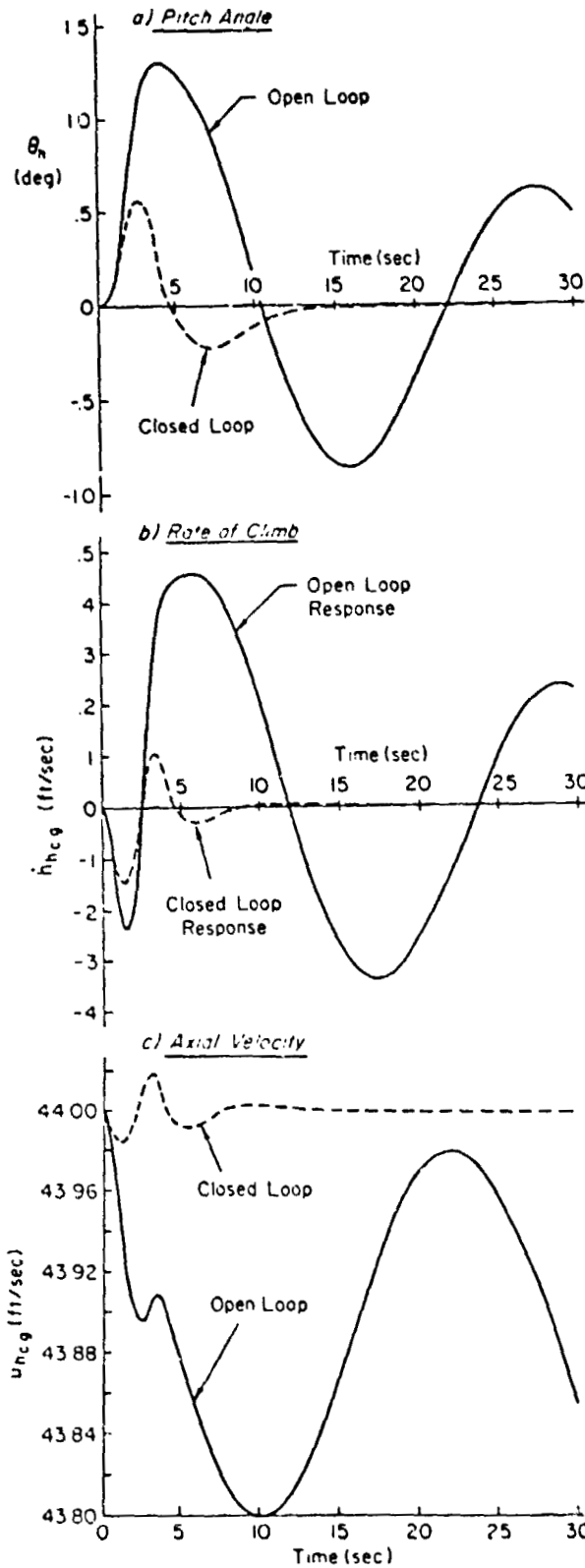


Figure 3. Comparison of Open- and Closed-Loop Responses to Tail-Down Gust

**APPENDIX C**

ORIGINAL PAGE IS  
OF POOR QUALITY

SYSTEMS TECHNOLOGY, INC.

13700 SOUTH HAWTHORNE BOULEVARD • HAWTHORNE, CALIFORNIA 90250 • PHONE (213) 879-2281

Paper No. 313

THE EFFECTS OF ATMOSPHERIC TURBULENCE ON A  
QUADROTOR HEAVY LIFT AIRSHIP

Mark B. Tischler  
Henry R. Jex

June 1982

AIAA Paper No. 82-1542CP

For presentation at the

AIAA Guidance and Control Conference  
San Diego, CA  
August 9-11, 1982

THE EFFECTS OF ATMOSPHERIC TURBULENCE ON A  
QUADROTOR HEAVY LIFT AIRSHIP

Mark B. Tischler and Henry R. Jex\*  
Systems Technology, Inc.  
Hawthorne, CA 90230

Abstract

The response of a Quadrotor Heavy Lift Airship to atmospheric turbulence is evaluated using a 4-point input model. Results show interaction between gust inputs and the characteristic modes of the vehicle's response. Example loop closures demonstrate tradeoffs between response regulation and structural loads. Vehicle responses to a tuned discrete wave front compare favorably with the linear results and illustrate characteristic HLA motion.

Nomenclature

$a_z$  Acceleration of the hull center of gravity along the positive (downward) z-body axis, ft/sec<sup>2</sup> (g)

c.g. Center of gravity of the hull (i.e., envelope/tail/support structure assembly, excluding LPUs)

$C_w$  Traveling upgust wave celerity, i.e., inertially referenced crest velocity, ft/sec

dB Decibels [= 20 log<sub>10</sub> (gain)]

$F_{cz1}$  Constraint force exerted on the hull support structure at the attachment point of LPU-1, along the positive (downward) z-body axis, lb

LPU Lift propulsion unit; each unit is comprised of one rotor, one propeller, and one nacelle; numbering system shown in Fig. 2

$L_{zg}$  Characteristic scale length for vertical turbulence, ft

$l_h$  Hull length, ft

s Laplace transform operator

$1/T_h$ ,  
 $1/T_h'$  Heave mode inverse time constants for the open-loop (bare airframe) and closed-loop (control system engaged) vehicle, respectively; rad/sec (time-to-hs.f-amplitude = 0.693T; T =  $T_h$ ,  $T_h'$ )

$V_a$  Reference relative airspeed, ft/sec

$V_o$  Reference inertial velocity along the x-body axis (ground speed), ft/sec

$v$  Velocity of the hull center of gravity along the positive (downward) z-body axis, ft/sec

$w_c$  Heave axis control deflection;  $w_c = 1$  degree + 1 degree of negative collective pitch on each rotor, deg

$w_g^1, w_g^2,$   
 $w_g^3, w_g^4$  Gust velocities along the inertial z-axis at input sources 1-4, respectively; positive downward, ft/sec

$\zeta_p$  Pitch oscillation mode damping ratios for the open-loop (bare airframe) and closed-loop (control system engaged) vehicle, respectively

$\theta, \phi$  Pitch and roll Euler angles, respectively; rad (deg)

$\sigma$  Root-mean-square value (rms)

$\sigma_{a_z}$  Root-mean-squared (rms) level of hull acceleration ( $a_z$ )

$\sigma_{F_{cz1}}$  Root-mean-squared (rms) level of vertical constraint force at LPU-1 ( $F_{cz1}$ )

$\sigma_{w_g}$  Intensity level (rms) for turbulence along the inertial z-axis, ft/sec

$\phi_{w_g w_g}^*$ ,  
 $\phi_{w_g w_g}^*$  Power spectral density function and truncated power spectral density function, respectively, for vertical turbulence, ft<sup>2</sup>/rad-sec

$\omega$  Frequency, rad/sec

$\omega_{BW_h}$  Heave control system bandwidth; defined as the -3 dB frequency (Fig. 3), rad/sec

$\omega_c$  Butterworth filter cutoff frequency, rad/sec

$\psi_w$  Traveling upgust wave encounter angle (Fig. 2), deg

$\omega_p, \omega_p'$  Pitch oscillation mode frequencies for the open-loop (bare airframe) and closed-loop (control system engaged) vehicle, respectively; rad/sec

Superscripts

- Average value

( $\cdot$ ) Time derivative with respect to nonrotating axes

I. Introduction

The effects of atmospheric turbulence on the airship motions and structures are a continuing

\*Staff Engineer, Research, Member AIAA; and Principal Research Engineer, Associate Fellow AIAA.

concern.<sup>1,2,3</sup> Low speed and mooring operations are especially difficult since the reduced control power and ground clearance increase the vehicle's vulnerability to turbulence. Recently, both the British AD-500 and Goodyear Columbia have suffered considerable damage in mooring accidents which are largely attributable to severe turbulence.

Current design concepts emphasize requirements of precision vehicle control and gust response suppression in low speed and hover flight operations.<sup>4,5</sup> These requirements are especially formidable for the Heavy Lift Airship (HLA) logging configuration<sup>6</sup> and the Maritime Patrol Airship (MPA).<sup>4</sup> The utility of these vehicles depends on their ability to operate in all weather conditions.

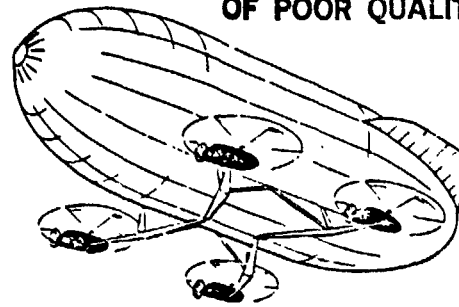
Studies by DeLaurier<sup>1</sup> on the effects of atmospheric turbulence on conventional airships showed the existence of significant coupling between airship pitch dynamics and vehicle structural loads. Maximum vehicle response and attendant loads were found to occur where turbulence wave lengths corresponding to those of the airships' normal modes. Nagabhushan<sup>2</sup> analyzed the effects of closed-loop control on the hovering performance of quad-rotor HLAs in crosswind flight conditions. His analysis showed that considerable improvement in the radius of hover could be achieved by feedbacks of inertial vehicle position to the rotor cyclic controls. The associated effects on the structural loads of HLAs were not investigated.

An analysis of the dynamics and performance of a generic quad-rotor heavy lift airship (Fig. 1) using the STI/NASA simulation was discussed in Refs. 7 and 8. One significant conclusion was that gust accelerations have a considerable impact on the loads experienced by airships due to apparent mass effects. This will be especially important for the HLA logging mission where large and rapid changes in the local atmospheric conditions result from the geographic surroundings.

In this paper, we further develop analysis of turbulence effects on quad-rotor heavy lift configurations with the use of the four point atmospheric input model outlined in Refs. 7 and 8. This multiple-input model allows a more accurate description of gust gradient effects than is obtainable with a more conventional single point aircraft model.<sup>3</sup> An assessment of the effects of atmospheric turbulence on the vehicle dynamics was made with an adaptation of design military gust specifications for piloted aircraft<sup>10</sup> (MIL-F-8785C). This paper presents an overview of the four-point atmospheric input model, a discussion of its range of validity, and an application of the Mil Spec for a typical low speed unloaded flight condition. The results show the effects of closed-loop control on vehicle turbulence response and associated structural loads.

## II. Atmospheric Input Model

Analyses of turbulence effects on aircraft are generally based on the assumption that the local atmosphere may be represented by gust velocities and linear gradients at a single point (nominally the aircraft center of gravity), then extrapolated outward therefrom. As noted by Etkin,<sup>9</sup> this leads to significant overestimation errors for large aircraft and small gust wavelengths. Airships,



### Hull

Length	240 ft
Diameter	103 ft
Volume	$1.5 \times 10^6$ ft <sup>3</sup>
Tail Area	2500 ft <sup>2</sup>
Weight	$8.8 \times 10^4$ lb

### Lift Propulsion Unit (LPU)

Rotor Diameter	56 ft
Propeller Diameter	13 ft
Engine Horsepower (One per LPU)	1524 hp
Weight (Each LPU)	$9 \times 10^3$ lb

Composite Vehicle	Unloaded	Loaded
Weight (lb)	125,000	165,000
Buoyancy Ratio	0.92	0.70

Fig. 1. Generic quadrotor heavy lift airship used in present study

with their nearly neutral buoyancy, large dimensions and relatively low cruise speeds, are especially sensitive to large-scale atmospheric gradients and accelerations. A multiple-point input model allows the calculation of these gradient effects at smaller wavelengths (and larger aircraft size) than is possible with a single-point model. This results from the spatial interpolation scheme which is used to calculate average gradients and velocities from the velocities at the various input sources. Based on these considerations, we have implemented a four-point atmospheric input model. This model, which is an extension of the work of Holley and Bryson,<sup>11</sup> and Etkin,<sup>8</sup> is discussed in detail in Refs. 7 and 8.

Figure 2 shows the location of the four input sources for the present analysis, which are selected as a compromise to be close to the more distal vehicle components, (i.e., hull ends, tail surfaces, and lift/propulsion units (LPUs)). These sources are assumed to be statistically uncorrelated because of their large separation relative to gust characteristic lengths at low altitudes. Hence, linear superposition can be used to determine the total (Gaussian) turbulence response of the vehicle by summing the isolated responses of the vehicle to individual gust velocity sources. Each input gives rise to effective gust accelerations, velocities, and gradients at

ORIGINAL PAGE IS  
OF POOR QUALITY

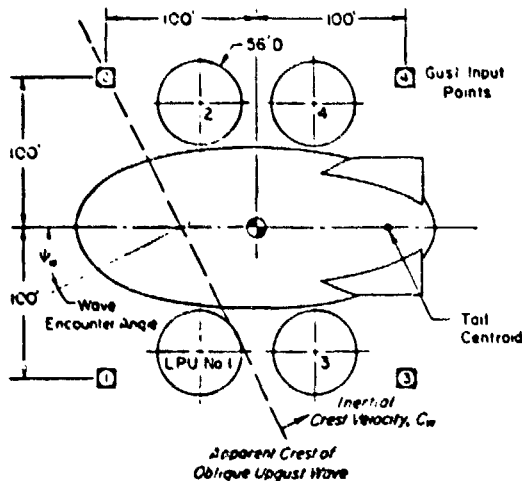


Fig. 2. Atmospheric input model

the hull, tail, and LPUs. These, in turn, are used to calculate aerodynamic forces and moments for use in the dynamic equations of motion. The many interpolation formulas and equations for the associated aerodynamic forces are presented in Ref. 7 and are not repeated here.

Discrete wave fronts are generated by tailored sequencing among the input sources. These waves can be tuned to the vehicle's dynamic modes to evaluate critical non-Gaussian phenomena. The four-point model is valid for all discrete disturbances within the assumption of linear interpolation of local gust velocity between input sources.

The use of a four-point atmospheric model allows the calculation of gradient effects to shorter gust wavelengths than is possible with a single-point model; however, a lower gust wavelength limit exists on the validity of the model in simulating the response to sinusoidal inputs. This results from the assumption of gust velocity linear interpolation between the various input sources, and the use of a closed-form hull aerodynamic model dependent only on the relative motion between the hull center of volume and air mass.

Analyses using a multiple segment hull model<sup>1</sup> show that the response power spectra fall off rapidly for gust wavelengths shorter than twice the hull length ( $2L_h$ ). This is due to the pressure averaging effect of the hull. In the present single-point model, the spectral-power reduction is modeled with a third-order Butterworth filter. The filter break frequency corresponds to a wavelength of  $2L_h$ , the assumed limit of the four-point input model.

While the more accurate multiple segment model is necessary to evaluate distributed structural loads along the airship hull, the simplified approach adopted here is felt to be sufficient for dynamics and control analyses of heavy lift airships, where the loads between widely separated elements are of prime importance. This approach allows the easy incorporation of measured atmospheric data (e.g., at four towers more than 100 ft apart) and is well suited for the study of

vehicle responses to discrete waveforms, such as traveling gust "waves" and thermal currents. A comprehensive experimental effort with an instrumented flight vehicle would be needed to validate the preceding assumptions.

### III. Analysis Techniques

The present analysis procedures are broadly based on the MIL-F-8785C turbulence requirements.<sup>10</sup> This specification requires analysis of both continuous random (Gaussian) statistical turbulence and discrete (non-Gaussian) disturbances. As noted by Etkin,<sup>9</sup> the Gaussian statistical analyses account the Gaussian loads of up to 3g, important for fatigue assessment. The discrete turbulence (wave front) analysis accounts for the critical loads which occur in thunderstorms with far greater frequency than their Gaussian probability ( $\text{Pr } 4.5\sigma = 7 \times 10^{-6}$ ) would indicate. A discussion of the application of these analysis techniques to the four point atmospheric model is presented below.

#### Statistical Turbulence Analysis

The longitudinal gust response transfer functions for each input source (e.g.,  $\theta/w_g^3$ ,  $a_z/w_g^3$ ,  $\theta/w_g^2$ , etc.) are generated by exercising the numerical linearization option of the STI/NASA Heavy Lift Airship simulation.<sup>7</sup> These transfer functions provide valuable insight into the dynamics of HLA gust responses. Constraint force transfer functions give the gust-imparted loads in the support structure between the central buoyant envelope (hull) and the lift propulsion units (LPUs). Statistical information is obtained through analysis of the gust transfer functions and the relevant atmospheric spectra. In the present analysis we used a simplified form of the Dryden model<sup>12</sup> with the high frequency spectrum truncated for wavelengths shorter than twice the hull length ( $2L_h = 480$  ft). The turbulence model's scale length and intensity parameters were obtained from Ref. 10. Open-loop (bare airframe) and closed-loop (flight control system engaged) studies were completed to investigate tradeoffs between requirements for response suppression and structural integrity.

#### Discrete Gust Response

Discrete gust responses show the vehicle reaction to non-Gaussian disturbances. A tuned upgust wave front was developed based on the MIL Spec guidelines.<sup>10</sup> This wave consists of sequenced (1 - cosine) discrete waves, one at each of the four input source locations, designed to excite the vehicle at its natural frequencies of motion about the pitch and roll axes. The resulting large amplitude time histories provide information on critical loads and motions.

### IV. Linearized Transfer Functions

The open-loop linearized and decoupled longitudinal transfer functions were calculated for a flight condition of 44 fps (13.4 m/s) (axial airspeed), which corresponds to that analyzed in Ref. 8. The present model includes the effect of aerodynamic interference among the vehicle components (e.g., hull/rotor, rotor/tail, etc.). A comparison of the present transfer functions with those of Ref. 8 shows interference effects on the

vehicle's transient dynamics to be small to negligible. As noted in Ref. 7, the dominant effects are changes to vehicle trim controls and power conditions.

Closed-loop transfer functions were calculated for the nominal flight control system described in Ref. 8. Feedbacks of attitude, and inertial linear and angular velocities to the rotor, propeller and tail control surfaces stabilize the vehicle against unwanted motion and maintain the commanded flight path. A forward loop integrator is used in each axis to insure zero steady-state error.

Figure 3 shows the vertical velocity response ( $w$ ) to vertical command inputs ( $w_c$ ) for the open-loop (feedbacks disconnected) and closed-loop (feedbacks connected) vehicle. The open-loop response is characterized by the dominant heave mode frequency ( $1/T_h = 0.22$  rad/sec), the pitch oscillation mode frequency ( $\omega_p = 0.27$  rad/sec), and the -3 dB heave bandwidth ( $\omega_{3dB} = 0.36$  rad/sec). When the nominal feedback gains are used, the pitch oscillation mode is well damped, and the augmented heave mode frequency is increased ( $1/T_h = 0.85$  rad/sec). The associated increased heave bandwidth ( $\omega_{3dB} = 0.8$  rad/sec) implies improved command following and disturbance suppression characteristics. Attendant effects on gust-induced structural loads was a central question of the present study and is discussed in the following sections.

Additional increases in the vertical velocity feedback gain results in higher bandwidth systems (Fig. 3) with further improvements in the dynamic characteristics. Increased gains result in larger control deflections which may cause surface limiting in heavily loaded conditions. However, for the present unloaded flight condition this is not a problem, even for very high bandwidth systems ( $\omega_{3dB} = 5$  rad/sec).

The gust transfer functions examined in the study were: pitch attitude,  $\theta$ ; vertical acceleration at the hull center of gravity,  $a_z$ ; and vertical constraint force exerted on the hull structure at the attachment point of LPU-1,  $F_{C21}$ . These variables exemplify the motions and loads which are characteristic of the vehicle longitudinal response to turbulence.

#### Pitch Attitude Response

The open- and (nominal) closed-loop pitch attitude responses to vertical gusts on input Source 1,  $\theta/w_g^{s1}$ , are shown in Fig. 4. The vehicle pitch response to input Source 1 is representative of the response of the vehicle to the

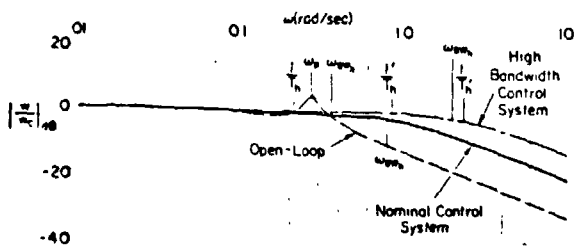


Fig. 3. Vertical velocity response to heave command inputs

ORIGINAL PAGE IS  
OF POOR QUALITY

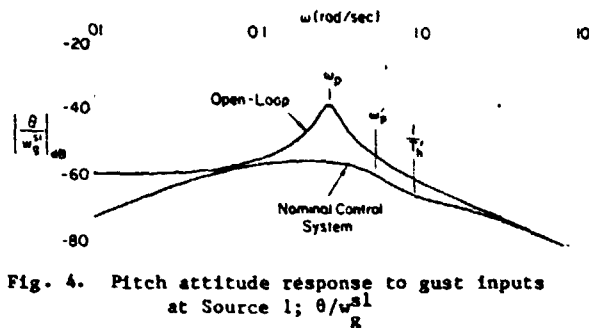


Fig. 4. Pitch attitude response to gust inputs at Source 1;  $\theta/w_g^{s1}$

other gust input sources ( $w_g^{s2}$ ,  $w_g^{s3}$ ,  $w_g^{s4}$ ). This results from the assumed symmetrical distribution of the gust input sources about the hull center of volume, the hull's fore/aft symmetry, and the relatively small tail compared to the hull. The transfer functions for gust inputs Sources 3 and 4 have a slightly higher gain in the high-frequency region. This is due to the unsteady tail forces which are predominantly influenced by the rearward sources ( $s3$ ,  $s4$ ).

Referring to Fig. 4, we note that the open-loop dominant pitch response is at the damped natural pitch oscillation frequency ( $\omega_p$ ) as expected. These results agree with those of DeLaurier,<sup>1</sup> who also showed maximum gust responses at vehicle damped pitch natural frequencies. The peak closed-loop response is significantly reduced from the open-loop case due to the desired function of the pitch attitude control system. In the frequency range above the nominal closed-loop bandwidth ( $\omega_p$  highest closed-loop pole,  $1/T_h$ ), the open- and closed-loop transfer functions are identical; therefore, the initial time responses (i.e., slopes) for both cases will also match. For low-frequency inputs the attitude response asymptotically approaches zero due to the installed trim integrator. These linear results correlate well with nonlinear time histories of Ref. 8 and those presented in the next section.

#### Vertical Acceleration Response

As with the pitch response, the vertical acceleration ( $a_z$ ) transfer functions are quite similar among the four input sources. This again is due to the symmetrical orientation of the sources about the hull center of volume and the small relative size of the tail. The acceleration response to a vertical gust on input Source 1 ( $a_z/w_g^{s1}$ ) is shown in Fig. 5 for the open- and closed-loop systems.

Ignoring the excitation of the pitch oscillation mode ( $\omega_p$ ), we obtain, from Fig. 5, the following approximate relationship between the vehicle open-loop vertical acceleration response and the gust acceleration at input source 1:

$$a_z \approx s \left( \frac{w_g^{s1}}{4} \right) = \frac{\dot{w}_g^{s1}}{4} \quad (1)$$

The approximately identical results of the remaining input sources give:

$$a_z \approx \dot{w}_g \quad (2)$$

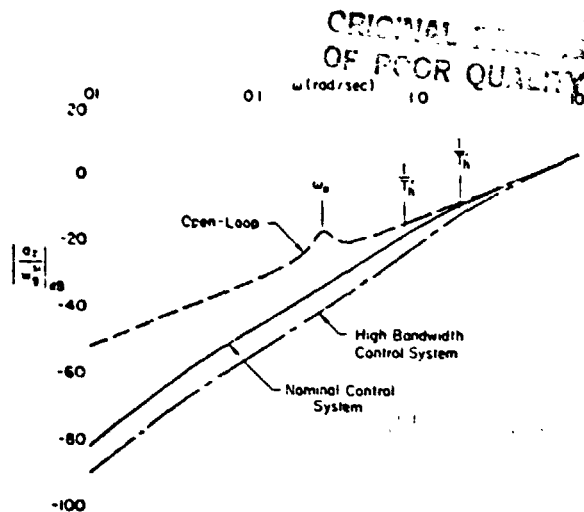


Fig. 5. Vertical acceleration response to gust inputs at Source 1;  $a_z/w_g^s$

where

$$\ddot{u}_g = \frac{(\ddot{u}_g^s1 + \ddot{u}_g^s2 + \ddot{u}_g^s3 + \ddot{u}_g^s4)}{4} \quad (3)$$

Equation 2 indicates that the open-loop vehicle is subject to pure convective motion. This results from the near-neutral buoyancy ratio condition (0.92) of the present vehicle. Analyses by DeLaurier<sup>1</sup> and Nagabhushan<sup>2</sup> verify this conclusion for other neutrally buoyant vehicles. Conceptually, the open-loop vehicle may be considered as a soap bubble or particle in the air mass, connecting with the local motion.

This result is especially important for mooring and other power-off flight conditions; attempts to restrain the vehicle will require the attachment structures between the hull and LPU to absorb the large energy of the local air mass motions. This explains the historical policy of allowing airships to float freely away from the mooring mast in severe turbulence conditions.<sup>3</sup> Also, current Goodyear policy<sup>13</sup> is to allow the moored airship to freely "kite," thereby relieving the otherwise large air mass forces associated with constraining the vehicle against its natural convective motion.

The closed-loop response below the augmented heave mode ( $1/T_h^*$ ) is significantly reduced from the open-loop case due to the desired function of the (nominal) vertical axis control system. The pitch axis control system damps the previous excitation of the open-loop pitch mode ( $w_p$ ). Additional increases in the vertical loop bandwidth are shown in Fig. 5 to further reduce the vertical acceleration gust response. This is expected from the improved command response characteristics shown in Fig. 3. Again, the high-frequency characteristics (above  $1/T_h^*$ ) are unchanged since the unsteady (accelerated flow) aerodynamics of the rotors are neglected.

The retention of significant acceleration responses out to high frequencies suggests potential interaction between the accelerometer measurements and structural (high-frequency modes), possibly causing degradation of the control system effectiveness and resulting gust suppression

performance. Careful attention will have to be paid to insure that the accelerometers are located at appropriate points relative to the mode shapes of the dominant structural modes for appropriately tailored control system/structure interaction.

#### Constraint Force Response

The frequency response of vertical constraint force between the hull and LPU-1 due to gust inputs at Source 1, ( $F_{Cz1}/w_g^s1$ ), is shown in Fig. 6 for the open- and closed-loop vehicle. The high-frequency response of  $F_{Cz1}$  to each of the other remaining gust input sources is nearly identical, again due to the symmetry of the input sources about the hull, the relatively small tail and the constant hull response to gust accelerations. However, the low-frequency characteristics of the remaining transfer functions are quite different, especially near the open-loop pitch mode ( $w_p$ ). This results from the coupling of the constraint force and pitch mode responses due to the rotor damping forces.

Figure 6 shows a significant increase in the constraint force loads from the use of closed-loop control to regulate hull motion against turbulence. For the closure selected in the present study, the mid-frequency load response increases by a factor of 6. Further increases in the vertical gain indicate an inverse relation between vertical acceleration response suppression ( $a_z/w_g$ ) and constraint force response amplification ( $F_{Cz1}/w_g$ ). The limiting condition of a vertically constrained vehicle is being approached with this high bandwidth case.

The increase in constraint loads associated with the higher bandwidth control systems is due to the attempt of the rotors to restrain the hull in the presence of large gust acceleration loads. Reductions in quasi-steady (i.e., velocity dependent crossflow) forces which arise from the closed-loop (stabilized) hull motion are overshadowed by this effect. DeLaurier<sup>1,15</sup> cites such reductions in structural loads on classic airships with increases in control gain since the gust acceleration dependent terms were not included in his dynamic model.

An important conclusion of this analysis is the existence of a direct tradeoff between requirements for precision control and structural integrity. This will be especially important for the hover and near-hover precision control tasks which are essential to the Heavy Lift Airship logging and payload positioning roles. Design and performance specifications for these vehicles need to include this tradeoff.

#### V. Statistical Response to Turbulence

The statistics of the vertical acceleration ( $a_z$ ) and vertical constraint force at LPU-1 ( $F_{Cz1}$ ) response to statistical turbulence were evaluated for the open-loop (control system not engaged) and several closed-loop systems. These analyses were based on the linearized decoupled longitudinal transfer functions of the previous section for a flight condition having an airspeed ( $V$ ) of 44 ft/sec (30 mph), with a headwind of 30 ft/sec (20 mph), resulting in a groundspeed ( $V_0$ ) of 14 ft/sec (10 mph). The statistical analysis was

ORIGINAL PAGE IS  
OF POOR QUALITY

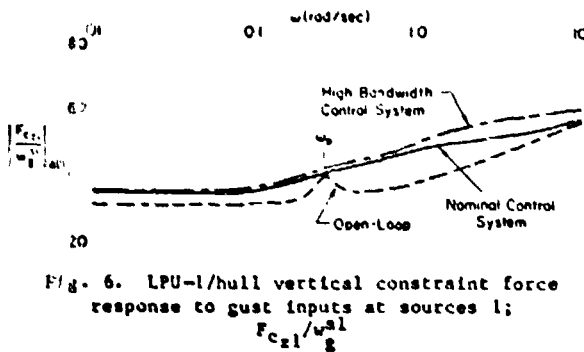


Fig. 6. LPU-1/hull vertical constraint force response to gust inputs at sources 1;

computed using the following simplified first order approximation of the Dryden spectrum:<sup>12</sup>

$$\sigma_{w_g}^2 = \sigma_w^2 \left( \frac{3V_{t1}}{Lw_g} \right) \left[ \frac{1}{s + (3V_{t1}/2Lw_g)} \right]^2 \quad (4)$$

The following numerical values were selected, based on the guidelines given in Ref. 10, for the given flight condition at an altitude of 2000 ft:

- $\sigma_w = 6.4 \text{ ft/sec}$
- Intensity level for "moderate turbulence"
- $Lw_g = 1750 \text{ ft}$
- Turbulence scale length,

As previously discussed, the assumed applicability of the four-point atmospheric input model is limited to turbulent wavelengths not exceeding two body lengths. In order to restrict the calculation of statistics to wavelengths within this limitation, a standard third-order Butterworth filter was used to truncate the input power spectral density function of Eq. 4. For the present flight condition, the Butterworth cutoff frequency is  $\omega_c = 31.1/2L = 0.57 \text{ rad/sec}$ . Note that this cutoff frequency is a decade above the break frequency of the (simplified) Dryden input power spectral density filter; hence, the truncation of the spectrum will not represent a severe restriction of the analyses for this flight condition. The following truncated input power spectral density function is obtained by combining the simplified Dryden model with the Butterworth filter:

$$\sigma_{w_g}^2 = \sigma_w^2 \left[ \frac{\omega_c^3}{(s + \omega_c)(s^2 + \omega_c s + \omega_c^2)} \right] \quad (5)$$

where the asterisk denotes that the input power spectrum has been truncated.

The output root mean square (rms) value for a response to a specific gust input source is obtained as follows:

$$\sigma^2 = \int_0^\infty |G(j\omega)|^2 d\omega \quad (6)$$

where  $G(j\omega)$  are the complex transfer functions, typified by  $(a_z/w_g^{s1})$  and  $(F_{Cz1}/w_g^{s1})$ , discussed earlier.

The total response to all four gust input sources is obtained by superposition, as explained earlier. For example, the total vertical acceleration rms response ( $\sigma_{a_z}$ ) is calculated from:

$$\sigma_{a_z} = [\sigma^2(a_z/w_g^{s1}) + \sigma^2(a_z/w_g^{s2}) + \sigma^2(a_z/w_g^{s3}) + \sigma^2(a_z/w_g^{s4})]^{1/2} \quad (7)$$

A statistical analysis of vertical acceleration and constraint force response to turbulence was completed. The output rms levels were normalized by the turbulence intensity ( $\sigma_w$ ) and converted to decibels (dB) to allow easy scaling to other intensity levels. These results are shown in Fig. 7 as a function of the heave control system bandwidth,  $\omega_{gw_h}$ .

As expected from the previous transfer function results, the vertical acceleration rms response decreases with increasing closed-loop bandwidth. Associated with this acceleration response reduction is an increase in the constraint force response. As the gain (and associated bandwidth) of the heave control system is increased, the acceleration response asymptotically approaches zero as the constraint force response approaches a constant value. These asymptotic values are representative of a vertically constrained condition (i.e., infinite closed-loop bandwidth).

The assumption of a constrained condition would provide a simplified approach for specifying extreme random load design requirements, e.g., for fatigue and failure mode analyses. Such assumptions have been previously used to determine structural loads on classical airships.<sup>14</sup> One possible design requirement might be the 2g constraint-force level, which could be expected roughly 2 percent of the time in a given turbulence flight condition. For the present flight condition, the 47.7 dB ratio of  $\sigma_{F_{Cz1}}/\sigma_w$  shown in Fig. 7 indicates a 2g requirement of 3100 lb (above trim). This criterion does not appear to be an overly conservative estimate of the nominal closed-loop level for statistical loads analyses. However, the results in the next section show that, for discrete turbulence encounters, a design requirement based on constrained motion would be very stringent, leading to an undesirably heavy structure.

The results of these statistical analyses reemphasize the previous transfer function results concerning the tradeoff between requirements for response suppression and structural integrity. A significant increase in the constraint forces occurs with the implementation of any inertially referenced closed-loop control systems. This suggests that the low speed and precision hover

## CHAPTER 15 OF REPORT NO. 15

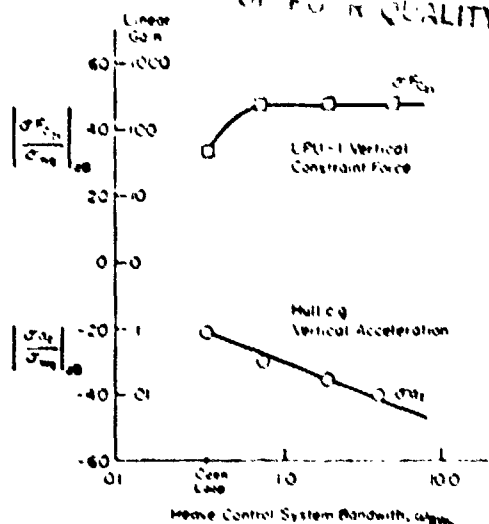


Fig. 7. Statistical response to turbulence

tasks, which require large flight control bandwidths, are critical for both disturbance suppression and structural load considerations. Further analyses are required to examine the moored flight condition, where large nose loads are expected to occur from the partially constrained condition.

### VI. Vehicle Nonlinear Response to a Tuned Discrete Gust Input

The discrete gust input is designed to excite the vehicle at its natural pitch and roll mode frequencies to provide information on critical motions and loads. This is conveniently done by having the vehicle encounter an obliquely oriented traveling upgust wave, whose celerity (inertially referenced crest velocity), wavelength, and relative heading, are adjusted to maximally and simultaneously excite the pitch and roll modes. Here, the wave is simulated by applying a tuned series of  $(1 - \cosine)$  gusts at the four input sources, and by properly selecting the wavelength and timing. The procedure is summarized in Fig. 8.

The present flight condition is an airspeed of 40 ft/sec and a windspeed of 10 ft/sec; the natural frequencies are 0.27 rad/sec in pitch and 0.47 rad/sec in roll. With the symmetrical 100 ft spacing of the gust input sources, the procedure yields an apparent wave encounter ( $\theta_w$ ) angle of 27 deg from the nose (Fig. 2), a crest celerity ( $C_w$ ) of 5.4 ft/sec (Fig. 2), and (overlapping) input periods of 5 sec for each source (Fig. 7). The selected peak gust magnitude of 13.4 ft/sec results in the four gust inputs (one at each input source) which are shown in Fig. 8. This peak gust value is 17 percent of the mean windspeed of 10 ft/sec. It was obtained from the Mil Spec requirements to be consistent with the previous statistical rms level for free air turbulence.

Peak  $(1 - \cosine)$  values expected in thunderstorm encounters by conventional aircraft are specified as a function of airspeed in the Mil Spec. An alternate peak value based on typical

airship scenarios has been proposed.<sup>3</sup> The selection of an appropriate thunderstorm peak value and vehicle penetration airspeed is crucial to the resulting load requirements and depends largely on the specific mission and allowable operational weather conditions. For the present generic study, an analysis of extreme gust encounters has not been completed; however, the trends obtained using the moderate 13.4 ft/sec gust are representative of the results that may be expected for more severe gust levels.

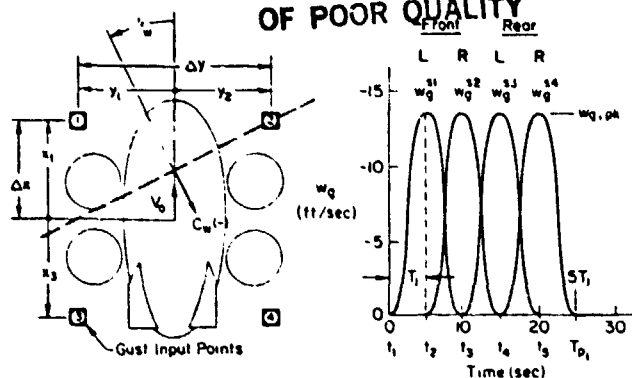
The open-loop pitch ( $\theta$ ) and roll ( $\phi$ ) responses (dashed lines in Figs. 9a and 9b) to the 13.4 ft/sec peak upgust show that the vehicle is being excited at its damped natural frequencies. As expected from the linearized responses, the attitude and acceleration excursions (Figs. 9a-9c) are significantly reduced due to the desired operation of the closed-loop flight control system. Strictly speaking, the oblique upgust parameters should be returned to the closed-loop natural frequencies, but this was not done here.

In the open-loop case, the vertical constraint force in LPU-1 (Fig. 9d) responds at the same frequency (but roughly 180 deg out of phase) as the (open-loop) pitch response. A significant increase in the constraint force excursions and frequency results from the operation of the closed-loop system with the transient forces (from trim values) rising from about 600 to over 2300 lb. This is largely due to the attempt of the rotors to restrain the vehicle in the presence of large relative air-to-hull acceleration loads on the hull. The importance of these unsteady aerodynamic loads, compared with the quasi-steady forces (those due to relative velocities), has been previously discussed and demonstrated.<sup>8</sup> The gradual rise in the open-loop constraint force, at the end of the time history, arises from the steady increase in relative vertical airspeed due to unstable vehicle lateral characteristics<sup>9</sup> as reflected in Figs. 9a and 9b.

As discussed earlier herein, increasing the tightness (bandwidth) of the closed-loop system causes the constraint forces to approach the limiting values for an inertially restrained vehicle. Then the forces are just those that arise from the gust inputs. For the selected flight condition and discrete gust inputs, this limiting case yields a maximum constraint force load of 19,500 lb. The incremental load of 13,000 lb (above trim) is five times that (2300 lb) obtained for the nominal control system. While the constrained vehicle approximation provides a reasonable estimate for statistical turbulence analyses, this approximation is seen to be overly conservative for the analysis of discrete gust encounters, thereby leading to an over-designed structure. Especially unrealistic loads are to be expected from similar analyses of thunderstorm level discrete gust encounters where peak  $(1 - \cosine)$  values exceed 35 ft/sec.<sup>1,10</sup>

The constrained vehicle calculation suggests that large loads would be imparted to a vehicle in a fully restrained mooring condition. The necessity of allowing unrestrained angular motion to relieve the otherwise large nose moments suggests the advantage of utilizing a mooring system which allows increased, but properly impeded, linear motion to relieve the associated nose forces.

ORIGINAL PAGE IS  
OF POOR QUALITY



1. SELECT

- a. Type: "Semi-diagonal" upgust; roll frequency  $\hat{=} 2 \times$  pitch frequency
- b. Dominant Pitch Period:  $T_p = 2\pi/\omega_p$  (open-loop;  $\omega_p + \omega_p'$  for closed-loop)
- c. Peak Magnitude:  $w_{g, pk} = f(\text{weather condition})$ , e.g., Mil-F-8785-C, Para. 3.7  
or  
for  $\hat{=} 0.1g$  of vertical air-mass acceleration:  $w_{g, pk|0.1g} \hat{=} 3T_1$  (ft/sec)
- d. Flight Condition: Airspeed =  $V_a$  (ft/sec); Groundspeed along x-body axis =  $V_o$  (ft/sec)

2. COMPUTE:

- a. Overall Pitch Node Period:  $5T_1 = T_p$
- b. Rise Time  $\hat{=} 3$  Peak spacing:  $T_1 \hat{=} 0.4 \pi/\omega_p$
- c. Onset Times:  $t_1 = 0$ ;  $t_2 = T_1$ ;  $t_3 = 2T_1$ ;  $t_4 = 3T_1$
- d. Waveform ( $i = 1, 2, 3, 4$ ):

$$w_g^i(t) = \begin{cases} 0 & ; \quad t < t_i \\ 0.5 w_{g, pk} [1 - \cos \{\pi(t - t_i)/T_1\}] & ; \quad t_i \leq t \leq t_i + 2T_1 \\ 0 & ; \quad t > t_i + 2T_1 \end{cases}$$

- e. Transient Computation Period:  $2T_p \hat{=} 10T_1$

3. OBLIQUE WAVE PROPERTIES (not required for simulation):

- a. Encounter angle from nose:  $\psi_w = \tan^{-1}(\Delta x/\Delta y)$  (deg)  
where  $\Delta x = 0.5(x_1 - x_3)$  ;  $\Delta y = y_2 - y_1$  (ft)  
 $x_1, y_2$  are positive quantities as shown above; and  $x_3, y_1$  are negative quantities as shown above
- b. Apparent wave celerity (crest velocity with respect to HLA; negative means traveling backwards past hull)  
 $C_{w, a} = (-\Delta x/T_1) \cos \psi_w$
- c. Inertial wave celerity (crest velocity with respect to ground; positive means traveling same direction past hull as  $V_o$ )  
 $C_w = (V_o - \Delta x/T_1) \cos \psi_w$

Fig. 8. Tuned oblique traveling upgust relationships

ORIGINAL PAGE IS  
OF POOR QUALITY

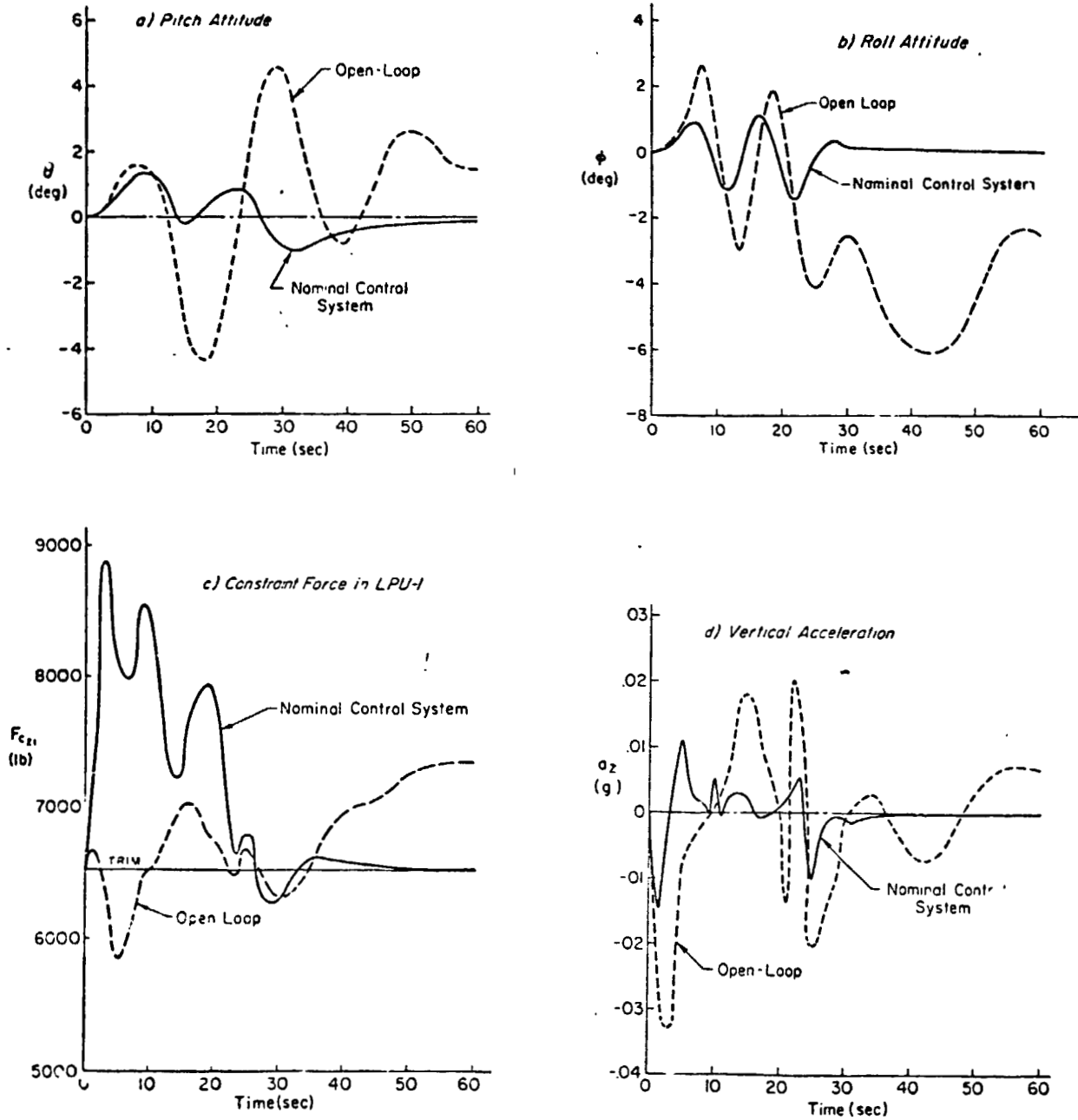


Fig. 9. Nonlinear open- and closed-loop responses to a tuned traveling oblique upgust

The nonlinear time history responses underscore the results of the previous linearized analysis. The responses verify the earlier conclusion that a (closed-loop) reduction in acceleration response due to gust inputs is gained at the expense of significant transient increases in the constraint forces between the LPUs and the hull. Further increases in control system tightness accentuate this penalty. The increase in the constraint force frequency characteristics reflects higher loop bandwidths and implies increased fatigue loads in the LPU and hull support structure. These fundamentally opposing trends require consideration in the flight control system performance and design load specification process.

### VII. Conclusions

An analysis of typical quad-rotor heavy-lift airship motions and loads due to atmospheric disturbance was completed. The results presented in this paper revealed the following conclusions:

1. Vehicle motions due to gust responses were maximum at frequencies corresponding to those of the airship's natural motions.
2. Loads between the rotor units and hull are dominated by static (trim) loads and the unsteady aerodynamic hull forces due to its acceleration relative to the gusting air mass.
3. Implementation of a multi-axis closed-loop control system causes a significant reduction in the vehicle dynamic motion to statistical and discrete gust inputs, but also causes large increases in the transient constraint forces between the hull and LPUs.
4. The loads computed by assuming that the vehicle is fully constrained by the lift/propulsion unit arms are overly conservative for cruise calculations, but suggest the advantages of a compliant mooring system which would allow some linear motion, impeded in a proper manner.
5. An extension of the aircraft MIL Spec discrete tuned (1 - cosine) gust input for loads requirements is suggested. It simulates the effects of an oblique traveling upgust wave, tuned to simultaneously excite both pitch and roll dominant modes, for which constraint forces are worst.
6. The existence of tradeoffs between tight vehicle response and resulting increases in vehicle constraint forces suggests that closer attention than usual needs to be paid to operations in the low speed and hover flight regimes where gust responses are most significant. Future studies should focus on:
  - a. Opening up of motion tolerances for precision hover and load handling, e.g., by different load handling techniques.
  - b. Flight control laws that allow some high-frequency vehicle attitude and linear motions while constraining the low-frequency linear motions.
  - c. Hull and tail gust load relief (e.g., via tail controls responsive to hull gust angles or loads.)

### Acknowledgment

The work reported in this paper was sponsored by the National Aeronautics and Space Administration under Contract NAS2-10330. The Project Monitor was Peter D. Talbot.

### References

- <sup>1</sup>DeLaurier, J. D., and K. C. K. Hui, "Airship Survivability in Atmospheric Turbulence," A Collection of Technical Papers; Proc. of AIAA Lighter-Than-Air Systems Technology Conference, Annapolis, MD, 8-10 July 1981, pp. 48-61.
- <sup>2</sup>Nagabhushan, B. L., and N. P. Tomlinson, "Dynamics and Control of a Heavy Lift Airship in Cross Wind Hover," A Collection of Technical Papers; Proc. of AIAA Lighter-Than-Air Systems Technology Conference, Annapolis, MD, 8-10 July 1981, pp. 90-95.
- <sup>3</sup>Troller, T. H., "Airships in Gusts: Apprehensions and Assurance," Proc. of AIAA Lighter Than Air Technology Conference, AIAA Paper 75-951, 15-17 July 1975.
- <sup>4</sup>Bailey, David B., and Harold K. Rappoport, Maritime Patrol Airship Study (MPAS), NADC-80149-60, 19 Mar. 1980.
- <sup>5</sup>Ardema, Mark D., Vehicle Concepts and Technology Requirements for Buoyant Heavy-Lift Systems, NASA TP 1921, Sept. 1981.
- <sup>6</sup>Fries, Gordon H., and John J. Schneider, "HLH and Beyond," SAE Paper 791086, presented at Aerospace Meeting, Los Angeles, Dec. 1979.
- <sup>7</sup>Ringland, Robert F., Mark B. Tischler, Henry R. Jex, et al., Flight Dynamics Analysis and Simulation of Heavy Lift Airships, Systems Technology, Inc., TR-1151-2, forthcoming.
- <sup>8</sup>Tischler, M. B., H. R. Jex, and R. F. Ringland, "Simulation of Heavy Lift Airship Dynamics over Large Ranges of Incidence and Speed," A Collection of Technical Papers; AIAA Lighter-Than-Air Systems Technology Conference, Annapolis, MD, 8-10 July 1981, pp. 96-115.
- <sup>9</sup>Etkin, Bernard, "The Turbulence Wind and Its Effect on Flight," UTIAS Review 44, Aug. 1980 (AIAA Wright Brothers Lecture, 1980; summarized in AIAA Paper 80-1836).
- <sup>10</sup>"Flying Qualities of Piloted Airplanes," MIL-F-8785C, 5 Nov. 1980.
- <sup>11</sup>Holley, William E., and Arthur E. Bryson, Jr., Wind Modeling and Lateral Aircraft Control for Automatic Landing, Stanford U., Rept. SUDAAR No. 489, Jan. 1975.
- <sup>12</sup>Jewell, Wayne F., Gust Response of the Super King Air 200 Aircraft, Systems Technology, Inc. TR-2139-2R, Oct. 1981.
- <sup>13</sup>Preliminary Study of Ground Handling Characteristics of Buoyant Quad Rotor (BQR) Vehicles, NASA CR-166130, July 1980.
- <sup>14</sup>Burgess, C. P., Airship Design, New York, Ronald Press Co., 1927.
- <sup>15</sup>DeLaurier, J. D., D. M. Schenck, and C. K. Hui, An Investigation of the Operational Reliability of Large Airships in Regularly-Scheduled Missions, Research Report 68, Apr. 1980.